E-740

Color Coherent Radiation in Multi-Jet Events from $p\bar{p}$ Collisions at $\sqrt{s} = 1.8$ TeV

by

David E. Cullen-Vidal

B.A., The Johns Hopkins University, 1986
Sc.M., Brown University, 1990

Thesis

Submitted in partial fulfillment of the requirements for
the Degree of Doctor of Philosophy
in the Department of Physics at Brown University

March 1997

Abstract of "Color Coherent Radiation in Multi-Jet Events from $p\bar{p}$ Collisions at $\sqrt{s} = 1.8$ TeV," by David E. Cullen-Vidal, Ph.D., Brown University, March 1997

Results from a study of color coherence phenomena in multi-jet events produced by $p\bar{p}$ collisions are presented. Approximately 13 pb^{-1} of data were collected by the DØ detector during the 1992–1993 run of the Fermilab Tevatron $p\bar{p}$ collider at a center of mass energy of $\sqrt{s} = 1.8$ TeV. Demonstration of initial-to-final state color interference effects is done by measuring spatial correlations between the softer third jet and the second leading-E_T jet in the events. The data are compared to several Monte Carlo simulations with different color coherence implementations and to the predictions of a Next-to-Leading Order parton level calculation.

Thesis 1997

AAF 2012
Jets (Nuclear physics)
Radiation.

This dissertation by David E. Cullen-Vidal is accepted in its present form by
the Department of Physics as satisfying the
dissertation requirement for the degree of
Doctor of Philosophy

Date April 29, 1997 Dave Cutts

Dave Cutts, Director

Recommended to the Graduate Council

Date 29 April 1997 H. M. Fried

Herbert Fried, Reader

Date April 29, 1997 Richard Partridge

Richard Partridge, Reader

Approved by the Graduate Council

Date .....

.....

Peder J. Estrup, Dean of the Graduate School and Research

To Eneida, who makes it all worthwhile...

La Nada

En la intersección de las calles Una y Otra del Viejo Más Allá, vivía una Señora Cualquiera que solía cantar y gustaba soñar. Ella, como muchas otras, no distinguía el día de la noche ni la soledad de la amistad, la juventud de la vejez ni los sueños de la realidad; tampoco la vida de la muerte ni la Una de la Otra.

Sentada en su balcón, podía ella ver claramente todo a su alrededor; hasta los más lejanos tejados del Viejo Más Allá. Divisaba desde allí los otros balcones de la antigua ciudad y a las señoras que éstos contenían. A veces, notando el lejano rostro que otra dirigía hacia ella, saludaba. Otras veces era ella la saludada por un rostro diminuto y extraño que no podía reconocer.

Así, sin sentir frío ni calor, meciendóse en el sillón de la vida y observando desde su balcón todo a su entorno en el teatro de las iluciones, pasaba ella sus noches-mañanas-días-tardes escuchando atentamente el silencio o ruido cotidiano del vecindario que la intoxicaba y la bañaba con su ardor de la nada.

Un día o noche observó ella algo nunca antes visto. Cerca de la luna o el sol fijó su vista a las siluetas de unos delfines que volaban en elipses sobre su balcón. No pudo contener lo que sentía y bajó apresurada a la calle. Siguío a las siluetas misteriosas que la conducían hacia el mar por la Una o por la Otra; viejas calles de adoquines grises donde brotaban los murmullos silentes de los que allí ya no transitaban ni extistían y de los rostros que observaban desde los balcones distantes sin saludar.

Al llegar a la orilla del gran Océano, sintió la cálida sonrisa del sol unirse a las palmadas húmedas del viento que le susurraban la bienvenida dulcemente. Adentrándose al celoso mar que la abrazaba a la misma vez que la iba absorbiendo, notó, por primera vez, que los lazos que mantenían su futuro y su pasado unidos y

prisioneros allí se disolvían. En las serenas profundidades del oscuro mar palpó una gran tranquilidad hasta que fué agitada suavemente por unas juguetonas cotorras que allí nadaban y que ella destinó seguir. Con sus cantos marinos, estas aves de colores brillantes la condujeron a una ciudad desolada donde se unían muchas calles parecidas. En una de esas intersecciones ella, hallándose sin saber si era de noche o de día, se adentró en un edificio vacío y se detuvo en un viejo balcón. Como solo había un mueble allí, se sentó en él y comenzó a mecerse a la vez que observaba todo a su alrededor. Divisaba desde allí los otros balcones de la antigua ciudad y notó que un lejano rostro indistinguible que otra dirigía hacia ella la saludaba.

David E. Cullen-Vidal

16 de julio de 1986

San Juan, Puerto Rico

Acknowledgments

I wish to thank all who in one way or another helped to bring this dissertation to life. The list of those who did so, either directly or indirectly, is impossibly long so I will start off by apologizing to — and thanking — those whose names do not appear here but should have been mentioned.

What is a graduate student (or a thesis) without an advisor? Dave Cutts gave me the opportunity to enter the world of high energy physics, allowed me to work on a number of interesting and challenging projects, encouraged and supported me throughout this process and displayed remarkable patience and understanding as the writing of the dissertation kept being interrupted by the latest and greatest developments in the analysis. Dave, your probing questions and timely suggestions helped me gain a better understanding of the subject matter and of how to best communicate it. Thanks for everything you've done. I hope to make you proud some day.

To Nikos Varelas I owe a very special thanks. Soon after arriving at DØ, he decided to take on the difficult task of working on and coordinating the color coherence analyses which were then in progress, and to see them through to fruition. At the time, I'm sure he didn't know how much sleep he would lose as a consequence of this decision. Sometimes it's better not to know... Nikos, became intimately involved with color coherence and contributed many valuable ideas and countless questions which helped solidify this analysis and above all showed me how to relentlessly tackle a task and look at any given problem from at least seven different perspectives. I am very fortunate to have had the chance of working with you and can only hope

that I'm not solely responsible for your hair loss. Please receive my best wishes in your new and well-deserved capacity, Professor Varelas!

On any voyage, one needs solid landmarks and good reference points to help guide one's navigation through unfamiliar terrain. Jerry Blazey was my compass when I needed him the most — during my transition from detector work into real physics analysis. This occurred at a somewhat chaotic junction in the halcyon days of DØ when many things and people at the experiment were new and constantly in flux as the building and commissioning of the detector metamorphosed into actual data taking. Jerry acted as the dynamic, de facto on-site advisor to many students in the QCD group, including me — a superhuman task I still don't know how he managed to balance together with the tons of other responsibilities he fulfilled. Jerry was the one who brought the subject of color coherence to my attention, made sure I was moving in the right direction as the analysis germinated and was always available for impromptu discussions. Throughout, he remained interested in this analysis and, in turn, was repaid by having to proofread a barrage of successive revisions of the physics note, each one longer than the one before it. Well Jerry, there are no more revisions now and here is the final result! I am most grateful for your energy, your dedication and for your efforts in showing me the way.

Many thanks to professors Richard Partridge and Herbert Fried for graciously accepting my last-minute invitation to sit on my thesis committee and for their participation during the defense on that wintry snowing March morning in Providence, Rhode Island. Thanks, Rich for proofreading the thesis and finding errors that may have otherwise slipped by unnoticed. I also wish to thank the entire Brown high energy physics group for its vital support of my research.

I would like to express my gratitude to the members of my editorial board who patiently survived innumerable meetings in which I showed up with more questions than answers. Harry Melanson provided continuity and balance along with many valid questions (and solutions!) and was an excellent sounding board (and a great source) for numerous ideas. Sharon Hagopian brought her expertise to bear on the analysis and helped to make it that much stronger by keeping a watchful eye on the developments and by providing very useful feedback.

I am also thankful to Torbjörn Sjöstrand for his help in unraveling the features of his creation, PYTHIA, and for interesting and helpful discussions.

I wish to express my appreciation for Harry Weerts, the original leader of the QCD group, a very classy individual, and a great example of what a person, who is a physicist, can be.

In my earlier days at DØ, I had the good fortune to work with one of Harry's disciples, Rich Astur ("Mr. Jet"), on a number of projects which provided a useful introduction into the world of jet physics. Rich, I wish you well wherever you may go.

Special thanks to Freedy Nang, with whom I've shared many important moments dating back to our first days as young graduate students at Brown (has it been that long already?). Another 'Brownie', my officemate Tom Fahland, demonstrated how physics and gambling are not mutually exclusive while blazing his own path in life. Keep hanging dude...

I have had the opportunity to meet many wonderful individuals and to make a number of lasting friendships in my time at Fermilab. Cary, Colleen and Emily Yoshikawa have become part of my extended family as have Andrew, Mary, Jan

and Lawrence Brandt. To Daniel Elvira and Cecilia Gerber and to Azriel and Elisa Goldschmidt, I wish you all the best. Having Gene ("el primo") Álvarez around always made things more interesting — and much more fun.

Swimming beside me on the color coherence swimathon was Jim Jaques, an honorary Oak Parker-for-life, who along with his wife Kelly, I'm very happy to be able to call friends. Thanks to you both from Eneida and from me for making life here more enjoyable. See you in the land of the Rude People!

There are a number of very dedicated, capable and determined people without any of whom the success of the DØ experiment would have been in question. Jan and Joan Guida certainly belong to this group, along with Dean Schamberger. All three managed to frequently skip meals and sleep (specially when they all worked together) while dealing with the latest hardware and software crises. Thanks to each of you!

A very special individual at DØ Herman Haggerty, seems to find funny and amazing things at every turn. Herman, thank you for helping me find my way around DØ upon my arrival and for demonstrating that fun is all around us.

To my buddies in the Fermilab gym who have livened up many dreary Illinois evenings: Carl, Ryan, Tony, Lenny, Rick, Steve and Linden I say: "Anyone up for another game?"

For many years, Jean Miller was my lifeline to Brown. She smoothly and reliably handled the myriad checks, travel reports and miscellaneous administrative chores without which my survival would have been in doubt. Thanks Jean! You have certainly earned a well deserved break from all that extra work.

To Dean Bruce, my very special thanks for his personal concern and involvement

dating back to the time he spent a couple of hours on the phone with my mother trying to explain why I should go to graduate school at Brown and consequently following through and finding the funding that made it all possible. He has always been extremely supportive of students and continues to leave his door wide open for anyone to come in.

Of the many outstanding teachers I've had, I must thank three who had a particularly lasting impact on me. Mariloly López, my high school chemistry teacher, gave so much of herself in each and every class, I thought she would run dry. She taught and, above all else, inspired me to reach for the stars. I can't thank you enough for giving so much of yourself to your students. Professor Marya Axtmann taught me in one year of senior English, what I hadn't learned before: to truly love and appreciate good writing. I consider myself privileged to know you, Marya. Professor Alfredo Torruella exemplified what I thought a physicist should be. In a year's worth of physics, he seemed to never look at his notes nor at the textbook as he made all derivations from scratch and very elegantly, finishing each class just seconds before the bell. Well, after all, he is a theorist you know...

No achievement is complete without sharing it with those who feel the greatest pride by it. To my mother Alicia and to my father David, it is not enough to say thank you. I am satisfied that you can finally see this dream become a reality.

Thanks to my great family-in-law who were always on my side because I was, in their own words, "colliding molecules". I am grateful for their support, encouragement and good humor and for accepting me as part of the family.

Finally, thanks to my loving wife Eneida who was so understanding and helpful during the writing of this thesis that I am now considering writing another one —

NOT!!! Eneida, you have given me so much and in such a special way that I can't imagine doing this without you. This accomplishment is so much more meaningful, thanks to you.

Contents

List of Tables

List of Figures

Chapter 1

Introduction

Throughout the ages, our human ancestors have pondered a variety of fundamental questions about the physical universe. Driven by curiosity and by the need to better understand their natural world, they posed countless questions, many not yet fully answered: How big is our universe? What is it composed of? Why does it behave in this way? Are there any rules which can explain what we observe?

High energy particle physics attempts to carefully answer some of these fundamental questions, in particular the last three. In the process of revealing the answers layer by layer, it also aims to shed some light on other relevant issues about our physical world that remain obscure. Our challenge is to understand the fundamental building blocks of matter and the forces that govern their interactions. The two complementary methods by which this understanding is advanced are the experimental observation and the theoretical consideration of natural phenomena.

This dissertation will report the results of an experimental analysis of data within the framework of a theoretical model in particle physics. It involves color coherent radiation from hadronic collisions. The model studied will be described in the next

chapter in greater detail. What follows now is a brief, and out of necessity, incomplete, description of high energy particle physics.

1.1 Early Beginnings...

The earliest written records of man thinking logically about the components of matter date back roughly 2400 years [1]. In the $5^{\underline{\text{th}}}$ century B.C., the Greek philosphers Democritus and Leucippus proposed that matter was made up of tiny indivisible particles in constant motion. The term "atom", meaning unbreakable or indivisible was used to refer to these particles. Democritus believed that nothing happens through chance and intention; that everything happens through cause and necessity. Furthermore, he stated that change is merely an aggregation or separation of parts and that nothing which exists can be reduced to nothing, and conversely, that nothing can come out of nothing.

And out of these early beginnings — through centuries of careful observation, experimentation and theorization, and aided by great moments of intuition, simple elegance and beauty, but not without undergoing much change and turmoil — developed our present understanding of the physical world.

1.2 Symmetry and the Quark Model

Following the birth of elementary particle physics in the late 19^{th} century with J. J. Thomson's discovery of the electron and the subsequent postulate on the quantizing of energy by Max Planck, modern physics entered an extremely challenging period of rapid growth which ultimately changed in a most fundamental way how we view

nature. The theories of Special and General Relativity, the development of Quantum Mechanics and the subsequent attempts to unify the fundamental forces of nature under a single theoretical mantle laid the foundation which led to the development of the Quark Model in the second half of the 20^{th} century.

By the start of the 1960's the field of particle physics was reaching maturity. Many particles had been discovered and were organized loosely into groups according to their masses: the light leptons (e.g., electrons, muons and neutrinos), the medium-weight mesons (e.g., pions and kaons) and the heavy baryons (e.g., protons and neutrons.) Mesons and baryons were further classified as hadrons: particles that interact by means of the strong force. Hideki Yukawa had, decades earlier, developed a theory for strong interactions, which describes the strong force as the one responsible for binding protons and neutrons to each other in an atomic nucleus and acting only over a very short distance. Nevertheless, the bewildering variety of known particles continued to grow and there was no structured relationship among them beyond the conservation of certain quantum numbers (e.g., charge, lepton and baryon numbers, spin and strangeness [1].)

An important step towards establishing order was taken in 1961 with the introduction of *The Eightfold Way* (named after Buddha's *Eightfold Path to Enlightenment*) by Gell-Mann and Yuval Ne'man [2]. The Eightfold Way classified the known particles into families by taking advantage of some inherent symmetries and arranging them in two-dimensional geometric figures. Figure 1.1 shows one such figure for

[1] Strangeness was introduced by Murray Gell-Mann and by Kazuhiko Nishijima, independently, in 1953 as a quantum number to describe particles that were produced via strong interactions and which decayed slowly by means of the weak interaction (e.g., K mesons.) Particles would be assigned a strangeness of ± 1 or 0. Strangeness was later found *not* to be conserved in the weak decay of single strange particles into non-strange particles.

the ground state (s-wave) baryon octet in which the strangeness (S) and the charge (Q) are related for the lightest baryons. Similar configurations were also developed for the lightest mesons.

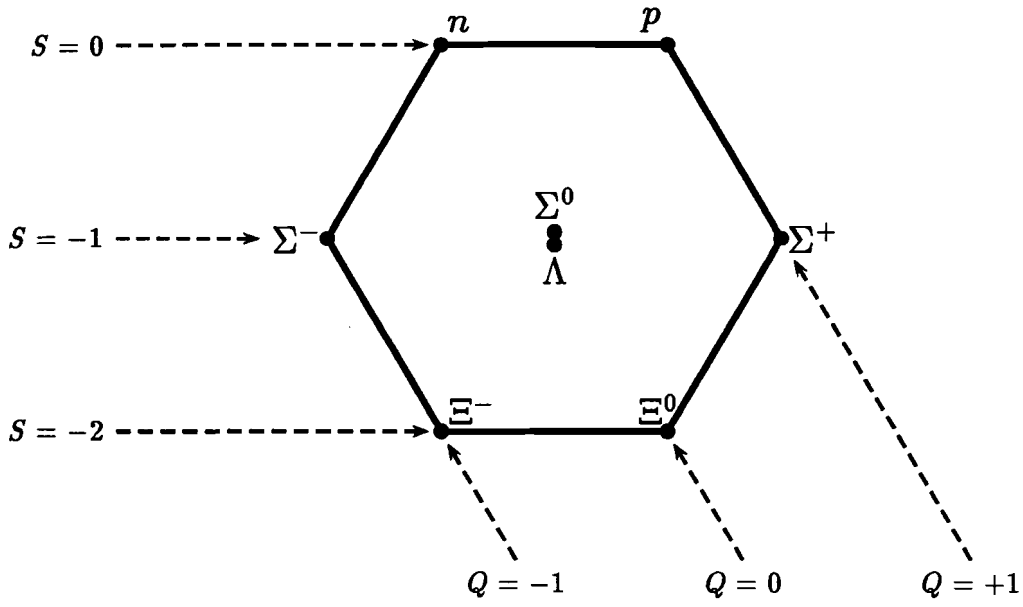

Figure 1.1: Baryon octet. Other representations exist for baryons and mesons, as well (e.g., baryon decuplet, meson nonet.)

The power of this symmetry-based approach is illustrated by the case of the baryon decuplet which had a gap in it since no particle with those properties had been observed. This led Murray Gell-Mann to predict the existence of the Ω^- particle three years before it was found [3]. The Eightfold Way's shortcomings were that it did not provide a rationale for the geometric relationships among the hadrons. That reasoning ultimately was provided by Gell-Mann [4] and G. Zweig [5] in 1964 with the Quark Model. In it, they proposed that all hadrons are composed of more

fundamental particles, which Gell-Mann termed quarks [2]. According to the Quark Model, baryons consist of three quarks, antibaryons contain three antiquarks, and mesons are made up of one quark and one antiquark. Three different quarks were proposed: the up (u), down (d) and strange (s) quarks. Each quark would have a fractional charge; the d and s quarks have a charge of $Q = -\frac{1}{3}$ and the u quark's charge is $Q = +\frac{2}{3}$. The antiquarks' charge has the opposite sign of the quarks'. The baryon number of each charge is $B = \frac{1}{3}$ and the strangeness of the s quark is $S = -1$, while the other two quarks have $S = 0$. So, through the Quark Model, the baryon octet created by the Eightfold Way can now be understood in terms of quark constituency, as shown in Fig. 1.2.

Experimental evidence for the Quark Model did not appear until 1968, when experiments at the Stanford Linear Accelerator (SLAC) involving collisions of protons and electrons verified that the proton was a composite object and not a point particle, as previously believed. The term *parton* was then used to indicate the components of the proton, rather than quark, since there remained some doubts about the Quark Model. The discovery of the J/ψ particle [6, 7] in 1974 led to the introduction of the *charm* (c) quark, first proposed in 1970 by Sheldon L. Glashow, Jean Iliopoulos and Luciano Maiani [8]. With this latest member, the Quark Model predicted new baryons and mesons which would contain the c quark. As more and more of these new states were observed, the evidence supporting the Quark Model

[2] The term *quark* comes from James Joyce's novel *Finnegans Wake* where the Irish author wrote:

Three quarks for Muster Mark!
Sure he hasn't got much of a bark
And sure any he has it's all beside the mark.

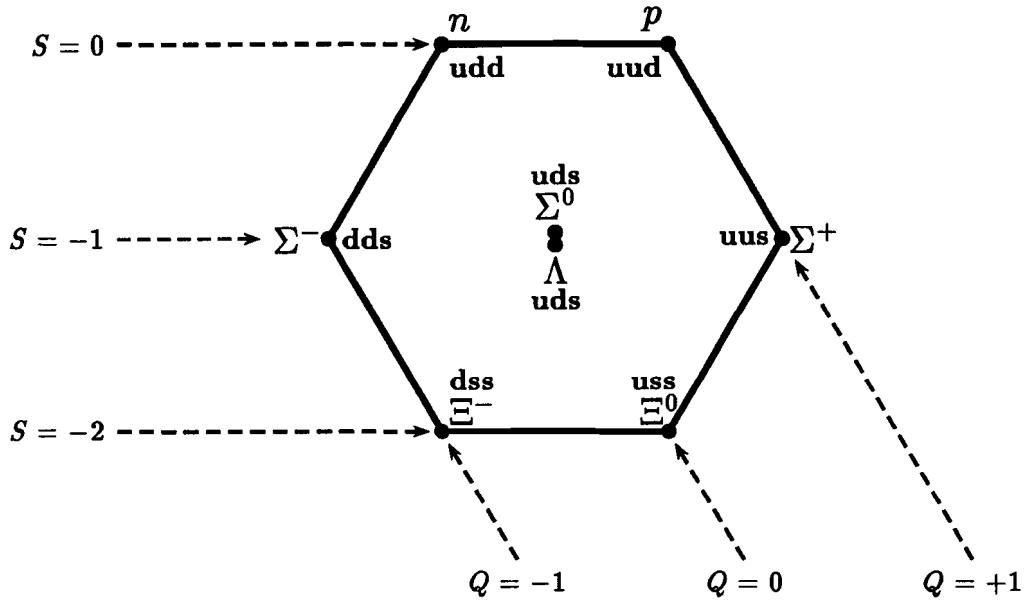

Figure 1.2: Modified baryon octet. Here, the quark composition for each baryon is shown with the baryon symbol. Notice that the number of s quarks scales with strangeness and the number of u quarks scales with charge.

continued to solidify. Thus far, quarks have been observed only in bound states, not as free objects.

1.3 The Standard Model

A necessary requirement in a theory for weak interactions capable of finite calculations is that the model contain the same number of quarks as leptons. This indeed was the case in 1974, as there were four known quarks (u, d, s and c) and four known leptons (e, ν_e, μ and ν_μ.) However, this comfortable balance was disturbed in 1975 by the observation of the τ lepton [9], which implied the existence of a sixth lepton, the tau neutrino (ν_τ), since both the electron and the muon had neutrinos associated with them. A fifth quark, the *bottom* (b), partially restored the balance when the

upsilon particle (Υ), a bound state of b and $\bar{b}$, was discovered in 1977 [10, 11]. However, full restoration of the quark-lepton symmetry did not occur until 1995, when the discovery of a sixth quark, the top (t) quark, was confirmed by the DØ [12] and CDF [13] experiments at Fermilab after years of searching there and elsewhere.

Force	Range (m)	Relative Strength
Strong	10^{-15}	1
Electromagnetic	∞	10^{-2}
Weak	10^{-18}	10^{-6}
Gravitational	∞	10^{-40}

Table 1.1: The fundamental forces of nature.

Quarks and leptons are known to interact with each other through four fundamental forces: the strong force, the weak force, electromagnetism and gravitation. Table 1.1 lists the range and the relative strength of these forces at energies of the order of a GeV. Interactions occur through the exchange of intermediary *vector* or *gauge bosons*. The mediators of the four forces are, respectively, the gluon (g), the $W^{\pm}$ and Z bosons, the photon (γ) and the graviton. They are described in Table 1.2. The graviton has not been observed, and gravity has traditionally been ignored in the study of particle physics due to failures in the attempts to include it in the same theoretical framework (Grand Unified Theories or GUTs) as the other three forces as well as because of its extreme weakness. For reasons that will be discussed later, free gluons have never been observed directly, but significant evidence supports their existence (such as the observation of three-jet events in e^+e^- collisions at PETRA in 1979.) The three weak vector bosons were first observed at CERN in 1983 [14, 15].

This set of elementary particles and fundamental forces currently make up the Standard Model for particle physics. It describes all of the currently known ele-

Force	Carrier	Mass (GeV/c^2)	Spin	Charge
Strong	g	0	1	0
Electromagnetic	γ	0	1	0
Weak	$W^{\pm}$	80.22	1	± 1
	Z^0	91.187	1	0
Gravitational	graviton$^{(a)}$	0	2	0

Table 1.2: The gauge bosons.(a) Not observed yet.

mentary particles (quarks, leptons and vector bosons) and their interactions. It also predicts the existence of additional particles not yet seen (such as the Higgs boson.) Table 1.3 lists the basic properties the currently known quarks and leptons.

1.4 Quantum Chromodynamics

The quantum field theory which describes strong interactions is known as Quantum Chromodynamics (QCD). As in Quantum Electrodynamics (QED), where charged particles interact through photon exchange, QCD describes quark interactions by means of the exchange of massless gluons, which are the charge carriers of the strong force. However, unlike QED, whose charge carriers can have two charges: positive and negative, QCD requires *three* charges, called color, which are carried by both gluons and quarks. The color charges are named "red", "green" and "blue" [3]. Similarly, the anti-color charges are named "anti-red", "anti-green" and "anti-blue". Quarks carry a single color charge while antiquarks carry a single anti-color charge. Gluons on the other hand carry a combination of one color and one anti-color charge, in

[3] After the three primary colors which when combined appropriately can produce any other color, though not uniquely. Other than in their names and number, the color charges bear no relation to actual color or to the visible light spectrum.

Particle Class	Particle Name	Mass (GeV/c^2)	Spin	Weak Isospin[a]	Charge	
					Electric	Color
Quarks	u	0.002 to 0.008	1/2	+1/2	+2/3	R,G,B
	d	0.005 to 0.015	1/2	−1/2	−1/3	R,G,B
	c	1.0 to 1.6	1/2	+1/2	+2/3	R,G,B
	s	0.100 to 0.300	1/2	−1/2	−1/3	R,G,B
	t	175 ± 6	1/2	+1/2	+2/3	R,G,B
	b	4.1 to 4.5	1/2	−1/2	−1/3	R,G,B
Leptons	ν_e	$< 1.5 \times 10^{-8}$	1/2	+1/2	0	–
	e	5.11×10^{-4}	1/2	−1/2	−1	–
	ν_μ	$< 1.7 \times 10^{-4}$	1/2	+1/2	0	–
	μ	0.106	1/2	−1/2	−1	–
	$\nu_\tau^{(b)}$	$< 2.4 \times 10^{-2}$	1/2	+1/2	0	–
	τ	1.777	1/2	−1/2	−1	–

Table 1.3: Quarks and leptons in the (Minimal) Standard Model [16].
(a) Weak isospin pertains only to the left-handed helicity states of the quarks and leptons. The right-handed components of quarks and charged leptons do not possess any weak isospin.
(b) Not observed yet.

contrast with photons which are uncharged. Like the electromagnetic charge, color charge is a conserved quantum number.

The color quantum number was proposed [17] in order to solve the spin-statistics problem created by the discovery of the Δ^{++} particle. The Δ^{++} is a baryon composed of three seemingly identical u quarks, each with spin $+\frac{1}{2}$ in an s-wave bound state. Such a state would violate the Pauli Exclusion Principle, which states that no fermions in the same state may have identical quantum numbers. The color quantum number solves this paradox by assigning each quark in the baryon a unique color charge. Quarks, therefore, can have any of three color charges. In the SU(3) group terminology of QCD, quarks are color triplets. Quark bound states (mesons and baryons), on the other hand, are required by theory to have no net color charge

and and to have completely symmetric wavefunctions with respect to color - making them color singlets. The quark configuration of the Δ^{++}, properly symmetrized is written (in the Dirac "bra"-"ket" notation) as:

$$\Delta^{++} = \frac{1}{\sqrt{6}}[|u_R u_G u_B\rangle + |u_B u_R u_G\rangle + |u_G u_B u_R\rangle$$

$$-|u_G u_R u_B\rangle - |u_B u_G u_R\rangle - |u_R u_B u_G\rangle]. \tag{1.1}$$

The existence of the quark color charge was supported by various experiments which measured quantities sensitive to color charge multiplicity. One such experiment was the measurement of the $\pi^o \to \gamma\gamma$ decay rate. The decay rate is given by:

$$\Gamma(\pi^o \to \gamma\gamma) = (\frac{\alpha}{2\pi})[N_c(e_u^2 - e_d^2)]^2 \frac{M_\pi^3}{8\pi f_\pi}, \tag{1.2}$$

where N_c is the number of colors, $e_{u,d}$ are the electromagnetic charges of the u and d quarks, M_π is the π^o mass, f_π is the pion decay constant and $\hbar = c = 1$. For $N_c = 1$ and $N_c = 3$, the predicted decay rates are:

$$\Gamma(\pi^o \to \gamma\gamma) = 0.86eV \quad (N_c = 1)$$

$$\Gamma(\pi^o \to \gamma\gamma) = 7.75eV \quad (N_c = 3). \tag{1.3}$$

The measured [18] value is:

$$\Gamma(\pi^o \to \gamma\gamma) = (7.86 \pm 0.54)eV, \tag{1.4}$$

which is in very good agreement with the $N_c = 3$ predicted rate.

1.4.1 Group Theory Representation

In group theory terminology, QCD is represented by the group $SU(3)$. This group has three degrees of freedom, corresponding to the three colors. The generators of the group are eight linearly independent hermitian 3×3 matrices with determinant $= 1$, known as the Gell-Mann matrices. They are numbered λ_1,...,λ_8. Together with the color eigenvectors, they generate the eight gluon color states [19]:

$$
\begin{array}{ll}
\frac{1}{\sqrt{2}}(R\overline{G} + G\overline{R}) & \frac{-i}{\sqrt{2}}(R\overline{B} - B\overline{R}) \\
\frac{-i}{\sqrt{2}}(R\overline{G} - G\overline{R}) & \frac{1}{\sqrt{2}}(G\overline{B} + B\overline{G}) \\
\frac{1}{\sqrt{2}}(R\overline{R} - G\overline{G}) & \frac{-i}{\sqrt{2}}(G\overline{B} - B\overline{G}) \\
\frac{1}{\sqrt{2}}(R\overline{B} + B\overline{G}) & \frac{1}{\sqrt{6}}(R\overline{R} + G\overline{G} - 2B\overline{B}),
\end{array}
\tag{1.5}
$$

where the simultaneous eigenvectors of the λ_i are:

$$
R = \begin{pmatrix} 1 \\ 0 \\ 0 \end{pmatrix}, \quad G = \begin{pmatrix} 0 \\ 1 \\ 0 \end{pmatrix}, \quad B = \begin{pmatrix} 0 \\ 0 \\ 1 \end{pmatrix}. \tag{1.6}
$$

The eight states form the color *octet* representation for gluons. Quarks can only be represented by the three colors (or three anticolors for antiquarks), and are therefore represented as color ***triplets***. There is a ninth possible gluon state,

$$
\frac{1}{\sqrt{3}}(R\overline{R} + B\overline{B} + G\overline{G}), \tag{1.7}
$$

but this state is actually a color ***singlet*** and carries no net charge. It would thus not interact with any other particles through the strong force. Its existence is therefore

not postulated in current QCD theory.

In general, the matrix generators of $SU(3)$ do not commute with each other. The commutation of any two $SU(3)$ generators can be represented by [19]:

$$[\lambda_i, \lambda_j] = i \sum_k f_{ijk} \lambda_k, \tag{1.8}$$

where f_{ijk} are constants of the group, called structure constants. Because of the anticommutation, QCD is known as a non-Abelian theory. This feature has direct physical consequences in QCD, which can be seen in the evaluation of the QCD Lagrangian.

1.4.2 The QCD Lagrangian

The full gauge invariant QCD Lagrangian can be written [19] as:

$$\mathcal{L} = \bar{q}(i\gamma^\mu \partial_\mu - m)q - g(\bar{q}\gamma^\mu \frac{\lambda_a}{2} q)G_\mu^a - \frac{1}{4} G_{\mu\nu}^a G_a^{\mu\nu}. \tag{1.9}$$

The index a sums over the eight $SU(3)$ gluon color states, while the indices μ and ν sum over the space-time variables. There is an implied summation over the six quark flavors. The first term is the Dirac Lagrangian describing a free spin-$\frac{1}{2}$ particle (quarks and antiquarks). The second term is necessary to fulfill the requirement of *local gauge invariance*, whereby the Lagrangian must remain invariant under any local phase (gauge) transformation. A local phase transformation is one that has space-time dependence,

$$\psi(x) \rightarrow e^{i\alpha(x)} \psi(x), \tag{1.10}$$

(where $\alpha(x)$ contains the space-time dependence), in contrast to a *global* phase transformation, such as:

$$\psi(x) \rightarrow e^{i\alpha}\psi(x), \tag{1.11}$$

in which α is a constant. The G_μ^a in the second term are the gluon fields. This term describes quark-gluon interactions with coupling strength g.

The last term is the free Lagrangian for the gluon fields. Unlike the free quark Lagrangian, there is no mass term, thus implying that gluons are massless. Each gluon field strength tensor $G_a^{\mu\nu}$ has the form [19]:

$$G_a^{\mu\nu} = \partial_\mu G_\nu^a - \partial_\nu G_\mu^a - g f_{abc} G_\mu^b G_\nu^c. \tag{1.12}$$

The last term in the tensor equation is a direct result of the non-Abelian nature of QCD and it is this term that sets QCD apart from QED. When inserted into the Lagrangian, this term provides for self-interaction among gluons. Since gluons themselves carry color charge, they can couple to other gluons as well as quarks. This is in contrast to QED, where photon-photon coupling is not allowed (since photons carry no charge). Gluon self-coupling alters the nature of the strong force coupling strength, as described in the next section.

1.4.3 Renormalization and the Running Coupling Constant

In QCD, the presence of gluon self-interaction affects the nature of the effective strong force coupling. Known as a running coupling constant, it takes the form [19]:

$$\alpha_s(Q^2) = \frac{12\pi}{(11N_c - 2N_f)\log(Q^2/\Lambda^2)}, \tag{1.13}$$

where Q is the momentum at which α_s is to be determined, N_c is the number of colors and N_f is the number of flavors. The parameter Λ^2 is the QCD scale parameter, and it corresponds to the Q^2 scale at which the effective coupling becomes large. This momentum scale is defined as [19]:

$$\Lambda^2 = \mu^2 \exp\left[\frac{-12\pi}{(11N_c - 2N_f)(\alpha_S(\mu^2))}\right]. \tag{1.14}$$

The parameter μ is a product of the calculation of $\alpha_s(Q^2)$ from perturbation theory. In attempting to evaluate interaction diagrams beyond leading order [4], divergences arise due to the inclusion of higher-order corrections. These divergences are removed by means of *renormalization*, a technique through which they are replaced by finite integral evaluations. The parameter μ is a scale (of arbitrary value) used in the renormalization that remains in the final expression.

For low values of Q^2 or, equivalently, at large distances, $\alpha_s(Q^2)$ becomes large. This is the opposite effect seen in QED, in which the effective coupling decreases with increasing distance. This increased coupling in QCD is thought to explain the concept of quark and gluon *confinement*, which restricts quarks and gluons to reside in bound states. Confinement explains why free quarks and gluons have never been experimentally observed.

At very high values of Q^2 (very short distances), $\alpha_s(Q^2)$ becomes very small. In this limit, quarks and gluons can effectively be treated as free objects. Known as *asymptotic freedom*, this weakening of the strong force greatly simplifies calculations at high Q^2. This realm of QCD is called the perturbative region, and perturbative

[4] A *leading order* diagram is one in which no secondary contributions, such as gluon bremsstrahlung and loop contributions, are considered.

QCD calculations form the foundation of much of our knowledge of the partons (quarks and gluons.)

The parameter Λ defines the momentum scale at which $\alpha_s(Q^2)$ becomes large, hence perturbative QCD begins to lose validity. In other words, it (loosely) defines the demarcation between the perturbative and non-perturbative regions. This parameter cannot be predicted by theoretical calculation and must be measured experimentally. Its value is typically $\sim$ 200 MeV.

1.4.4 Leading and Next-to-Leading Order Diagrams

The *Leading Order* (LO) Feynman diagrams for a two jet final state are shown in Fig. 1.3. The squared matrix elements corresponding to these processes are given in Table 1.4 and are expressed in terms of the Mandelstam variables s, t and u which for a process $1 + 2 \rightarrow 3 + 4$ are chosen as:

$$s \equiv (p_1 + p_2)^2, \quad t \equiv (p_1 - p_3)^2 \quad \text{and} \quad u \equiv (p_1 - p_4)^2. \tag{1.15}$$

The eight diagrams in Fig. 1.3 are of the order $\mathcal{O}(\alpha_s^2)$, which corresponds to each diagram having two vertices. Accordingly, at *Next-to-Leading Order* (NLO), the diagrams are of the order $\mathcal{O}(\alpha_s^3)$ due to an additional vertex. Figure. 1.4 shows several NLO diagrams. In NLO, there can be processes with either two incoming partons and three outgoing partons and no loops or with two incoming and two outgoing partons and one loop. For the NLO calculations, all terms up to order $\mathcal{O}(\alpha_s^3)$ are kept, while higher-order terms are ignored. Ideally, one would like to calculate the theory to all orders, however there are practical limitations that require the use of approximations. At NLO there are over one hundred distinct diagrams. For higher

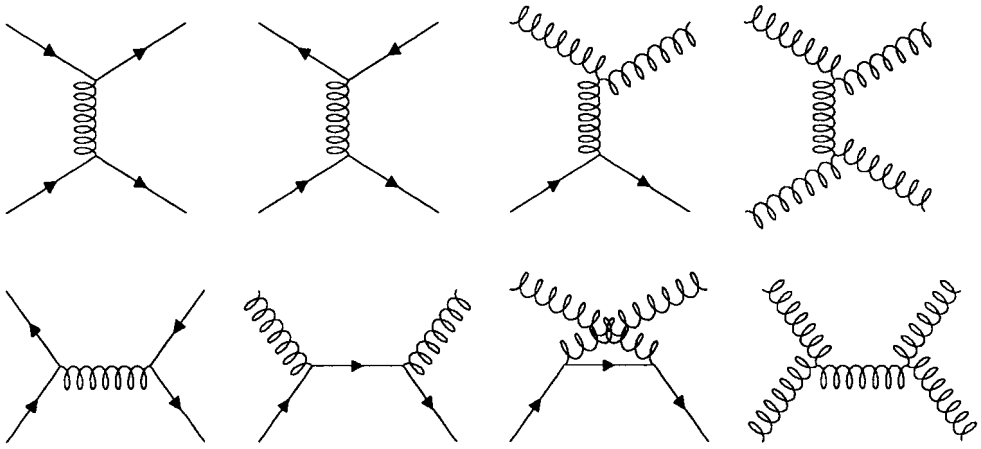

Figure 1.3: Leading Order Feynman diagrams.

orders, the number of diagrams is even greater. Presently, theoretical calculations are available only up to NLO. Figure 1.5 shows an illustration of a collision including higher order terms.

An advantage to using a NLO calculations over a LO one is that the NLO calculation includes higher order terms that the LO calculation ignores making it less sensitive to the renormalization scale. This scaling factor was introduced in QCD in order to handle the ultraviolet divergences of the theory. While LO calculations have a 30% normalization uncertainty for the resulting cross section, NLO calculations typically only have a 10% normalization uncertainty.

1.4.5 Parton Distribution Functions

In QCD, the parton distribution functions depend both on x, the momentum fraction, and on Q^2, the square of the interaction momentum transferred. The slowly varying Q^2 dependence is predicted by QCD evolution through the Gribov-Lipatov-Altarelli-

Subprocess	$\overline{\|\mathcal{M}\|^2}/g_s^4$
$gg \to gg$	$\frac{9}{2}\left(3 - \frac{tu}{s^2} - \frac{su}{t^2} - \frac{st}{u^2}\right)$
$gg \to q\bar{q}$	$\frac{1}{6}\left(\frac{t}{u} + \frac{u}{t}\right) - \frac{3}{8}\frac{t^2+u^2}{s^2}$
$gq \to gq$	$-\frac{4}{9}\left(\frac{s}{u} + \frac{u}{s}\right) + \frac{4}{9}\frac{s^2+u^2}{t^2}$
$q\bar{q} \to gg$	$\frac{32}{27}\left(\frac{t}{u} + \frac{u}{t}\right) - \frac{8}{3}\frac{t^2+u^2}{s^2}$
$q\bar{q} \to q\bar{q}$	$\frac{4}{9}\left(\frac{s^2+u^2}{t^2} + \frac{u^2+t^2}{s^2}\right) - \frac{8}{27}\frac{u^2}{st}$
$q\bar{q} \to q'\bar{q}'$	$\frac{4}{9}\frac{t^2+u^2}{s^2}$
$qq \to qq$	$\frac{4}{9}\left(\frac{s^2+u^2}{t^2} + \frac{s^2+t^2}{u^2}\right) - \frac{8}{27}\frac{s^2}{tu}$
$qq' \to qq'$	$\frac{4}{9}\frac{s^2+u^2}{t^2}$

Table 1.4: Squared matrix elements for $2 \to 2$ subprocesses in QCD (averaged over spin and color). q and q' denote distinct flavors of quark, $g_s^2 = 4\pi\alpha_s$ is the strong coupling squared.

Parisi (GLAP) equations [20, 21] and has been observed in *Deep Inelastic Scattering* (DIS) experiments [22, 23, 24, 25, 26, 27, 28] with leptons.

A more complex picture of the proton tells us that the two up quarks and the down quark contained therein are valence quarks that are held together by gluon exchange. In addition to these constituents, the proton also contains *sea* quarks and *sea* anti-quarks originating from the Dirac sea of virtual quark-antiquark pairs. Therefore, all varieties of partons are contained in the proton: the six known quarks and antiquarks, and the gluons (the gluon is its own antiparticle.)

The relationship between the parton distribution functions of the proton and the antiproton can be expressed as:

$$f_i^p = f_i^{\bar{p}} \equiv f_i, \tag{1.16}$$

by making use of charge conjugation invariance. Here, the indices i and j run over

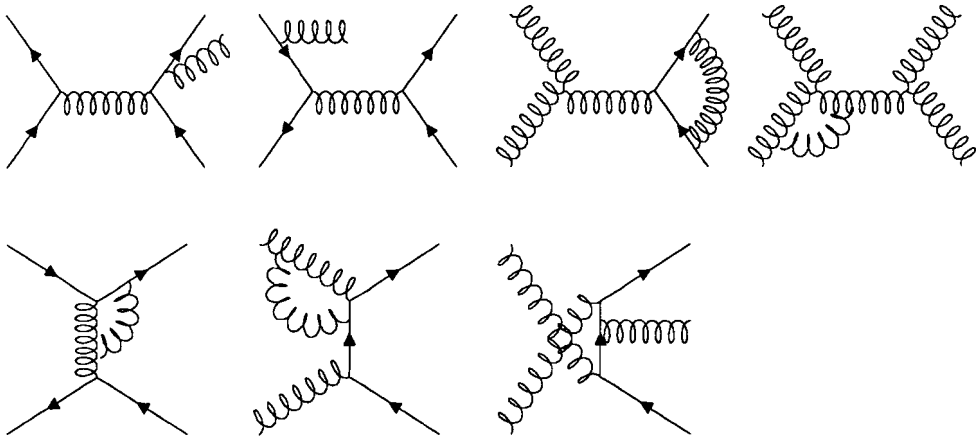

Figure 1.4: Some Next-to-Leading Order Feynman diagrams.

the six quarks, six antiquarks and the gluon.

A relevant quantity, the *parton structure function*, is constructed from the parton distribution functions, f_i, by multiplying each of these by the fractional momentum x. The quark and antiquark structure functions are then:

$$Q_i(x, Q^2) = x f_i(x, Q^2) \quad \text{with } i = u, \overline{u}, d, \overline{d}, ..., t, \overline{t} \tag{1.17}$$

and the gluon structure function is:

$$G(x, Q^2) = x g(x, Q^2). \tag{1.18}$$

By taking the color-weighted parton-parton scattering cross sections to be equal in the *single effective subprocess approximation* [29], the relative weights of the dif-

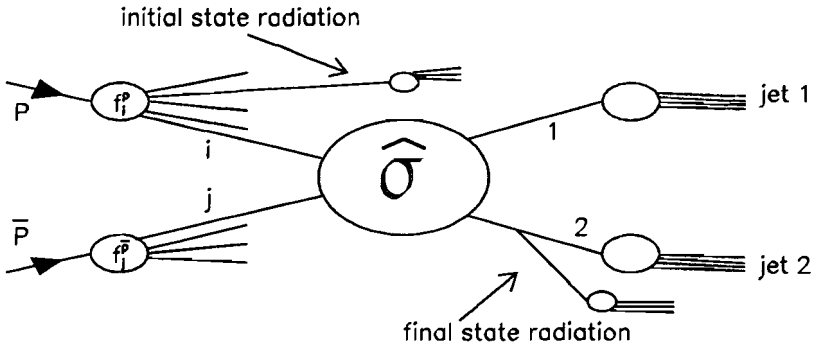

Figure 1.5: $2 \rightarrow 2$ process with higher order corrections.

ferent parton-parton processes are obtained. For the gluon-gluon, gluon-quark and quark-quark subprocesses, their ratio is, respectively, $1 : \frac{4}{9} : (\frac{4}{9})^2$. Thus, the *single effective parton density* is:

$$F(x, Q^2) = G(x, Q^2) + \frac{4}{9}(Q(x, Q^2) + \overline{Q}(x, Q^2)), \tag{1.19}$$

where

$$Q(x, Q^2) = \sum_i Q_i(x, Q^2) \quad \text{with } i = u, d, s, c, t, b, \tag{1.20}$$

and where

$$\overline{Q}(x, Q^2) = \sum_i Q_i(x, Q^2) \quad \text{with } i = \overline{u}, \overline{d}, \overline{s}, \overline{c}, \overline{t}, \overline{b}. \tag{1.21}$$

The quark distributions have been thoroughly studied in deep inelastic scattering of muons, electrons and neutrinos off protons [22, 23, 24, 25, 26, 27, 28]. Since

gluons do not couple by means of the electroweak interaction, other means to probe the gluon distribution must be found. There are ways this can be accomplished by using Drell-Yan pairs, direct photons, and — at the Tevatron — jets, given that at high energies the main contributing diagrams are gluon-gluon and gluon-quark interactions. In Fig. 1.6, we see that the gluon distribution dominates at low values of x, while the quark distribution occupies the high end of the spectrum.

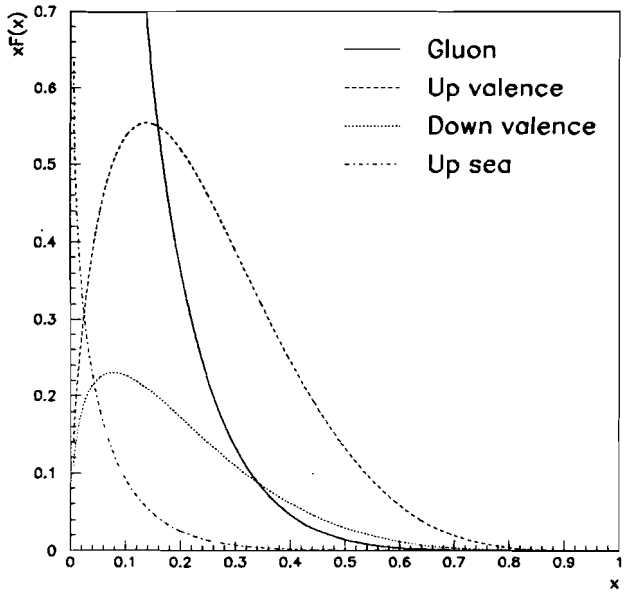

Figure 1.6: Distributions for different partons in the proton as a function of x at $Q = 50$ GeV with CTEQ2M.

There are a number of different methods for calculating the parton distribution functions. Various ones use different experimental results, renormalization schemes and fitting techniques. Among the most recent sets of *parton distribution functions* (pdfs), we find the CTEQ [30], GRV sets [31] and MRSD′ [32, 33] sets. The CTEQ family of pdfs is described below since the functions used in the theoretical models employed in the analysis belong to this group.

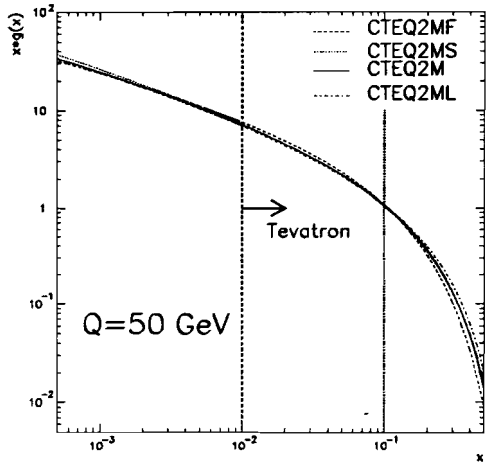

Figure 1.7: The gluon distribution as a function of fractional momentum x at $Q = 50$ GeV for several CTEQ pdfs at low values of x. The dashed line shows the minimum x-value that can be probed at the Tevatron using dijets. The dotted line shows the x-value at which the various CTEQ pdfs have roughly the same gluon content.

The CTEQ collaboration has developed a family of curves fit to the latest available electron-proton scattering data from HERA [34, 35, 36]. They include different predictions depending on how the gluon distribution is extrapolated to low values of x ($x \sim 0.0001$) in order to accommodate the upper and lower limits from the HERA gluon distribution results at these $x-$values. Their best fit is CTEQ2M. The CTEQ2MF prediction assumes less gluons, or a *flatter* gluon distribution at low x-values. For more gluons in the low-x region, or a more *singular* gluon distribution there, one can make use of the CTEQ2MS prediction. Finally, the CTEQ2ML prediction corresponds to setting Λ to the LEP value. Figures 1.7 and 1.8 show the gluon distributions from the CTEQ collaboration's predictions over a wide range of x. The first figure shows the distribution over several decades of low x-values and indicates the x-value limit at which Tevatron dijet production becomes sensitive to the gluon distribution. The second figure shows the distributions at relatively high

x-values.

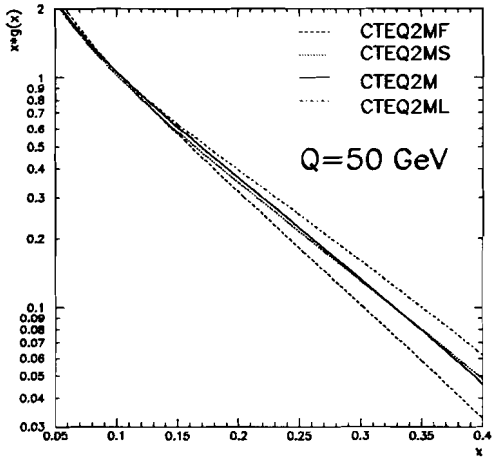

Figure 1.8: The gluon distribution as a function of fractional momentum x at $Q = 50$ GeV for several CTEQ pdfs at relatively high values of x.

1.5 Introduction to Color Coherence

In hadron-hadron collisions, interactions commonly occur between one parton from each hadron. A typical parton-parton interaction in a $\bar{p}p$ collision might be, for example, $q\bar{q}$ scattering through the exchange of a gluon. Since both quarks and gluons carry color charge, and color is a conserved quantity, it is possible to map the exchange, or flow, of color through these parton-parton interactions. This mapping is called a *color flow* diagram. A leading order Feynman diagram for the reaction $q\bar{q} \rightarrow q\bar{q}$ with an example color flow diagram is given in Fig. 1.9.

A leading order diagram does not account for higher order effects, such as gluon bremsstrahlung — each of the hard partons in such an event can radiate numerous soft gluons [5]. These gluons can then create additional soft gluons and soft $q\bar{q}$ pairs,

[5] A *soft* parton is defined by $q^2 \ll Q^2$ and a *hard* parton is defined by the momentum scale

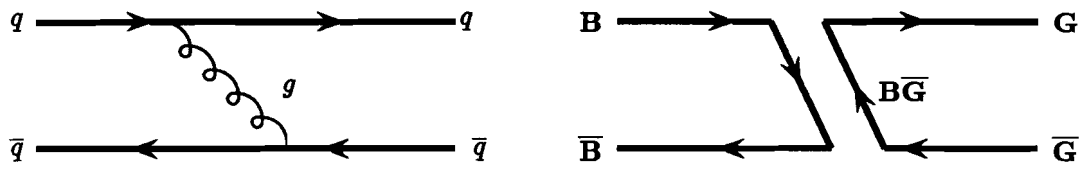

Figure 1.9: a) Feynman diagram and b) color flow diagram for $q\bar{q} \rightarrow q\bar{q}$

which can further radiate as well, in an iterative *cascade* process. The final distribution of partons emerges as hadrons at large distance scales from the interaction and are the objects actually observed in experimental detectors.

This soft parton distribution is not, in general, uniform in space. There are regions in which soft radiation is inhibited, resulting in local areas of lower multiplicity, as well as regions in which soft radiation is enhanced. This depletion/enhancement is partially the result of interference of soft gluon amplitudes radiated from partons that are color-connected [37], a phenomenon known as *color coherence.* The regions of depletion/enhancement are defined by the relative spatial orientation of the color-connected hard partons.

The local depletion/enhancement due to gluon interference can be modelled by the *angular ordering* approximation of sequential parton emissions. To leading order in N_c, angular ordering is the monotonic decrease in the emission angle for successive soft gluon radiation away from the interaction region [38]. Angular ordering will be described in detail in the next chapter. For now, Fig. 1.10 illustrates the effect.

Consecutive gluon production is depicted to demonstrate the angular ordering restriction in an outgoing gluon cascade (note the successive angle reduction.)

$q^2 \sim Q^2$, where q is the parton momentum and Q is the momentum scale of the interaction.

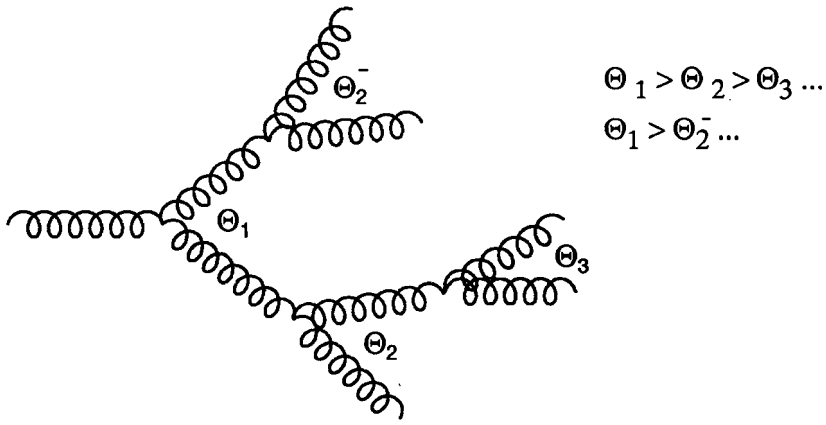

Figure 1.10: Example of angular ordering of successive gluon branchings. Notice that there is no direct relationship between Θ_2 and Θ_2'.

1.6 Goals of the Analysis

The analysis described in this thesis is an attempt to observe the characteristic distribution of partons resulting from color coherence in $p\bar{p}$ reactions at the Fermilab Tevatron. One of the most important aspects of this study is that, while the color coherence patterns are constructed at the partonic level, observation of these patterns may only occur at the hadronic level. Belief in the observability of this effect rests on the hypothesis of *Local Parton Hadron Duality* (LPHD) [37]. LPHD proposes that general features of hadronic systems, such as particle multiplicity and angular distributions of particles, may be described analytically at the parton level using perturbative QCD calculations [37]. Thus, the observation of color coherence requires that the hadronization [6] process not destroy the interference patterns created by soft gluon radiation.

[6] *Hadronization* is the process in which partons emerging from a collision combine to form hadronic bound states.

There may be, in fact, non-perturbative effects during hadronization that are qualitatively similar to perturbative color coherence effects. The relative contributions of these effects has direct implications for LPHD. The non-perturbative contributions are discussed in Chapter 2.

1.6.1 Previous Experiments

Several studies of three-jet [7] events at e^+e^- colliders have shown clear evidence for color coherence effects among the final-state partons [39, 40, 41, 42, 43, 44, 45, 46, 47, 48, 49, 50, 51]. In these studies, one of the jets is tagged as arising from a gluon and the other two as a separating $q\bar{q}$ pair (see Fig. 1.11). The gluon is connected to each quark by a color line (indicating the flow of color in the event.) Enhancements in particle multiplicity are observed in the regions between the gluon jet and each of the quark jets, while a significant depletion is observed in the region between the quark jets.

This result is then compared with multiplicity distributions in events with two quark jets and a photon (in place of the gluon.) In these events, the particle multiplicity is higher in the region between the two quarks than in either region bordered by the photon and one of the quarks. Further, the multiplicity between the quarks is significantly higher for events with the photon when compared with events with the gluon. This is believed to be the result of a quark-antiquark color connection in the $q\bar{q}\gamma$ events which is not present in the $q\bar{q}g$ events (as shown in Fig. 1.11).

Studies of color coherence are more complicated at hadron colliders, experimen-

[7] A *jet* refers is a collimated stream of hadrons directed outward from a collision point arising from multiple secondary emissions from an energetic parton. The definition of a jet at DØ will be more fully explored in Chapter 4.

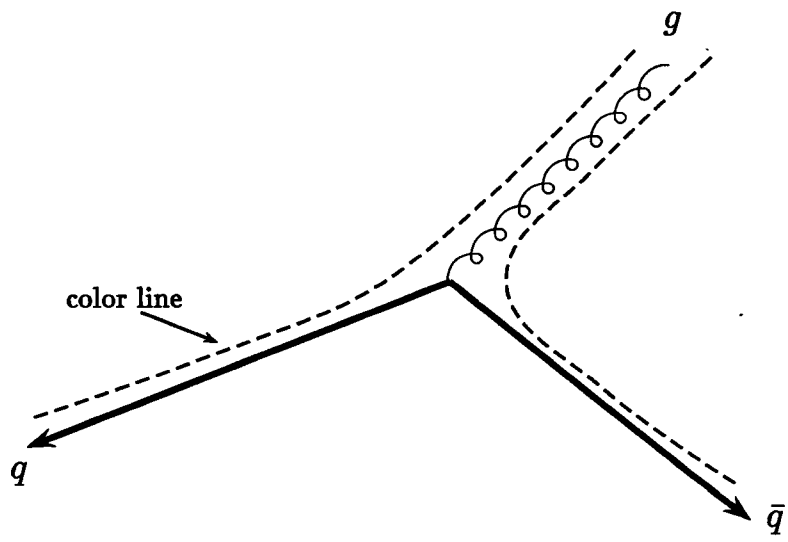

Figure 1.11: Color flow diagram for the $e^+e^- \rightarrow q\bar{q}g$ process.

tally and theoretically, than in e^+e^- annihilation due to the presence of colored constituents in the initial and final states. In addition to the large particle multiplicity from the hard scattering inherent in hadronic collisions, event-by-event fluctuations of the softer particle distribution produced by *spectator* [8] interactions further complicate experimental results. Recent studies by the DØ [38, 52] and CDF [53] experiments have sought to minimize these effects by exploiting the Tevatron's high center-of-mass energy [9]. Both search for three-jet events in which the coherent radiation is of sufficient energy to form a soft jet. The angular distribution of the third jet in the data is compared with similar distributions in Monte Carlo simulations that incorporate color coherence effects and also with those that do not incorporate such effects. In the following section and in Chapter 2, a more detailed discussion of this analysis, which is the focus of this thesis, will be provided.

[8] *Spectator* partons are the proton and anti-proton remnant partons that do not participate directly in the hard interaction.

[9] The center-of-mass energy ($\sqrt{s}$) of the proton-antiproton beam at the Fermilab Tevatron is 1800 GeV, currently the highest beam energy in the world.

In addition, DØ has also undertaken a study of color coherence in a lower energy domain using W+Jet events [54] in which a W boson is produced along with an opposing quark or gluon (which then fragments into one or more hadron jets.) The angular distributions of soft particles are measured around both the W boson and the opposing highest-E_T jet in the event and compared to each other. W bosons are not carriers of the color charge and therefore have no color connection with any parton in the event. The opposing parton is color-connected to the initial-state partons. Therefore, the pattern of soft particles on the parton side of the event is expected to be very different from that on the W boson side due to interference effects between the initial-state and final-state color connections. The W boson, in effect, provides a convenient template against which soft particle patterns around the opposing jet may be observed. The leading order color flow diagrams for W+Jets production are shown in Fig. 1.12 in the center-of-mass frame.

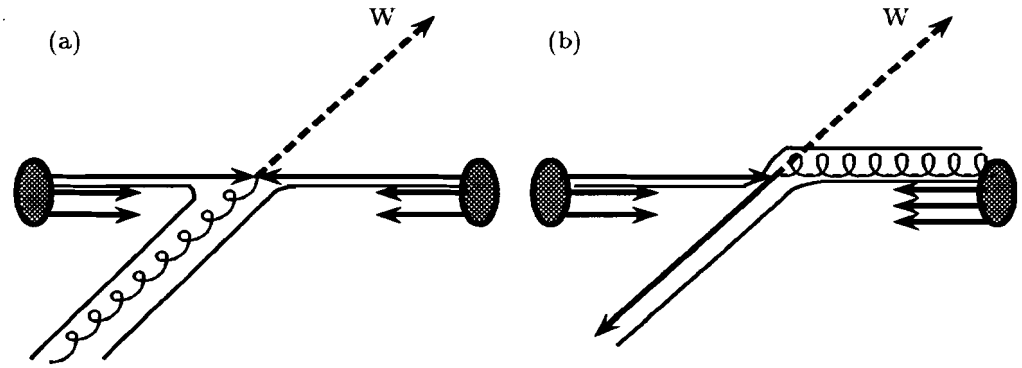

Figure 1.12: Color flow diagrams for (a) $q\bar{q} \rightarrow Wg$ and (b) $qg \rightarrow Wq$ in the center-of-mass frame. Thin solid lines represent the flow of color charge from the initial state partons to the final state partons. Gluons are represented by helices.

1.6.2 Multi-Jet Events as a Probe of Color Coherence

In this analysis, the color coherence pattern is studied through soft jet distributions rather than through soft particle distributions. The fine segmentation and good resolution of the DØ calorimeter system allow for direct measurement of the soft jets produced in hard scatterings. By accumulating statistics over many events (in order to reduce event-by-event fluctuations), the color coherence signal can be sought above the background (from underlying event fluctuations and detector effects.)

Events in which two leading jets have sufficiently high energies so that coherent radiation forms secondary jets (from gluon bremsstrahlung) are chosen for the *multi-jet* [10] study. The events are required to have three or more reconstructed jets. The leading order Feynman diagrams for these events were shown in Fig. 1.3. The interference effects between the initial-state and the final-state color connections of these diagrams determine the angular distribution of the soft gluon bremsstrahlung radiation about the radiating (harder) partons. This radiation is manifested as a soft jet which could originate from either the initial or the final state partons. However, since this radiation is soft, it typically will be radiated near to the direction of the radiating parton. By measuring the angular distribution of the softer jet, we can determine the effect from color coherence. Unlike the W + Jet case, there is no colorless template with which to compare in data. However comparison of the data distributions to those of different Monte Carlo implementations of color coherence effects are made.

The study of color coherence effects is interesting and important as a source of insight into the relationship between the perturbative and nonperturbative QCD

[10] A *multi-jet* event is an event with three or more jets.

realms. Hard scattering at the parton level can be reasonably described using analytical models, and predictions can be made using perturbative calculations. Descriptions at the nonperturbative/hadron level, however, must rely on phenomenological models. It is therefore important to know what effects at the parton level survive the hadronization phase, which is a probe of the LPHD hypothesis. A more complete treatment of color coherence follows in the next chapter.

Chapter 2

Theoretical Overview

The phenomenon of color coherence will be developed analytically in this chapter, beginning with well-known Leading Order (LO) $2 \rightarrow 2$ processes. The derivation relies on matrix element factorization, applicable to additional radiation in the soft limit. The procedure is applied to selected processes which result in a quark-gluon and a gluon-gluon final state so that interference effects pertinent to this analysis may be understood. Following is a discussion of the *angular ordering approximation*, which is a consequence of simplifying the analytical color coherence expressions. Next, non-perturbative effects which are qualitatively similar to color coherence are described. And lastly, various implementations of color coherence and related non-perturbative effects in Monte Carlo event simulations are presented, specifically those of the HERWIG, ISAJET and PYTHIA event generators, along with a Next-to-Leading Order (NLO) parton level calculation (JETRAD), all of which are used in this study for comparisons to collider data.

2.1 Soft Gluon Emission in Hadronic Scattering

In general, the description of additional gluon radiation in a hadronic $2 \to 2$ process

$$parton(p_1) + parton(p_2) \to parton(p_3) + parton(p_4), \tag{2.1}$$

requires a Next-to-Leading Order calculation of the $2 \to 3$ process

$$parton(p_1) + parton(p_2) \to parton(p_3) + parton(p_4) + gluon(k). \tag{2.2}$$

However, in the soft limit ($k \to 0$), the calculation of the process 2.2 reduces to the description of the LO process 2.1 with *additional* terms describing the soft gluon radiation ($q \equiv k$ in the soft limit) from each hard parton (q_1, q_2, q_3, q_4) [55].

The matrix amplitude $\mathbf{H}(q_1, q_2, q_3, q_4, q)$ for process 2.2 can be factorized (in the soft gluon limit) as [56, 57, 58]:

$$\mathbf{H}(q_1, q_2, q_3, q_4, q) \simeq g_s \mathbf{h}(q_1, q_2, q_3, q_4) \cdot \mathbf{J}(q), \tag{2.3}$$

where g_s is the strong force coupling, $\mathbf{h}(q_1, q_2, q_3, q_4)$ is the matrix amplitude for the hard scattering process 2.1 and $\mathbf{J}(q)$ is the non-Abelian semi-classical current for the emission of the soft gluon q from the external hard partons, defined as [55, 58]:

$$\mathbf{J}^{b,\mu}(q) = -\left(\frac{q_1^\mu}{q_1 \cdot q}\right) \mathbf{t}_1^b - \left(\frac{q_2^\mu}{q_2 \cdot q}\right) \mathbf{t}_2^b + \left(\frac{q_3^\mu}{q_3 \cdot q}\right) \mathbf{t}_3^b + \left(\frac{q_4^\mu}{q_4 \cdot q}\right) \mathbf{t}_4^b, \tag{2.4}$$

where b and μ are the color and polarization of the emitted soft gluon, and $\mathbf{t}_i^b$ is the color matrix of parton i.

The probability distribution for the soft gluon q is obtained by squaring the current. Therefore,

$$\begin{aligned}(2.5)\qquad \mathbf{J}^2(q) \;=\; & 2(\mathbf{t}_1\cdot\mathbf{t}_2)\frac{q_1\cdot q_2}{(q_1\cdot q)(q\cdot q_2)} - 2(\mathbf{t}_1\cdot\mathbf{t}_3)\frac{q_1\cdot q_3}{(q_1\cdot q)(q\cdot q_3)} \\ & -2(\mathbf{t}_1\cdot\mathbf{t}_4)\frac{q_1\cdot q_4}{(q_1\cdot q)(q\cdot q_4)} - 2(\mathbf{t}_2\cdot\mathbf{t}_3)\frac{q_2\cdot q_3}{(q_2\cdot q)(q\cdot q_3)} \\ & -2(\mathbf{t}_2\cdot\mathbf{t}_4)\frac{q_2\cdot q_4}{(q_2\cdot q)(q\cdot q_4)} + 2(\mathbf{t}_3\cdot\mathbf{t}_4)\frac{q_3\cdot q_4}{(q_3\cdot q)(q\cdot q_4)},\end{aligned}$$

which can be rewritten in the form

$$\begin{aligned}(2.6)\qquad \mathbf{J}^2(q) \;=\; & 2(\mathbf{t}_1\cdot\mathbf{t}_2)W_{12} - 2(\mathbf{t}_1\cdot\mathbf{t}_3)W_{13} - 2(\mathbf{t}_1\cdot\mathbf{t}_4)W_{14} \\ & -2(\mathbf{t}_2\cdot\mathbf{t}_3)W_{23} - 2(\mathbf{t}_2\cdot\mathbf{t}_4)W_{24} + 2(\mathbf{t}_3\cdot\mathbf{t}_4)W_{34},\end{aligned}$$

with

$$(2.7)\qquad W_{ij} \equiv \frac{q_i\cdot q_j}{(q_i\cdot q)(q\cdot q_j)}.$$

Each W_{ij} term corresponds to the emission of a soft gluon from partons i and j as a pair. Their meaning, which is explored in more detail below, is that a soft gluon may not be emitted from any hard parton i independently, but rather is influenced by interference from the other hard partons.

In the limit of massless partons, Equation 2.7 becomes:

$$(2.8)\qquad W_{ij} = \frac{1}{E_q^2}\frac{\alpha_{ij}}{\alpha_{iq}\alpha_{jq}} \equiv \frac{1}{E_q^2}\widehat{(ij)},$$

where

$$(2.9)\qquad \alpha_{ij} = 1-\cos\theta_{ij} \qquad \alpha_{iq} = 1-\cos\theta_{iq}.$$

In the massless limit, therefore, the emission amplitudes W_{ij} are seen to depend only upon the gluon energy and simple angular relationships among the partons i and j and the gluon. To further illustrate the interference inherent in the W_{ij} amplitudes, they may be expanded and separated into components, such as

$$(2.10) \qquad \begin{aligned} (E_q^2)W_{ij} &= \frac{\alpha_{ij}}{\alpha_{iq}\alpha_{jq}} + \frac{1}{\alpha_{iq}} - \frac{1}{\alpha_{iq}} + \frac{1}{\alpha_{jq}} - \frac{1}{\alpha_{jq}} \\ &= \frac{1}{2\alpha_{iq}}\left[1 + \frac{\alpha_{ij} - \alpha_{iq}}{\alpha_{jq}}\right] + \frac{1}{2\alpha_{jq}}\left[1 + \frac{\alpha_{ij} - \alpha_{jq}}{\alpha_{iq}}\right] \\ &\equiv (E_q^2)(W_{ij}^i + W_{ij}^j) \equiv \widehat{[ij]} + \widehat{[ji]}. \end{aligned}$$

In the expressions above, the W_{ij} amplitudes have been split into individual components for each parton, W_{ij}^i and W_{ij}^j. The component W_{ij}^i may be thought of as describing the emission of a gluon from parton i in the pair (i,j) (and similarly for W_{ij}^j). In this form, several interesting details regarding soft gluon emission are illuminated. It is instructive to consider the term W_{ij}^i written as

$$(2.11) \qquad W_{ij}^i = \frac{1}{2E_q^2}\left[\frac{1}{\alpha_{iq}} + \frac{\alpha_{ij} - \alpha_{iq}}{\alpha_{iq}\alpha_{jq}}\right].$$

The first term in brackets, the *incoherent term*, corresponds to independent emission of a gluon from parton i. It contains no dependence on the azimuthal angle ϕ around that parton and exhibits a singularity at $\theta_{iq} = 0$. The second term, the *coherent term*, accounts for interference from parton j. To first order, it contains no singularities. Azimuthal dependence arises in this second term due to the angle θ_{jq} in the α_{jq} term (for a fixed θ_{iq}, the angle θ_{jq} varies with ϕ_{iq}). Thus, the probability amplitude for soft gluon emission from parton i is, in general, *not* uniform in ϕ and

depends upon the angle between the emitted gluon and the parton j.

When $\theta_{iq} < \theta_{ij}$, the interference term in W_{ij}^{i} is positive, corresponding to constructive interference. In fact, W_{ij}^{i} achieves its maximum value inside the cone $\theta_{iq} < \theta_{ij}$ and when the gluon lies in the plane defined by i and j (which minimizes θ_{jq}). This configuration is shown below in Fig. 2.1, where the gluon g is emitted in the plane of the page between the partons i and j. Outside of the cone ($\theta_{iq} > \theta_{ij}$), the interference term in W_{ij}^{i} is negative, leading to a suppression of gluon emission[59].

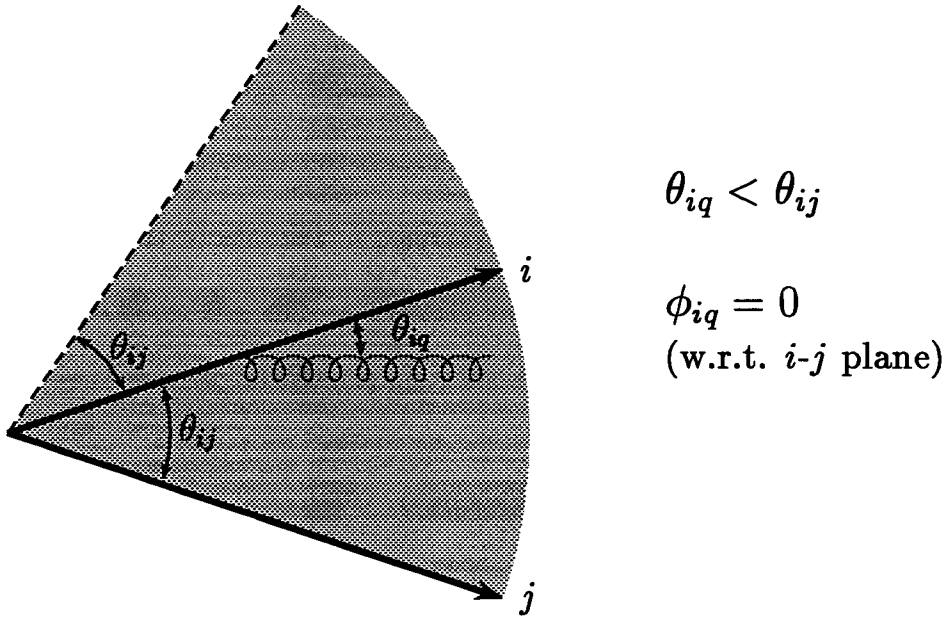

Figure 2.1: Emission cone around parton i as defined by partons i and j. The maximum probability for emission from parton i occurs when gluons are radiated between i and j.

2.2 Radiation Pattern in Leading Order Dijet Processes

The gluon probability distribution $\mathbf{J}^2(q)$ may be expressed in terms of the individual amplitudes in order to obtain the full soft gluon radiation pattern [57] once the

color matrices have been evaluated. For quark-gluon hard scattering $qg \to q'g'$, for example, and to leading order in $\frac{1}{N_c}$ the pattern is given by [57]:

$$\begin{aligned} \mathbf{J}^2 &= -h^C(t,s,u)\left[2C_F\left(W^q_{qg}+W^{q'}_{q'g'}\right)+C_A\left(W^g_{qg}+W^{g'}_{q'g'}+W^g_{gg'}+W^{g'}_{gg'}\right)\right] \\ &\quad -h^C(t,u,s)\left[2C_F\left(W^q_{qg'}+W^{q'}_{q'g}\right)+C_A\left(W^{g'}_{qg'}+W^g_{q'g}+W^g_{gg'}+W^{g'}_{gg'}\right)\right], \end{aligned} \tag{2.12}$$

where $C_F = (N_c^2-1)/2N_c = \frac{4}{3}$ and $C_A = N_c = 3$ are, respectively, the quark and gluon color charges squared. $h^C(t,s,u)$ and $h^C(t,u,s)$ are functions of the Mandelstam variables as follows:

$$h^C(t,s,u) = g_s^4 C_F \frac{u}{s}\left(\frac{s^2+u^2}{t^2}-\frac{1}{N_c^2}\right). \tag{2.13}$$

The leading order color flows for this process, in Feynman diagram form, are shown in Fig. 2.2 below.

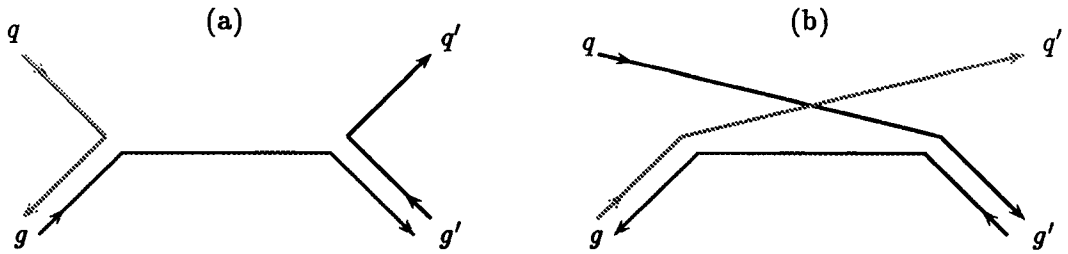

Figure 2.2: Color flow diagrams for $qg \to q'g'$. Initial-initial, final-final and initial-final color connections occur in (a), while (b) consists entirely of initial-final color connections.

Both terms in Equation 2.12 sum to the exact lowest order $qg \to q'g'$ amplitude squared. The first term in this equation (with the function $h^C(t,s,u)$) corresponds to the color configuration shown in Fig. 2.2(a) and the second term (with the function

$h^C(t,u,s)$, corresponds to that in Fig. 2.2(b). In each of these terms, the component terms with the coefficient $2C_F$ describe soft gluon emission from the quarks due to the quark-gluon color-connected pairs. They include contributions due to independent emission from the quarks and interference from the hard gluon color partner. Similarly, the terms with the coefficient C_A describe soft emission from the hard gluons that form the color connected pairs with the quarks and with the hard gluon color partner.

A more intuitive feel for the radiation pattern can be obtained by diagraming the radiation pattern $\mathbf{J}^2$ for a soft gluon of fixed energy $E_{g''}$ as a function of solid angle (Ω). For such a calculation, it is simpler to write $\mathbf{J}^2$ in terms of the spatial components of the color-pair amplitudes $\widehat{[ij]} = E_{g''}^2 W_{ij}^i$, resulting in:

$$\begin{aligned}
\mathbf{J}^2 &= -\frac{h^C(t,s,u)}{E_{g''}^2}\left[2C_F\left(\widehat{[qg]}+\widehat{[q'g']}\right)+C_A\left(\widehat{[gq]}+\widehat{[g'q']}+\widehat{[gg']}+\widehat{[g'g]}\right)\right] \\
&\quad -\frac{h^C(t,u,s)}{E_{g''}^2}\left[2C_F\left(\widehat{[qg']}+\widehat{[q'g]}\right)+C_A\left(\widehat{[g'q]}+\widehat{[gq']}+\widehat{[gg']}+\widehat{[g'g]}\right)\right] \\
&\equiv \mathbf{P}(E_{g''},\Omega), \qquad (2.14)
\end{aligned}$$

to leading order in N_c, where the Ω dependence in $\mathbf{P}$ is defined by the $\widehat{[ij]}$ amplitudes.

In order to match the DØ experimental variables, an additional modification to $\mathbf{P}(E_{g''},\Omega)$ is required. The change in variable is $E_{g''} \rightarrow E_{T(g'')}(= E_{g''}\sin\theta_{g''q})$, where $E_{T(g'')}$ is the energy of the soft gluon transverse to the initial-state partons (a Lorentz invariant quantity). The radiation pattern for a soft gluon of fixed E_T is then:

$$\mathbf{P}(E_{T(g'')},\Omega) = -\frac{(\sin^2\theta_{g''q})}{E_{T(g'')}^2}\left\{h^C(t,s,u)\left[2C_F\left(\widehat{[qg]}+\widehat{[q'g']}\right)\right.\right.$$

$$+C_A\left(\widehat{[gq]}+\widehat{[g'q']}+\widehat{[gg']}+\widehat{[g'g]}\right)\Big]$$

$$+h^C(t,u,s)\left[2C_F\left(\widehat{[qg']}+\widehat{[q'g]}\right)\right.$$

$$\left.+C_A\left(\widehat{[g'q]}+\widehat{[gq']}+\widehat{[gg']}+\widehat{[g'g]}\right)\Big]\right\}. \tag{2.15}$$

Figures 2.3 and 2.4 depict the relative probability of soft gluon emission in this process for a typical event. Axes represent the absolute coordinates for azimuth (ϕ) and *pseudorapidity* (η), where $\eta \equiv -\log(\tan\theta/2)$ is a measure of the polar angle θ of the quark/gluon with respect to the initial-state partons. Labels indicate the locations of the initial-state partons and final-state hard gluon and quark. The overall scale in each figure is not relevant - the shapes of the distributions contain the salient features.

The most prominent feature in Fig. 2.3 is the singularity at the final-state hard gluon and quark[1] (truncated in this picture). Of greater significance, however, is the pattern at some fixed radius from the gluon or quark jet. The combined probability amplitude is seen in Fig. 2.4 to reach a maximum in the plane of the event as defined by the jet, the initial-state quark and the initial-state gluon. This is the same effect described previously in Fig. 2.1. Interference effects are maximized in the event plane. By contrast, the probability amplitude is at a minimum *transverse* to the event plane, and falling with increasing radius $\mathcal{R} = \sqrt{\Delta\eta^2 + \Delta\phi^2}$ from the jet.

This particular example is a typical case, in which the final-state partons are centrally located in pseudorapidity and back-to-back in azimuth, the quark is located at $(\eta, \phi) = (0.5, 1.5)$ and the hard gluon at $(-0.6, 4.6)$. The region centered on each final-state parton is excluded, since, besides containing a singularity, the radiation

[1] Singularities exist at the initial-state quark and gluon, as well, but these are truncated in the figures and additionally suppressed by the $\sin^2\theta_{g''q}$ term.

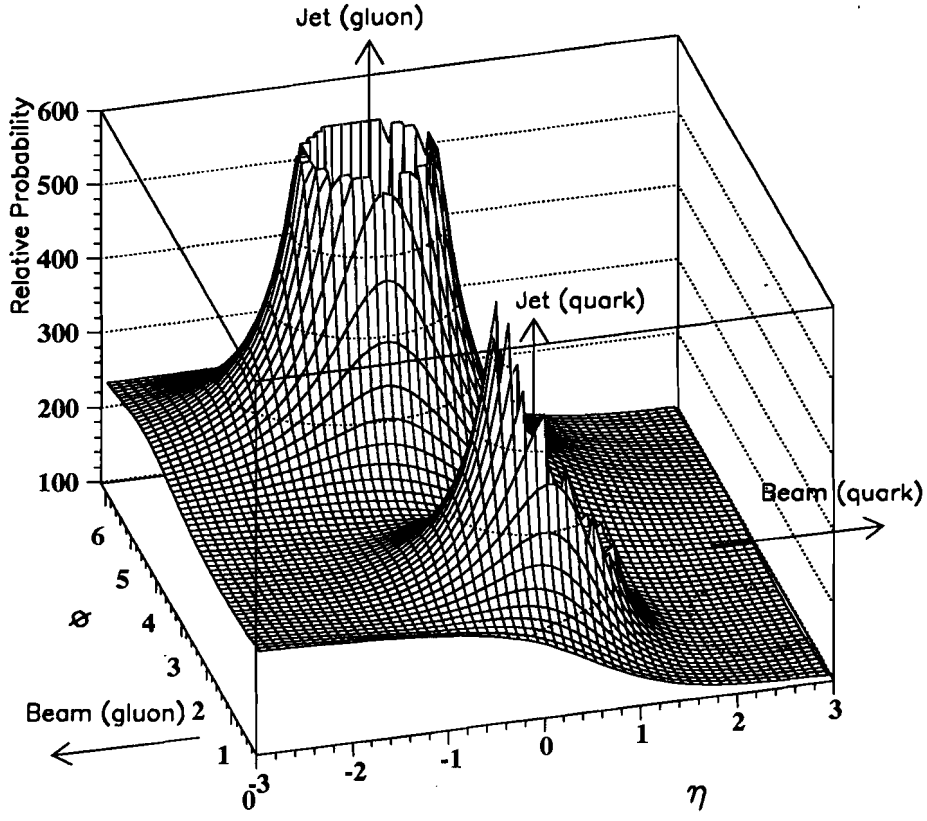

Figure 2.3: Soft gluon radiation pattern $(E^2_{T(g'')})\mathbf{P}(\Omega)$ for the process $qg \to q'g'$ with $\eta_{g'} = -0.6$ and $\eta_{q'} = 0.5$. Radiation enhancement between the gluon jet and the beam as well as between the quark jet and the gluon beam are present.

present there would be detected experimentally as part of the observed jet. The size this excluded region ($\mathcal{R} = 0.6$ units in $\eta - \phi$ space) is comparable to that occupied by a jet.

In Fig. 2.4 one observes that the radiation around the hard gluon is enhanced between it and both beam directions by noticing the 'stretching' of the contours around the gluon jet towards both beams. This is due to the gluon's color connections with both initial-state partons in the event. However, the enhancement in the *near-*

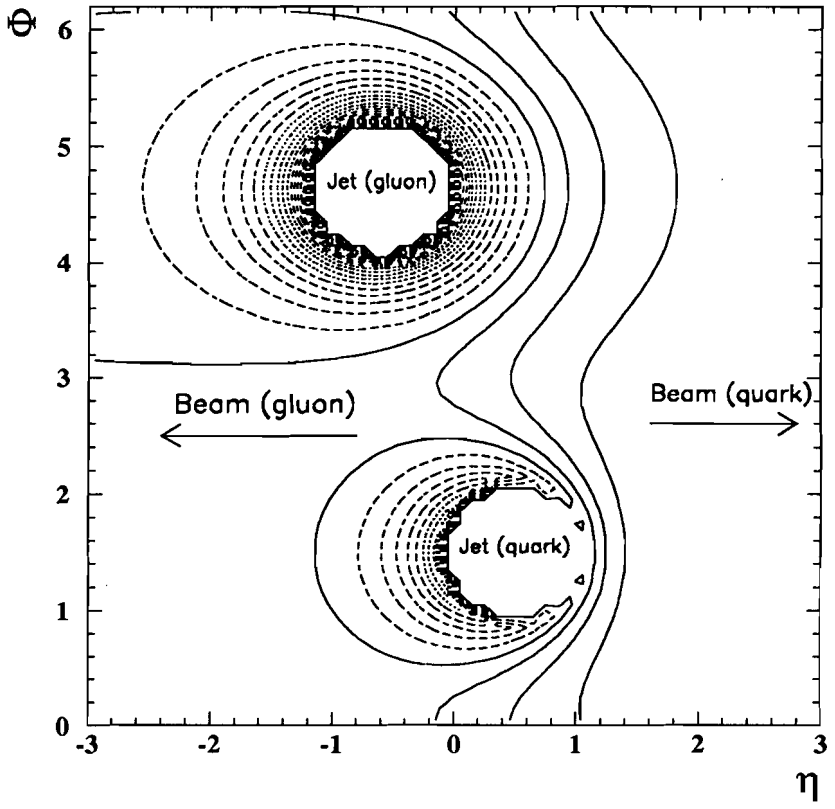

Figure 2.4: Curves of equal probability for soft gluon radiation pattern $(E^2_{T(g'')})\mathbf{P}(\Omega)$ for the process $qg \to q'g'$ with $\eta_{g'} = -0.6$ and $\eta_{q'} = 0.5$. Excess radiation is present between the gluon jet and both beam directions as well as between the quark jet and the gluon jet.

beam region[2] is greater than in the *far-beam* region[3] on the opposite side, due to its greater proximity to the beam there. Meanwhile, in the vicinity of the final-state quark, soft gluon radiation is enhanced only in the *far-beam* region between it and the initial-state gluon. This is evidence of the fact that, in this example, the final-state quark's sole color connection (to leading order in N_c) is to a hard gluon in the

[2]The *near-beam* region is defined as the region between the final-state parton and the initial-state parton direction, or beam, closest to it — in this case the gluon.

[3]Conversely, the *far-beam* region is the region between the final-state parton and the beam farthest from it.

initial state as illustrated in Fig. 2.2b.

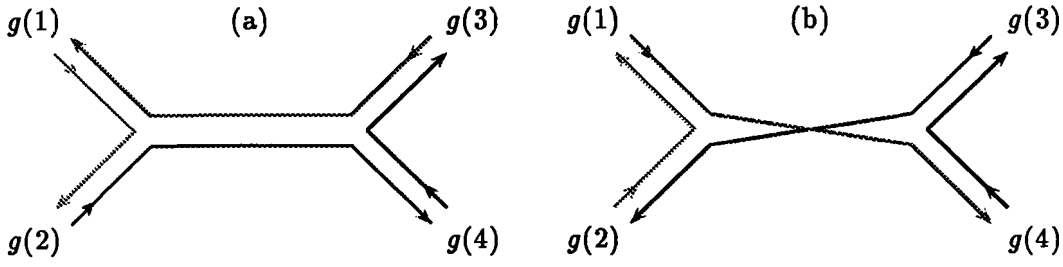

Figure 2.5: Color flow diagrams for $g(1)+g(2) \rightarrow g(3)+g(4)$. Initial-initial, final-final and initial-final color connections occur in both (a) and (b).

The radiation pattern from a second LO diagram, gluon-gluon hard scattering $g(1) + g(2) \rightarrow g(3) + g(4)$ is now examined in order to study this very common process. The leading order color flows for this process, are shown in Fig. 2.5. To leading order in $\frac{1}{N_c}$ the pattern is given by [59]:

$$\begin{aligned} \mathbf{P}(E_{T(g'')}, \Omega) &= \frac{(\sin^2 \theta_{g''g})}{2E^2_{T(g'')}} \left\{ \widehat{(13)} + \widehat{(24)} \right. \\ &\left. + \frac{1}{2} \left[\widehat{(12)} + \widehat{(14)} + \widehat{(23)} + \widehat{(34)} \right] \right\}. \end{aligned} \tag{2.16}$$

Examining Equation 2.16 it is clear that the radiation pattern for gluon-gluon hard scattering is dominated by the contributions from initial-final state interference, as four of the six dipole emitters (including the two which are not suppressed) involve radiation from initial-final state pairs of partons.

The relative probability of soft gluon emission in this process is shown in Figs. 2.6 and 2.7 for the same location of final state partons as in the quark-gluon instance. The radiation enhancement occurs mainly between each jet and the beam closest to it. A weaker but still noticeable excess of radiation is present in the region between

the final state gluons, as shown in Fig. 2.7.

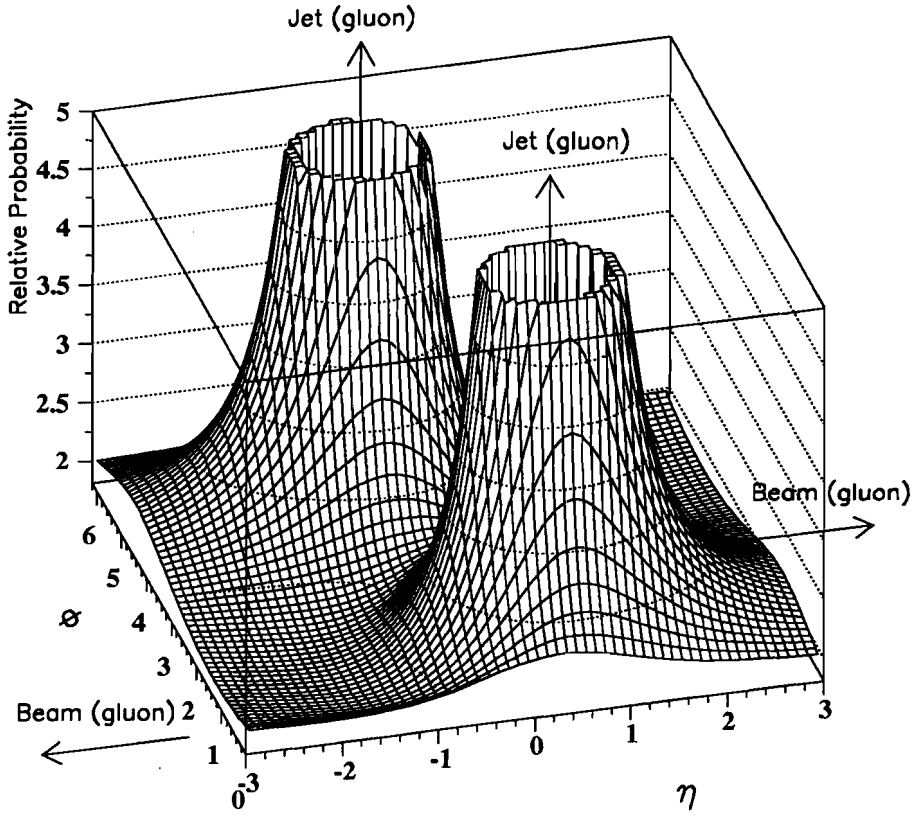

Figure 2.6: Soft gluon radiation pattern $(E^2_{T(g'')})\mathbf{P}(\Omega)$ for the process $g(1)+g(2) \rightarrow g(3)+g(4)$ with $\eta_{g(3)} = -0.6$ and $\eta_{g(4)} = 0.5$. Radiation enhancement is seen here most clearly in the region between each jet and the corresponding near-beam direction.

Radiation patterns such as those shown here for quark-gluon and gluon-gluon hard scattering are affected by kinematic effects, given that the $E^2_{T(g'')}$-weighted probability of soft gluon emission was the variable plotted and that less energy is required to radiate a given amount of E_T at lower pseudorapidities. In order to examine these kinematic contributions, a purely kinematic model of radiation around a jet-like object was constructed. This model assumes a gaussian distribution of radiation in the radial variable $\mathcal{R}$ which is uniform around the jet axis. Any

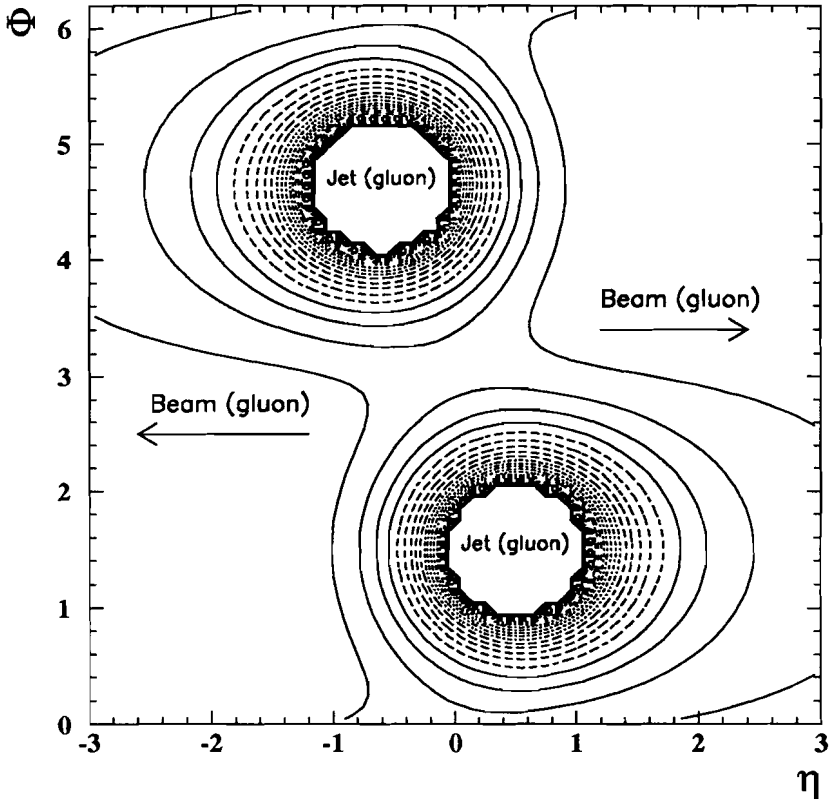

Figure 2.7: Curves of equal probability for soft gluon radiation pattern $(E^2_{T(g'')})\mathbf{P}(\Omega)$ for the process $g(1) + g(2) \rightarrow g(3) + g(4)$ with $\eta_{g(3)} = -0.6$ and $\eta_{g(4)} = 0.5$. Excess radiation is produced mainly between each jet and the corresponding near-beam direction but is also present in the region between the jets.

distortions in the emission pattern and regions of excess or depleted radiation are due solely to kinematic effects. In order to facilitate the comparison with Figs. 2.3–2.7, the location of the jets is the same in all cases.

The radiation patterns with no color interference effects but rather with only kinematic effects are shown in Figs. 2.8 and 2.9. In the first of these figures, it is clear that there is no excess of radiation in the event plane since the distribution is at a minimal level there and remains flat. Moreover, the amount of radiation

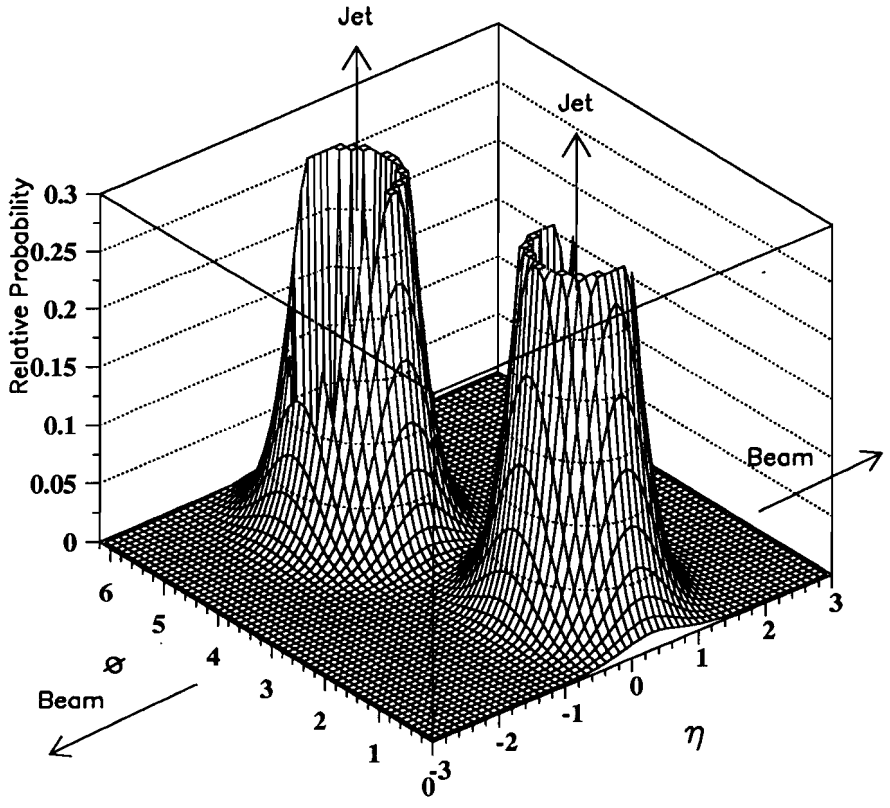

Figure 2.8: Purely kinematic radiation pattern $(E^2_{T(g'')})\mathbf{P}(\Omega)$ with $\eta_{\text{Jet1}} = -0.6$ and $\eta_{\text{Jet2}} = 0.5$. No radiation enhancement occurs between each jet and the corresponding beam directions.

near the jet is seen to fall with increasing $|\eta|$, which explains the gap on the high-η side of the distributions. The 'saddle-shaped' pattern visible around the jets in the two LO diagrams is absent here. In Fig. 2.9, very little kinematic distortion of the curves of equal probability occurs (relative to that caused by color interference effects), suggesting that the color interference effects may be more significant than the kinematic effects at the parton level. The radiation pattern shows the expected kinematic preference for low pseudorapidities and a slight enhancement near the transverse plane. One may note that the enhancement seen in the jet-jet region of

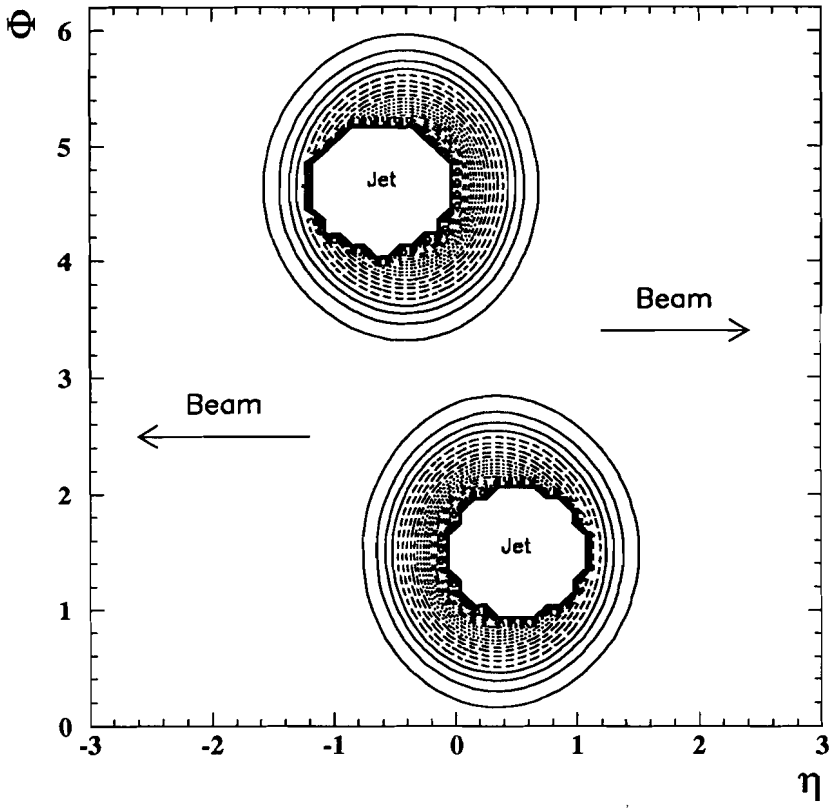

Figure 2.9: Curves of equal probability for purely kinematic radiation pattern $(E^2_{T(g'')})\mathbf{P}(\Omega)$ with $\eta_{\text{Jet1}} = -0.6$ and $\eta_{Jet2} = 0.5$. No radiation enhancement occurs between each jet and the corresponding beam directions. The distortion in the curves is due to E_T being favored at low values of η solely due to kinematic effects.

Fig. 2.7 is more pronounced and occurs farther away from the transverse plane than does this slight kinematic enhancement, supporting the claim that the former is due to the color connection between the partons in the final state.

Descriptions of other LO processes resulting in a two-jet final state may be found in [55, 57, 59].

Figures 2.3–2.7 provide a useful visual representation of the leading-N_c behavior of the soft emission amplitude in a diagram of dijet production resulting from matrix element factorization. These amplitudes may be incorporated into Monte Carlo sim-

ulations to model higher-order processes such as multiple consecutive gluon emission. In order to do this, a further modification of the amplitude appropriate to the Monte Carlo technique is required. This modification, the *angular ordering approximation*, is described next.

2.3 Angular Ordering Approximation

Monte Carlo simulation of physics processes makes use of randomly generated event attributes weighted by known probability distributions. Non-negative probabilities are thus required. Unfortunately, leading-N_c probability distributions for color coherence effects, such as Equation 2.12, are not suitable for Monte Carlo simulation due to the interference terms in the individual amplitudes (W_{ij}^i terms). Recall the expression for these terms as given by Equation 2.11. When a soft gluon with momentum q is emitted from parton i of the color pair (i,j) such that $\theta_{iq} > \theta_{ij}$, the interference term $(\alpha_{ij} - \alpha_{iq})/(\alpha_{iq}\alpha_{jq})$ is negative [57, 59]. Thus, the amplitude W_{ij}^i is not positive-definite outside the cone $\theta_{iq} < \theta_{ij}$ centered on parton i (see Fig. 2.1). However, by integrating over the azimuthal angle ϕ, the amplitude reduces to [57, 55, 59]:

$$\langle W_{ij}^i \rangle = \int \frac{d\phi_i}{2\pi} W_{ij}^i = \frac{1}{E_q^2 \alpha_{iq}} \Theta(\theta_{ij} - \theta_{iq}), \tag{2.17}$$

which is positive-definite.

This leads to the *angular ordering approximation.* The implication of this expression is that, when $\theta_{iq} < \theta_{ij}$, the parton i may emit a soft gluon independently of parton j, thus resulting in a uniform ϕ distribution within the emission cone. Outside the emission cone ($\theta_{iq} > \theta_{ij}$) the emission probability vanishes. The W_{ij}^i

amplitude has therefore been reduced to a non-negative form which is appropriate for Monte Carlo simulation of color coherence effects.

An improvement is possible to the angular ordering approximation that allows for interference effects on the ϕ-distribution of the gluon while retaining the non-negative requirement. This improvement consists of simply applying the full amplitude W_{ij}^{i} within the emission cone (where the interference term is positive) and requiring that it vanish outside the emission cone. This restriction is just [57]:

$$W_{ij}^{i} \rightarrow W_{ij}^{i}\Theta(\theta_{ij} - \theta_{iq}). \tag{2.18}$$

The effect of angular ordering (AO) on parton shower evolution following a hard scatter was briefly discussed in Chapter 1 and illustrated in Fig. 1.10. Another description is shown below for a shower originating from a color-connected $q\bar{q}$ pair.

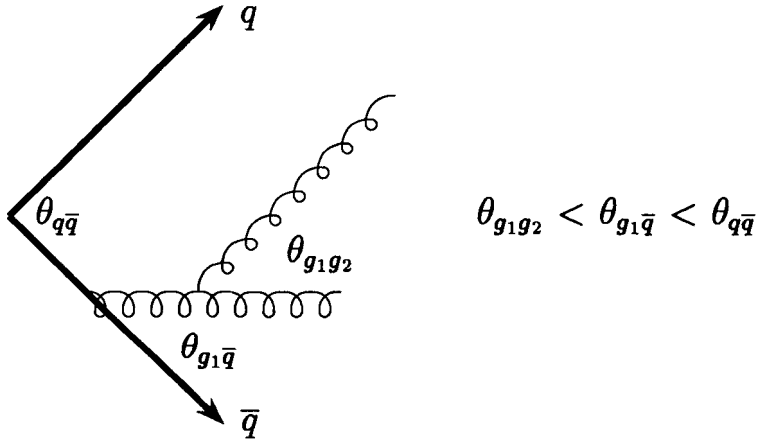

Figure 2.10: Example of angular ordering of successive gluon branchings.

AO is an iterative process that dictates the maximum opening angles for consecutive soft gluon emission in a parton cascade. For the first gluon, Equations 2.17

and 2.18 require that the opening angle for the gluon emission be less than the angle between the originating color-connected partons. Once a branching has occurred, the emitted gluon forms two new color-connected parton pairs, one with each of the parent partons, and the process is repeated. The second gluon may be emitted either from the g_1-q pair or the $g_1-\overline{q}$ pair (g_1 denotes the first gluon). If emitted from the $g_1-\overline{q}$ pair (as shown), the probability amplitude is non-vanishing only if $\theta_{g_1g_2} < \theta_{g_1\overline{q}}$. If emitted from the $g_1 - q$ pair, the corresponding amplitude is non-vanishing for $\theta_{g_1g_2} < \theta_{g_1q}$. Therefore, for successive parton branchings, the opening angles are expected to decrease sequentially. This is the definition of the AO approximation.

The final distribution of partons (upon reaching the cascade cutoff point[4]) is seen to be confined by AO to specific regions defined by the originating partons. The principle of LPHD states that this distribution ought to be unaltered at the hadron level, as described in Chapter 1. However, there can be contributions to the hadron distribution due to non-perturbative fragmentation. In particular, certain fragmentation schemes can mimic color coherence/AO effects.

2.4 Non-Perturbative Effects

Parton shower evolution proceeds, beginning from the hard scattering partons, until some cutoff limit is reached. This does not end the description of the process, however, because the resulting partons must combine to create color-singlet bound states (hadrons). The formation of hadrons from partons (known as *fragmentation* or *hadronization*) is a poorly understood process, however, from the standpoint of

[4]This is the energy limit below which partons are not evolved further. It is not unique and varies for different simulation programs.

analytical calculations. Perturbative QCD, which describes hard interactions so well and which is the foundation for the development of AO, is not useful in this regime. The coupling strength α_s is large enough to make higher-order terms in perturbative expressions relevant, causing the calculations to break down. At the moment, no proven system based on first principles has been found to satisfactorily describe the non-perturbative evolution of partons to hadrons.

Several phenomenological schemes exist for modelling the fragmentation-hadronization [5] process which have been tuned to reproduce various experimental distributions. The three most relevant to this analysis are the Lund String Fragmentation model [60], the Independent Fragmentation model [61, 62], and the Cluster Hadronization model [63, 64]. All three models are described below.

2.4.1 String Fragmentation

The Lund String Fragmentation model is founded on the notion of linear confinement, whereby the color field potential between a QCD charge and anti-charge (e.g. a color-connected $q\bar{q}$ pair) increases linearly with spatial separation of the charges [65, 66]. As the charges move apart, the color potential energy between them increases. The String model invokes the concept of a one-dimensional *string*, stretched between the charges, to represent the field. The energy stored within this string (κ) is assumed to be uniform in length, with magnitude

$$\kappa \simeq 1 \text{ GeV/fm}. \tag{2.19}$$

[5] These two terms are often used interchangeably in QCD literature, although, strictly speaking, they are not the same thing. Fragmentation refers to additional parton shower evolution beyond the perturbative scale, while hadronization refers to the subsequent formation of hadrons from these partons and the ensuing decay of unstable particles.

As the potential energy between the charges increases, there is a finite probability that the string may *break* through the formation from vacuum of a quark-antiquark pair $q'\overline{q'}$. Two string segments are thus created, one for the $q\overline{q'}$ pair and another for the $\overline{q}q'$ pair (see Fig. 2.11).

Figure 2.11: Description of color string stretched between a separating $q\overline{q}$ pair. A string break is shown in the middle accompanied by the production of a new $q\overline{q}$ pair.

The quarks may continue to move apart and, with sufficient potential energy in either string segment, another $q\overline{q}$ string break may occur. This process continues to occur until no more string breaks are possible.

The probability for creation of a new $q\overline{q}$ pair with accompanying string break is governed by the mass and transverse momentum of the pair [65, 66, 67],

$$P(m, p_T) \propto \exp\left(-\frac{\pi m^2}{\kappa}\right) \exp\left(-\frac{\pi p_T^2}{\kappa}\right). \tag{2.20}$$

The transverse momentum of the quark and antiquark are determined by a Gaussian distribution, subject to the constraint that $p_T^q + p_T^{\overline{q}} = 0$ (i.e. there is no transverse motion allowed for the string). There is also a small ($\sim 10\%$) probability that, rather than producing a quark-antiquark pair at a string break, a diquark-antidiquark pair may be created [65]. In such a case, each diquark and antidiquark is treated as if it were a single parton for the purposes of mass and p_T distributions.

Once the string fragmentation is complete, the picture is one of a linear chain of quark-antiquark pairs, joined by short string segments and bounded by the original $q\overline{q}$ separating pair. Mesons are created from these pairs in color-singlet states. Baryons can be created by either joining three quarks along the chain or by joining a quark with a diquark. As with mesons, color-singlet states must result. This scheme is shown below in Fig. 2.12 [65].

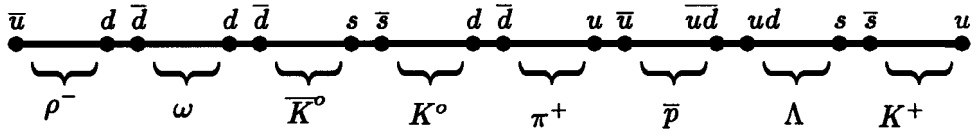

Figure 2.12: Hadron formation from a chain of quark-antiquark pairs created along a $u\overline{u}$ color string.

The p_T of each hadron is the sum of the p_T's of its constituent partons. The energy E and longitudinal momentum p_z are determined in an iterative fashion, beginning with the leftmost (or rightmost) hadron and working right (or left). Each hadron takes some fraction z of the total $E + p_z$ remaining from the original $q\overline{q}$ system, so that this total decreases successively for each hadron along the chain. The z fraction is determined from the distribution [66]

$$f(z) = N\frac{(1-z)^a}{z}\exp\left(-\frac{bm_T^2}{z}\right), \tag{2.21}$$

where m_T is the hadron's transverse mass, while N, a, and b are free parameters. For the $i^{\underline{\text{th}}}$ hadron, E and p_z are then determined by the following expressions [66]:

$$(E+p_z)_i = (1-z)(E+p_z)_{i-1} \tag{2.22}$$

$$(E - p_z)_i = (E - p_z)_{i-1} - \frac{m_T^2}{z(E + P_z)_{i-1}}. \tag{2.23}$$

The end result for the expansion of a single string is an assortment of hadrons oriented along the string's length, each with known momentum relative to the string. For a system of partons resulting from a hard scattering and shower evolution, the picture is conceptually the same. Each color connection among the partons results in a one-dimensional string drawn between them. Each gluon, having two color connections, gives rise to two string segments. This can be seen in Fig. 2.13, which shows one possible string arrangement for a system of partons in an event.

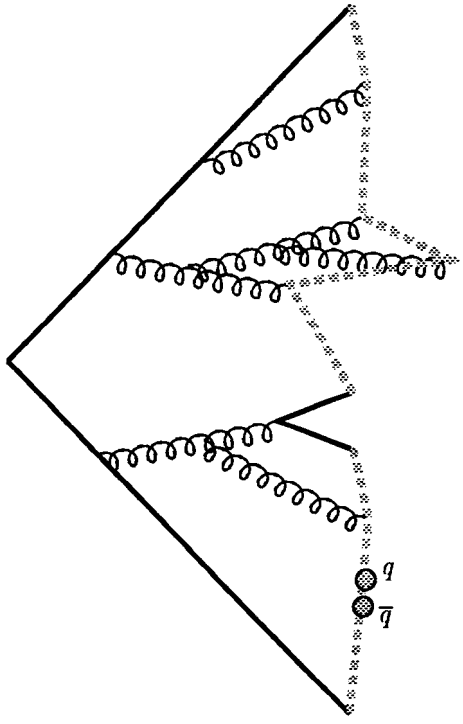

Figure 2.13: Visual description of String model. One-dimensional string spans all color-connected partons following cascade process from a $q\bar{q}$ pair. The light gray circles represent a $q\bar{q}$ pair being pulled from the vacuum along a string.

Each string segment is treated separately. The fragmentation is performed in the center-of-mass system of the string, such that the end partons are moving in the $\pm z$ directions. Following the fragmentation procedure, the resulting hadrons are then boosted back into the lab frame. If the hadron momenta relative to the string are much smaller than the boost, their trajectories will follow the string direction. Since the string direction was determined during the partonic shower evolution, it is greatly influenced by color coherence effects. Therefore, by accounting for color connections among the partons, the String Fragmentation scheme may produce hadrons in a pattern similar to the partonic pattern created by angular ordering. In effect, the String model treats each color-connected parton pair as a dipole, much the same as for the leading-N_c interference calculations. The contribution of String Fragmentation relative to AO in hadron distributions is an interesting attribute of hadronic physics to study. It has never been explicitly tested in a hadron-hadron collider.

2.4.2 Independent Fragmentation

The Independent Fragmentation model assumes that each parton in an event fragments independently of all other partons, so the system of fragmenting partons can be described as an incoherent sum of independent fragmentation procedures for each parton separately. Therefore, there is no conceptual picture of a string or any other connection with surrounding partons. Furthermore, the fragmentation takes place for all partons in the center-of-mass frame of the event, as opposed to the frame of the string in the String model.

A quark q in the Independent Fragmentation model fragments into a $q\overline{q_1}$ pair and

a remainder quark q_1, where the pair $q_1\overline{q_1}$ is pulled from the vacuum. As with String fragmentation, the p_T of each member of the pair is generated from a Gaussian distribution and the requirement of no net p_T for the pair is imposed. The energy and longitudinal momentum with respect to the original quark are also chosen as in the String model, with the splitting fraction z following the distribution given by Equation 2.21. The remainder quark is then fragmented into another $q_2\overline{q_2}$ pair and another remainder quark q_2. This process is iterated until the remainder quark no longer has sufficient energy to fragment. Baryons are formed using the same method as the String model.

No unique procedure exists for the fragmentation of gluons. The most common method is to split the gluon into a $q\bar{q}$ pair and then fragment the quark and antiquark separately. The two partons would share the total gluon energy according to the Altarelli-Parisi splitting function [68].

The Independent Fragmentation model leads to hadron trajectories that closely follow the original parton direction. This is in contrast to the String model, which populates the region between color-connected partons as well. Studies of the *string effect* (described in Chapter 1) in e^+e^- experiments have shown that the string picture more accurately reproduces the particle distributions in data, but this has never been explicitly tested at a hadronic collider [6].

2.4.3 Cluster Hadronization

The Cluster Hadronization model is predicated on the property of *preconfinement* which is predicted by perturbative QCD [69]. *Preconfinement* is the tendency of the

[6] Color coherence studies of W+Jet events at DØ (described in Chapter 1) have shown some sensitivity to fragmentation effects, supporting this thesis.

partons generated in the branching process to be arranged in color-singlet clusters with limited extension in both coordinate and momentum space. Hence, the Cluster Hadronization model is local in color and is independent of the hard process and the energy.

After the perturbative parton branching process, all final state gluons are split non-perturbatively into light (u or d) quark-antiquark pairs (as in the Lund String Fragmentation model, diquark splitting is suppressed). At this point, each jet consists of a set of outgoing quarks and antiquarks (also possibly some diquarks and antidiquarks). Spacelike jets, which consist of a single incoming valence quark or antiquark are replaced by an outgoing spectator carrying the opposite color and the residual flavor and momentum of the corresponding beam hadron.

For each quark q there is a neighboring (as defined by the shower) color partner antiquark $\bar{q}$ (or antidiquark $\bar{q}\bar{q}_1$), with which the quark would normally be color-connected and paired to form a color-singlet cluster $(q\bar{q})$. In the case of the antidiquark, two clusters $(q\bar{q})$ and $(\bar{q}_1 q_1)$, where q_1 is the corresponding color partner quark of $\bar{q}_1$, are formed. These clusters satisfy the preconfinement property previously mentioned — they have a distribution of mass and spatial size that peaks at low values, falls rapidly for large cluster masses and sizes and is asymptotically independent of the hard subprocess scale. The clusters thus formed are then fragmented into hadrons. The cluster decays are isotropic, in their own rest frame, except when a perturbative quark is involved, i.e., one from the hard sub-process or from a $g \to q\bar{q}$ splitting. In this case, the hadron containing this quark is aligned with the quark direction in the cluster rest frame.

The Cluster Hadronization model, like the String model, also populates the region

between color-connected partons with hadrons. And both models reproduce the particle distributions observed in e^+e^- annihilation experiments.

2.5 Monte Carlo Simulation

The implementation of color coherence in Monte Carlo simulations is of prime importance in this analysis. Of the many available simulations available today, only the PYTHIA program allows a user to explicitly test angular ordering and fragmentation separately in a consistent manner. This is because PYTHIA allows the user to turn angular ordering on or off and also to choose between string and independent fragmentation. HERWIG, on the other hand, uses cluster fragmentation which takes into account color effects, and like *PYTHIA*, also incorporates initial and final state interference effects by means of angular ordering of soft gluon radiation. HERWIG provides an additional coherent sample for comparison to data. In addition to these two shower-level simulations, a third one, ISAJET, uses independent fragmentation for the partons and, although it provides for both initial and final state gluon radiation, this radiation is completely incoherent. Finally, JETRAD which uses an $\mathcal{O}(\alpha_s^3)$ parton-level calculation allows a user to observe what features of perturbative hadronic processes survive hadronization.

Based on the above discussions, a sample of multi-jet events simulated with angular ordering and with string or cluster fragmentation is expected to exhibit a very different jet distribution pattern than one with no angular ordering and independent fragmentation. Studying the NLO parton-level simulation will give a measure of the importance of fragmentation and hadronization effects in multi-jet events.

2.5.1 PYTHIA

For final-state soft radiation in parton shower evolution, soft gluon emission is governed in PYTHIA [70] by the improved angular ordering approximation (Equation 2.18), thereby leading to non-isotropic azimuthal gluon distributions in consecutive branchings. The parton shower evolves according to the Altarelli-Parisi equations [66, 71] with evolution variable $Q^2 = m_a^2$, where m_a is the mass of the parent parton a in a branching $a \rightarrow bc$. The branching products each get a fraction of the parent energy, defined by the splitting variable z such that $E_b = zE_a$ and $E_c = (1 - z)E_a$. The masses of the branching products are required to be monotonically decreasing at each branching, so that $m_b + m_c < m_a$. This may or may not lead to a decrease in the opening angle for consecutive branchings, but PYTHIA ensures this through angular ordering – if parton b in the $a \rightarrow bc$ branching then branches as $b \rightarrow de$, angular ordering requires that $\theta_{de} < \theta_{bc}$, where $\theta_{bc(de)}$ is the opening angle for branching products b and c (d and e). The azimuthal angle ϕ for each branching is chosen by Equation 2.18 using a standard rejection method. Parton branching continues until the mass of each branching product is below the minimum mass $m_{min} = 1$ GeV.

For initial-state radiation, the backward evolution procedure is used [72, 73], whereby the branching process proceeds backwards from the scattering partons toward the original parton/antiparton. Initial-state partons have space-like virtuality ($m^2 < 0$). The virtuality $Q^2 = -m^2$ is the evolution variable for the Altarelli-Parisi equations governing the shower development – it is highest at the interaction point and decreases backwards toward the parent hadron. Consecutive branchings are therefore required to have strictly decreasing virtualities.

At first glance, it appears that initial-state parton evolution is just the time-reversal of final-state evolution. However, there are two significant differences. First, coherence influences the branching process much less for initial-state radiation than for final-state radiation due to the kinematics of initial-state radiation [74]. This is because, for time-like showers ($m^2 > 0$), both energies and masses decrease as the shower evolves. Emission angles, which are approximately the ratio of p_T over energy, behave approximately as mass over energy, and thus a priori can go either way. Coherence here makes a big difference, since kinematics has little influence over the emission angles. In space-like branchings, on the other hand, energies are still decreasing toward the interaction but Q^2 is increasing, so emission angles also tend to increase as the initial-state hard parton approaches the scattering region. Ordering in Q^2 therefore, usually ensures angular ordering without the need for coherence contributions [75]. The second difference is that, for branchings from the initial-state partons, ϕ is chosen randomly, without the inclusion of interference effects. This is a characteristic of the current version of PYTHIA (v5.7) and not due to any theoretical considerations.

Some inconsistency therefore exists in the treatment of the two forms of radiation in PYTHIA. However, each gluon emitted from the space-like initial-state partons can then initiate its own shower, just as gluons emitted from the final-state parton can. These secondary emissions are treated as time-like, and interference effects therefore contribute.

2.5.2 HERWIG

HERWIG (Hadron Emission Reactions With Interfering Gluons) [76] is a general-

purpose MC event generator for high energy hadronic processes. One of the distinguishing attributes of HERWIG is that it employs very sophisticated, partonic treatment of the calculable QCD showers to provide an accurate description of the QCD jet evolution. Included in this treatment are: color coherence of initial-state and final-state partons in hard processes, QCD jet evolution with soft gluon interference via AO, backward evolution of initial-state partons including interference and azimuthal correlations within jets due to gluon polarization. In contrast, the description of the so far incalculable hadronization and beam remnant components is in terms of very simple models. For the hadronization phase HERWIG uses the Cluster Hadronization model, while for the soft and underlying hadronic events a similar cluster model is used. HERWIG has been thoroughly tested against QCD collider data and found to most closely model data distributions among current MCs.

The modelling of color coherence effects in HERWIG makes it useful to compare to the data in order to test the validity of these theoretical representations.

2.5.3 ISAJET

ISAJET [77] simulates $p\bar{p}$ and pp interactions at high energy by incorporating perturbative QCD cross sections. The event is simulated by generating a primary hard scattering. All $2 \rightarrow 2$ processes which involve quarks and gluons are included and the masses for c and lighter quarks are neglected. Higher order processes are also included by adding QCD radiative corrections in the leading log approximation to both the initial and final states in order to obtain the correct event structure. Partons involved in the hard scatter are evolved through repeated parton branchings, as modeled by Sjöstrand's branching approximation for initial state gluon radiation [78], and

by Fox and Wolfram's branching approximation for final state radiation [79]. Events containing three or more partons are obtained in this way. The cascade process continues until the energy of the partons falls below 6 GeV. At this point, quarks and gluons are fragmented independently into hadrons using the Feynman and Field model [80]. The generation is then completed with the addition of *beam jets* resulting from the soft interactions between spectator partons.

Since ISAJET incorporates neither perturbative-level nor non-perturbative contributions to color coherence, and therefore provides a purely kinematical representation of radiation, it provides a useful template against which to compare the data to identify any interference effects present there.

2.5.4 JETRAD

JETRAD ia a very general $\mathcal{O}(\alpha_s^3)$ MC program for one-, two- and three-jet production at the parton level. It allows a particularly revealing comparison with data since it excludes completely the effects of fragmentation, hence providing some insight into the validity of LPHD. JETRAD [81] is a partonic generator and includes the one-loop $2 \rightarrow 2$ and the tree-level $2 \rightarrow 3$ parton scattering amplitudes, some of which were shown in Fig. 1.4. In JETRAD there is a direct correlation between the parton and the jet since fragmentation is absent.

Since JETRAD is an exact calculation of the theory to $\mathcal{O}(\alpha_s^3)$, it includes interference between colored partons to this order. Therefore, it is expected to correctly replicate the leading-order color interference effects correctly at the partonic level.

2.6 Color Coherence Study

The analysis which forms the basis of this thesis is an attempt, using multi-jet data from the DØ detector, to observe the various effects described in this chapter. Global event shapes in the data will be compared with multi-jet events simulated by the PYTHIA simulation package with the implementation of both perturbative effects (angular ordering) and non-perturbative effects (fragmentation) toggled to determine what combination is most consistent with the data, if any. In addition, data will be compared to two other MC simulations which implement color coherence effects differently: HERWIG which incorporates perturbative QCD effects, and ISAJET which does not. Finally, data will be compared to JETRAD, a partonic simulation which utilizes an $\mathcal{O}(\alpha_s^3)$ calculation and excludes all non-perturbative effects.

The following chapter describes the next step in this process. There, the powerful Fermilab accelerators which supplied the necessary collisions, and the delicate DØ experimental apparatus which collected beautiful events from amongst the chaos are described.

Chapter 3

Experimental Apparatus

The DØ detector was designed to study proton-antiproton ($p\bar{p}$) collisions at the world's highest center of mass energy (1.8 TeV). These collisions are produced in the Tevatron at the Fermi National Accelerator Laboratory (Fermilab for short) located in Batavia, Illinois, USA, about 30 miles west of Chicago. The detector's name corresponds to the DØ interactive region, which is one of the Tevatron's two high luminosity locations where p and $\bar{p}$ beams collide.

3.1 The Tevatron

Most protons at Fermilab lead rather ordinary lives. However, the life of a select group of protons at the laboratory is very different from that of most protons in the world — and quite remarkable! These are the protons that are accelerated to today's highest man-made energies inside the Tevatron before being smashed into an antiproton at a center of mass energy ($\sqrt{s}$) of 1.8×10^{12} electron-volts (1.8 TeV). In many of these collisions, the components of the proton and antiproton interact so violently that they produce hundreds or even thousands of particles, some of

which can be seen on Earth only in such events. The experimental observation of these particles allow us to learn and to test the fundamental rules that govern their structure and behavior.

An overview of the system of accelerators used at Fermilab to produce and collide protons and antiprotons is shown in Fig. 3.1.

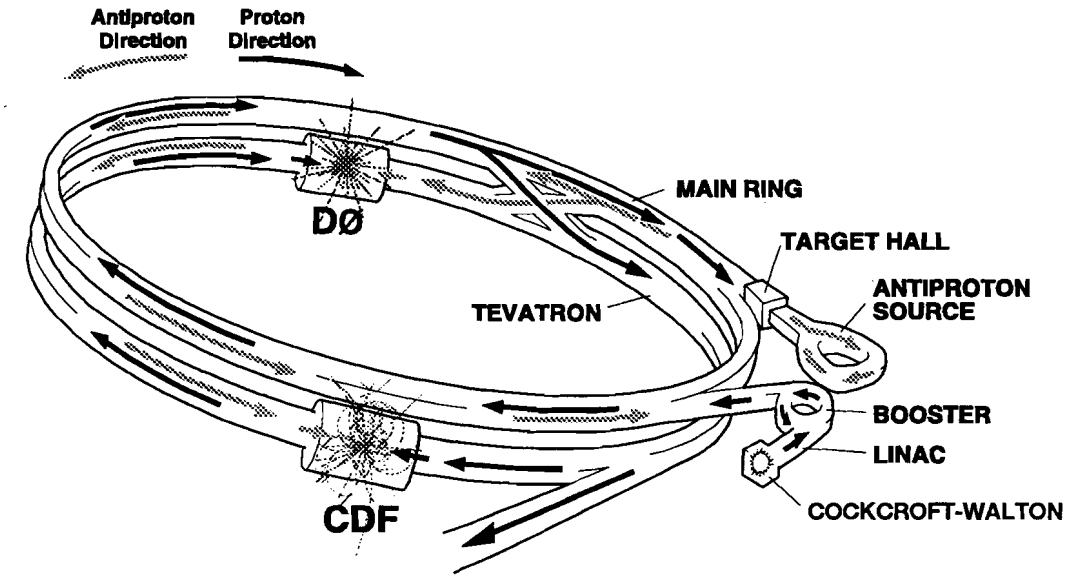

Figure 3.1: An overview of the Fermilab accelerators with the DØ and CDF detectors shown.

The protons' special journey begins inside a single compressed hydrogen tank from which the protons accelerated and collided have been drawn for many years, and ends in fierce collisions against their alter-egos, the antiprotons inside the Tevatron. Inside this tank, they sit patiently awaiting the moment in which they will embark on this most unusual trip.

The first steps of this journey take the hydrogen gas to one of the two pre-accelerators [82] where each H atom acquires an extra electron and is accelerated

to 18 keV before entering a Cockcroft–Walton generator. There, the H^- ions pass through an electrostatic accelerating column from which they emerge at 750 keV. The beam of ions is then bunched at 201.24 MHz, the radio frequency (RF) of the linear accelerator (Linac), and focused before being transported to the Linac.

The Linac is a two-stage linear accelerator that produces a pulsed beam of 400 MeV H^- ions. Its first stage, an Alvarez drift tube accelerator, accelerates the ions to 116 MeV. Then the beam of ions enters a side-coupled section of the Linac which boosts their energy to 400 MeV before injection into the Booster, which provides the next phase of acceleration.

During injection, the H^- beam passes through a carbon foil which strips off the electrons from the negative hydrogen ions. A magnetic field separates out the remaining unstripped ions from the protons and dumps them outside the Booster. The protons are maintained in a closed orbit in this fast-cycling proton synchrotron until the Booster is filled with around 3×10^{12} protons. This typically takes six orbits of the particles. Afterward, the proton beam is grouped into bunches before being accelerated to its final energy of 8 GeV by ramping up the magnet currents synchronous with the RF increasing from 37.9 MHz at injection to 52.813 MHz during extraction from the Booster to the Main Ring, at which time the RFs of each are phase-locked to each other in order to maximize the number of protons transferred.

The Main Ring, as its name implies, is one of the two major accelerators at Fermilab (the other one is the newer Tevatron.) It is a 400 GeV proton synchrotron with a radius of 1 km and is located in a tunnel beneath the Illinois prairie. It is composed of 774 dipole and 240 quadrupole magnets and has 18 dual gap RF

cavities. The Main Ring operates with 1113 RF buckets at about 53 MHz. During collider operations, the Main Ring serves both as a 150 GeV injector of protons and antiprotons for the Tevatron as well as a source of 120 GeV protons for the production of antiprotons.

Most of the protons whose journey takes them to the Main Ring are used to harvest their counterparts, the antiprotons. Only a handful of them will participate or even witness the violent collisions with their alter-egos. Antiprotons with an energy of 8 GeV are produced by extracting a beam of 120 GeV protons from the Main Ring onto a nickel target disk (other target materials have also been used.) It takes 2.4 seconds for the Main Ring to complete a $\bar{p}$ cycle and typically 10^5 protons are required to strike the target for every antiproton that is produced. Thus, with a typical Main Ring beam consisting of about 3×10^{12} protons, it takes around 10 hours to produce the approximately 3×10^{11} antiprotons normally required for a collider "store" — in which, ultimately, the Tevatron is filled with collimated proton and antiproton bunches circulating in opposite directions to collide against each other. The antiprotons produced for this purpose are collected, cooled stochastically and accumulated in the Antiproton Source before being bunched and injected into the Main Ring, where they will be accelerated and then transferred to the Tevatron to complete the store.

The orbit of the protons (and their alter-egos) in the Main Ring is circular, with the exception of two regions (BØ and DØ) where the Main Ring deviates vertically out of the plane of the circle. These two regions are occupied by large collider detectors: the first one by CDF (Collider Detector at Fermilab) and the second one by the DØ detector. The tunnel in which the Main Ring resides was extensively modified

at BØ in order to bypass the detector there. The vertical separation between this detector and the Main Ring is about 5.8 meters. DØ was not as fortunate, however. The Main Ring tunnel at DØ was not modified accordingly, hence the DØ detector has the Main Ring passing right through it just 2.3 meters above the Tevatron which is at its center. Since the Main Ring is often in operation during a colliding beam store, this is a substantial complication in the operation of DØ as care has to be taken that the detector not collect data while the beam in the Main Ring is near DØ in order to avoid any spillover effects of the Main Ring beam. Because of this, when the Main Ring is in operation during a store, the time DØ can be actively collecting data is reduced by around one third.

Once a sufficient number of antiprotons have been accumulated, "shot setup" commences. After being accelerated to 150 GeV in the Main Ring, the p and $\bar{p}$ beams are injected into the Tevatron one bunch at a time, first the proton bunches (since they are more readily obtained) and then the antiproton bunches (a much scarcer resource.)

The Tevatron is a proton-antiproton colliding beam synchrotron accelerator. It occupies the same circular underground tunnel as the Main Ring and is located just 0.65 m below it at the same radius. It was the first large scale superconducting synchrotron to be constructed. All of its 774 dipole, 216 quadrupole and correction magnets are superconducting and are cooled by liquid helium to a temperature of 4.6°K. For optimal beam transfer from the Main Ring, the Tevatron's RF system also operates at around 53 MHz and has the same 1113 RF bucket structure as the Main Ring. During its 1992–1993 run it operated in "six-on-six" mode, in which six bunches each of protons and antiprotons circulate in opposite directions in the ring

which, in turn, has two high luminosity regions at DØ and at BØ.

The instantaneous luminosity $\mathcal{L}$ is given by Equation 3.1.

$$\mathcal{L} = \frac{\nu N_b N_p N_{\bar{p}}}{4\pi {\sigma_L}^2} = \frac{N_{int}}{\sigma} \tag{3.1}$$

Here ν is the crossing frequency, N_b is the number of bunches of either particle type, N_p and $N_{\bar{p}}$ are, respectively, the number of protons and antiprotons, $\pi {\sigma_L}^2$ is the area of a transverse section of the beam, N_{int} is the interaction rate and σ is the cross section. Note that the interaction rate is proportional to the number of protons and antiprotons and inversely proportional to the area of the beam.

The peak instantaneous luminosity measured in this run was $\sim 1.0 \times 10^{31}$ cm^{-2}s^{-1}.

A few moments before a store, the six proton bunches are injected individually into the Tevatron. Each bunch consists of $\sim 150 \times 10^9$ protons. Then, each one of the six antiproton bunches (with about a third as many antiprotons as protons) is injected into the Tevatron. Their energy is ramped up to 900 GeV, after which some special superconducting magnets, the low beta quadrupoles, located at either side of both luminous regions, squeeze the beams and greatly reduce the beam spot size to $\sigma_x \approx \sigma_y \approx 40$ μm, which dramatically increases the luminosity. A brief summary of the Tevatron parameters is given in Table 3.1.

An unfortunate feature of these quadrupole magnets was that during the 1992–1993 collider run, they were not of equal strength and this difference shifted the region where the proton and antiproton bunches cross by about eight centimeters upstream (toward the incoming protons) from the center of the detector. The longitudinal distribution of event vertices measured by the tracking chambers yielded a width measured along the beam axis $\sigma_z \approx 30$ cm for the interaction region.

Accelerator radius	1000 m
Maximum Beam Energy	900 GeV
Peak Instantaneous Luminosity	$\simeq 1.0 \times 10^{31}$ cm^{-2}s^{-1}
Bunch Configuration	$6p \times 6\bar{p}$
Bunch Intensities	$\approx 150 \times 10^9(p), \approx 50 \times 10^9(\bar{p})$
Bunch Length	50 cm
Transverse Beam Radius	43 μm
RF Frequency (# of RF Buckets)	53 MHz (1113)
$\bar{p}$ Stacking Rate	$\approx 3.5 \times 10^{10}$/hour
Time Between $p\bar{p}$ Interactions	3.5 μs

Table 3.1: Summary of Tevatron Parameters [82].

Once the beams in the Tevatron have been ramped up fully to 900 GeV ("flat-top"), they are kept at this energy and usually continue to circulate for a period of several hours. The typical duration of a store is around 12–18 hours, during which time the luminosity gradually decreases as beam conditions deteriorate and bunch populations decrease.

During a store, antiprotons usually continue to be produced and accumulated to enable the start of a new store once the luminosity and beam conditions warrant ending the old store. The store is then ended by directing the beams of protons and antiprotons into the beam dump just outside the tunnel at a fixed location of the accelerator. Afterward, the cycle of shot setup, bunch injection into the Tevatron, ramping and squeezing of the beams and new store is repeated.

In the lattice of the Tevatron each p and $\bar{p}$ bunch occupies one RF bucket and is always 186 RF buckets away from it's closest same particle bunch on one side and 187 RF buckets away from the other bunch on the opposite side. Since an RF bucket corresponds to 18.8×10^{-9} seconds, the beam crossings occur every 3.5 μsec.

Synchronization of the DØ detector to the accelerator is handled by the DØ clock system which is phase locked to the Tevatron. Additionally, Beam Position Monitors (BPMs) on either side of the detector enable the clock system to verify every beam crossing. Typically, one of the first indications received in the DØ control room when the beam is lost is from the clock system alarms that are generated when synchronization to the beam in the Tevatron fails.

3.2 DØ Detector Overview

The DØ detector was designed to serve as a multi-purpose collider detector for the study of short distance phenomena in proton-antiproton ($p\bar{p}$) collisions. The designers' intent was to build a detector that would help shed light on a wide range of physics topics by providing accurate measurements to test the predictions of the Standard Model and to search for new phenomena [83]. The DØ detector was optimized for the study of high mass states and high p_T phenomena, for the identification of both electrons and muons over a large solid angle and for good jet and missing transverse energy ($\not\!\!E_T$) measurement. Specifically, its physics goals include the search for (and subsequent discovery) of the top quark and measurement of its mass, various studies of perturbative QCD by means of jets and photons, precision studies of the W and Z bosons, studies of the production of b-quark hadrons and searches for new phenomena.

Figure 3.2 shows a cutaway view of the DØ detector with its nested components visible. At the center of the detector and surrounding the thin and brittle beryllium beam pipe which traverses it are the cylindrical central tracking and transition radiation detectors. Enveloping these is the vessel-like calorimeter consisting of three

distinct quasi-cylindrical sections. Finally, the rectangular muon detector lies just outside and around the calorimeter.

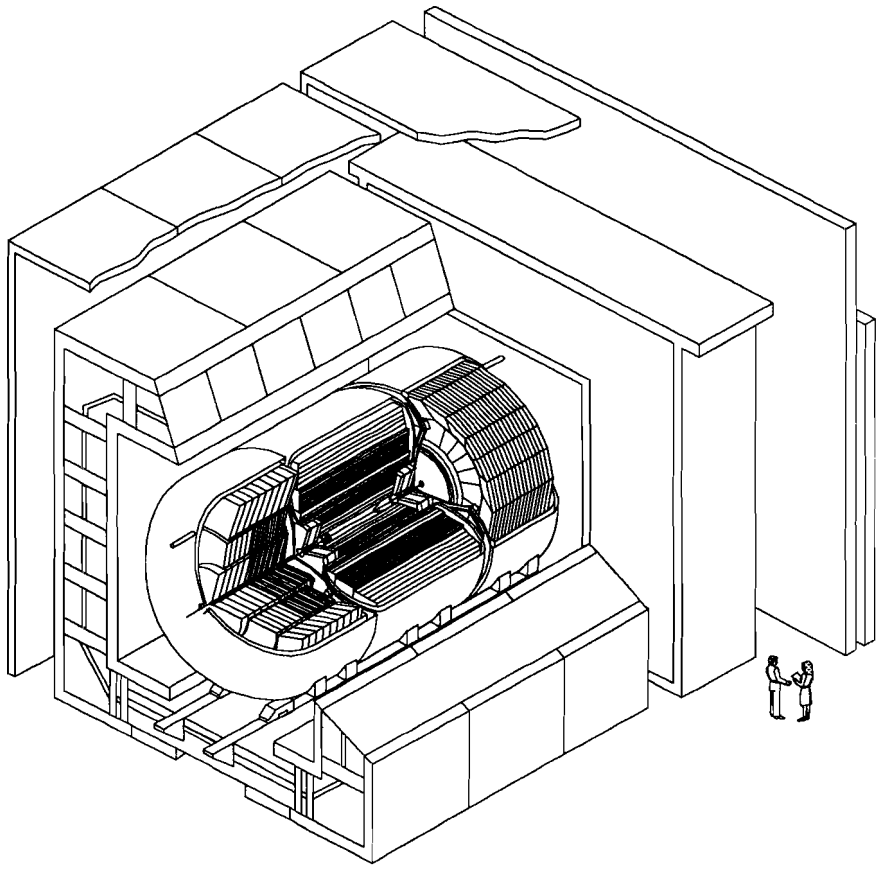

Figure 3.2: An isometric cutaway view of the DØ detector.

Of primary importance in this analysis is the nearly complete coverage and hermeticity of the calorimetry, which allows jets to be contained over a wide region and enables good measurement of their transverse energy (E_T).

A detailed description of the DØ detector has been published and may be found in reference [83] and in references contained therein.

3.2.1 Coordinate System

The standard coordinate system used to describe the DØ detector is a right-handed Cartesian system which has its $+\hat{x}$ direction pointing radially outward from the center of the accelerator ring (approximately toward the geographic east;) the $+\hat{y}$ direction is upward, leaving the $+\hat{z}$ direction to be the same as that of the proton beam in the Tevatron at DØ (roughly toward the geographic south). The angles ϕ and θ are, respectively, the azimuthal and polar angles of a spherical coordinate system. The r coordinate denotes the radial distance of cylindrical coordinates from the beam axis.

Due to the relativistic energies of the particles produced in the $p\bar{p}$ collisions in the Tevatron, we can use the pseudorapidity defined in Equation 3.2 as an approximation to the true rapidity, given in Equation 3.3 [1]. This approximation is valid in the limit of Equation 3.4.

$$\eta \equiv -\ln\left[\tan\left(\frac{\theta}{2}\right)\right] \tag{3.2}$$

$$y = \frac{1}{2}\ln\left[\frac{E+p_z}{E-p_z}\right] \tag{3.3}$$

$$\eta \to y \text{ as } \frac{m}{E} \to 0\,, \text{ for } 0 < \theta < \pi \tag{3.4}$$

The principal reason pseudorapidity is used in our measurements is that a particle's spatial and angular position can be determined more accurately than its energy

[1] Rapidity distributions are invariant under Lorentz transformations, as a transformation to another reference frame simply amounts to a shift in the origin of y.

and z component of momentum.

3.3 Central Detectors

The DØ Central Detector (CD) is a compact set of four drift chambers and a transition radiation detector whose principal goal is to provide tracking and lepton identification information within a limited space and without the aid of a central magnetic field. Such a field was not included in the detector design so as to allow a hermetic calorimeter to be built at an acceptable cost. The CD is contained inside the inner cavity of the calorimeters in a cylindrical volume which is bounded radially and longitudinally by, respectively, $r = 78\,cm$ and $z = \pm 135\,cm$ and which contains, at its center, the interaction region.

The primary features of the tracking system are good two-track resolution, high efficiency and good ionization energy measurement which enable the system to distinguish single electrons from closely spaced photon conversion pairs. This information provided by the CD is used to aid in the identification of leptons in the calorimeter and muon systems by finding the location of the primary interaction vertex so that directed energy vectors in the calorimeter may be correctly reconstructed.

The Central Detector consists of four distinct subsystems, as shown in Fig. 3.3. Beginning nearest to the center of the detector and going outward we will find: the Vertex Drift Chamber (VTX), the Transition Radiation Detector (TRD), the Central Drift Chamber (CDC) and the two Forward Drift Chambers (FDC), one at each end of the cylinder and perpendicular to the beam. Each of these subsystems is filled with a unique blend of gases which are continuously monitored and corrected for atmospheric conditions by means of special 'canary' monitoring chambers, one for

each gas mixture.

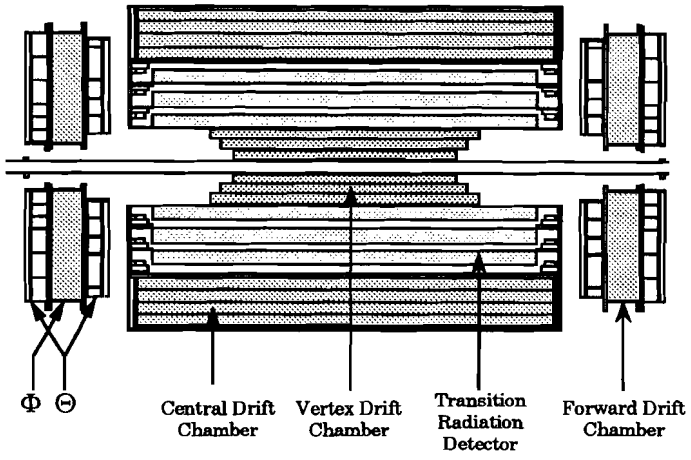

Figure 3.3: A side view of the DØ Central Detector.

3.3.1 Vertex Chamber

The Vertex Chamber is the innermost drift chamber of the DØ Central Detector. Located just outside the beam pipe and radially surrounding it, the purpose of the VTX is to help reconstruct accurately the z position of the interaction vertex. This information is later used to determine the jet E_T.

The active region of the VTX has inner and outer radii of 3.7 cm and 16.2 cm, respectively, and a length of 116.8 cm. The chamber is composed of three concentric layers of cells. Each cell is an azimuthal section which spans the entire length of the chamber in the $\hat{z}$ direction. The innermost layer has 16 cells; the other two have 32 cells each. The cells of the three layers are offset in ϕ in order to enhance pattern recognition and facilitate calibration. In each cell, eight staggered sense wires parallel to the beam direction are used to determine the r–ϕ coordinate of each hit. The gas used in the VTX is a mixture of 95% CO_2 and 5% ethane at one atmosphere of

pressure with a small admixture of H_2O. This gives an average drift velocity of 7.3 μm/ns in an electric field of $<\vec{E}> \approx 1kV/cm$.

The VTX chamber was used for the vertex reconstruction of a small fraction of the events in this analysis.

3.3.2 Transition Radiation Detector

The Transition Radiation Detector lies in the space between the VTX and the CDC. It provides independent electron identification in addition to that afforded by the calorimeters.

Transition radiation is a purely classical electrodynamics phenomenon that occurs when highly relativistic charged particles traverse boundaries between media with different dielectric constants. Dipole radiation is produced by the polarization which is induced by these particles, as a function of the media's dielectric constant. This results in significant emission of transition photons when the velocity v of the charged particle, hence its Lorentz γ factor in Equation 3.5, are large [84]. When $\gamma > 10^3$ — a frequent event for electrons during collider operation at DØ — transition radiation X-rays are produced.

$$\gamma = \sqrt{\frac{1}{1 - \frac{v^2}{c^2}}} \tag{3.5}$$

The TRD consists of three separate units, each of which contains a radiator and an X-ray detection chamber. The radiator section of each TRD unit consists of 393 foils, spaced 150 μm apart, of 18 μm thick polypropylene in a volume filled with nitrogen gas. Detection of X-rays is carried out in a two-stage time-expansion radial-drift proportional wire chamber (PWC) mounted immediately after the radiator.

The gap between both regions is filled with dry CO_2 gas kept flowing to prevent contamination of the recirculating chamber gas with nitrogen from the radiator. The detection chamber is filled with a gas mixture of 91% Xe, 7% CH_4 and 2% C_2H_6. The Xe serves primarily as a photon absorber and converter, due to its high atomic number. Most X-rays convert in the first stage of the chamber and the resulting charge drifts radially outward to the sense cells where an avalanche occurs. The magnitude of the charge collected and the time of arrival of the charge clusters provides information useful for distinguishing electrons from hadrons.

The TRD was not used in this analysis as the calorimeter's ability to differentiate electrons from jets was deemed to be sufficient.

3.3.3 Central Drift Chamber

The Central Drift Chamber provides coverage of charged particle tracks at large angles. It serves to provide tracks to distinguish between photons and electrons found in the calorimeter, to aid in the identification and momentum measurement of muons observed in the muon detector and to find the z location of the interaction vertices.

The CDC occupies a cylindrical shell located outside the TRD whose inner and outer radii are 49.5 and 74.5 cm, respectively, and which measures 184 cm in length. It has four concentric rings with 32 azimuthal cells in each ring. The cells in each ring are staggered in ϕ with respect to those in the adjoining rings to help resolve left-right ambiguities in the location of hits as illustrated in Fig. 3.4 which shows the cells in a ϕ section of the CDC. Every cell has seven gold plated tungsten sense wires and two delay lines one of which is placed at a smaller radius than any of the

sense wires, while the other is placed at a greater radius. Adjacent sense wires are staggered by 0.2 mm to further reduce the left-right ambiguity in the location of hits. The cells are filled with a 'fast' gas mixture (i.e., one in which electrons have a high drift velocity) consisting of 92.5% Ar, 4% CH_4, 3% CO_2 and 0.5% H_2O. The position resolution in the $\rho - \phi$ and z directions, as measured in a test beam setup, are $150 \sim 200$ μm and $\simeq 2$ mm, respectively.

For spatial calibration, a single layer scintillating fiber detector was installed between the CDC and the surrounding Central Calorimeter. The 128 individual fibers are aligned parallel to the beam and cover $\frac{1}{32}$ of the full azimuth. The spatial information from the scintillating fibers combined with the measured CDC drift time, permits the rapid determination of new calibration constants when operating conditions change.

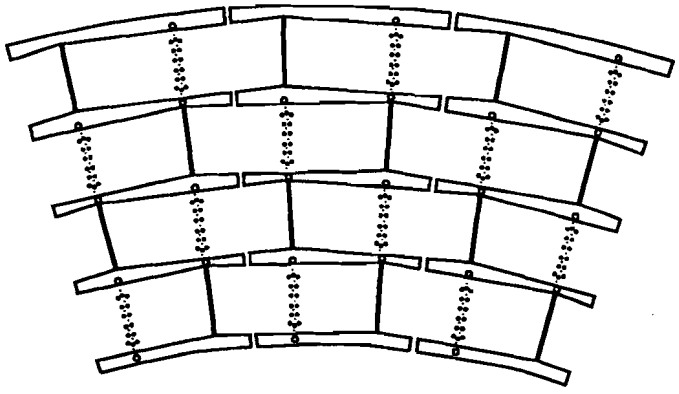

Figure 3.4: A ϕ section of the CDC showing its cell structure.

The CDC was the primary sub-detector used for vertex reconstruction in this analysis.

3.3.4 Forward Drift Chambers

The Forward Drift Chambers, circular in shape, are located at both ends of the concentric barrels of the nested VTX, TRD and CDC with their axes parallel to the beam direction, as shown in Fig. 3.3. Consequently, the FDC extends the coverage for charged particle tracking down to around 5° from the beam.

Each FDC consists of three separate chambers: one Φ module whose sense wires are radial and measure the ϕ coordinate is sandwiched between two Θ modules whose sense wires approximately measure the θ coordinate. The Φ module has 36 ϕ sectors over the full azimuth, each of which holds 16 anode wires along the beam direction. The Θ module is made up of four similar quadrants all of which contain six rectangular cells at increasing radii. Every cell has eight anode wires in z. The sense wires in the three inner cells are at one end of the cell, so electrons drift in just one direction, hence eliminating the left-right ambiguity. The Θ cells each have one delay line identical to that used in the CDC which provides local measurement of the orthogonal coordinate. Adjacent anode wires in both the Θ and Φ modules are staggered by $\pm 200\,\mu$m to aid in resolving ambiguities. The two Θ modules are offset by 45° in ϕ relative to each other for improved track measurement.

The gas mixture used in the FDC is the same as that used in the CDC. Therefore, these chambers are able to share the same gas system.

The FDC were used in this analysis to determine the z location of the interaction vertices for forward events.

3.4 Calorimeters

The heart and soul of the DØ detector is a finely segmented uranium-liquid argon (U-LAr) sampling calorimeter [85, 86]. As the most dense part of the detector, it was designed to intercept the primary particles produced in the proton-antiproton collisions and to cause them to interact and deposit their energy inside the calorimeter volume in the subsequent cascade or 'shower' of increasingly lower-energy particles. Parts of the ensuing showers are sampled in order to determine the primary particles' energies and directions.

The calorimeter provides hermetic coverage and excellent containment of particle showers (over six nuclear interaction lengths throughout) for $|\eta| < 4$ as well as accurate measurement of the transverse energy balance in events, including determination of the missing transverse energy ($\not\!\!E_T$). In the absence of a central magnetic field, the calorimeter provides good energy measurement and identification of electrons, photons and jets. Furthermore, it also provides identification of muons but can't determine their energies as muons generally deposit only a small fraction of their total energy in the calorimeter before 'punching through' to the muon chambers and beyond.

As shown in Fig. 3.5, the calorimeter consists of three main sections, each one housed in a separate double-walled stainless steel cryostat: the Central Calorimeter (CC) and a pair of End Calorimeters (EC); one to the north (ECN) and another to the south (ECS) of the CC. In each region between the cryostats, a set of scintillating tiles and associated phototubes known appropriately as the Intercryostat Detector (ICD) is present. Each calorimeter consists of both electromagnetic and hadronic layers. The electromagnetic layers are traversed first by the byproducts of a hard

proton-antiproton collision and are optimized for the identification and measurement of electrons and photons — which produce narrow electromagnetic showers that rapidly deposit their energy in the detector. The hadronic layers, which are traversed after the electromagnetic layers by the surviving, mostly hadronic, particles, are optimized to contain and measure the showers of hadrons which are wider and occur later than the electromagnetic showers. These hadronic showers are better known as jets. Please refer to Appendix A for an examination of a sample jet event.

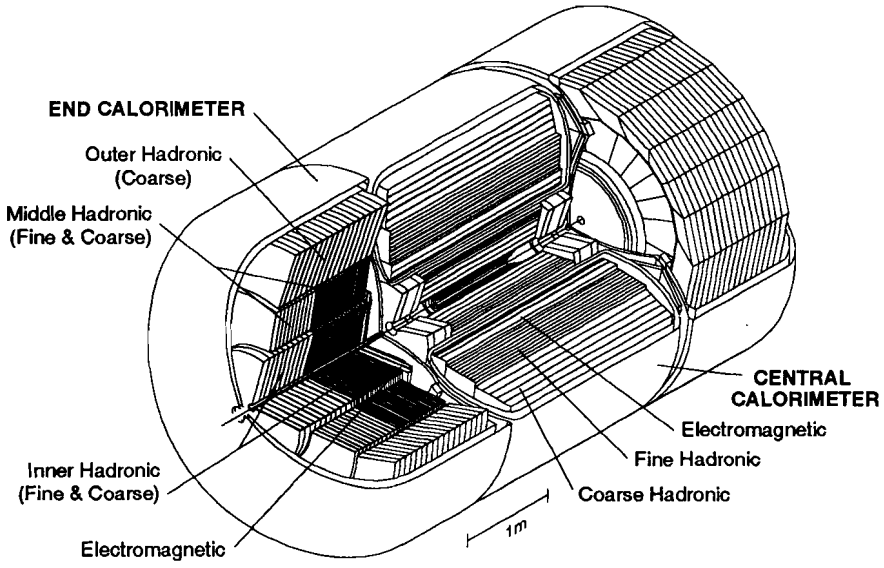

Figure 3.5: A detailed view of the DØ calorimeters: CC and two ECs, with the CD contained within.

Figure 3.5 illustrates the layout of the three cryostats, the location of the calorimeter modules within each cryostat and the presence of the central detector with respect to the central calorimeter.

The fundamental detection mechanism of the DØ calorimeters can be more easily described with the aid of Fig. 3.6 which displays a calorimeter unit cell. Such a

cell contains a dense metal absorber plate and a composite signal board which is covered with a coat of high resistivity carbon-loaded epoxy on the outside and has a segmented copper surface in between two G-10 sheets which is used for readout. The absorber plate and the signal board are separated by a gap filled with liquid argon serving as the active material. The metal plate is connected electrically to ground while the resistive surfaces of the signal board are kept at a positive voltage of 2–2.5 keV, resulting in an electrostatic field in the argon gap. As particles traverse the calorimeter, they interact most strongly with the array of absorber plates, producing a shower of particles that deposit most of their energy there. A small fraction of the total energy is deposited in the gaps as energetic particles ionize argon atoms. The charge released in this fashion drifts to the signal board inducing a signal in the copper readout pads. This signal is transmitted to preamplifiers located on the surface of each cryostat. It is then shaped and further amplified before being digitized and read out to the *Data Acquisition* (DAQ) system. The zero-suppression applied to the signal eliminates the need to read out cells that had no energy deposited in them. This helps minimize both the time and the amount of data to read out.

The calorimeter was designed to have a pseudo-projective geometry for its readout towers, with each tower subdivided in depth. Therefore, the centers of the cells of a given readout tower all lie along a ray projecting from the middle of the interaction region outward through the detector. In addition, the transverse η-ϕ area subtended by these cells is approximately constant.

For a more detailed view of the cell structure of the calorimeter, Fig. 3.7 displays a quarter of the full calorimeter viewed from the side, showing the transverse and longitudinal segmentation of the calorimeter, its pseudo-projective tower structure,

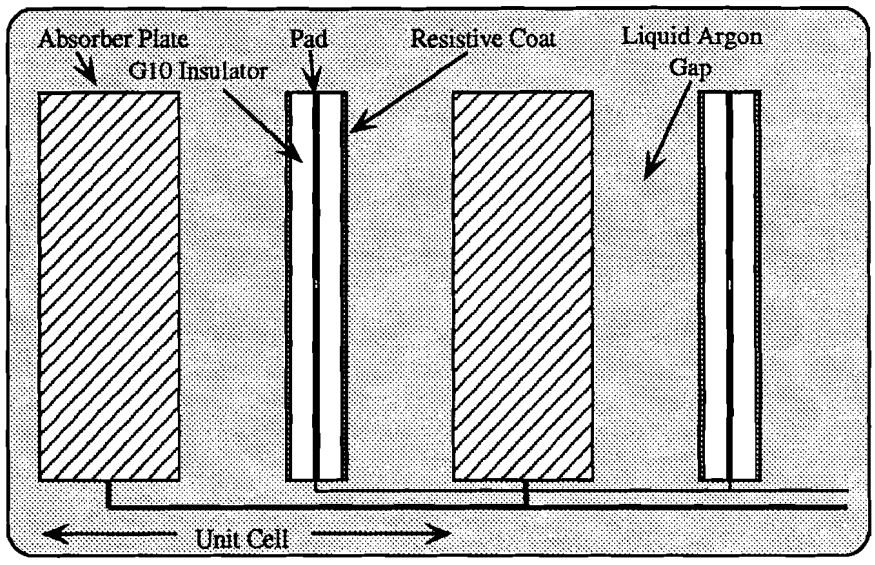

Figure 3.6: A calorimeter cell.

as well as the location of the CC, both ECs, their boundaries, the ICD and the CD. Also pictured is the location of the Main Ring bypass, which passes through the Coarse Hadronic section of all three calorimeters.

3.4.1 Central Calorimeter

The Central Calorimeter (CC) resides in the middle cryostat and encompasses the region $|\eta| < 1$. It consists of three concentric cylindrical shells, each one with a different type of module. There are 32 CC Electromagnetic (CCEM) modules in the inner shell, 16 CC Fine Hadronic (CCFH) modules in the middle shell and, around these, 16 CC Coarse Hadronic (CCCH) modules. Each module is finely segmented in both the transverse and longitudinal directions. The transverse segmentation is 0.1×0.1 in $\eta \times \phi$ throughout the calorimeter except in the third of four CCEM longitudinal layers, at the depth of the electromagnetic (EM) shower maxima, where

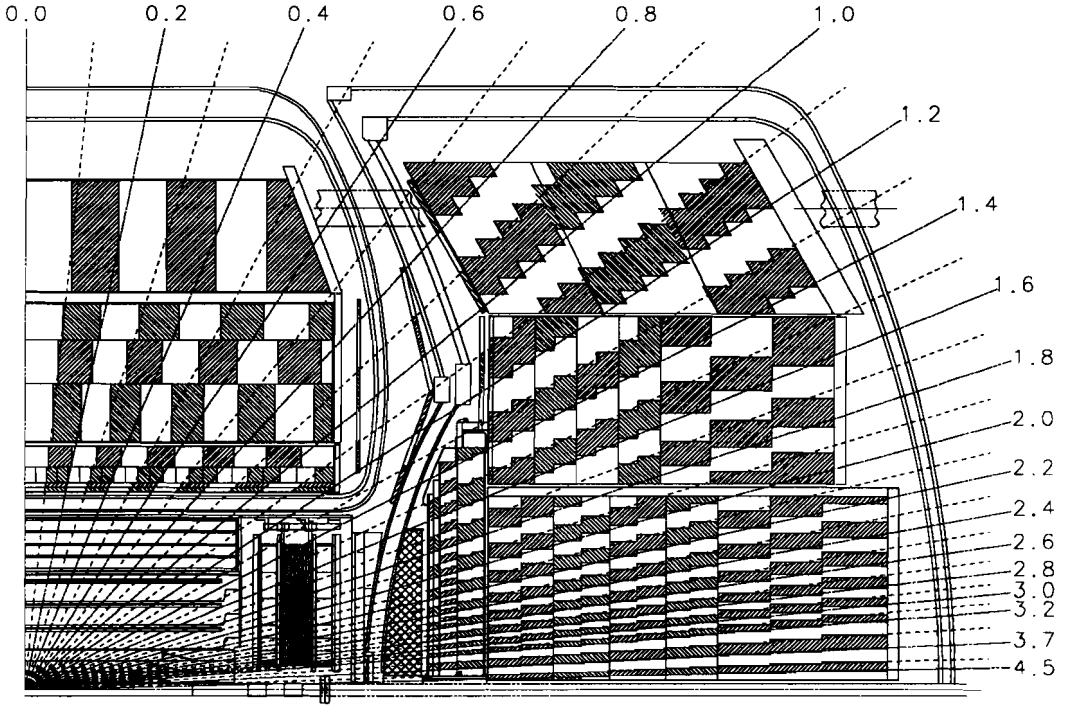

Figure 3.7: A side view of a quarter section of the DØ calorimeters and central tracking detectors. The pseudo-projective towers of the calorimeter are shown by alternate shading, along with its transverse and longitudinal segmentation. The numerical scale shown corresponds to units of the pseudorapidity, η, at each tower boundary. Also displayed is the Main Ring Bypass tube (the horizontal tube in the upper right and in the upper part of the CC-EC boundary region), the beryllium Tevatron beam pipe (horizontal along the bottom of the figure) and the ICD scintillator array, located on the inner face of the end cryostat in the region where $0.8 < |\eta| < 1.4$.

the segmentation is twice as fine in both η and ϕ. The longitudinal segmentation is different for each of the modules and the energy deposited in every segment, or cell, is read out separately. A summary of relevant CC parameters is given in Table 3.2.

CC Electromagnetic Section

The CCEM section was designed to contain and measure electromagnetic showers. It is made up of four longitudinal layers whose thicknesses are from inner to outer layer, respectively, 2.0, 2.0, 6.8 and 9.8 radiation lengths (X_0). The cumulative depth of 20.6 radiation lengths effectively contains electromagnetic showers which generally peak in the more finely segmented third layer. From the hadronic point of view, the CCEM is rather thin, consisting of only 0.76 nuclear interaction lengths (λ_A) which is why there is little hadronic activity in this section of the CC.

CC Hadronic Sections

Having traversed the EM section of the CC, surviving particles encounter the thick hadronic sections of the calorimeter. These sections contribute 6.4 λ_A to fully contain most jets as well as minimize unwanted leakage outside the calorimeter, and cover the region of $|\eta| \leq 0.9$. There are two such sections in the central calorimeter.

The fine hadronic (CCFH) section is composed of 16 modules and is segmented into three longitudinal layers of 1.3, 1.0 and 0.9 λ_A. The CCFH ring is oriented so that no inter-module boundaries of the CCEM ring align with those of the CCFH.

The outermost coarse hadronic (CCCH) section also has 16 modules but these are grouped in a single layer of 3.2 λ_A. The CCCH modules differ from the other CC modules in that they use copper plates, rather than uranium, as their absorber.

The CCCH ring is oriented in such a way that none of its inter-module boundaries coincide with those of the CCFH.

Parameter	CCEM	CCFH	CCCH
Number of Modules	32	16	16
Absorber	U	U-Nb	Cu
Absorber Thickness (mm)	3	6	46.5
Argon Gap (mm)	2.3	2.3	2.3
Number of Readout Layers	4	3	1
Cells per Readout Layer	2, 2, 7, 10	20, 16, 14	9
Radiation Lengths (X_0)	20.5	96.0	32.9
Interaction Lengths (λ_A)	0.8	3.2	3.2
Sampling Fraction (%)	11.79	6.79	1.45

Table 3.2: Summary of Central Calorimeter Parameters[83, 87].

3.4.2 End Calorimeters

The two End Calorimeters (ECN and ECS) are of identical construction and each resides in one of the two outer cryostats. Like the central calorimeter, each EC consists of a finely segmented electromagnetic section, followed by both fine and coarse hadronic calorimetry. Unlike the CC, however, the ECs contain four module types. To avoid the dead spaces in a multi-module design, there is just one large module each of the electromagnetic (ECEM) and inner hadronic (ECIH) types. Outside these, there are two concentric rings, each of which is composed of 16 hadronic modules of a given type: middle hadronic (ECMH) in the inner ring and outer hadronic (ECOH) in the outer ring. The transverse segmentation in the EC is identical to that of most of the CC, with the same $\eta \times \phi$ segmentation of 0.1×0.1 throughout except in the more central part of the third EM layer which is twice as finely segmented in

both η and in ϕ, and in the very forward region of the hadronic section where the segmentation is reduced in both η and ϕ due to the small physical size of cells at high η. A summary of relevant EC parameters is given in Table 3.3.

EC Electromagnetic Sections

The ECEM modules (one per EC) are shaped as disks and their axes coincide with the Tevatron beam. Their combined coverage is $1.4 \leq |\eta| \leq 4.0$. Each module is divided into four EM layers which have 0.3, 2.6, 7.9 and 9.3 X_0, respectively. Including the material in the cryostat wall, the total absorber thickness in the first layer is about 2.0 X_0. The third layer is more finely segmented than the rest of the calorimeter up to $|\eta| = 2.6$. At higher $|\eta|$, the segmentation is the same as the majority of the calorimeter because of the small physical size of the cells in the far forward region.

EC Hadronic Sections

After passing through the EM section of the calorimeter, surviving high rapidity particles enter the hadronic sections of the ECs.

The ECIH section in each EC resides behind the ECEM module and is cylindrical in shape, the beam located at its center, with inner and outer radii of 3.92 and 86.4 cm. It has five longitudinal sections: four fine hadronic sections each with 1.1 λ_A of uranium as absorber and a single coarse hadronic section with 4.1 λ_A of stainless steel as absorbing medium.

The ECMH and ECOH modules, each one a cylindrical wedge, are arranged in rings around the beam. Each one of the ECMH modules has four (fine hadronic)

longitudinal segments of 0.9 λ_A of uranium absorber, backed by a coarse hadronic section with stainless steel absorber of 4.4 λ_A. The ECOH modules are composed of a single longitudinal segment with stainless steel absorber plates of about seven λ_A. These plates are inclined at an angle of about 60° with respect to the beam axis.

The hadronic coverage of the ECs extends from the region covered by the CC ($|\eta| \leq 0.9$) out to $|\eta| = 4.45$. In the region $|\eta| > 3.2$, the small physical size of calorimeter towers requires increasing the ϕ segmentation to 0.2. The η segments are also larger, and of varying size, for large η.

Parameter	ECEM	ECIH-f*	ECIH-c*
Number of Modules	1	1**	1**
Absorber	U	U-Nb	SS
Absorber Thickness (mm)	4	6	46.5
Argon Gap (mm)	0.23	0.21	0.21
Number of Readout Layers	4	4	1
Cells per Readout Layer	2, 2, 6, 8	16	14
Radiation Lengths (X_0)	20.5	121.8	32.8
Interaction Lengths (λ_A)	0.95	4.9	3.6
Sampling Fraction (%)	11.9	5.7	1.5

Parameter	ECMH-f*	ECMH-c*	ECOH
Number of Modules	16**	16**	16
Absorber	U-Nb	SS	SS
Absorber Thickness (mm)	6	46.5	46.5
Argon Gap (mm)	0.22	0.22	0.22
Number of Readout Layers	4	1	3
Cells per Readout Layer	15	12	8
Radiation Lengths (X_0)	115.5	37.9	65.1
Interaction Lengths (λ_A)	4.0	4.1	7.0
Sampling Fraction (%)	6.7	1.6	1.6

Table 3.3: Summary of End Calorimeter Parameters [83, 87].
* The "-f" and "-c" suffixes represent fine and coarse hadronic regions.
** The single ECIH and the 16 ECMH modules all contain both fine and coarse hadronic regions.

3.4.3 Inter-cryostat Detectors and Massless Gaps

Figure 3.7 illustrates that the region $0.8 < |\eta| < 1.4$, near the boundaries between the central and end calorimeters, has a large amount of un-instrumented material consisting of cryostat walls, stiffening rings and module endplates. In order to correct for the energy deposited in these dead sections and to keep the resolution of the calorimeter as uniform as possible, we have instrumented the face of each cryostat with an array of scintillating plastic tiles, known as the Inter-cryostat Detector (ICD).

Each ICD consists of 384 scintillator tiles of size 0.1×0.1 in $\eta \times \phi$, exactly matching the cell size of the liquid argon calorimeters, and is mounted on the face of each end cryostat as shown in Fig. 3.7. Additional, separate single cell devices called 'massless gaps' were installed in both the CC and EC to instrument the otherwise dead material of the CCFH endplates and the inner wall of the EC cryostat.

3.4.4 Calorimeter Performance

In a sampling calorimeter, the energy is measured on a statistical basis [85]. The total energy of a shower is not measured directly but inferred from components of the shower sampled in the active regions of the calorimeter, resulting in sampling fluctuations about the mean energy response. Furthermore, the energy resolution of the calorimeter is affected by electronic noise, background radiation and by the very nature of the incident particles. The fractional energy resolution is defined as the ratio of the energy resolution σ_E to the mean energy response E and can be expressed as

$$\left(\frac{\sigma_E}{E}\right)^2 = \frac{N^2}{E^2} + \frac{S^2}{E} + C^2 \tag{3.6}$$

where the parameters N, S and C correspond to noise contributions, sampling errors and calibration uncertainties, respectively, and are given in Table 3.4.

The particular dependencies of the noise contributions, sampling errors and calibration uncertainties on E can be readily explained. The electronic and uranium noise is independent of the energy of incoming particles that shower in the calorimeter. The sampling of secondary particles in the shower is a statistical process, where the average number of secondary particles produced in the shower $< n >$ is proportional to the energy of the incident particle. The uncertainty in the energy measurement is governed by statistical fluctuations of $< n >$, so $\frac{\sigma_E}{E} \propto \frac{1}{\sqrt{<n>}} \sim \frac{1}{\sqrt{E}}$. There are some additional contributions to the energy resolution from higher-order terms in E due to the different responses of the calorimeter to electromagnetic and hadronic components of particle showers. Through calibration with test beam data, an energy dependent term for the resolution is obtained ($\sigma_E \propto E$).

The performance of the DØ Calorimeter has been studied in a number of different ways. Prior to the data taking run of the Tevatron, several types of calorimeter modules were exposed to a test beam at Fermilab. By using beams of electrons and pions at different energies, the calorimeter's energy response and resolution were analyzed [88].

The energy resolution of the CCEM and ECEM modules to electrons and of the ECMH modules to pions was measured in the DØ testbeam. The corresponding parameters from Equation 3.6 are given in Table 3.4.

These and other studies determined that:

- The calorimeter energy resolution is approximately $\frac{15\%}{\sqrt{E}}$ for electrons and $\frac{50\%}{\sqrt{E}}$ for pions.

Calorimeter Section	N (GeV)	S ($GeV^{\frac{1}{2}}$)	C
CCEM [88]	0.140	0.162 ± 0.011	0.003 ± 0.004
ECEM [89]	0.29 ± 0.03	0.157 ± 0.006	0.003 ± 0.003
ECMH [88]	1.28	0.439 ± 0.042	0.047 ± 0.005

Table 3.4: Measured Noise, Sampling and Calibration constants which determine the energy resolution of Equation 3.6 for various calorimeter modules.

- The energy response to both electrons and pions is linear to within 0.5 % in the range $10 \leq E \leq 150$ GeV.
- The $\frac{e}{\pi}$ response ratio, which is a measure of the relative response of the calorimeter to electromagnetic and hadronic showers and is closely related to the energy resolution and linear energy response that can be obtained in the calorimeter, falls from about 1.11 at 10 GeV to 1.04 at 150 GeV.
- A minimum ionizing particle (MIP) crossing the central calorimeter typically liberates approximately 10^4 electrons in each gap and loses a total energy of nearly 2 GeV. Therefore, muons can be observed by the calorimeter independently of the muon detector.

The calorimeter energy resolution for jets is obtained from collider data. Its effect on the study of color coherence effects will be discussed in Chapter 5.

3.5 Muon Detectors

Surrounding the calorimeter, the DØ muon detection system consists of three layers of muon chambers with proportional drift tubes (PDTs), which measure charged particle tracks down to approximately 3° from the beam axis, and five separate

solid-iron toroidal magnets. Its purpose is to identify the muons produced in the $p\overline{p}$ collisions and to determine their trajectories and momenta. Since muons are minimally ionizing particles (MIPs) and decay weakly, they generally survive long after the electromagnetic and hadronic showers have deposited most of their energy in the calorimeter. Thus muons can be identified amidst hadron jets much more readily than electrons.

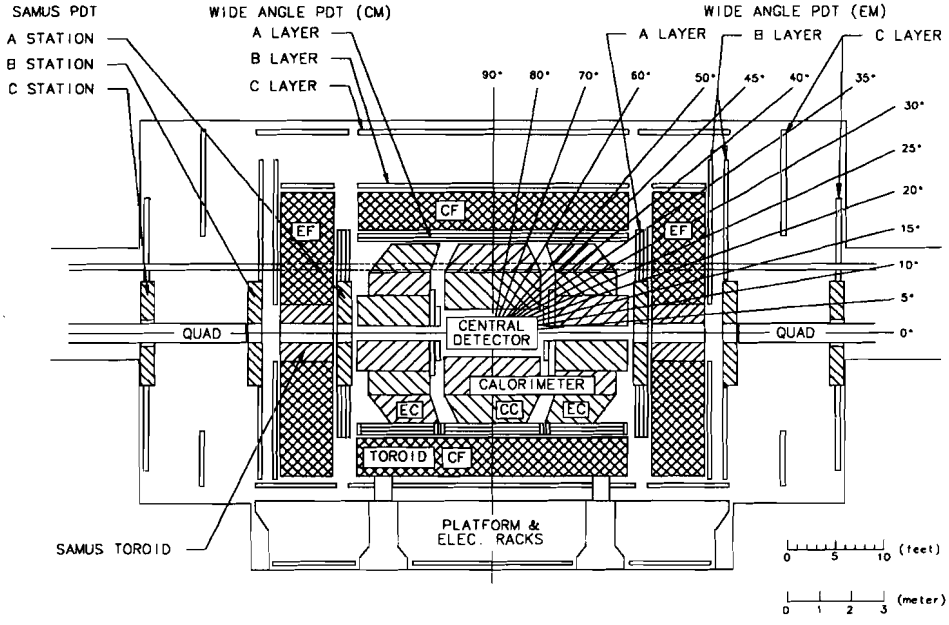

Figure 3.8: Side view of the DØ detector showing the entire muon system [83].

Figure 3.8 is a side view of the full DØ detector showing the location of each toroid, the muon chamber layers and the calorimeters and central detectors within. The central (CF or "central iron") region of the muon system covers the range of pseudorapidity $|\eta| \leq 1$, while the end toroids (EF or "end iron") extend this coverage to $|\eta| \leq 2.5$. Together, the CF and EF, and their associated muon chambers, form the Wide Angle Muon System (WAMUS). The first layer of WAMUS muon chambers

— the "A" layer — is located before the iron toroids and contains four planes of PDTs. Just past the magnets are the B and C layers, each containing three planes of PDTs. These last two layers are separated by about one meter, to provide a lever arm for momentum measurement. Adjacent planes of PDTs within each layer are offset to reduce the left-right ambiguity associated with hit finding in drift tubes. The purpose of the additional PDT plane in the A layer is to allow for a better track measurement given this layer's closer proximity to the interaction vertex.

The PDTs are oriented so that the bend direction of the magnetic field (approximately the r-z plane) coincides with the direction of greatest accuracy of position measurement. The non-bend coordinate (ϕ), along the length of the wire, has less accuracy. The hit location along this direction is determined by a combination of timing and pad signals.

The Small Angle Muon System (SAMUS) extends the coverage for detection of muons to $|\eta| \leq 3.6$. The SAMUS toroids fit in the central hole of the EF toroids and, similar to the WAMUS, the SAMUS has an A station before each toroid and B and C stations after it. Each of these "stations" consists of three doublets of cylindrical PDT chambers; the doublets are oriented in the x, y and u directions — where u is half-way between x and y and all three are coplanar.

The combination of calorimeter and muon system are quite thick in the DØ detector. The nuclear interaction length as a function of the polar angle θ is shown in Fig. 3.9

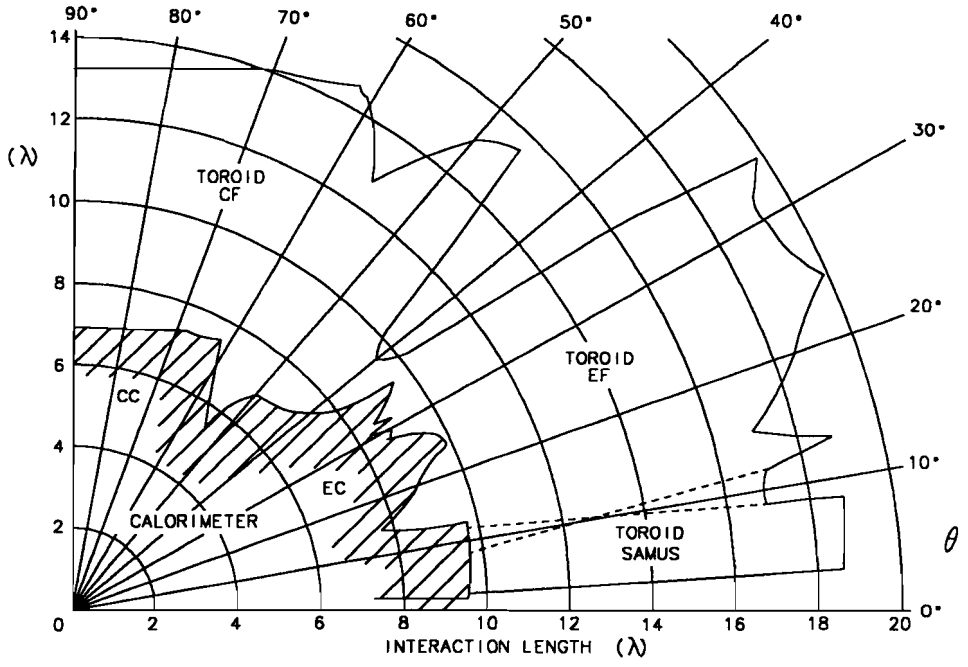

Figure 3.9: Nuclear interaction lengths vs. polar angle [83].

3.6 Trigger and Data Acquisition Systems

As described earlier in this chapter, the Tevatron produces a beam crossing in the DØ interaction region every 3.5 μs during collider operations. If each crossing were to produce a proton-antiproton interaction resulting in fragments detected by the interaction trigger, there would be an event rate of around 286 kHz. However, not all beam crossings result in this type of inelastic collision — many crossings produce small angle scattering that go unseen outside the detector. The number of events that produce an inelastic collision depends upon the instantaneous luminosity $\mathcal{L}$ and the inelastic part of the cross-section σ mentioned in Equation 3.1. For the 1992–1993 collider run, on average, about one half of the beam crossings produced inelastic collisions. Now, given the fact that a typical event in the DØ detector requires about

300 kilobytes (kB) of data to adequately describe it, one would need to be able to handle a data flow of around 40 Gigabytes (GB) per second if all of these events were to be indiscriminately recorded. Such a high rate of data would challenge any presently existing data processing and collection facility.

However, not all interactions result in what are deemed 'interesting' events worthy of study. In order to keep only those events which may be of interest and reduce the stream of data to more manageable proportions, some selection criteria must be applied — or 'triggered' upon — as early as possible in order to keep only those events that pass such 'triggers'. To this end, the DØ detector uses a three-level triggering system, with each successive level characterizing the event in an increasingly sophisticated fashion. The Level Ø (LØ) scintillator-based hardware trigger indicates that an inelastic event has occurred and determines its z vertex within 400 ns. At an instantaneous luminosity $\mathcal{L} = 5 \times 10^{30}$ cm^{-2}s^{-1} (typical of the 1992-1993 run), the LØ rate is about 150 kHz. A second hardware trigger, Level 1 (L1), is a group of hardware triggers elements arranged in a flexible programmable architecture to enable easy modification. All L1 triggers operate within the 3.5 μs window between beam crossings and thus contribute no dead time. However, others requiring multiple bunch crossings to complete are known as the Level 1.5 (L1.5) triggers. The rate of successful L1 triggers is about 200 Hz and is reduced to under half after action by the L1.5 triggers. Candidate events from L1 (and L1.5) are digitized and then sent through the DØ data acquisition pathways to a farm of microprocessors which serve the dual role of event builders and of Level 2 (L2) triggering system. Sophisticated algorithms in the L2 processors reduce the event rate to about 2 Hz before sending the selected events to the host computer cluster for event monitoring and recording

on permanent storage media.

3.6.1 Level Ø

The Level Ø trigger detects when and where an inelastic collision has occurred and serves as the luminosity monitor for the experiment. It consists of two hodoscopes of scintillation counters which are mounted on the inside faces of the end calorimeters and are surrounded by the ICD. The LØ hodoscopes are located just outside the central tracking region, 140 cm from the center of the detector. Each array has a checkered pattern of scintillators located within a circle whose radius is 45 cm, centered on the beam axis, and gives partial coverage in the region $1.9 < |\eta| < 4.3$ but nearly complete coverage in $2.3 < |\eta| < 3.9$. A schematic drawing of the scintillator arrays is shown in Fig. 3.10.

The total cross section can be divided into the elastic and inelastic parts. Since elastic events result in small angle scattering, DØ does not observe these events. The inelastic cross section can be divided further into diffractive and non-diffractive components, with the diffractive part further subdivided into single- and double-diffractive. In a single-diffractive event, one of the initial particles survives while the other one diffracts into a low mass ensemble of particles. In double-diffractive events, both colliding particles diffract. By requiring a coincidence between both scintillator arrays, the LØ detector identifies over 97% of the inelastic non-diffractive beam-beam interactions. Most diffractive events cannot be observed with the L0 detector because they occur almost exclusively at small angles.

In addition to identifying inelastic collisions, the LØ detector is able to utilize its excellent time resolution (typically 250 ps) and provide a measurement of the

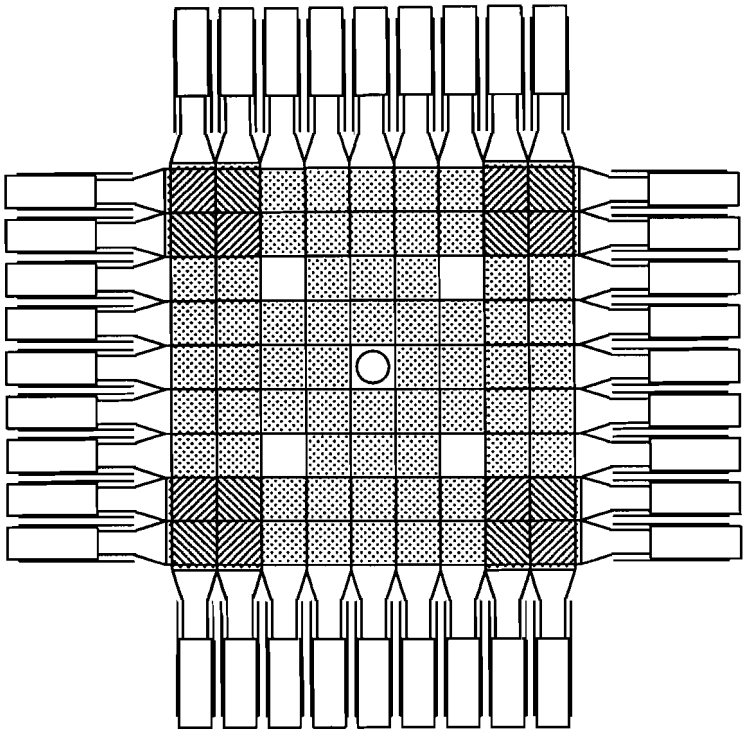

Figure 3.10: Schematic drawing of a Level Ø scintillator array. A horizontal and a vertical plane of scintillators are superposed, producing a checkered pattern, with the beam pipe passing through the center. Around the periphery of the array lie the tapered waveguides connecting the scintillators and the photo-multiplier tubes (PMTs).

z-coordinate of the primary collision vertex by comparing the different times that particles from an interaction arrive at the two arrays. At high luminosities, where the probability for multiple interactions grows appreciably, the LØ time difference information becomes ambiguous, so instead a flag is set to identify these events to the subsequent trigger levels.

3.6.2 Levels 1 and 1.5

The purpose of the Level 1 trigger is to reduce the event rate signalled by the LØ trigger (around 150 kHz) to the more manageable vicinity of 200 Hz by rapidly applying some coarse selection criteria within the 3.5 μs window between beam crossings. This reduction is to be done without causing any significant "dead time" during which the detector would be unable to observe interactions.

The L1 trigger consists of both calorimeter and muon triggers, as shown schematically in Fig. 3.11. The L1 calorimeter trigger system is activated when it receives from LØ a signal that an inelastic collision has occurred. The front end calorimeter electronics feeds data to the trigger to quickly determine the approximate energy in each of the calorimeter cells. Electromagnetic and hadronic cells are summed separately, then combined into trigger towers of size 0.2×0.2 in $\eta \times \phi$. The transverse energy (E_T) of each trigger tower is read from a lookup table while the missing transverse energy ($\not\!\!E_T$) and scalar E_T are determined from the tower quantities. Muon triggers in L1 and L1.5 triggers were not required in this analysis and hence will not be described here.

Selection of triggers is done using a two-dimensional AND-OR network consisting of 256 latched bits called *AND-OR Input Terms.* Each one of these hardware-based Input Terms corresponds to some specific detector requirement such as a given number of calorimeter towers with E_T above some threshold. The outputs of the AND-OR network are 32 orthogonal AND-OR lines each of which correspond to a *Specific L1 Trigger.* Every one of these software-based Specific Triggers is defined by a unique pattern indicating for each AND-OR Input Term, whether that term is required to be asserted, negated or whether it is to be ignored. The full description

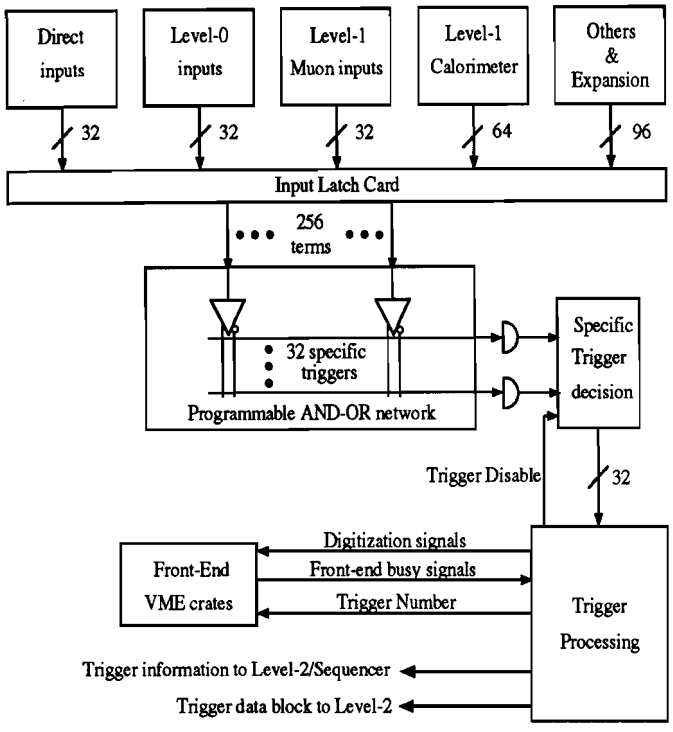

Figure 3.11: Schematic diagram of the Level 1 trigger system.

of all 32 triggers is specified in a *trigger menu.* The scalar E_T and $\not\!\!E_T$ for the trigger tower are compared to the trigger requirements present in the current trigger menu. An event that satisfies the conditions of at least one trigger will result in a request from the L1 Trigger Framework for readout by the data acquisition hardware, provided that there are no front-end busy conditions and no other vetoes are being asserted at the time. The L1 decision must be made within 2.2 μs in order to allow sufficient time to reset the front end electronics before the next beam crossing.

3.6.3 Data Acquisition System and Level 2

The Level 2 system serves multiple functions. In addition to acting as a software trigger and reducing the event rate from approximately 100 Hz to about 2 Hz, it

is responsible for coordinating the transfer of information digitized in the detector's front end crates for selected beam crossings, collecting this information while ensuring its integrity, directly constructing an event in the final format for offline processing, carrying out some limited analysis on the event and — for an event that satisfies the L2 software trigger requirements — shipping it to the host computer for permanent storage and offline monitoring and analysis.

As shown in Fig. 3.12, the L2 system is based upon a farm of 50 parallel nodes (48 were actually installed and used) connected to the detector electronics and triggers by a set of eight 32-bit wide high speed data cables. Each node consists of a VAXstation processor coupled via a VME bus adapter to multi-port memory (MPM) which receives the data in parallel from the eight data cables and an output *VME Buffer Driver* board (VBD) which in turn buffers the selected events for transfer to the host computer. L2 nodes can be expanded to include an attached co-processor which would allow certain repetitive computations to be performed on the data rapidly and in parallel with the VAX processor analysis.

When a valid L1 or L1.5 trigger is received by the 80 VME crates which contain the calorimeter and muon chamber *Analog to Digital Converters* (ADCs) and the tracking and TRD chamber *Flash ADCs* (FADCs), digitization of the analog detector information begins. It takes around 1 msec for this data to be fully digitized and to be placed in one of the two data buffers present on every crate. Each crate has a VBD which controls the data transfer from VME locations in the crate to an output high speed data cable consisting of 32 twisted pair lines for data and 13 pairs for control and parity. A clock rate of 100 ns on the data cable allows data to be transferred at the rate of 40 Megabytes (MB) per second on each data cable. One

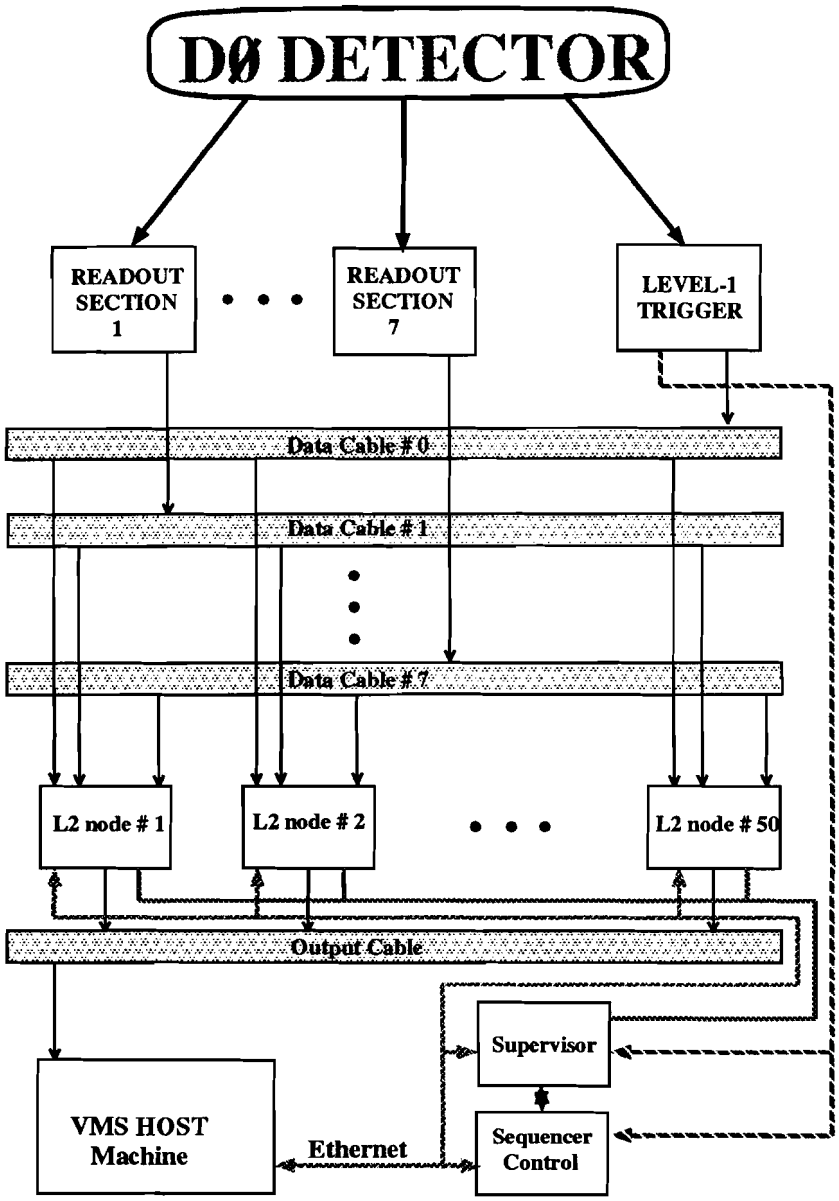

Figure 3.12: Schematic overview of the DØ data acquisition system. Data collected by the DØ detector are digitized by the front end electronics corresponding to each readout section, then read out in parallel through eight data cables, under the direction of the Level 2 system, to a farm of VAXstation processors where events satisfying the Level 2 software triggers are assembled, then shipped to the VMS host machine for off-line analysis and safekeeping.

data cable is dedicated to each of the following eight detector sectors: VTX, TRD, CDC, FDC, North Calorimeter, South Calorimeter, Muon and finally, Levels Ø and 1. Figure 3.13 shows schematically the configuration of one readout section and its data cable with respect to the rest of the DAQ system.

Due to the high clock rate, data cable segments are restricted to be less than 12 m long to allow for transmission of the data in synchronicity with the clock. However, since most DØ data cables must circulate over a longer path than this, repeaters are used to de-skew the signals. Readout control of the VBDs and arbitration is achieved with a token passing scheme. Tokens are passed at the rate of 1 MHz around a token ring spanning all the VBDs on each particular data cable. When a token is received by the VBD, its external port processor compares the low order bits of the event number contained in the token to the event number loaded by the L1 trigger; if a match occurs, pending buffers are transferred to the data cable.

The L2 Supervisor processor manages the real time operation of the DAQ system (refer to Fig. 3.13). A Sequencer processor controls the operation of the data cables by means of a Sequencer control board on each data cable which in turn manages the token circulation and data readout on that cable. For each valid hardware trigger, the L1 system interrupts the Supervisor with the 32-bit pattern of Specific Triggers for that event, together with a 16-bit event number. Upon receiving a L1 trigger, the Supervisor assigns a L2 node to the event and then interrupts the Sequencer. The Sequencer, in turn, constructs readout tokens for a particular list of crates appropriate to the specific trigger pattern, including low order bits of the event number to ensure the integrity of the readout, and then circulates these tokens from crate to crate all around the token ring until readout is complete. The L2 Supervisor

can send to the Level 1 a 32-bit disabled-trigger pattern that changes with the state of the run and the availability of L2 nodes for specific trigger bits. This system is flexible in the extreme: any combination of data cables can collect data from any desired set of crates.

All eight data cables circulate to each of the L2 nodes. Since the VME digitization crates and the L1 trigger system are located in a separate and electrically isolated three-story movable structure — the *Moving Counting House* (MCH) — the connection of each data cable is made through an optical isolator circuit that isolates the electrical signals on either side from each other. During the setup of a DAQ cycle, the Supervisor polls the processor nodes to find one available to receive the detector data. The data for each L2 node are read in by four MPM modules, each having two channels of 2 MB multi-ported memory which appear as contiguous I/O space memory to the processor. A key feature of the data handling is that the incoming data are mapped directly into the desired raw data ZEBRA format, thus reducing processing time. Particular event types may be steered to specific nodes for special calibration or debugging purposes. Typically, each node will contain an identical copy of the filter software, although special calibration or test nodes may be loaded with different code. The software algorithms and control code used in the L2 processors are developed in high-level languages (FORTRAN, C and EPASCAL) and downloaded over Ethernet lines into the nodes from the VMS host machine.

Once the L2 filter code has selected an event for subsequent data-logging and analysis, the event and added information from the L2 analysis is sent directly from the MPMs through a VBD to the host computer. This transfer is managed by the *Sanitizer* control processor through token circulation in a similar way to how the

readout of the VME crates is handled by the Supervisor/Sequencer.

A final *Surveyor* processor monitors the operation of the data flow, the L2 nodes and the Sequencer and Supervisor processors. The Surveyor collects statistics for on-line monitoring of the full system and provides diagnostic real-time displays and alarms.

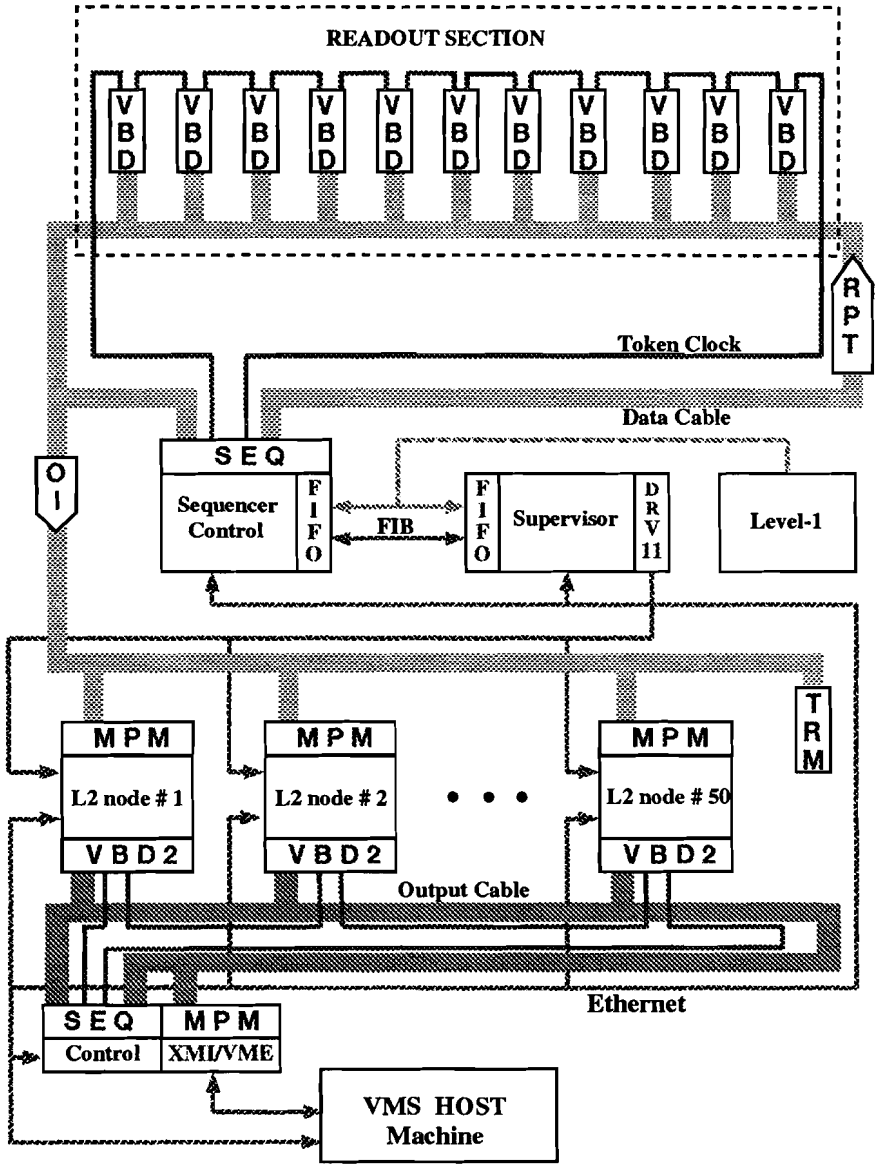

Figure 3.13: Schematic representation of the DØ data acquisition system showing a single readout section and its data cable. Data collected by the DØ detector are digitized by the VME crates then sent out onto the data cable by means of a VBD on each crate. VBD readout is managed by the Sequencer which circulates an arbitration token through the VBDs on the data cable under the direction of the Level 2 Supervisor. A farm of VAXstation processors, then read in the data for processing and event building.. Finally, the data transfer from the L2 nodes to the VMS host is managed in a similar way to the readout of the VME crates.

Chapter 4

Data Reconstruction and Preliminary Selection

Approximately one out of every 1000 inelastic $p\overline{p}$ collisions at the Fermilab Tevatron produce jets which are sufficiently energetic to be distinguished from the ocean of background particles that accompany each of these collisions. In order to collect these jet events, one must look for large collimated depositions of energy in the calorimeter (see Appendix A). This chapter describes how jet data are selected from the large number of collisions by means of the various levels of the online trigger and how additional offline selection criteria are used to reconstruct jets. It then discusses how backgrounds are identified and removed from the sample. The chapter concludes by describing preliminary selection criteria used to choose a sample for subsequent physics analysis. The remaining event selection criteria will be discussed in Chapter 6. The data were collected during a collider run from August 1992 to May 1993 and correspond to an integrated luminosity of (13.3 ± 0.7) pb^{-1}. This run, called Run Ia, was the inaugural run of the DØ detector.

4.1 Online Event Selection

The DØ detector was exposed to a $p\bar{p}$ interaction rate of up to ~ 180 kHz during Run Ia. To reduce this rate to one more easily managed by the data recording system (~ 2 Hz), it was necessary to decide very quickly in real time which events were of interest and should be collected and which could be discarded. The general online requirements for jet triggers were:

- That both Level Ø (LØ) hodoscopes provide signals which are in coincidence, indicating a non-diffractive inelastic collision.
- That the z-vertex position determined by the LØ trigger from timing information be within a specified fiducial region (see Table 4.1).
- At the Level 1 (L1) trigger, that there be a specified number of calorimeter trigger towers, each with energy depositions above a prescribed threshold.
- At the Level 2 (L2) trigger, that the jets obtained after applying a jet reconstruction algorithm which clusters L1 energy depositions be above a given threshold.

The L1 and L2 requirements are described in more detail in the following sections.

4.1.1 Level 1 Trigger Selection

The smaller readout towers in the calorimeter are combined to form calorimeter trigger towers which measure 0.2×0.2 in $\eta \times \phi$. At L1, the E_T of a trigger tower is

calculated in Equation 4.1 as:

$$E_T = \sum_i [E_T^{EM}(i) + E_T^{FH}(i)] \tag{4.1}$$

where the sum is over all the i cells (both electromagnetic and fine hadronic) within the given tower. In order to satisfy a given L1 trigger condition, the event had to have a specified number of trigger towers above a certain threshold. A number of L1 triggers were defined, each with a different threshold requirement. For Run Ia, the calorimeter trigger towers were instrumented for $|\eta| \leq 3.2$.

Since the jet E_T spectrum falls rapidly as a function of increasing E_T [90, 91, 92], the jet triggers with low E_T thresholds are satisfied at a higher rate than those with higher thresholds. Because not all events that satisfied these standard trigger conditions could be processed, two additional methods were used to reduce the trigger rate.

The first method was to impose another requirement that the triggers had to satisfy. Since the calorimeter towers are of a pseudo-projective nature, a ray from the center of the detector passes through the center of each tower. Consequently, events with a primary vertex far from $z = 0$ have a greater chance of having their transverse energies mis-measured. To improve the quality of the data, only events that satisfied the LØ z-vertex $|z_v| \leq$10.5 cm requirement were kept.

For several low threshold jet triggers, the vertex requirement was not sufficient to reduce the rate to an acceptable level. Consequently, those triggers were "prescaled". A trigger prescale of n indicates that one event is allowed to pass on to the next trigger level for every n that satisfied the trigger. Low E_T jet triggers were heavily

prescaled while the highest E_T jet triggers did not require prescaling. Given that the trigger rate increases with the instantaneous luminosity, different sets of prescale values were used based on this latter quantity.

In Table 4.1 the different L1 jet triggers and their threshold and LØ vertex requirements are listed. The first three triggers had the tight vertex cut applied to them. JET_3_HIGH had this cut applied only during the early stages of the run — it was substantially loosened later on; JET_4_MED had a much looser vertex position requirement.

L1 Trigger	Requirement	Vertex Position
JET_1_LOW	1 tower $\geq$ 3 GeV	$\|z_v\| \leq$ 10 cm
JET_1_HIGH	1 tower $\geq$ 7 GeV	$\|z_v\| \leq$ 10 cm
JET_2_HIGH	2 towers $\geq$ 7 GeV	$\|z_v\| \leq$ 10 cm
JET_3_HIGH	3 towers $\geq$ 7 GeV	$\|z_v\| \leq$ 10 cm, 97 cm
JET_4_MED	4 towers $\geq$ 5 GeV	$\|z_v\| \leq$ 97 cm

Table 4.1: QCD L1 trigger bits and their corresponding requirements. The z-vertex measurement was obtained from the LØ trigger. The vertex position requirement for JET_3_HIGH was loosened during the run.

4.1.2 Level 2 Trigger Selection

The third and final level of the online trigger is based on high-level software algorithms. The L2 processor farm first receives complete detector information for the events that satisfied the L1 trigger conditions and then determines, by means of rapid event reconstruction (in which physically useful information such as hits, tracks and energy deposition is quickly extracted from raw data), whether the candidate events

are of interest and should be kept. As there are more L2 *filter bits*[1] (128) than L1 *trigger bits*[2] (32), in general, more than one L2 filter bit can require a particular trigger bit in L1. For jet triggers, however, there is a one-to-one correspondence between their L1 trigger and L2 filter bits.

Trigger requirements in L2 can be more sophisticated than those of the L1 trigger, since the former has more time available in which to make a decision due to its parallel architecture. Typical event processing time for L2 was under 200 ms, while the L1 trigger only had 3.5 μs in which to reach a decision. The L2 trigger uses a more detailed algorithm, has available to it complete information from the entire calorimeter and the rest of the detector, as well as more precise vertex information than is available to the L1 trigger. Therefore, the L2 trigger can calculate E_T more accurately for jets and other objects.

A list of all the L1 towers that contain $E_T \geq 3$ Gev, known as the *L1 tower candidate list*, is sent to the L2 trigger for each event. For a particular jet trigger, the L2 trigger orders all the jet candidates that satisfy the corresponding L1 trigger by decreasing E_T and tests them to determine which ones satisfy the L2 conditions. Then, the following algorithm was utilized in jet-finding:

1. Commencing with the highest-E_T L1 tower candidate from the list, draw a cone of radius $\mathcal{R} = \sqrt{(\Delta\eta)^2 + (\Delta\phi)^2} = 0.7$ around the center of the tower. Remove any other L1 tower candidates found inside this cone from the L1 tower candidate list.

[1]Each L2 *filter bit* or *tool* has a specific software function related to identification of a type of particle or event characteristic, such as those for jets, muons and calorimeter electromagnetic clusters, to name a few.

[2]Same as Specific L1 Triggers, described in Chapter 3.

2. Determine the jet candidate E_T by summing the transverse energy of all calorimeter cells in towers whose centers are within the cone defined in Step 1 using:

$$E_{TJ} = \sum_i E_{Ti} = \sum_i E_i \sin\theta_i \tag{4.2}$$

where i is the index of all cells in the cone. The calculation is made using finely determined cell energies in L2. The polar angle θ_i was obtained from the (x,y,z) position of the center of the cell relative to the nominal event vertex of $z_v = 0$.

3. Calculate an E_T-weighted average η and ϕ for the jet candidate using:

$$\eta_J = \frac{\sum_i E_{Ti}\eta_i}{\sum_i E_{Ti}} \tag{4.3}$$

$$\phi_J = \frac{\sum_i E_{Ti}\phi_i}{\sum_i E_{Ti}} \tag{4.4}$$

4. Remove the current tower candidate from the list and repeat Steps 1-4 until the L1 tower candidate list is exhausted. At this point, all L2 jet candidates are defined.

5. Calculate the electromagnetic fraction (EMFR — discussed later in this chapter) of the total energy and the energy-weighted average η and ϕ deviation for each L2 jet candidate. These deviations were later used to determine the jet width and are defined as:

$$\Delta\eta_J = \frac{\sum_i |\eta_{tower} - \eta_i| E_i}{\sum_i E_i} \tag{4.5}$$

$$\Delta\phi_J = \frac{\sum_i |\phi_{tower} - \phi_i| E_i}{\sum_i E_i}, \tag{4.6}$$

where the sum is over all the cells i comprising the jet.

6. Correct the E_{TJ} and η_J using the z-vertex position measured by the LØ trigger for each jet candidate.

7. Determine whether the list of jet candidates satisfies the set of requirements particular for each L2 filter bit as described below.

The requirements for the L2 jet filter bits typically consisted of the number of jets and the minimum jet E_T. For all the QCD triggers, only one L2 jet was required to be above a preset threshold in order to satisfy the L2 trigger condition. The requirements for the QCD L2 filter bits are given in Table 4.2.

L2 Filter Bit	L1 Requirement	L2 Requirement
JET_MIN	JET_1_LOW	1 L2_JET $\geq$ 20 GeV
JET_LOW	JET_1_HIGH	1 L2_JET $\geq$ 30 GeV
JET_MEDIUM	JET_2_HIGH	1 L2_JET $\geq$ 50 GeV
JET_HIGH	JET_3_HIGH	1 L2_JET $\geq$ 85 GeV
JET_MAX	JET_4_MED	1 L2_JET $\geq$ 115 GeV

Table 4.2: QCD L2 filter bits and their requirements.

4.2 Offline Jet Reconstruction

Electrons, muons, photons, jets and other physically interesting objects undergo an online reconstruction which is limited by time constraints. This reconstruction, although optimized to provide the best information available within a limited amount of time, sacrifices some accuracy and completeness in order to operate under these tight time restrictions. However, once the data has been collected, these constraints

are no longer present; so all data was reconstructed again, offline, where more sophisticated and time consuming programming code (DØRECO) was used to determine these physics objects as accurately as possible. Next, a description in some detail of the offline jet reconstruction algorithm is provided.

The DØ standard for reconstructing jets utilizes a fixed cone algorithm similar to that used by the UA1 and CDF collaborations [91, 93, 94]. The procedure consists of the following steps [95]:

1. From the candidate list, order by decreasing E_T, the calorimeter readout towers or "seeds" (measuring 0.1×0.1 in $\eta \times \phi$). All towers were required to be above an E_T threshold of 1 GeV.

2. Draw a cone of radius $R = 0.3$ around the highest-E_T tower on the list. Any other seeds inside this cone are considered part of this "pre-cluster" and removed from the list. The pre-cluster's (η, ϕ) values are calculated with an E_T weight from its component seeds.

3. Repeat Step 2 until the calorimeter tower list is exhausted.

4. For each pre-cluster created, calculate a new E_T-weighted (η, ϕ) center, using Equations 4.3 and 4.4, containing all towers within a cone of a specific radius $\mathcal{R}$ of the previous (η, ϕ) center. Several cone sizes were available: 0.3, 0.5, 0.7 or 1.0. This analysis used a cone size of $\mathcal{R} = 0.5$. Repeat this process until the centroid of the jet cone stabilizes, i.e., until $\Delta\mathcal{R} = \sqrt{(\Delta\eta)^2 + (\Delta\phi)^2} \leq 0.01$ between successive iterations.

5. Check whether the E_T of the pre-cluster is above the 8 GeV threshold required in order for it to be considered a jet. Discard those clusters that do not satisfy

this criterion.

6. Recalculate the E_T and the jet angular parameters of all jets using the following formulae:

$$E_{Tjet} = \sqrt{E_x^2 + E_y^2} \tag{4.7}$$

$$\tan\phi_{jet} = \frac{E_y}{E_x} \tag{4.8}$$

$$\eta_{jet} = -\ln\left[\tan\left(\frac{\theta_{jet}}{2}\right)\right], \tag{4.9}$$

where

$$\tan\theta_{jet} = \frac{\sqrt{E_x^2 + E_y^2}}{E_z} \tag{4.10}$$

$$E_x = \sum_i E_i \sin\theta_i \cos\phi_i \tag{4.11}$$

$$E_y = \sum_i E_i \sin\theta_i \sin\phi_i \tag{4.12}$$

$$E_z = \sum_i E_i \cos\theta_i. \tag{4.13}$$

Here i is the cell index.

7. Split or merge overlapping jets based on the fractional energy shared relative to the lower E_T jet. If the shared energy is greater than 50%, the jets are merged and the (η, ϕ) values are recalculated using all cells. If the fractional energy shared is less than 50%, the jets are split and each shared cell is assigned to the nearest jet.

4.3 Removal of Background

After a sample of events has been selected by means of a particular trigger, special care must be taken to remove background events from the data. Typically, background can be classifed in one of the following two categories: a physics background consisting of other physical processes producing the same final state and mimicking the signal of interest, and an instrumental background mostly due to detector effects. Given that the QCD cross sections are much larger than any other cross sections of processes which also produce jets, there is no significant physics background. However, there are several instrumental sources of background: electronic failures, cosmic rays, calorimeter noise, and accelerator losses in the form of protons from the Main Ring entering into the detector. As mentioned in the previous chapter, the DØ detector has the peculiarity of enclosing two accelerators: the Tevatron and the Main Ring. The instrumental background and noise from the Main Ring leave energy depositions in the calorimeter which, if isolated, can be misidentified as jets, or if near a good jet, can alter its measured characteristics. In order to remove these "fake" and altered jets, a set of quality cuts based upon the characteristics of real jets have been devised. This group of cuts is called the *Standard Jet Quality Cuts* and each cut in the group is applied to each of the three highest-E_T jets in an event. In addition to these quality cuts, a missing E_T cut was applied to each event as well.

4.3.1 Standard Jet Quality Cuts

The Standard Jet Quality Cuts [96] are based upon the following three quantities:

- **Coarse Hadronic Fraction** (CHFR) is the fraction of the jet's energy deposited in the Coarse Hadronic (CH) section of the calorimeter. By cutting on

this quantity, we can remove activity caused by the Main Ring. Since it passes through the CH section, any energy deposition related to the Main Ring will be concentrated in this part of the calorimeter. It has been observed [97] that fake jets due to Main Ring contributions tend to deposit more than 40% of their energy in the CH region, while real jets more commonly have only around 10% of their energy in the coarse hadronic section, as shown in Fig. 4.1a. Therefore jets were required to have a CHFR of less than 40%.

- **Electromagnetic Fraction** (EMFR) is the fraction of a jet's energy deposited in the electromagnetic portion of the calorimeter. Screening jets on this quantity removes from the jet sample electrons and/or photons, which characteristically deposit nearly all their energy in the electromagnetic section of the calorimeter. As a result, depositions from electrons and photons have a very high EMFR. Fake jets, caused by the Main Ring or by hot cells, generally do not have energy depositions in the electromagnetic section of the calorimeter, and thus have a low EMFR. In general, jets leave energy in both electromagnetic and hadronic sections of the calorimeter, since they are composed of a mixture of hadrons and photons (the latter from π^0 decays). Figure 4.1b shows the EMFR distribution of our data. Jets were required to have an EMFR between 5% and 95% everywhere except in the *Inter-Cryostat Region* (ICR) which lacks EM modules. For this reason, the lower EM threshold was eliminated there.

- **Hot Cell Fraction** (HOTFR) is the ratio of the energy of the highest E_T cell to the energy of the second highest E_T cell within a jet in the calorimeter. This variable is useful for removing noisy cells with detector breakdown. Oc-

casionally, a calorimeter cell will begin sparking, or undergo electronic failure, and this signal will be wrongly interpreted as actual energy deposition. Since this occurs randomly and usually without affecting neighboring cells, it may appear that there is a large amount of energy in a single isolated "hot" cell, in which case the HOTFR variable will be large. Energy deposition from a real jet is spread over many cells and normally, several of these cells receive comparable amounts of energy, resulting in the HOTFR distribution shown in Fig. 4.1c. For a jet to be accepted, its HOTFR was required to be below 10.

The threshold values used for the Standard Jet Quality Cuts are summarized below.

- CHFR < 0.4
- $\left.\begin{array}{ll} \text{if } 1.0 \leq \eta_{det} \leq 1.6 & 0.0 \\ \text{elsewhere} & 0.05 \end{array}\right\} <$ EMFR < 0.95
- HOTFR < 10.0

The standard cuts are applied everywhere except for the EMFR cut in the inter-cryostat region, as discussed above. The global mean efficiency of these cuts over a large jet E_T and η range is $> 96\%$ [98].

4.3.2 Missing E_T Cut

An additional cut based on the missing E_T of the event is introduced to remove cosmic showers as well as other unusual fake jets that survive the standard cuts.

A byproduct of cosmic showers and of some physics events of interest to other analyses, neutrinos are identified by relying on momentum conservation since they

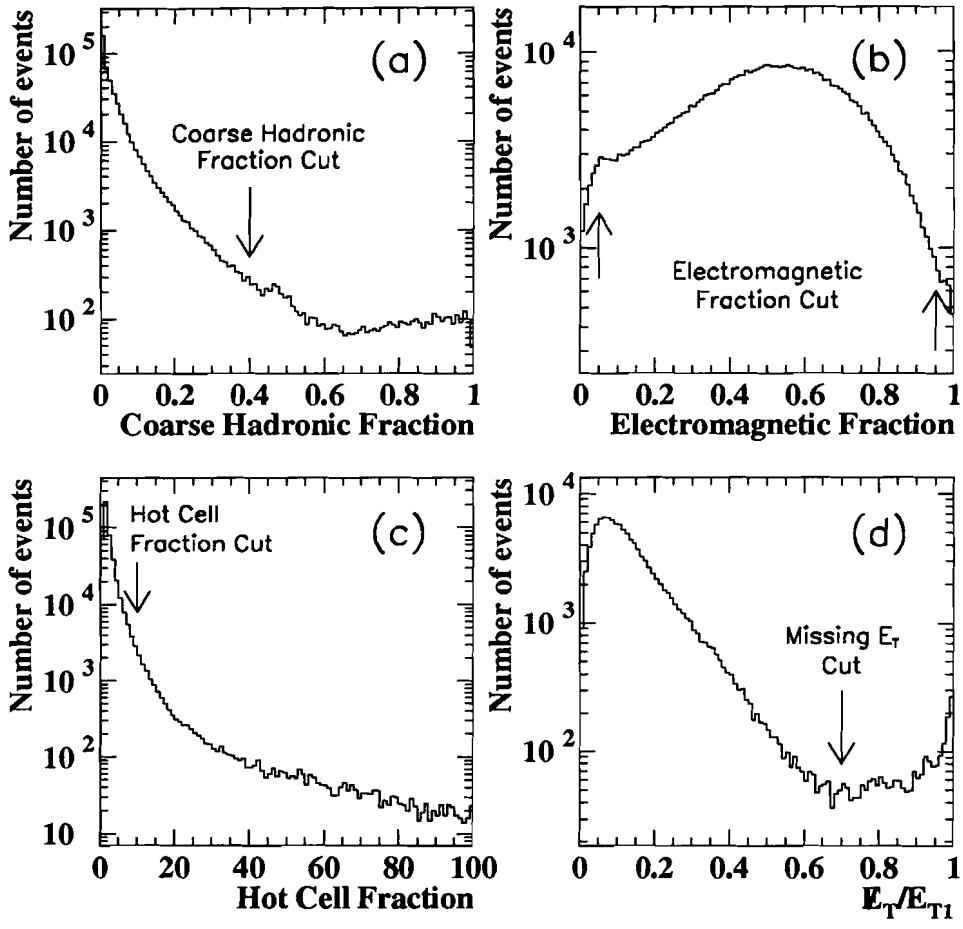

Figure 4.1: Standard Jet Quality Cuts and $\not\!\!E_T$ Cut: (a) Coarse Hadronic Fraction, (b) Electromagnetic Fraction, (c) Hot Cell Fraction, (d) Missing E_T cut. The data consisted of multi-jet events.

elude direct observation when traversing the detector (around one in 10^9 100 GeV neutrinos, or one in $\sim 10^{11}$ 1 GeV neutrinos can be directly observed). We can only apply conservation of momentum in a direction transverse to the beam, as particles travelling along the beam direction, in the vicinity of the beam pipe, go undetected. The negative of the vector sum of the E_T of all the calorimeter cells is called "Missing E_T" ($\not\!\!E_T$), and is used to measure the transverse momentum from undetected sources. Neutrinos contribute to the $\not\!\!E_T$ of an event, as does any mis-measurement of the transverse momentum of jets. The vector components of $\not\!\!E_T$ are given by:

$$\not\!\!E_x = -\sum_i E_i \sin\theta_i \cos\phi_i \tag{4.14}$$

$$\not\!\!E_y = -\sum_i E_i \sin\theta_i \sin\phi_i, \tag{4.15}$$

while the magnitude and direction of the total $\not\!\!E_T$ vector are:

$$\not\!\!E_T = \sqrt{\not\!\!E_x^2 + \not\!\!E_y^2} \tag{4.16}$$

$$\text{Direction of } \vec{\not\!\!E}_T = \frac{1}{\not\!\!E_T}(\not\!\!E_x \hat{x} + \not\!\!E_y \hat{y}), \tag{4.17}$$

where i runs over all calorimeter cells, E_i is the energy deposited in the $i^{\underline{th}}$ cell, and θ_i and ϕ_i are, respectively, the polar and azimuthal angles of the $i^{\underline{th}}$ cell.

For the events of interest in this analysis, no neutrinos are expected in the event's final state. Thus, the $\not\!\!E_T$ information is useful, as it provides a way to remove from the data undesired events which have excessive $\not\!\!E_T$ such as fake jets that failed to be removed by the Standard Jet Quality Cuts. For instance, if there is a fake jet caused by a hot cell not sufficiently spurious to be removed by the HOTFR cut, it will result

in an increase of the $\not\!\!E_T$ since the energy contribution from the cell is independent of the $p\bar{p}$ interaction. Generally, good multi-jet events will have a low $\not\!\!E_T$, whose value arises only from jet mis-measurement. Studies have shown [97] that the $\not\!\!E_T$ is a useful criterion for removing events when the standard cuts fail to remove fake jets. The $\not\!\!E_T$ requirement to retain the event is:

- $\frac{\not\!\!E_T}{E_{T1}} < 0.7$,

where E_{T1} is the E_T of the leading-E_T jet of the event. Figure 4.1d shows the distribution of data for this cut.

Table 4.3 gives the total number of events that survive the Standard Jet Quality Cuts and the $\not\!\!E_T$ cut and the corresponding integrated luminosities for some of the QCD jet triggers. The lower jet triggers were more heavily prescaled, therefore accounting for their reduced integrated luminosity values.

Bit Number	Trigger Name	Number of Events	$\int \mathcal{L}dt\ (nb^{-1})$
18	JET_LOW	265,552	74.7
19	JET_MEDIUM	318,799	991.8
20	JET_HIGH	148,242	7762.7
21	JET_MAX	48,435	13321.0

Table 4.3: Number of QCD events surviving the Standard Jet Quality and $\not\!\!E_T$ cuts and their integrated luminosities for selected jet triggers. Lower jet triggers were more heavily prescaled.

4.4 Additional Event Selection

The Standard Jet Quality Cuts were applied to all jets in an event. Any jet failing a cut would cause the event to be discarded. The $\not\!\!E_T$ cut was applied to all events

used in this analysis.

An additional requirement made on the data was based on the number of multiple interactions in an event. Some of the events collected demonstrate the presence of additional $p\bar{p}$interactions. Since it is difficult to determine the correct interaction vertex from the energy depositions in the calorimeter, we decided to use the LØ information to screen events that had likely multiple interactions. The LØ trigger assigns a value to a variable called **MIFLAG** based on the likelihood that the event had a single or multiple interaction as described in Table 4.4. In this analysis, a loose cut on the number of multiple interactions was applied. Only events with MIFLAG $= 4$ were rejected.

MIFLAG value	Description
0	No vertex information or failure.
1	Most likely a single interaction.
2	Likely a single interaction.
3	Likely a multiple interaction.
4	Most likely a multiple interaction.

Table 4.4: Description of the LØ Multiple Interaction Flag (**MIFLAG**) values.

Finally, a requirement on the z-vertex position of the event was made. The event vertex was calculated by the both VTX detector and the LØ trigger. Generally, the VTX information was used. However, when the VTX was unable to determine the z-vertex position, the best calculation from LØ was used. The z-vertex was required to be within 50 cm of the center of the detector. This was done in order to eliminate events that, due to their highly asymmetric vertex position, would be difficult to measure. For these events, the physics coordinates (measured in relation to the z-

vertex position) would differ substantially from the detector coordinates (measured relative to the center of the detector) and this would result in a mis-measurement of E_T and η. It should be noted that during Run Ia, the beam crossing position (where the center of the proton and anti-proton beams cross) was offset by -7.6 cm in z on average. This was due to the unequal strengths of the Tevatron magnets at DØ. In Fig. 4.2, the z-vertex distribution is shown.

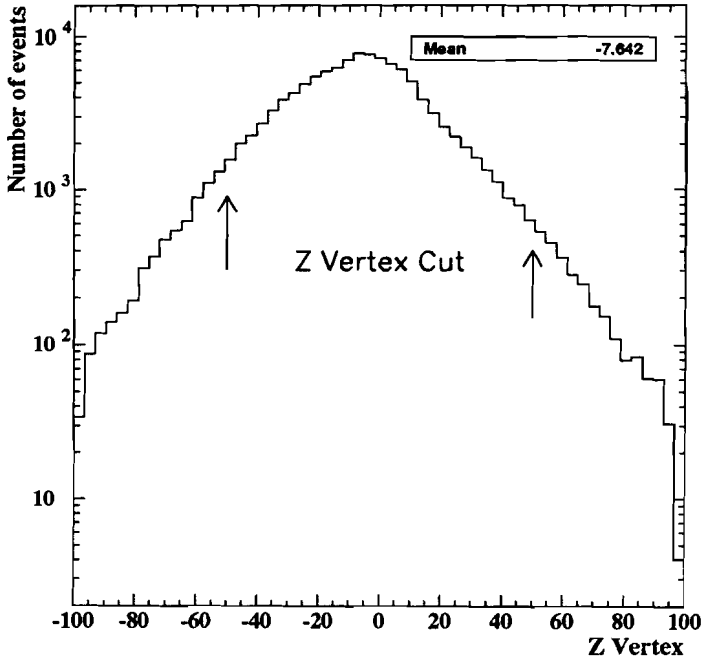

Figure 4.2: Z-vertex distribution of multi-jet events and cut of ± 50 cm applied.

In summary, for the removal of background and to reduce the likelihood of mis-measured events in the data sample, the following requirements were applied to the data:

- Using the Standard Jet Quality Cuts, discard all events most likely to contain fake jets.

- Reject all events that fail the missing E_T cut.
- Require the LØ trigger to indicate that multiple interactions were not very likely: **MIFLAG** = 0, 1, 2 or 3.
- Restrict the z-vertex position of the interaction to be $|z_v| < 50$ cm.

The efficiencies of these cuts are presented in Table 4.5. For the individual jet quality cuts, the values correspond to the jet efficiencies (for the three leading-E_T jets in the event). For the other cuts these values represent the event efficiencies.

Cut	Efficiency (%)
EMFR	98.5
CHFR	98.7
HOTFR	96.7
$\not\!\!E_T$	97.0
Jet Quality and $\not\!\!E_T$	86.4
MI Flag	99.5
Z-Vertex	92.0

Table 4.5: Efficiency values for jet quality, $\not\!\!E_T$, MI Flag and z-vertex cuts. The values for the individual jet quality cuts are jet effficiencies, the remaining values are event efficiencies.

Before applying the physics selection requirements to the sample thus obtained, we must apply certain corrections to the data for the energy scale, calorimeter response and resolution effects, among others. These corrections will be described in the following chapter.

Chapter 5

Data Correction

Before carrying out the physics analysis on the data, corrections for various detector and algorithm effects need to be made. Each jet should be corrected for contributions from the underlying event, which produces a uniform background of energy, for zero suppression and uranium noise in the calorimeter, for out-of-cone showering and for energy scale errors. In this chapter, these corrections to the jet energy are discussed. Furthermore, the calorimeter resolution in both E_T and η is also considered. These resolution effects will be useful when comparing data to theoretical predictions in the next chapter.

5.1 Jet Energy Scale

In order to measure accurately the jet E_T, one must understand how the response of the DØ calorimeter varies with different particle types (e.g., electrons, pions and muons). The response is the fraction of the input energy of a particle that the calorimeter detects. In general, the response depends on the type of particle interacting with the calorimeter. DØ measured the calorimeter response to single electrons

and charged pions using calorimeter modules in a test beam [89, 99, 100, 101]. The response was found to be linear as a function of the energy of the particles for energies above 10 GeV. However, for charged pions below this energy the non-linearities are of order 10% to 20%. Since jets are collimated sprays of hundreds of particles produced in a hadronic shower, it is not uncommon to find most of the total energy of a jet to be contributed by particles with less than 10% of the total jet energy. Therefore, since a substantial portion of a jet's energy is typically carried by particles with less than 10 GeV, large corrections are necessary to obtain the jet's true energy.

Part of the energy measured in the calorimeter comes from sources unrelated to the jet and corrections for these contributions must be made before we can determine the true energy contained in a jet. In a hard-scatter process, particles produced by the partons that do not take part in the interaction (appropriately known as *spectators*) can also be detected in the calorimeter. There is an energy contribution from these particles, which together constitute what is called the *underlying event*, a product of the underlying components of the proton and antiproton which do not participate directly in the hard-scatter event. Additionally, the energy from ionization produced by the decay of the uranium present in the absorber layers of the calorimeter (the *uranium noise*) can also be detected in the calorimeter. Since jets typically occupy a wide area, they can be 'contaminated' with energy from the underlying event and from uranium noise.

Another correction, one which depends on the measurement of the jet itself, is due to the algorithm used to identify the jet. As described in the previous chapter, we define the jet's energy in terms of the particles contained within a cone with a

fixed radius in η-ϕ space. As the particles shower in the detector, some parts of the shower extend past the cone boundaries and deposit their energy in the calorimeter outside the jet cone. This effect is known as *out-of-cone showering.*

The distortions of the jet E_T measurement can be expressed as:

$$E_{measured} = (1 - C(E_{true}, \eta, \mathcal{R}))R_{had}(E_{true}, \eta, W_{\rm RMS})E_{true} + O(\eta, \mathcal{L}, \mathcal{R}), \quad (5.1)$$

where R_{had} is the overall hadronic response dependent on the energy (E_{true}), pseudo-rapidity (η), and Root-Mean-Square (RMS) width ($W_{\rm RMS}$) of the jet; O is a constant offset for noise and particles (from the underlying event and calorimeter noise) which depends on the jet pseudorapidity, the instantaneous luminosity ($\mathcal{L}$) and the jet cone size (R) and is unrelated to the hard interaction; C is a correction (dependent on the jet energy, pseudorapidity and cone size) for the energy that crosses the jet cone boundary due to particle showering in the detector (out-of-cone showering). The width of a jet is defined as:

$$W_{\rm RMS} = \sqrt{\frac{1}{N}\sum_{i=1}^{N}((\Delta\eta_i)^2 + (\Delta\phi_i)^2)}, \quad (5.2)$$

where $\Delta\eta_i$ and $\Delta\phi_i$ are the distance between a calorimeter cell i in a jet and the jet centroid along the coordinate axes; the sum is over the N cells associated with the jet.

The jet energy scale correction used in this analysis was CAFIX v5.0 [102]. It is a complicated function of the jet energy, E_T, η, ϕ, EMFR, CHFR, ICDFR (the fraction of the energy deposited in the ICR), $W_{\rm RMS}$, and algorithm cone size. The

overall correction to the jet energy was roughly 18%. It is the largest source of the systematic uncertainty in the study of color coherence in multi-jet events.

5.1.1 Underlying Event and Zero Suppression

The underlying event and the calorimeter noise, due to the decay of uranium, electronic noise, and other detector effects, are the additive corrections to the jet energy scale. Both corrections were determined using a sample of minimum bias events, which are events triggered with the minimum amount of trigger bias achievable. For these events, the sole requirement is that the Level Ø trigger flag the event as an inelastic collision. Minimum bias events are overwhelmingly populated by the soft scattering of the incoming partons and are expected to mimic the behavior of the underlying event.

The amount of energy contributed by the underlying event was measured by taking the difference of the transverse energy density per unit area in η-ϕ space (ρ_{E_T}) between events with single interactions (**MI Tool** = 1, 2) and events with multiple interactions (**MI Tool** = 3, 4; which for run Ia meant, on average, two interactions). The **MI Tool** values are defined [103] the same way as those of the **MIFLAG** discussed in the previous chapter and given in Table 4.4. The main difference between the two is that the **MI Tool** is an offline algorithm which has additional information available to it (the Level Ø *Slow Z* vertex position — the most precise vertex calculation available from LØ, the Central Detectors' vertex results and the total energy seen in the calorimeter) which enable it to make a better determination of the number of interactions. The **MIFLAG** was used to signal multiple interactions in our data sample, as the **MI Tool** was not available

until after Run Ia. The E_T density contributed by the underlying event is:

$$U_{E_T} = \rho_{E_T}(\text{MI Tool} = 3,4) - \rho_{E_T}(\text{MI Tool} = 1,2) \tag{5.3}$$

$$= (0.310 + 0.034|\eta_d|)\ \frac{\text{GeV}}{\eta \cdot \text{rad}}, \tag{5.4}$$

where η_d is the pseudorapidity of the jet in detector coordinates. In the Inter-Cryostat Region (ICR: $1.2 < |\eta| < 1.5$), the underlying event contribution is $U_{E_T} = 0.2\ \frac{\text{GeV}}{\eta \cdot \text{rad}}$.

During most proton-antiproton interactions, a substantial fraction of the cells in the calorimeter undergo no energy deposition. Consequently, a scheme was implemented in order to optimize the readout process by bypassing the reading out of these cells.

Each cell has a pedestal offset due to electronics noise with a unique mean and variance. This offset is determined in special "pedestal runs". If the pedestal-subtracted energy contribution in a cell is less than two standard deviations from zero, the cell is not read out for that particular event. A pedestal due only to electronics noise is gaussian. However, the energy depositions from the uranium noise causes the pedestal to have an asymmetric distribution with a long positive tail. Therefore, the cells which were not zero suppressed, contain an excess of positive energy due to the uranium noise. The E_T density for minimum bias events with single interactions derives from both the underlying event and the calorimeter noise. So, in order to determine the calorimeter noise, one subtracts the underlying event

obtained, as described above, from the E_T density of these events:

$$N_{E_T} = \rho_{E_T}(\text{MI Tool} = 1,2) - U_{E_T} \tag{5.5}$$

$$= (0.196 + 1.44 \cdot \sin\theta_d)\,\frac{\text{GeV}}{\eta \cdot \text{rad}}, \tag{5.6}$$

where θ_d is the azimuthal angle of the jet in detector coordinates.

For the cone size used in this analysis ($R = 0.5$), typical values of the underlying event and calorimeter noise corrections are, respectively: 250 MeV and 1.3 GeV. Since these corrections are independent of the E_T of the jet being corrected, they are more significant for lower-E_T jets.

5.1.2 Jet Response

Due to the fact that electromagnetic showers are more uniform, narrower and deposit more of their energy early on than hadronic showers, the electromagnetic response of the calorimeter is known to greater precision than the hadronic response. Since jets are much larger hadronic objects than either electron or photon showers, it is not possible to exclude regions with large amounts of dead material, such as the ICR. Furthermore, jets typically have a substantial hadronic component, so they deposit a larger fraction of their energy deeper into the detector — where the likelihood of encountering cracks between calorimeter modules increases — than do electromagnetic showers, which deposit most of their energy in the first few layers of the calorimeter. For these reasons, the jet hadronic response is determined in relation to the electromagnetic response. The latter can be obtained by studying dielectron and diphoton decays of known resonances such as the Z boson, J/ψ and

π^0. The electromagnetic response of the calorimeter was calibrated using the mass of the Z boson and was checked against the mass of the π^0.

A precise way to calibrate the jet hadronic response would be to use the invariant mass of the dijet system from the hadronic decay of the W and Z bosons. However, the QCD dijet background makes it extremely difficult to select only those jet pairs. So, in order to determine the hadronic response, we resort to $\mathrm{E_T}$ balancing in dijet and direct photon candidates. More specifically, we use the so-called 'MPF' (Missing-E_T Projection Fraction) method [104] which is relatively independent of the jet algorithm used, since it relies on the $\not\!\!E_{\mathrm{T}}$ which is determined independently of the choice of jet-finding algorithm. This method was applied to two types of events: photon plus jet production, in which the final state contains a photon and at least one jet (usually from a gluon), and dijet events. The photon present in the former type of event must pass a photon trigger, while the jet(s) in the event remain unbiased. Similarly, one of the jets in a dijet event must pass a single jet trigger, leaving the other jet unbiased. The unbiased jet in either case is denoted the 'probe' jet. Using this method, the ratio of the hadronic response to the electromagnetic response is obtained as follows:

$$R_{\mathrm{had}}(E^{\mathrm{probe}}) = 1 + \frac{\vec{\not\!\!E}_T \cdot \hat{n}_T^{\mathrm{trigger}}}{E_T^{\mathrm{trigger}}}. \tag{5.7}$$

Here $\hat{n}_T^{\mathrm{trigger}}$ and E_T^{trigger} are, respectively, the transverse unit vector and transverse energy of the trigger photon or jet.

The hadronic response, R_{had}, is less than one when $\vec{\not\!\!E}_T$ is pointing in the direction opposite to the trigger jet or photon, indicating that the measured $\mathrm{E_T}$ for the 'probe'

jet was too low. The photons were required to be central ($|\eta_\gamma| \leq 0.9$) as well as the hadronic jet ($|\eta_{\rm jet}| < 0.7$). We can take advantage of the fact that both the E_T of the photon candidate (note that photon candidates include real photons as well as electrons and electromagnetic jets) and the direction of the probe jet are well measured quantities and use the following relation for the energy of the probe jet:

$$E^{\rm probe} = E_T^\gamma \cosh(\eta_{\rm probe}). \tag{5.8}$$

This is an exact relation in $2 \rightarrow 2$ processes. Even in multi-jet events, the energy of the probe jet is still highly correlated with the quantity $E_T^\gamma \cosh(\eta_{\rm probe})$. For events with one highly electromagnetic (trigger) jet the expression for $R_{\rm had}$ was rewritten as:

$$R_{\rm had}(E_T^\gamma \cosh(\eta_{\rm jet})) = 1 + \frac{\vec{\not\!\!E}_T \cdot \hat{n}_T^{\rm trigger}}{E_T^{\rm trigger}}. \tag{5.9}$$

Before using this equation, several additional effects were considered:

- Electromagnetic clusters in jets were corrected separately, using the precise EM calibration, and were then added back into the jet. Results were propagated to the $\not\!\!E_T$.
- The low E_T reconstruction bias due to the poorer hadronic energy resolution near the 8 GeV jet reconstruction threshold was measured using the response of Equation 5.7 in photon events with and without requiring a jet and a correction was applied.
- Energy scale variations between the different parts of the DØ calorimeter sys-

tem were determined and corrected.

- The dependence of the energy response on the width of jets was measured using dijet events in central and forward regions that excluded the ICR. A correction for this dependence was subsequently applied.

- The response of the soft energy in the calorimeter which is not contained in any found object but which, nevertheless, is part of the $\not\!\!E_T$ was determined with the response of Equation 5.7 in $Z \rightarrow e^+ + e^-$ events where no jets were reconstructed. The correction was not applied as it would magnify the comparably sized noise and signal.

In order to determine an absolute hadronic scale from Equation 5.9, one needs to determine the average jet energy as a function of $E_T^\gamma \cosh(\eta_{\rm jet})$. Both the jet energy and the hadronic response are expressed in terms of $E_T^\gamma \cosh(\eta_{jet})$ and can be combined to give the average response as a function of the average jet energy. The energy and E_T of the jets are then scaled by the reciprocal of this response. Finally, the $\not\!\!E_T$ must be adjusted since the energy scale of the objects was changed.

5.1.3 Out-of-Cone Showering

The corrections discussed so far are independent of the jet-finding algorithm used. There is one additional correction that must be applied to jets. Jets, unlike electrons or muons, are not uniquely defined objects. Their identification and selection depends to some extent on the particular jet definition that is used. This is true for the fixed cone algorithms which are utilized at the parton, particle and detector levels. As mentioned previously, for this analysis jets were reconstructed using a fixed-cone

algorithm with a cone size of $R = 0.5$.

The out-of-cone showering correction accounts for the energy that is deposited outside the cone of the jet by particles showering in the detector. This correction was determined using data obtained by subjecting central calorimeter modules to calibration beams of fixed energy electrons and pions. The transverse energy profile measured for these particles was then combined with Monte Carlo predictions of the particle composition of jets to estimate the losses due to showering. In jets with a cone size of 0.5, less then 4% of their energy was deposited outside the jet cone.

Figure 5.1 shows the jet energy scale correction for two different detector η regions as a function of the jet E_T for CAFIX v5.0. The dotted lines show the uncertainty of the correction.

5.2 Jet E_T Resolution

In addition to the energy scale of jets, the E_T resolution [105, 106] of this special sample is studied. The E_T resolution is a good measure of the precision of the calorimeter in determining the E_T of data. Moreover, this resolution must be determined in order to include this effect properly in the Monte Carlo simulations.

For mono-energetic jets with transverse energy E_T the resolution is given by the standard deviation (σ_{E_T}) of the distribution of measured transverse energy values. The jet energy scale correction factor is obtained by comparing the mean value of this distribution with that of of actual E_T values. The jet E_T resolution was determined as a function of the physics pseudorapidity (η) of the jet, which differs from the detector pseudorapidity (η_d) if the z-vertex of the event deviates from the center of the detector ($z_v = 0$). The E_T resolution was determined by selecting a sample of

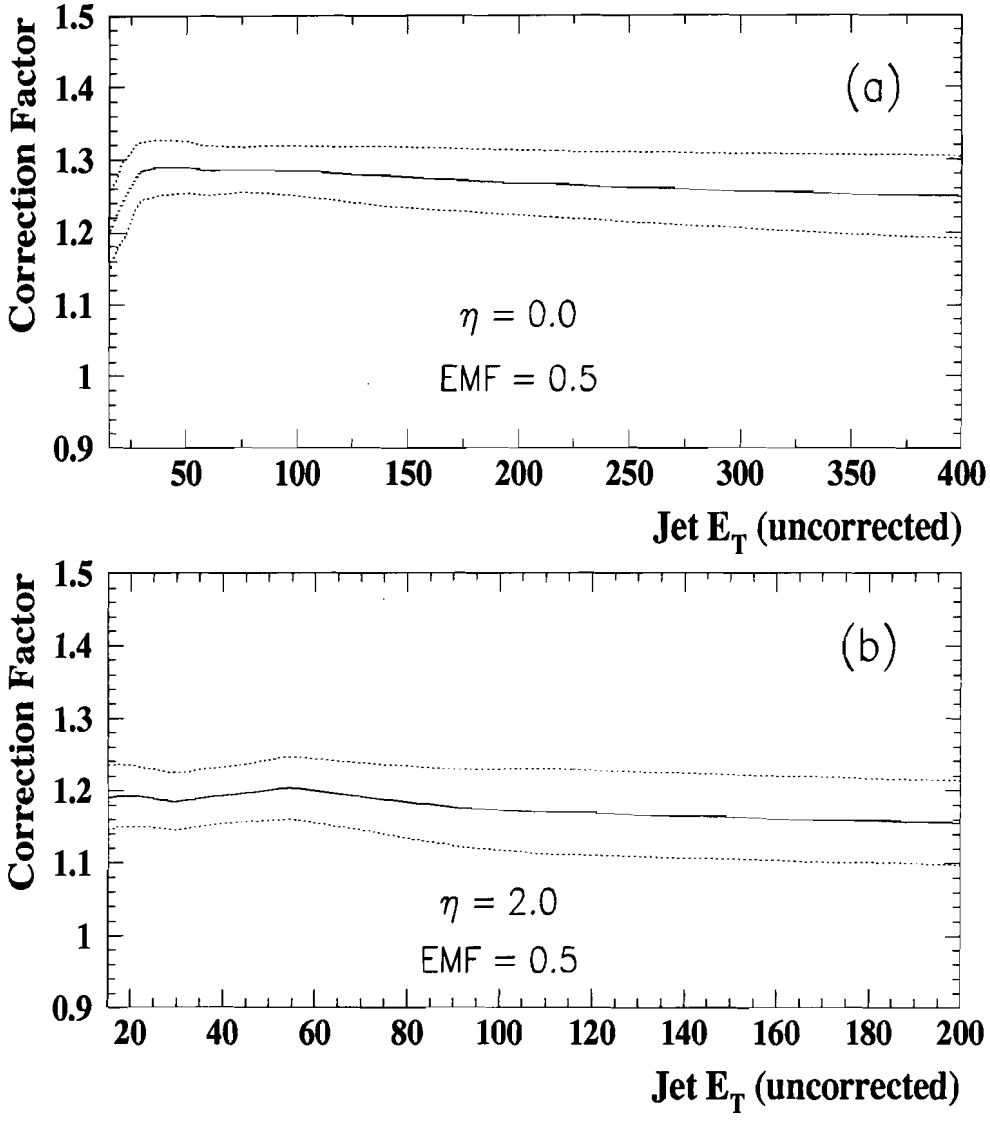

Figure 5.1: Jet energy scale correction factors for two different η regions as a function of the uncorrected jet E_T. The dotted lines show the scale correction uncertainty.

dijet events and defining a variable — the asymmetry — as follows:

$$A \equiv \frac{E_{T1} - E_{T2}}{E_{T1} + E_{T2}}, \tag{5.10}$$

where E_{T1} and E_{T2} are the transverse energies of Jets 1 and 2, respectively. The variance of A is then:

$$\sigma_A^2 = \left|\frac{\partial A}{\partial E_{T1}}\right|^2 \sigma_{E_{T1}}^2 + \left|\frac{\partial A}{\partial E_{T2}}\right|^2 \sigma_{E_{T2}}^2. \tag{5.11}$$

For dijet events, it is reasonable to assume that $E_{T1} = E_{T2} \equiv E_T$ and that $\sigma_{E_{T1}} = \sigma_{E_{T2}} \equiv \sigma_{E_T}$. Using these assumptions in Equation 5.11, the fractional E_T resolution can be expressed as:

$$\left(\frac{\sigma_{E_T}}{E_T}\right) = \sqrt{2}\sigma_A. \tag{5.12}$$

The resolution was then parametrized as a function of corrected jet E_T in six η regions using the equation:

$$\left(\frac{\sigma_{E_T}}{E_T}\right)^2 = \frac{N^2}{E_T^2} + \frac{S^2}{E_T} + C^2, \tag{5.13}$$

which has the same functional form as Equation 3.6.

Values for the three parameters N, S and C are given in Table 5.1 along with their values for the parametrizations one standard deviation above and below the nominal parametrization. The parametrizations are plotted in Fig. 5.2. The theoretical predictions will be smeared with these E_T resolutions before being compared with the data.

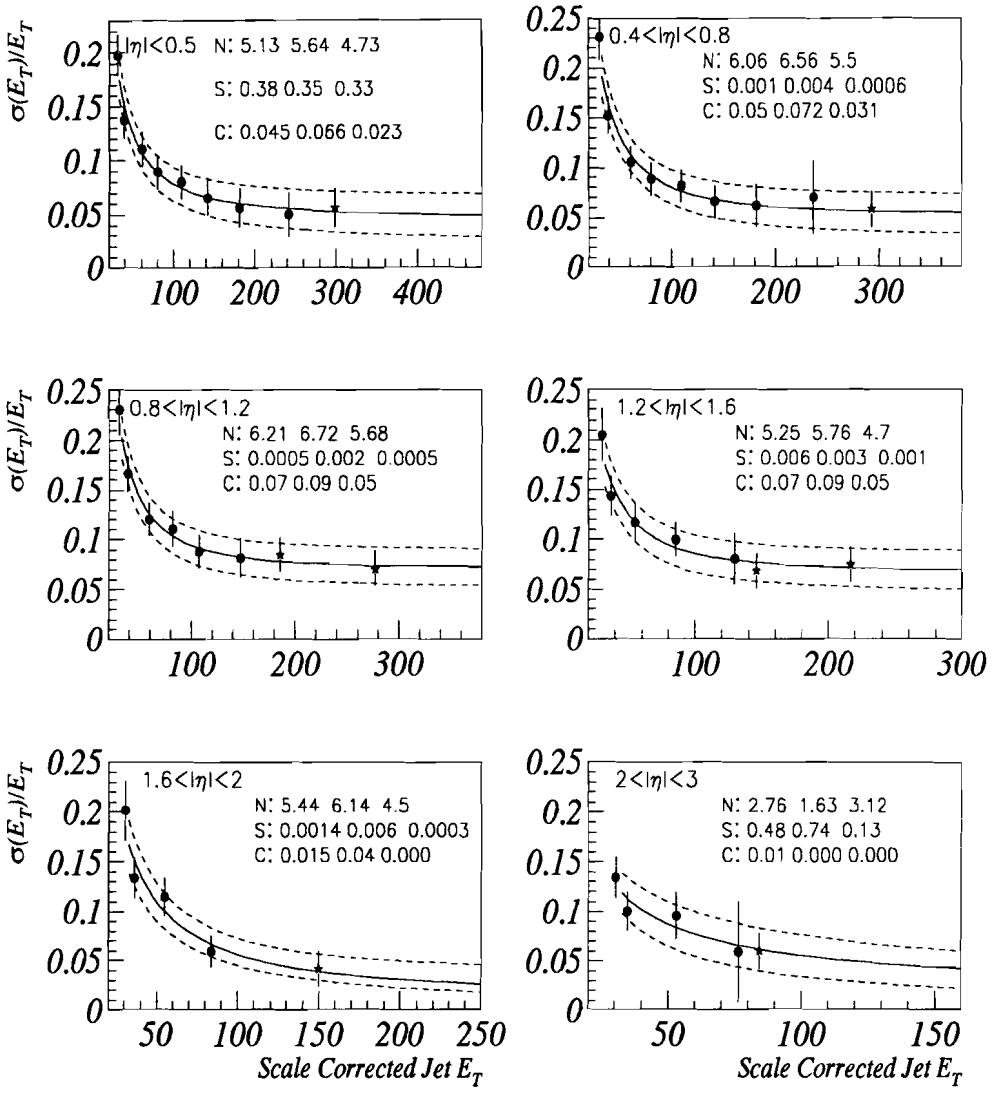

Figure 5.2: Parametrization of the fractional E_T resolution as a function of the energy scale corrected jet E_T. The points were obtained from jet-jet data.

$\|\eta\|$	N (GeV^2)	S (GeV)	C
0.0–0.4	$5.13\ ^{(5.64)}_{(4.73)}$	$0.38\ ^{(0.35)}_{(0.33)}$	$0.045\ ^{(0.066)}_{(0.023)}$
0.4–0.8	$6.06\ ^{(6.56)}_{(5.5)}$	$0.00087\ ^{(0.004)}_{(0.0006)}$	$0.05\ ^{(0.072)}_{(0.031)}$
0.8–1.2	$6.21\ ^{(6.72)}_{(5.68)}$	$0.0005\ ^{(0.002)}_{(0.0005)}$	$0.07\ ^{(0.09)}_{(0.05)}$
1.2–1.6	$5.25\ ^{(5.75)}_{(4.7)}$	$0.0055\ ^{(0.003)}_{(0.0008)}$	$0.07\ ^{(0.09)}_{(0.05)}$
1.6–2.0	$5.44\ ^{(6.14)}_{(4.5)}$	$0.0014\ ^{(0.006)}_{(0.0003)}$	$0.015\ ^{(0.04)}_{(0.0002)}$
2.0–3.0	$2.76\ ^{(1.63)}_{(3.12)}$	$0.48\ ^{(0.74)}_{(0.13)}$	$0.008\ ^{(0.0005)}_{(0.0004)}$

Table 5.1: Values of the parameters used to describe the fractional jet E_T resolution ($\frac{\sigma_{E_T}}{E_T}$) as a function of the energy scale corrected jet E_T(see Equation 5.13). The values one standard deviation above and below nominal are shown in parentheses.

5.3 Jet η Bias and Resolution

The finite η resolution of the detector is the remaining effect that will be examined in this chapter. Through Monte Carlo studies, it was determined that jets are systematically mis-measured in η [107] by a small amount. The average difference between the parton η and the reconstructed jet η is non-zero, indicating a bias in the way jets are reconstructed. This bias is related to the asymmetry of the size of calorimeter cells in real vs. η-ϕ space. It is expected that the magnitude of the η bias diminish with a smaller cone size, as the effect of the asymmetry is restricted to a smaller region. The extent of the bias has been studied using a cone size of $R = 0.7$ and it was found to be a rather small effect overall. On average, the η bias produces a shift of $\Delta\eta \sim 0.01$ towards the center of the detector in the reconstructed η of the jet. At its worst, the shift can be as large as $\Delta\eta \sim 0.08$ at high pseudorapidities ($|\eta| \sim 3$) and low energies. Since the η bias for $R = 0.7$ overestimates the true bias corresponding to the cone size used in this analysis ($R = 0.5$), this correction is not applied to data. Instead we will examine what the overall effect of this correction is on our data when we examine systematic uncertainties in the next chapter.

The η resolution of the detector was determined using a Monte Carlo sample which included a simulation of the detector. By plotting the differences between the reconstructed jet η and the parton η, a standard deviation of this distribution can be calculated which, in turn, determines the η resolution of the detector. The η resolution was parametrized for six detector η regions, η_d, using the functional form:

$$\sigma_\eta(E, \eta_d) = \mathrm{A} + \frac{\mathrm{B}}{E} + \frac{\mathrm{C}}{E^2}, \tag{5.14}$$

where A, B and C are parameters and E is the energy of the jet.

The results of the parametrization are given in Table 5.2 and plotted in Fig. 5.3. Due to the good η resolution of the detector, no η resolution correction was required in this analysis.

$\lvert\eta_d\rvert$	A	B (GeV)	C (GeV^2)
0.0 – 0.5	0.0057	0.82	−0.96
0.5 – 1.0	0.0039	1.19	−3.86
1.0 – 1.5	0.0052	1.74	−10.98
1.5 – 2.0	0.0037	2.42	−17.10
2.0 – 2.5	0.0011	4.90	−100.3
2.5 – 3.0	0.00081	8.08	−248.9

Table 5.2: Values of the parameters used to describe the jet η resolution as a function of parton jet energy, for different η_d bins.

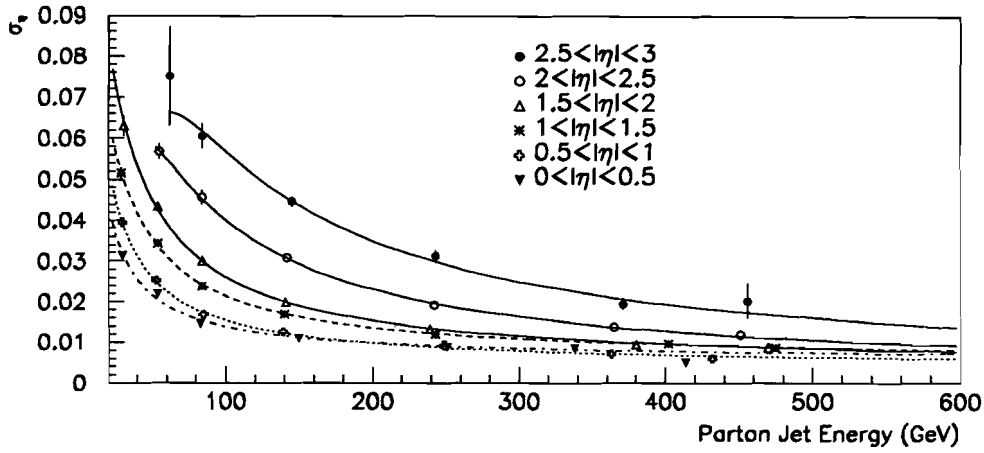

Figure 5.3: Jet η resolution, $\sigma_\eta(E,\eta_d)$, as a function of the parton jet energy, derived using a Monte Carlo simulation. The points represent the HERWIG sample in six different η regions, while the curves show the parametrizations used.

Chapter 6

Data Analysis

Although the journey of our protagonist proton has ended in a fierce collision inside the DØ detector, it was a most valuable odyssey. This journey, and many others like it, made possible the study of color coherence which now follows...

6.1 Overview

As described in Chapters 1 and 2, color interference effects among partons in hadron-hadron interactions result in a non-isotropic distribution of secondary jets from soft gluon radiation in the event. In particular, for interactions in which the final state contains two hard opposing partons (which produce hard primary jets), production of softer jets is expected to be suppressed in regions transverse to the plane of the event, where there is minimal color flow, and enhanced near the plane of the event, where color flow is greatest. Furthermore, secondary jets are expected to be found preferentially in the vicinity of the hard parton that contributed to the emission. These two notions determine the analysis strategy for the multi-jet sample. Although there is no reason, a priori, to expect that color coherence effects should be absent

within the primary jet cones, the principal objective in this dissertation is the study of coherence effects in multi-jet events, so the examination of energetic particles within the jet is beyond the scope of this study. Consequently, the investigation of color interference effects in the data centers on a measurement of the angular correlations of secondary jets with respect to the primary jets of the event.

6.2 Method of Analysis

The best way to observe multi-jet events with the DØ detector is to measure the energy deposited in the various layers of the calorimeter, truly the heart and soul of the detector. Several views of a sample three-jet event observed in the detector are shown in Appendix A.

The analysis requires soft gluon radiation to materialize as a secondary jet in an event with two primary hard jets produced by the partons involved in the hard scattering. For this reason, only events with three or more reconstructed jets which satisfy the JET_HIGH jet trigger are used. In order to avoid any biases introduced by the trigger threshold of 85 GeV, it was required that the transverse energy of the highest-E_T jet in the event be above 115 GeV. Using a higher jet trigger would have greatly reduced the number of events in the sample and therefore severely limited the statistics available. Building on previous discussions of color coherence, we now develop a way to observe its manifestations in multi-jet data.

After we order the jets in each event according to their transverse energy ($E_{T1} > E_{T2} > E_{T3} > \cdots$) we measure the angular distribution of the third jet around the second jet over many events. For each event, these distributions are measured in an annular region of fixed size in (η, ϕ) space centered on the second jet. A balance

between using relatively soft reconstructed jets while still requiring their E_T to be sufficiently high to maintain an acceptable reconstruction efficiency was achieved by requiring that the third jet have $E_{T3} > 15$ GeV. The color interference effects are then studied via analysis of these third jet distributions about the central and forward second leading-E_T jets.

Later on in this chapter, these jet distributions will be compared to those from several Monte Carlo event generators with different implementations of color coherence effects, in order to identify the color coherence contribution.

6.2.1 Annular Region

A three-dimensional representation of the event topology is shown in Fig. 6.1. The beam axis indicates the directions of the initial-state colliding partons. In most events, the final state partons which fragment into Jets 1 and 2 retain a color connection to the beam. The color flow in these events is therefore determined by the location of those jets relative to the beam direction.

Once the two leading-E_T jets have been reconstructed in the event, a circular-shaped annular region is drawn around Jet 2 in (η, ϕ) space. The inner radius of this region is 0.6 and the outer radius is $\frac{\pi}{2}$, where the radius $\mathcal{R}$ is:

$$\mathcal{R} = \sqrt{(\Delta\eta)^2 + (\Delta\phi)^2}. \tag{6.1}$$

The inner radius was chosen to lie just outside the reconstruction cone radius of the jet, so that measurements of secondary jets will be possible. Half of the events in which partons are separated by a distance $\Delta\mathcal{R} = 0.6$ have two jets with cone size $\mathcal{R} = 0.5$ reconstructed [108]. The outer radius of the annulus was chosen to exclude

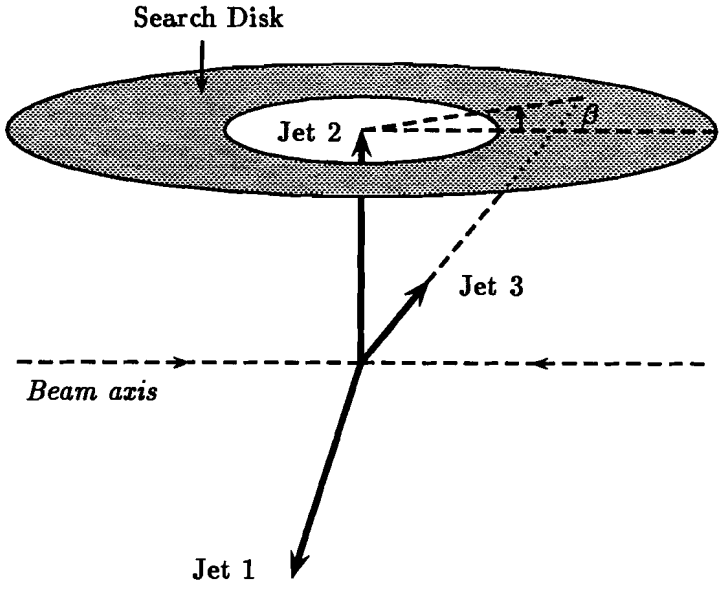

Figure 6.1: Three-jet event topology illustrating the search disk (gray area) for studying the angular distribution of the softer third jet around the second leading-E_T jet.

any overlap with the Jet 1 axis and to contain only the instrumented regions of the calorimeter, while also retaining good acceptance.

When Jets 1 and 2 have the same pseudorapidity, the distance between the two jets is determined solely by their separation in ϕ ($\Delta\phi_{12}$). If the outer radius of the annulus is set to $\frac{\pi}{2}$, the annulus completely covers one hemisphere of the detector in the ϕ direction ($2\mathcal{R} = \pi$). Nevertheless, an extremely loose $\Delta\phi_{12}$ requirement, can be applied to Jets 1 and 2, $\frac{\pi}{2} < |\Delta\phi_{12}| < \frac{3\pi}{2}$, which only constrains them to be in opposite ϕ hemispheres. This greatly reduces the probability of overlap of the Jet 1 axis and the annulus, as shown in Fig. 6.2, while just removing less than 0.3 % of the sample.

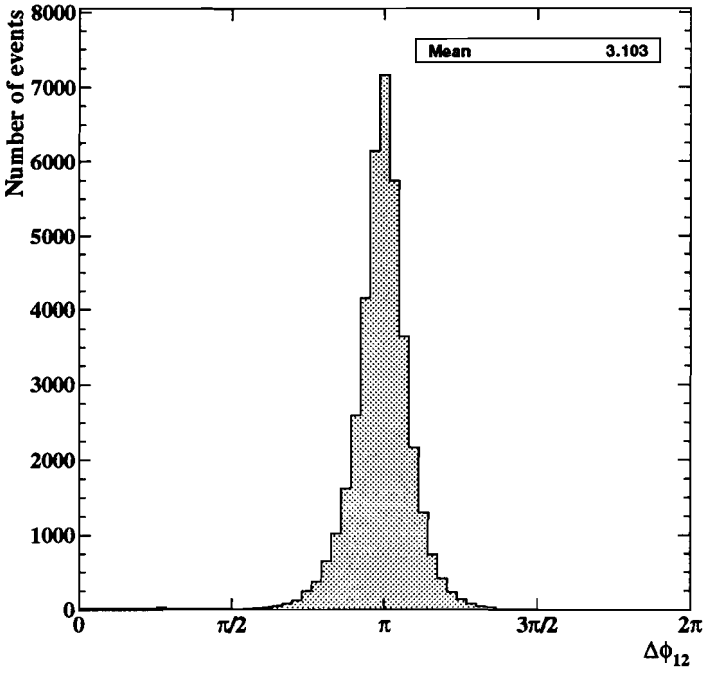

Figure 6.2: Distribution of $\Delta\phi_{12}$ separation in multi-jet sample. The distribution peaks at π and extends out to the limits imposed on the data of $\frac{\pi}{2}$ and $\frac{3\pi}{2}$.

6.2.2 Event Selection

A summary of the event selection criteria applied is tabulated in Table 6.1 along with the number of events surviving each cut.

In order to study interference effects in different pseudorapidity regions, Jet 2 was required to be either central ($|\eta_2| < 0.7$) or forward ($0.7 < |\eta_2| < 1.5$). The pseudorapidity of the leading jet was not explicitly constrained. The event population in each pseudorapidity region is detailed in Table 6.2. Note that the central region has over one-half times more statistics than the forward region as jet production is kinematically favored there.

Selection Criteria	Events Surviving
$N_{JETS} \geq 3$	842,159
JET_HIGH Trigger (85 GeV)	119,150
MI Flag (0,1,2 or 3)	118,523
$\|z_v\| < 50$ cm	109,106
Jet Quality and $\not\!\!E_T$ cuts	94,265
$E_{T1} > 115$ GeV	39,136
$\|\eta_2\| < 3.0$	39,133
$E_{T3} > 15$ GeV	31,771
$\frac{\pi}{2} < \|\Delta\phi_{12}\| < \frac{3\pi}{2}$	31,684
$0.6 < \mathcal{R} < \frac{\pi}{2}$	16,157

Table 6.1: Event selection criteria applied and the number of events surviving each cut.

Final Samples	Events
Central ($\|\eta_2\| < 0.7$)	9,048
Forward ($0.7 < \|\eta_2\| < 1.5$)	5,776
Combined ($\|\eta_2\| < 1.5$)	14,824

Table 6.2: Final event population in each η region.

6.3 Choice of Variables

6.3.1 β variable

An associated angle, β, is defined around the annulus such that $\beta = 0, 2\pi$ and $\beta = \pi$ correspond to the two beam directions (and therefore to the event plane), while $\beta = \frac{\pi}{2}$ and $\beta = \frac{3\pi}{2}$ lie in the transverse plane. For each event, β is determined as follows:

$$\beta \equiv \tan^{-1}\left[\frac{sgn(\eta_2)\cdot\Delta\phi_{32}}{\Delta\eta_{32}}\right], \tag{6.2}$$

where

$$\Delta\phi_{32} \equiv \phi_3 - \phi_2 \text{ and} \tag{6.3}$$

$$\Delta\eta_{32} \equiv \eta_3 - \eta_2. \tag{6.4}$$

The unit multiplier $sgn(\eta_2)$ was introduced into the definition of β so that $\beta = 0, 2\pi$ always points towards the beam nearest to Jet 2, regardless of which η hemisphere of the detector Jet 2 is located in. This region will be referred to as the *near-beam* region while the region defined by $\beta = \pi$ will be referred to as the *far-beam* region. The near-beam region, by definition, is smaller in phase space than the far-beam region. Differences in jet production and reconstruction are expected between the near-beam and far-beam regions, particularly when Jet 2 is located at higher pseudorapidities, so the distinction is stressed in the analysis.

An example of a three-jet event projected to the $\eta - \phi$ plane is illustrated in Fig. 6.3, where the annular region around the second leading-E_T jet and the β angle are shown. In this example, Jets 1 and 2 are perfectly back-to-back in ϕ and there is no overlap between the annular *search disk* and Jet 1, as expected. The near-beam and far-beam regions are clearly visible, along with the location of Jet 3 inside the search disk. The region near the event plane, where an excess of soft jet production would indicate enhanced soft radiation emission as predicted by color coherence, is marked with "+" signs in both the near-beam and far-beam regions.

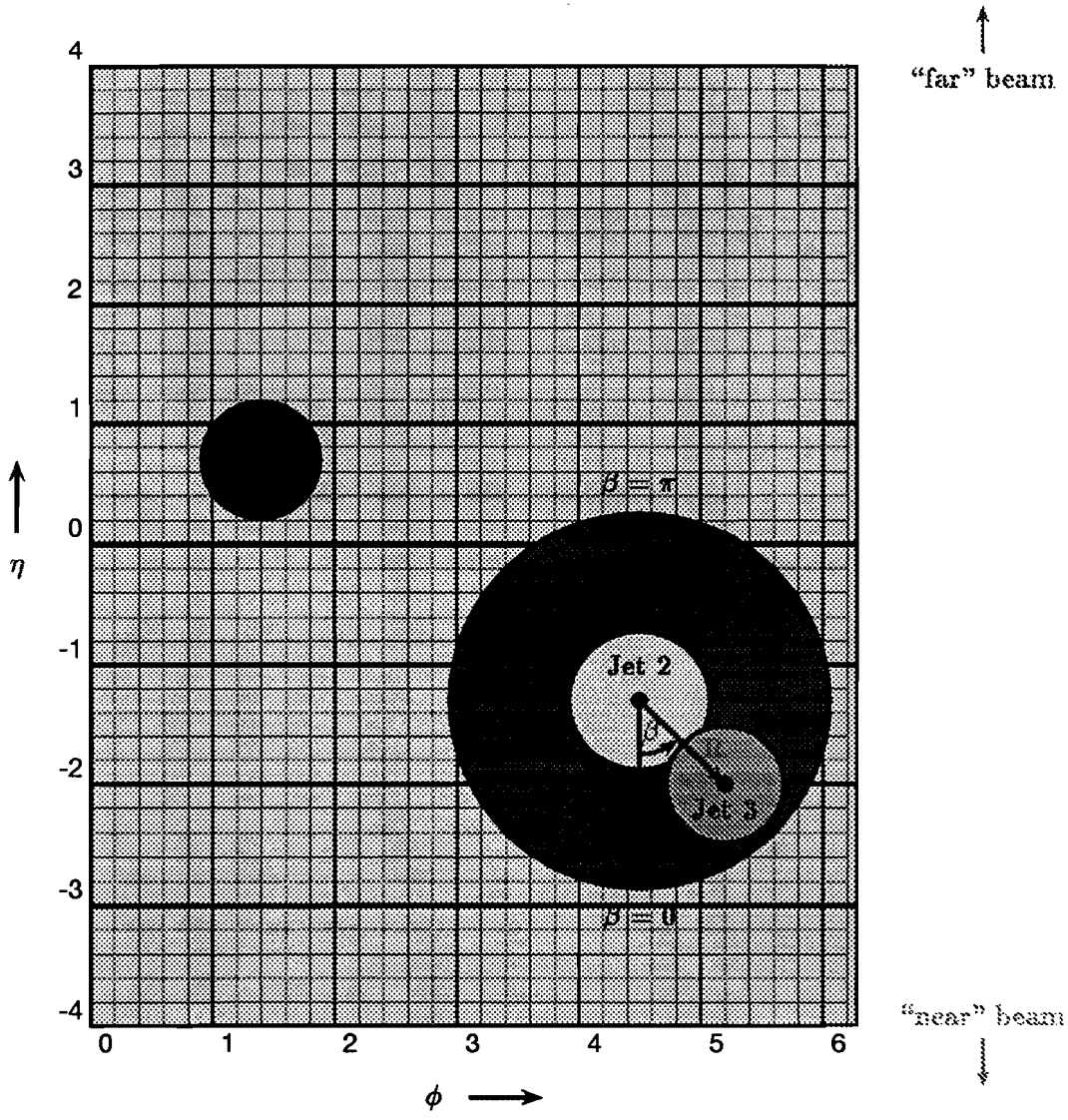

Figure 6.3: Definition of the β variable in the (η, ϕ) space of a three-jet event. The angle formed by the secondary jet (Jet 3) with respect to the second leading-E_T primary jet (Jet 2) and the near beam is determined for all qualifying events in which the softer jet is contained in the search disk around the harder jet. An excess of soft jets in the region marked by the "+" signs near $\beta = 0, \pi$ would indicate that the rate of soft radiation around the event plane is enhanced, as predicted by color coherence.

6.3.2 β Distributions

After construction of the annulus, it is sliced radially into equal sections of β. Eighteen such sections were used in the analysis. This allows a sufficiently fine segmentation in β to measure the full range of soft jet production in the annulus, while still maintaining good statistics. The resulting distribution is:

$$\frac{dN}{d\beta}, \tag{6.5}$$

where N is the total number of events in the sample.

In the analysis, we are only concerned with the relative β distribution, i.e., the shape of this distribution, and not with the absolute levels measured; therefore it is convenient to normalize this distribution to the total number of events in the sample, thereby giving the fraction content in each β section as follows,

$$\frac{1}{N}\frac{dN}{d\beta}. \tag{6.6}$$

The β distributions will reflect a superposition of color coherence and kinematic effects. In order to isolate the effect of color coherence, comparisons of the data to MC were made, as described in a later section. First, we review the Monte Carlo simulations used.

6.4 Monte Carlo Simulation

In order to determine whether color coherence effects in the data are observed, the measured angular distributions are compared to the predictions of several Monte

Carlo event generators that differ in their implementation of color coherence. We employ parton-shower Monte Carlo event generators, PYTHIA v5.7, HERWIG v5.8 and ISAJET v7.13, and a partonic event generator, JETRAD v1.2.

6.4.1 PYTHIA Simulation

PYTHIA is an excellent choice for this comparison due to the many options it provides the user with respect to angular ordering and fragmentation implementations. This MC generator simulates the hard scattering to leading-order and is capable of approximating color coherence effects during parton evolution in both the initial and final states. It employs the Lund string model by default in the fragmentation process, but also contains the full machinery for independent fragmentation if the user so desires.

PYTHIA approximates color coherence through angular ordering and azimuthal correlations. At each gluon branching, an opening angle is generated subject to the constraint set by the previous branching (the AO constraint). The azimuthal angle of the emitted gluon is chosen uniformly for branchings from the initial-state partons. For branchings from final-state partons, however, the azimuthal angle is influenced by the color partner of the emitting parton. This influence is manifested as a probability distribution for the azimuth that is maximized in the plane formed by the emitting parton and its color partner and in the region between them (as described in Chapter 2).

6.4.2 HERWIG Simulation

HERWIG is also a very good choice for comparison with data. Although it offers only a single implementation of angular ordering and fragmentation, it has been thoroughly tested at hadronic colliders and found to model QCD events reasonably well. Like PYTHIA, HERWIG also simulates the hard scattering to leading-order and is capable of approximating color coherence effects during parton evolution in both the initial and final states. Unlike PYTHIA, however, it employs the Cluster model in the hadronization process.

HERWIG also approximates color coherence through angular ordering of both initial and final state radiation and through azimuthal correlations between the partons.

6.4.3 ISAJET Simulation

ISAJET is most useful for comparing with data as it models all $2 \rightarrow 2$ processes which involve quarks and gluons, and also includes higher order processes by adding QCD radiative corrections in the leading log approximation to both the initial and final states, in order to obtain the correct event structure. ISAJET includes no color coherence effects during the parton shower nor during its hadronization process, which occurs independently for each parton.

The ISAJET angular distributions will therefore be purely kinematical and devoid of any effects from color coherence.

6.4.4 JETRAD Simulation

JETRAD is a purely partonic event generator that fully calculates the $\mathcal{O}(\alpha_s^3)$ tree-level

$2 \rightarrow 3$ QCD predictions. As such, it does not include non-perturbative fragmentation and is therefore useful to investigate whether the perturbative color interference effects at the partonic level survive the hadronization process.

6.4.5 Simulation of Detector Effects

PYTHIA, HERWIG and ISAJET events were generated at the particle (hadron) level. JETRAD events were generated at the parton level. All Monte Carlo predictions had detector η and energy resolution effects (described in Chapter 5) included. In order to determine the validity of using data generated at the particle level, a subset of the HERWIG sample was processed instead with the Shower Library detector simulation [109].

Shower Library is a database of detailed calorimeter shower information from the *mixture-level* GEANT [1] detector simulation of a sample of about 1.2 million particles. These particles are binned according to specific kinematic variables: z vertex displacement, pseudorapidity, momentum, and azimuthal angle; and also according to their particle type: electromagnetic (e^+, e^-, γ, π^0or η), hadronic, or muon. The lowest momentum bin is 100-320 MeV. For each particle, the energy and location of each cell associated with its calorimeter shower is stored, up to a maximum of 42 cells. For each particle in a Monte Carlo event, a random shower from the Shower Library is chosen, subject to the requirement that the Monte Carlo particle and the Shower Library particle that initiated the shower belong to the same bin in each of the five variables above. The energy of the shower is scaled according to the Monte

[1] *Mixture-level* GEANT is a simulation of the detector in which the calorimeter layers are treated as a uniform mixture of uranium and liquid argon, as opposed to separate uranium absorber and liquid argon gap regions.

Carlo particle energy and the shower cell information is then stored in the event. Calorimeter noise effects are not included in this simulation. Following the Shower Library simulation, the events were reconstructed with the DØRECO package.

This method results in an "approximation of an approximation" for the DØ detector, but is expected to be precise enough for the study of large ensembles of particles. Shower Library has been shown to give results that are in excellent agreement with the full GEANT detector simulation, when distributions of total event energy, total event E_T, ICD/MG energy, $\not\!\!E_T$, and dijet invariant mass are compared.[109]

In the next section, the observed β distributions are presented.

6.5 Results

The β distributions for Jet 2 in the central and forward regions are shown below in Figs. 6.4 and 6.5. The number of events with a qualifying third jet in each β bin has been normalized by the total number of events in the sample. The vertical error bars on all points represent both statistical and systematic uncertainties (discussed later in this chapter) added in quadrature, while the horizontal error bars represent the bin widths in β.

The most prominent feature of both curves is their strong peaking near $\beta = \pi$. There is a substantial kinematic contribution to this peak, since secondary jets located in the annulus at this value of β, on average, tend to be more central than those at $\beta = 0, 2\pi$. Therefore, these jets are kinematically favored, as they require less energy to satisfy the 15 GeV jet threshold. This effect becomes more pronounced as Jet 2 is allowed to be more forward, as can be seen by examining the β pattern

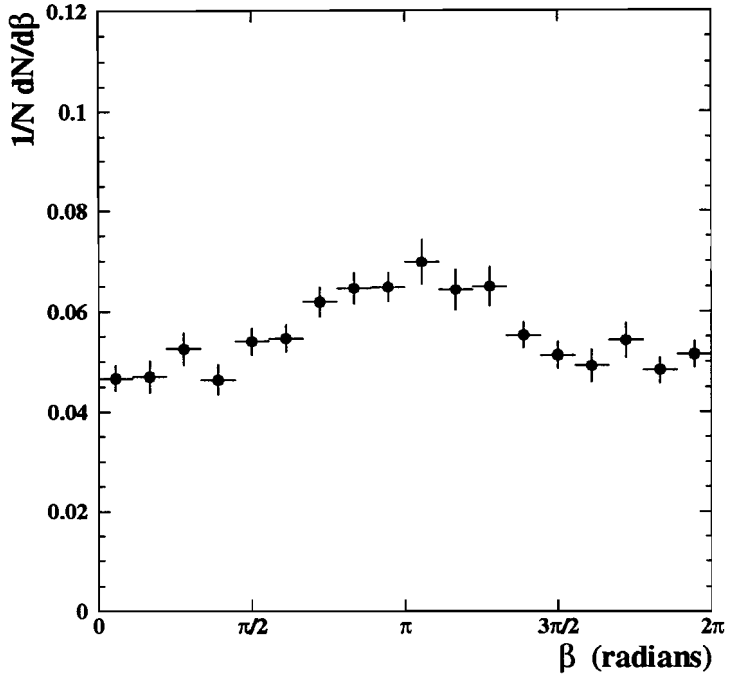

Figure 6.4: β distribution of data for $|\eta_2| < 0.7$. The error bars shown include statistical and uncorrelated systematic uncertainties.

(Fig. 6.6) of a jet-like object located at $\eta = 1.4$ which radiates in purely kinematic fashion, as described in Chapter 2. Conversely, when $|\eta_2| \simeq 0$, there will be little kinematic difference between secondary jets near $\beta = 0, 2\pi$ and those near $\beta = \pi$, as illustrated by now placing the kinematic radiator at $\eta = 0.05$ in Fig. 6.7. Instead, the transverse plane ($\beta = \frac{\pi}{2}, \frac{3\pi}{2}$) will be kinematically favored as it will correspond to the most central region of the annulus.

In reality, the central β distribution (6.4) is a superposition of a variety of events, ranging from those in which the far beam region is favored by kinematics (when $|\eta_2| \simeq 0.7$) to those in which the transverse plane is favored ($|\eta_2| \simeq 0$). In Fig. 6.8, the kinematic model illustrates an intermediate case in which the jet-like object is located at $\eta = 0.5$. There, the β pattern has an obvious 'sinkhole' around $\beta = \pi$,

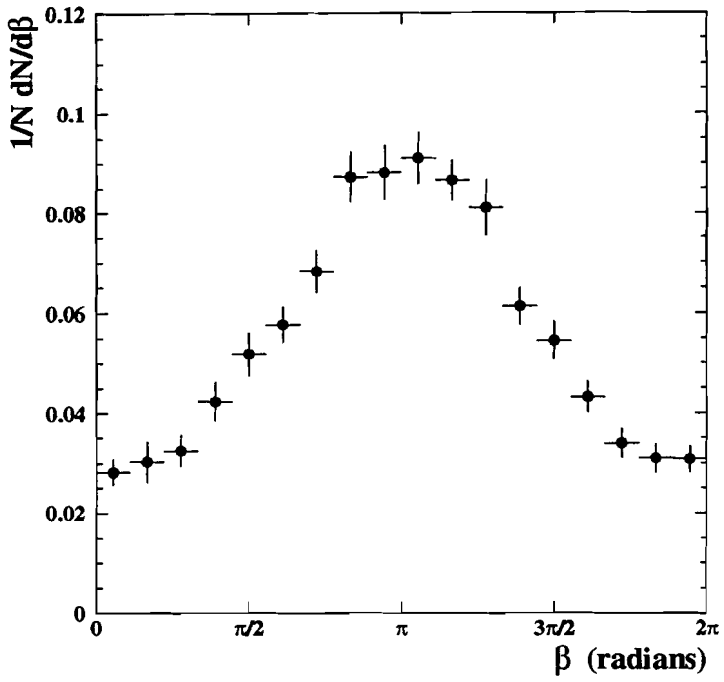

Figure 6.5: β distribution of data for $0.7 < |\eta_2| < 1.5$. The error bars shown include statistical and uncorrelated systematic uncertainties.

since the adjacent β regions on either side correspond to lower pseudorapidities. The forward β plot, on the other hand, is dominated by events in which the far beam region is strongly favored by kinematics.

In order to investigate the contribution of color coherence, we will next compare the data to several different Monte Carlo implementations of color coherence effects.

6.6 Analysis of Monte Carlo Events

The particle-level and parton-level Monte Carlo events were subjected to the same selection criteria as the data events, with the exception of the multiple interaction flag restriction and the jet quality cuts. Since there is no timing information available for the Level Ø scintillation counters in the Monte Carlo events, no multiple interaction

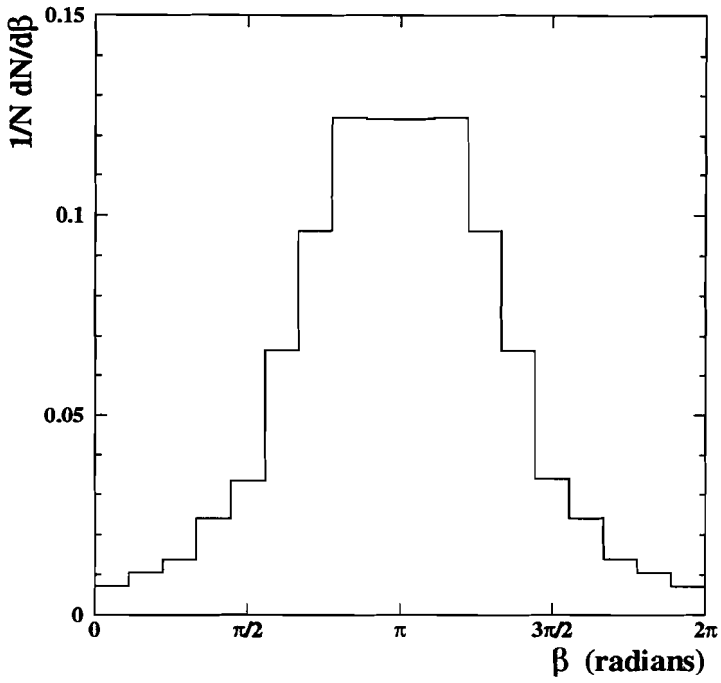

Figure 6.6: β pattern of a purely kinematic jet-like object located at $\eta = 1.4$.

probability is calculable. However, no multiple interaction events were generated, so this cut would be unnecessary in any case. Similarly, no calorimeter energy deposition information is available in these events, so the jet quality cuts are not applicable. However, no "bad" quality events were generated in the first place, so these cuts are unneeded. After the Shower Library simulation, the calorimeter-level sample was reconstructed with the same version of the DØRECO package used for the data and then subjected to the same selection criteria as the data, except for the multiple interaction flag restriction.

The total number of events in each of the Monte Carlo samples and in each η region is listed in Table 6.3. All the particle-level samples have the same level of statistics. In JETRAD, a higher number of generated events were required as each

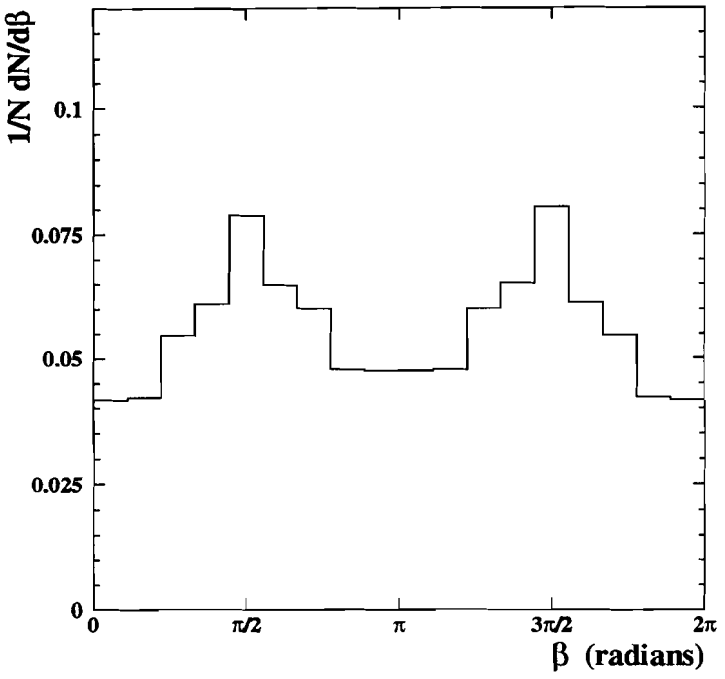

Figure 6.7: β pattern of a purely kinematic jet-like object located at $\eta = 0.05$.

event has a corresponding weight which can be negative for the two-parton matrix elements. Only when they are combined with the three-parton matrix elements to give jet predictions does one get positive results. The calorimeter-level sample has the lowest statistics due to the large computational resources required for the detector simulation.

6.6.1 Kinematic Comparisons with Data

In order to have confidence that the Monte Carlo generators represent multi-jet production well, certain kinematic comparisons must be made with the data. The transverse energy and pseudorapidity distributions for Jets 1 and 2 are particularly important, as they indicate how well the hard scattering is modelled by the simulations. Some differences in the distributions for Jet 3 are to be expected as the various

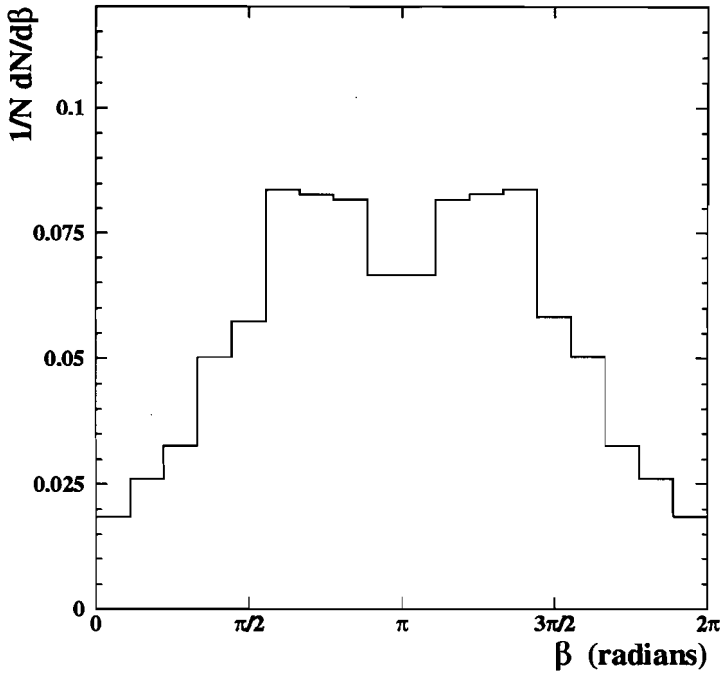

Figure 6.8: β pattern of a purely kinematic jet-like object located at $\eta = 0.5$.

Monte Carlos implement color coherence effects differently, or not at all, which primarily affects soft radiation. Furthermore, one must take into account that JETRAD provides a LO calculation to 3-jet production. As such, it does not include higher order events beyond three jets. Hence, its kinematical distributions are expected to reflect this difference.

The observed E_T distributions for Jet 1 and Jet 2 are shown in Figs. 6.9 and in Figs. 6.10, respectively, and are compared to the Monte Carlo samples at the particle level and at the parton level. These and succeeding distributions in this section are normalized to the total number of events. The error bars of the data and Monte Carlo samples are statistical only. In the E_T distributions of both Jet 1 and Jet 2, the particle-level simulations exhibit good agreement with the data. JETRAD also

Monte Carlo Sample	Events Generated	$\|\eta_2\| < 0.7$	$0.7 < \|\eta_2\| < 1.5$
HERWIG	2,036,236	35,390	23.332
ISAJET	2,000,000	32,180	19,449
PYTHIA:			
AO, SF	1,999,997	31,559	20,930
No AO, SF	2,000,000	37,757	24,704
AO, IF	1,999,997	23,476	14,969
JETRAD	40,000,000	913,044	536,539
HERWIG (Calorimeter)	129,935	2,204	1,510

Table 6.3: Monte Carlo samples and the number of events satisfying the selection criteria in each η region.

agrees with the observed E_{T1} distribution but can be seen to differ from the E_{T2} data distribution in Fig. 6.10f. As discussed before, these differences between JETRAD and data could be attributed to higher order effects not included in JETRAD as well as to the lack of additional smearing effects caused by parton fragmentation.

The observed η distributions for Jet 1 and Jet 2 are shown in Figs. 6.11 and in Figs. 6.12, respectively, and are compared to the Monte Carlo samples at the particle level and at the parton level. The difference in the data distribution for Jet 1 may be due to uncertainties in the jet energy scale, since Jet 1 is subjected to the most severe cut in E_T ($E_{T1} > 115$ GeV), which occurs on a steeply falling spectrum. Therefore, a small difference in the jet energy scale correction applied could cause a substantial shift in the events that pass this cut.

All implementations of color coherence effects in PYTHIA model the data η distribution for the leading-E_T jet reasonably well (Figs. 6.11c – 6.11e). However, ISAJET and HERWIG at the particle level (Fig. 6.11a and Fig. 6.11b), and to a lesser extent JETRAD at the parton level (Fig. 6.11f), have wider Jet 1 pseudorapidity distribu-

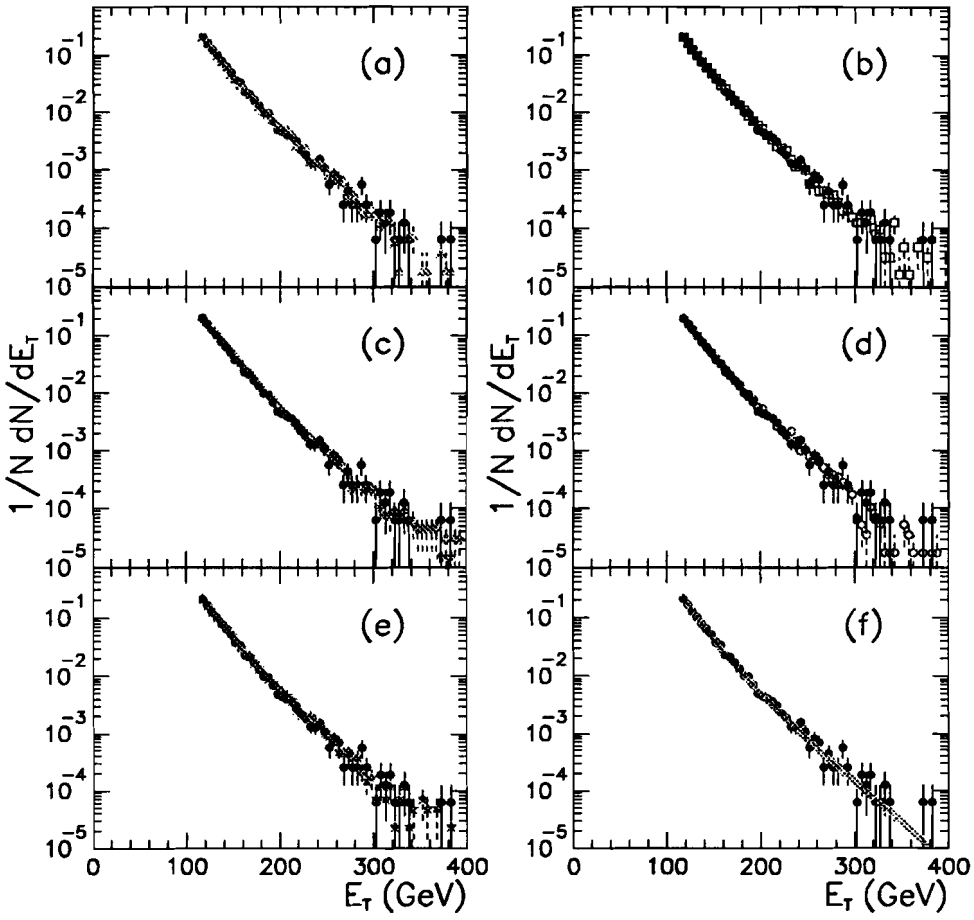

Figure 6.9: Leading-jet E_T distributions for data (filled circles) and (a) ISAJET, (b) HERWIG, PYTHIA with (c) Angular Ordering off and String Fragmentation, (d) Angular Ordering and String Fragmentation, (e) Angular Ordering and Independent Fragmentation and (f) JETRAD. All distributions are for events with $E_{T1} > 115$ GeV. The error bars shown represent statistical uncertainties.

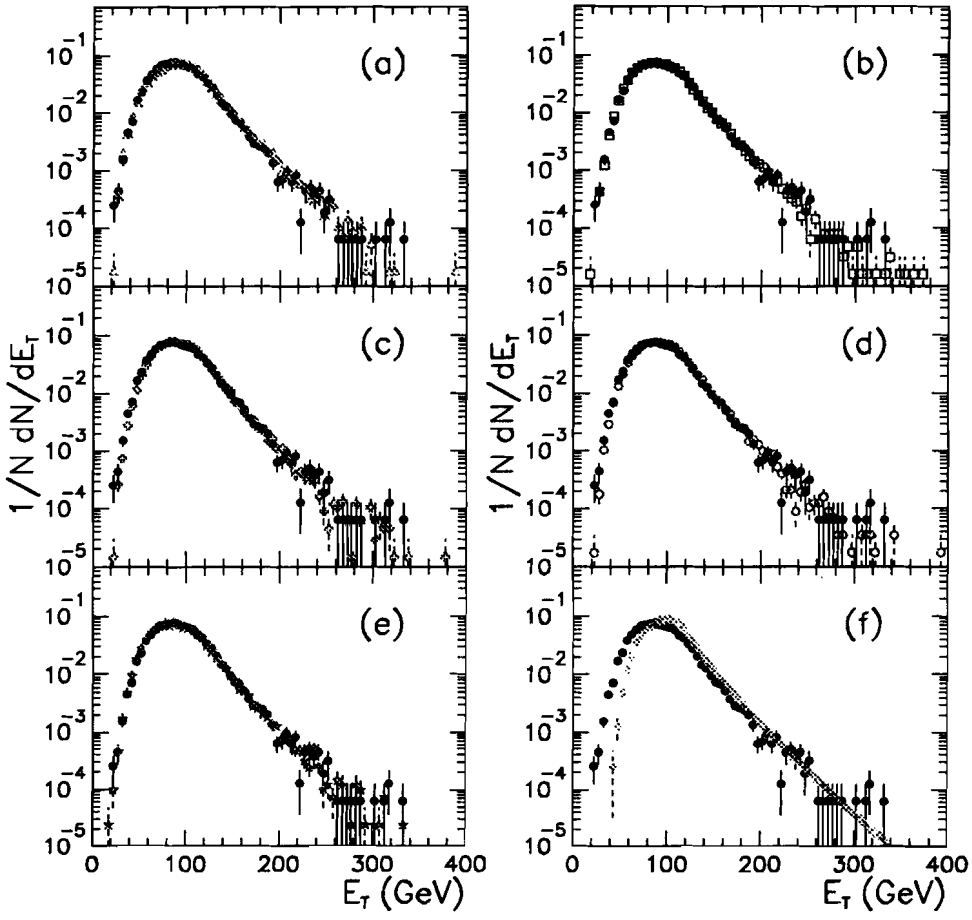

Figure 6.10: Second leading-jet E_T distributions for data (filled circles) and (a) ISAJET, (b) HERWIG, PYTHIA with (c) Angular Ordering off and String Fragmentation, (d) Angular Ordering and String Fragmentation, (e) Angular Ordering and Independent Fragmentation and (f) JETRAD. There is no explicit E_T requirement for Jet 2. The error bars shown represent statistical uncertainties.

tions than the data. The Monte Carlo samples show mostly good agreement with the data η distributions for Jet 2. However, ISAJET has a slightly narrower distribution than the data (Fig. 6.12a) for this jet.

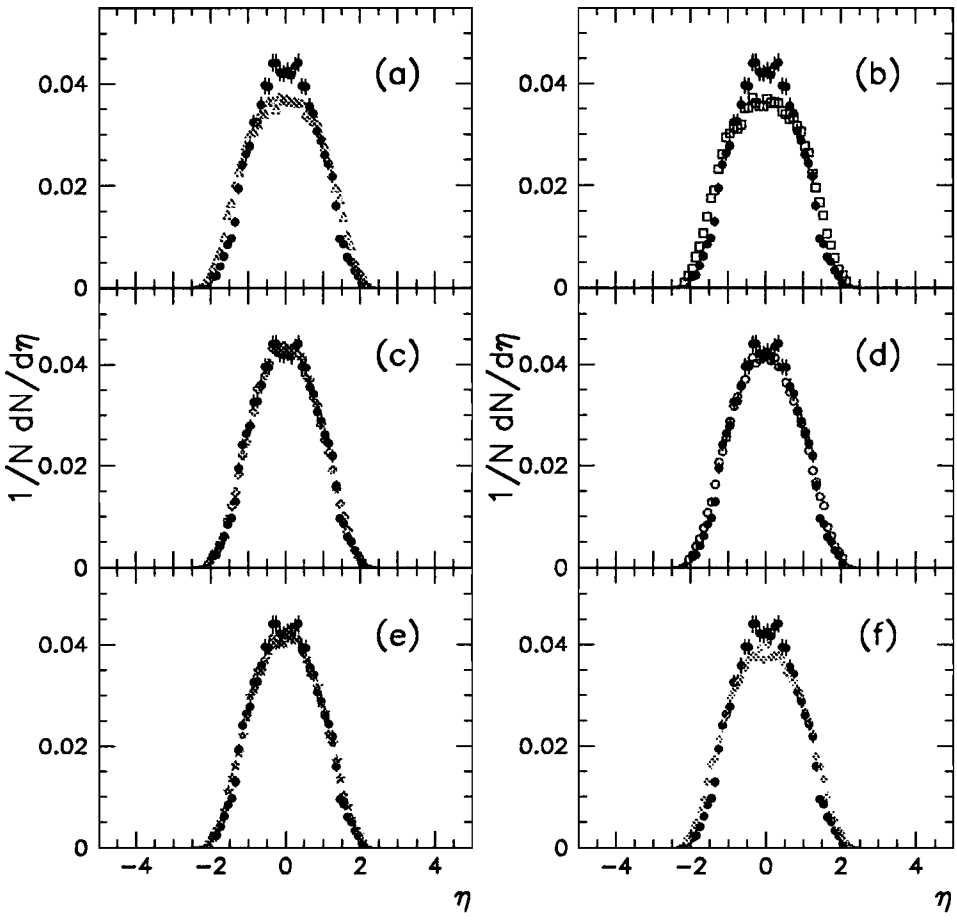

Figure 6.11: Leading-jet η distributions for data (filled circles) and (a) ISAJET, (b) HERWIG, PYTHIA with (c) Angular Ordering off and String Fragmentation, (d) Angular Ordering and String Fragmentation, (e) Angular Ordering and Independent Fragmentation and (f) JETRAD. The error bars shown represent statistical uncertainties.

In direct contrast, the distributions of variables sensitive to interference exhibit some differences between the different Monte Carlos. Figure 6.13 shows the third

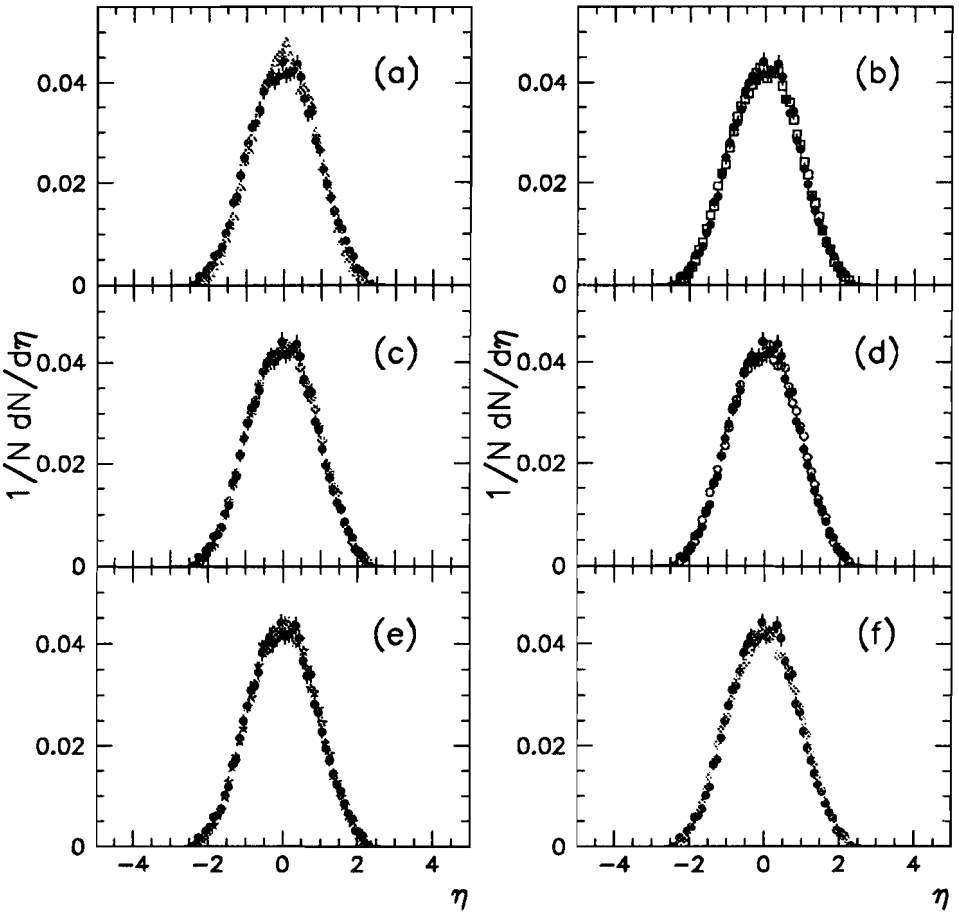

Figure 6.12: Second leading-jet η distributions for data (filled circles) and (a) ISAJET, (b) HERWIG, PYTHIA with (c) Angular Ordering off and String Fragmentation, (d) Angular Ordering and String Fragmentation, (e) Angular Ordering and Independent Fragmentation and (f) JETRAD. The error bars shown represent statistical uncertainties.

jet transverse energy distributions. The two Monte Carlo implementations whose distributions differ most noticeably from the data distribution are those that don't include interference effects — PYTHIA with AO turned off and String Fragmentation (Fig. 6.13c), and ISAJET (Fig. 6.13a). It should also be noted that JETRAD shows some differences with the observed E_T distribution, particularly for very soft jets. This could be a consequence of excluding higher order effects and parton fragmentation, as discussed previously. The remaining samples (which include interference and parton fragmentation), reasonably model the data Jet 3 E_T spectrum.

The pseudorapidity distributions for the third jet are shown in Fig. 6.14. Here slightly narrower distributions result from the simulations that don't include interference effects (ISAJET in Fig. 6.14a and PYTHIA with AO off in Fig. 6.14c) and from those that fragment partons independently (PYTHIA in Fig. 6.14e and ISAJET). It can be seen that the remaining distributions, HERWIG, PYTHIA with AO and String Fragmentation and JETRAD (in Figs. 6.14b, 6.14d and 6.14f, respectively) model the data reasonably well. As expected from kinematics, the tails of both the observed and the simulated η distributions for the third jet extend farther to forward pseudorapidities than do those for the first or second jets.

6.6.2 $\mathcal{R}$ Spectra

The $\mathcal{R}$ distributions (defined in Equation 6.1) for data are presented in Fig. 6.15 and compared to the Monte Carlo samples at the particle and at the parton levels. A salient feature is the difference between the data and the various simulations at low values of $\mathcal{R}$. The Monte Carlo samples contain a greater fraction of jets in close vicinity. For small $\mathcal{R}$, i.e., when jets 2 and 3 are near each other, the differences in

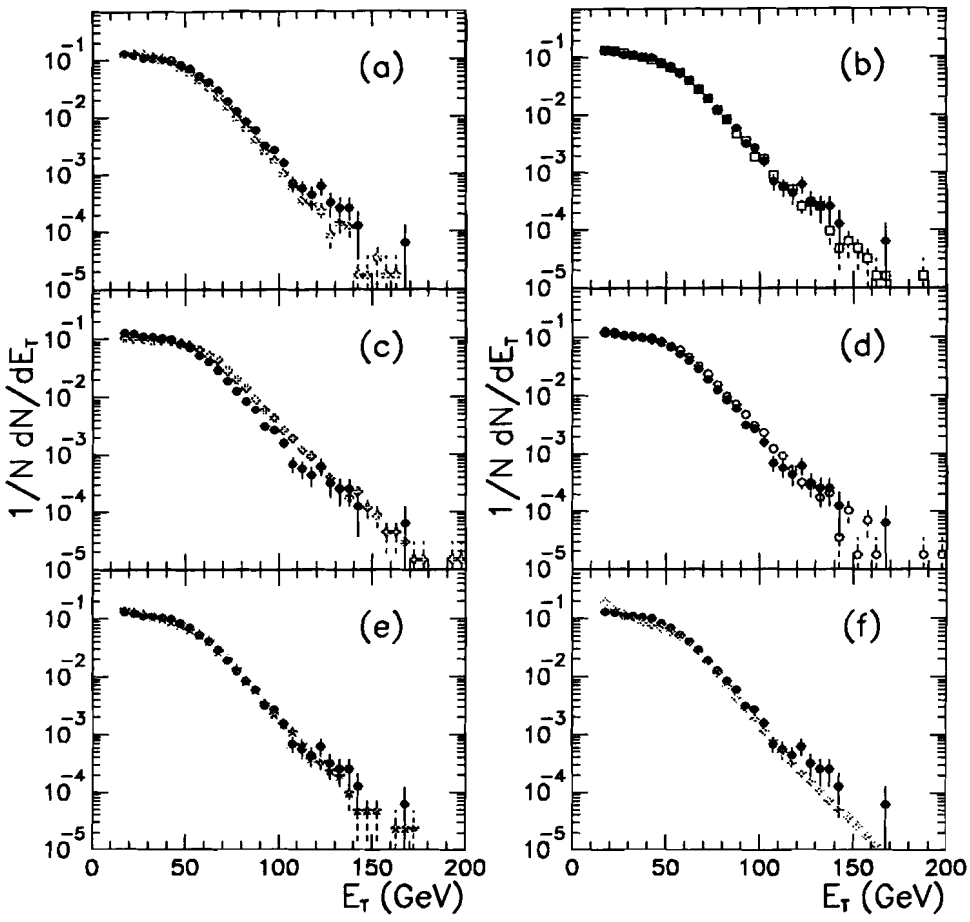

Figure 6.13: Third leading-jet E_T distributions for data (filled circles) and (a) ISAJET, (b) HERWIG, PYTHIA with (c) Angular Ordering off and String Fragmentation, (d) Angular Ordering and String Fragmentation, (e) Angular Ordering and Independent Fragmentation and (f) JETRAD. All distributions are for events with $E_{T3} > 15$ GeV. The error bars shown represent statistical uncertainties.

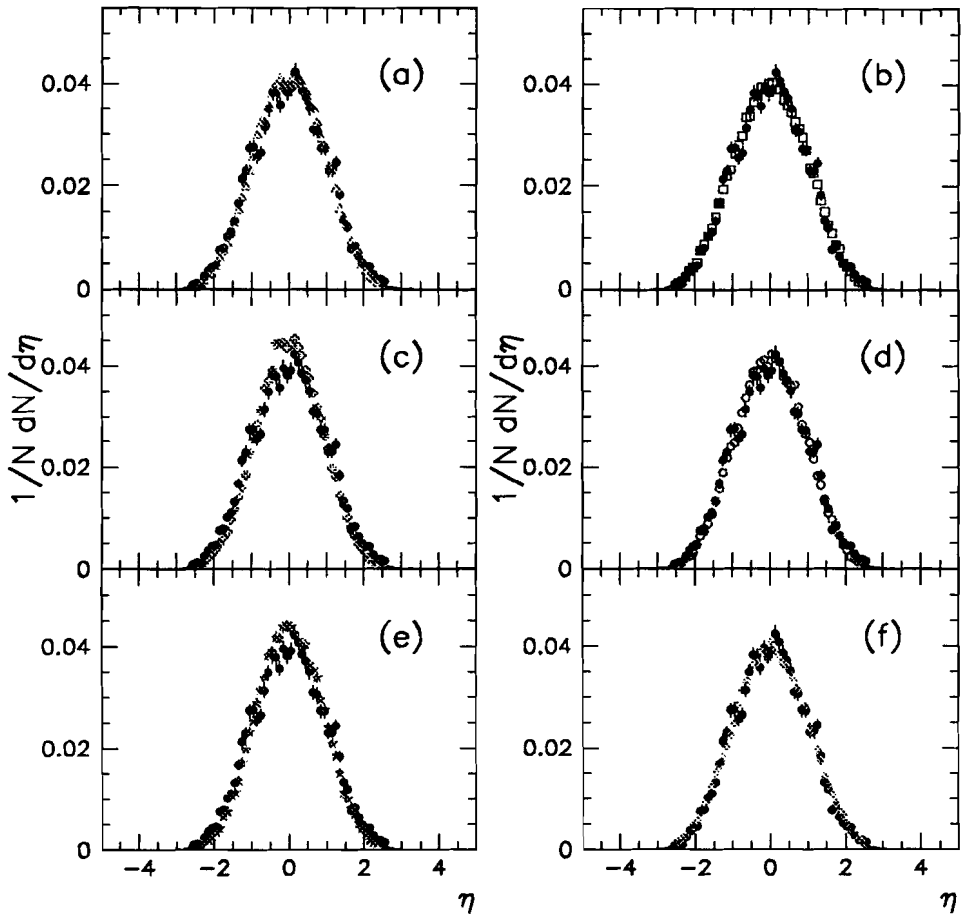

Figure 6.14: Third leading-jet η distributions for data (filled circles) and (a) ISAJET, (b) HERWIG, PYTHIA with (c) Angular Ordering off and String Fragmentation, (d) Angular Ordering and String Fragmentation, (e) Angular Ordering and Independent Fragmentation and (f) JETRAD. The error bars shown represent statistical uncertainties.

the acceptances of parton, particle and calorimeter jets are most prominent. The depletion of observed jets is due to the merging of neighboring jets which is performed as part of the offline jet reconstruction, described in Chapter 4. As can be seen in Fig. 6.15, there are no observed cases when $\mathcal{R} < 0.5$, the jet radius used in the offline reconstruction. Jet merging (or splitting for that matter) was not applied to particle or parton jets, allowing a greater number of them to survive at low $\mathcal{R}$ compared to calorimeter jets, which were banished from this region.

To shed more light on this issue, the difference between $\mathcal{R}$ distributions at the particle level (with which most of the comparisons to data are made) and at the calorimeter level is examined explicitly, using the two HERWIG samples. Figure 6.16 shows their $\mathcal{R}$ distributions. Although the shapes of both distributions are very similar, their behavior at low $\mathcal{R}$ values account for the distributions to be shifted from each other. This difference can be eliminated by cutting the distributions at a value of $\mathcal{R}$ where the acceptances of particle jets and of calorimeter jets are equal and then normalizing each to the total number of events remaining in each sample, as shown in Fig. 6.17.

Similarly, the same procedure can be applied to the observed and simulated $\mathcal{R}$ distributions of Fig. 6.15. The result is Fig. 6.18. Having removed the differences due to the acceptances of parton, particle and calorimeter jets, the sensitivity of the $\mathcal{R}$ spectra to interference and fragmentation effects can now be examined. It is seen that simulations as diverse as ISAJET and JETRAD (Figs. 6.18a and 6.18f) reasonably model the data, while HERWIG (Fig. 6.18b) still differs noticeably. The implementations of interference and, to a lesser extent, the choice of fragmentation, cause a noticeable shape change in the simulated distributions. PYTHIA with AO

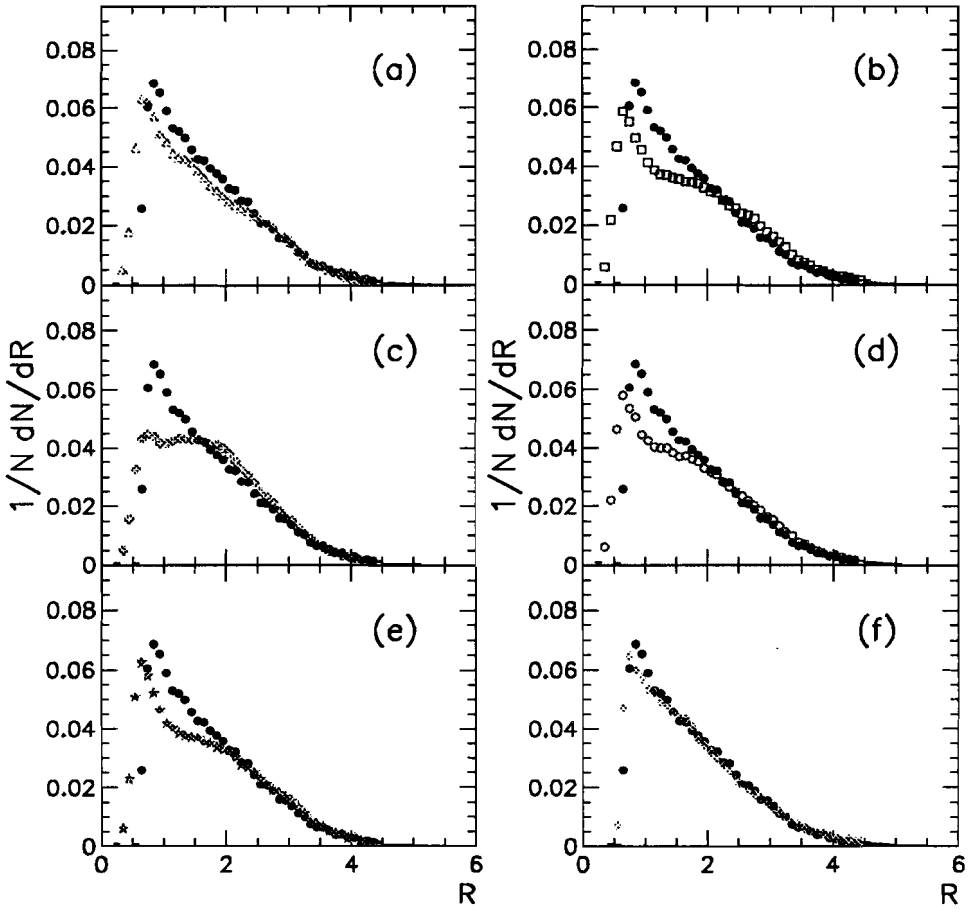

Figure 6.15: $\mathcal{R}$ distributions (uncut) for data (filled circles) and (a) ISAJET, (b) HERWIG, PYTHIA with (c) Angular Ordering off and String Fragmentation, (d) Angular Ordering and String Fragmentation, (e) Angular Ordering and Independent Fragmentation and (f) JETRAD. The error bars shown represent statistical uncertainties.

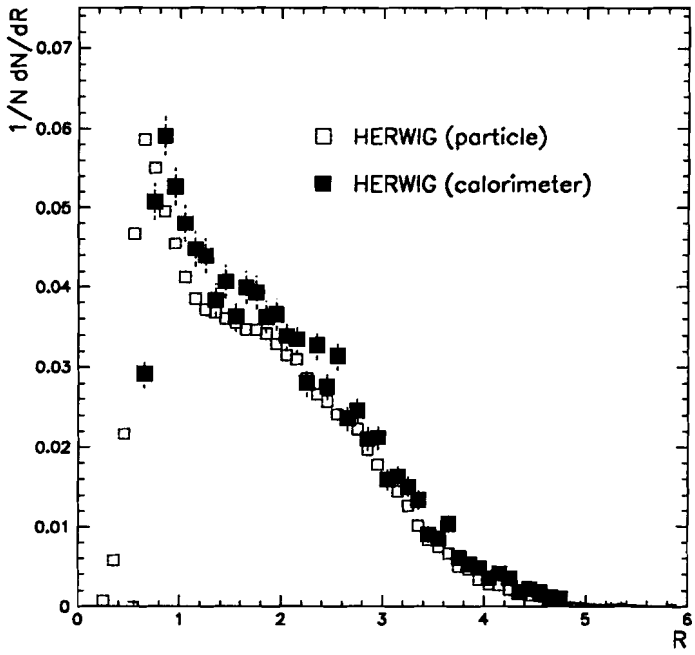

Figure 6.16: $\mathcal{R}$ distributions (uncut) for HERWIG at the particle level and calorimeter level. Both distributions share similar shapes, but they differ in the low $\mathcal{R}$ region. The error bars shown represent statistical uncertainties.

turned on (Figs. 6.18d and 6.18e) generally resembles HERWIG, although some sensitivity to the fragmentation is apparent by comparing Figs. 6.18d and 6.18e. A larger effect, though, is visible when AO is turned off in PYTHIA in Fig. 6.18c. There, a drop at very low values of $\mathcal{R}$ is evidenced, along with a corresponding overall shape change and a plateau out to about $\mathcal{R} = 2.5$. It is notable that turning off AO in PYTHIA leads to a depletion of secondary jets in the immediate vicinity of Jet 2.

The acceptance differences between particle and calorimeter jets in the region $0.6 < \mathcal{R} < 0.8$ will be discussed in the section on systematic uncertainties in this chapter.

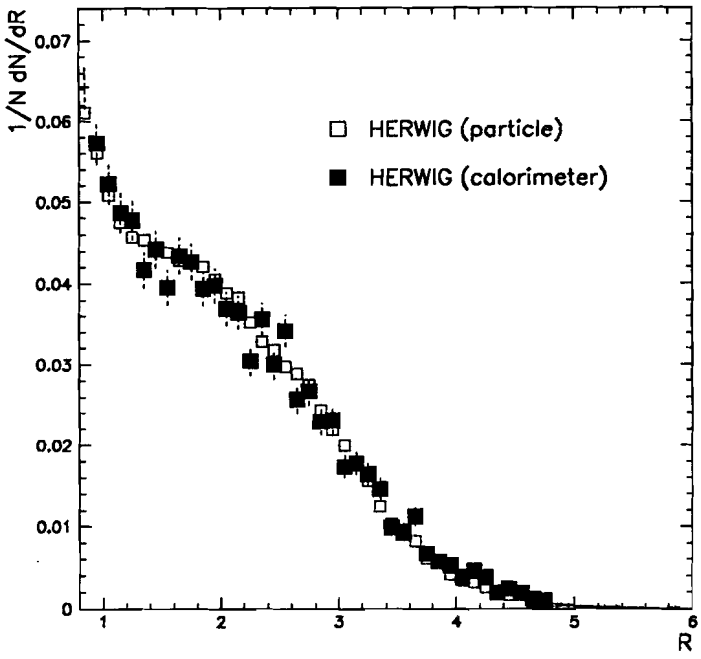

Figure 6.17: $\mathcal{R}$ distributions (cut below $\mathcal{R} = 0.8$) for HERWIG at the particle level and calorimeter level. After eliminating the low $\mathcal{R}$ region, the distributions are now in good agreement. The error bars shown represent statistical uncertainties.

6.6.3 Kinematic Particle-Calorimeter Level Comparisons

In this analysis, a number of Monte Carlo simulations at the particle level (with detector η and energy resolution effects included) are compared with the data. To evaluate the validity of this approach, we examined of the fundamental transverse energy and pseudorapidity distributions of two HERWIG samples identically generated, but differing in their simulation of detector effects. The calorimeter-level sample used the Shower Library parametrization of particle showers (discussed previously) in the GEANT detector simulation [2]. The particle-level sample had parametrizations of detector η and energy resolution effects (detailed in Chapter 5) applied to particle

[2] Without noise effects

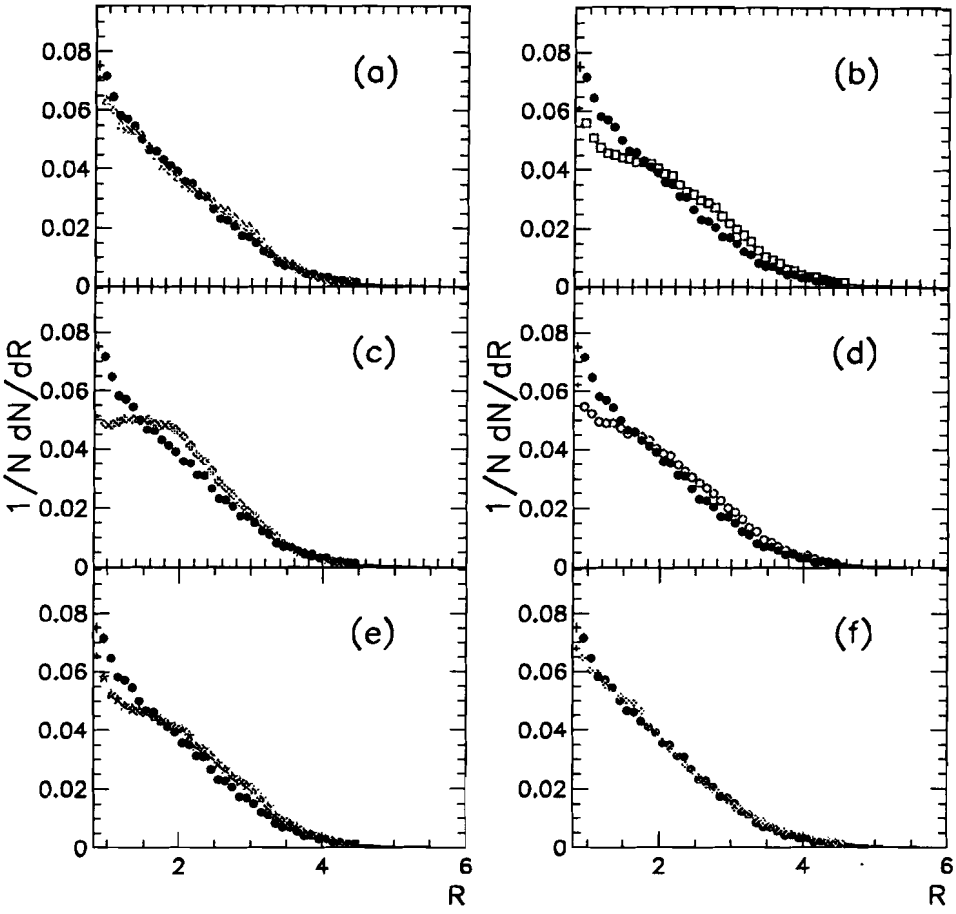

Figure 6.18: $\mathcal{R}$ distributions (cut below $\mathcal{R} = 0.8$) for data (filled circles) and (a) ISAJET, (b) HERWIG, PYTHIA with (c) Angular Ordering off and String Fragmentation, (d) Angular Ordering and String Fragmentation, (e) Angular Ordering and Independent Fragmentation and (f) JETRAD. The error bars shown represent statistical uncertainties.

jets.

The E_T spectra for the three leading-E_T jets in the events are shown in Fig. 6.19. There is good agreement between the particle and the calorimeter levels for Jets 1 and 2. The small decrease in the low end of the calorimeter-level Jet 3 spectrum, relative to the particle level (Fig. 6.19c), might be a result of uncertainties in the energy scale correction for low-E_T jets, or of the lack of calorimeter noise in the GEANTed MC sample. This would cause the rest of the normalized distribution for the calorimeter sample higher than that of the particle sample. The effect of the jet reconstruction efficiency on the data is evaluated in the section dealing with systematic uncertainties.

Due to the reduced statistics in the calorimeter-level sample, a number of high-E_T bins do not contain any calorimeter jets.

The η distributions for the three leading-E_T jets are shown in Fig. 6.20. The small valley in the calorimeter-level distribution for Jet 1 (Fig. 6.20a) is also present in the data and, as previously discussed, may be a consequence of the uncertainties in the jet energy scale. The second and third jet particle and calorimeter-level distributions exhibit reasonable agreement.

After comparing the particle-level and calorimeter-level E_T, η and $\mathcal{R}$ distributions, we conclude that the relevant physical features at the calorimeter-level are similar to the ones at the particle-level. Some differences between them, such as the uncertainty in the jet energy scale and the jet reconstruction efficiency are taken into account as systematic uncertainties. Furthermore, the particle-level and parton-level simulations are shown to reproduce the fundamental aspects of the hard scattering process. This validates their use in a direct comparison with data to study color

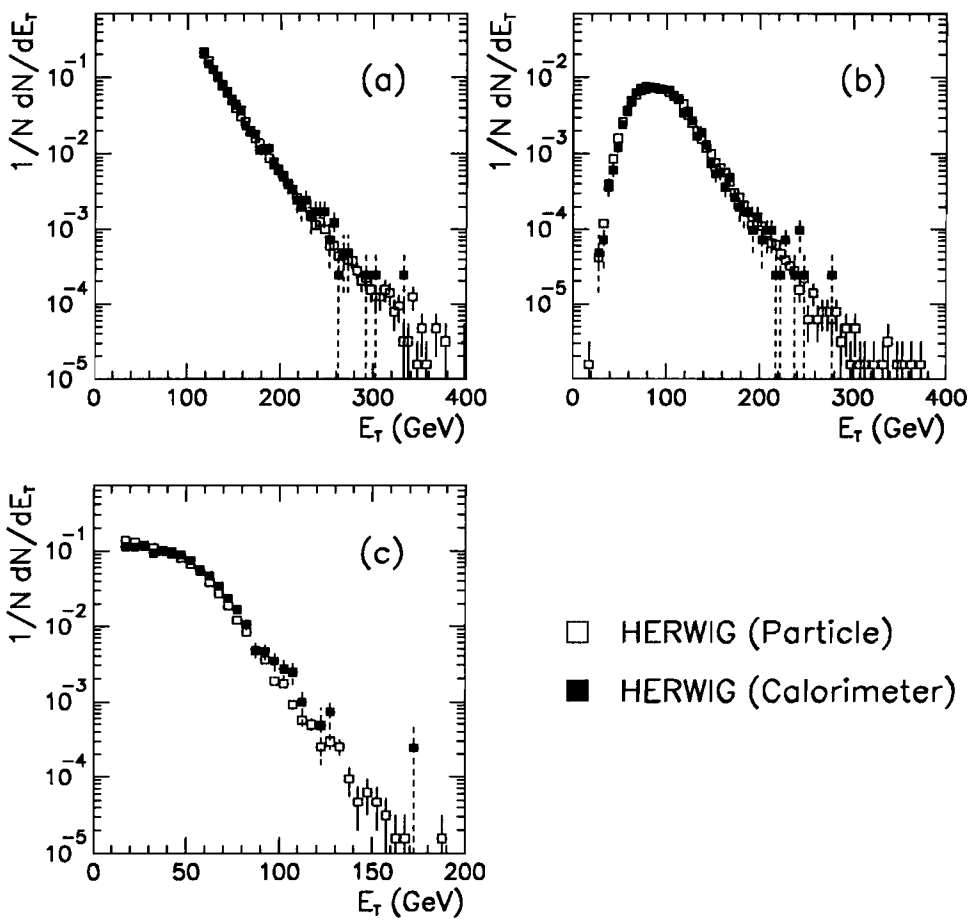

Figure 6.19: Particle and calorimeter level E_T spectra of (a) Jet 1, (b) Jet 2 and (c) Jet 3, simulated with the HERWIG Monte Carlo generator, with $E_{T1} > 115$ GeV and $E_{T3} > 15$ GeV. The error bars shown represent statistical uncertainties.

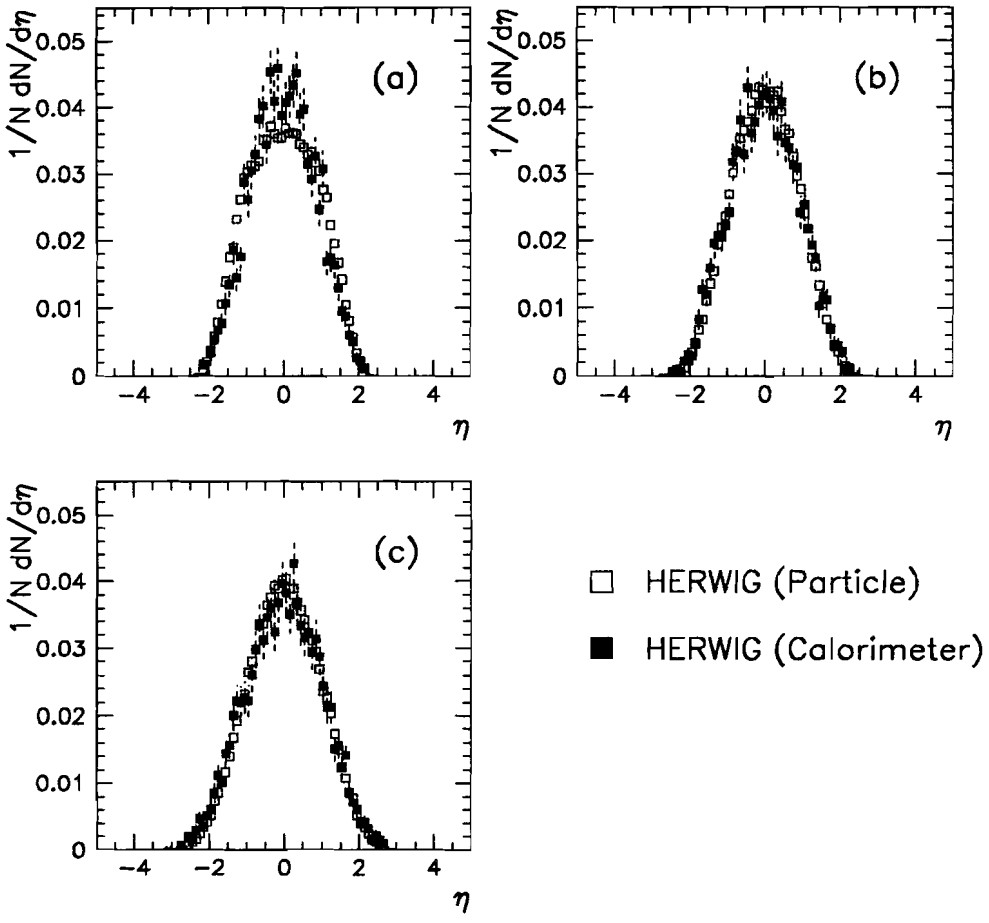

Figure 6.20: Particle and calorimeter level η distributions of (a) Jet 1, (b) Jet 2 and (c) Jet 3, simulated with the HERWIG Monte Carlo generator. The error bars shown represent statistical uncertainties.

coherence.

6.7 Color Coherence Results

In this section, the distributions most sensitive to coherence effects — those of the β variable — are examined. Various Monte Carlo implementations of color coherence are compared to data, first by a direct side-by-side comparison (or, more precisely, an overlay) and then by taking ratios with the data. The error bars shown include statistical and uncorrelated systematic uncertainties added in quadrature. As before, all individual distributions are normalized to the total number of events in the sample, as we are concerned with the shapes of the β patterns and not with their absolute levels. Finally, the examination of color coherence effects will be carried out in two distinct pseudorapidity regions: in the central region ($|\eta| < 0.7$), and in the forward region ($0.7 < |\eta| < 1.5$).

6.7.1 Data and Theory β Distributions

The first three DATA-Monte Carlo central region comparisons of the β patterns are shown in Fig. 6.21. These are done with ISAJET, HERWIG and JETRAD. The latter two simulations agree with the data, while ISAJET (in Fig. 6.21a) exhibits some marked differences. Notice that the observed distribution peaks around $\beta = \pi$ (towards the far beam), while ISAJET has a local minimum there instead and peaks near the plane perpendicular to the plane of the event — the so-called *transverse plane* — located along $\beta = \frac{\pi}{2}, \frac{3\pi}{2}$. As discussed in the Results section, this behavior of ISAJET is purely kinematical and due to the fact that for $|\eta_2| < 0.7$, the most central region, on the average, is near the transverse plane. HERWIG and JETRAD,

on the other hand, resemble the data more closely than ISAJET and show no evidence of transverse peaking. It is worth noting that in the direction of the near beam ($\beta = 0, 2\pi$), ISAJET has the least amount of radiation while HERWIG and JETRAD closely match the data.

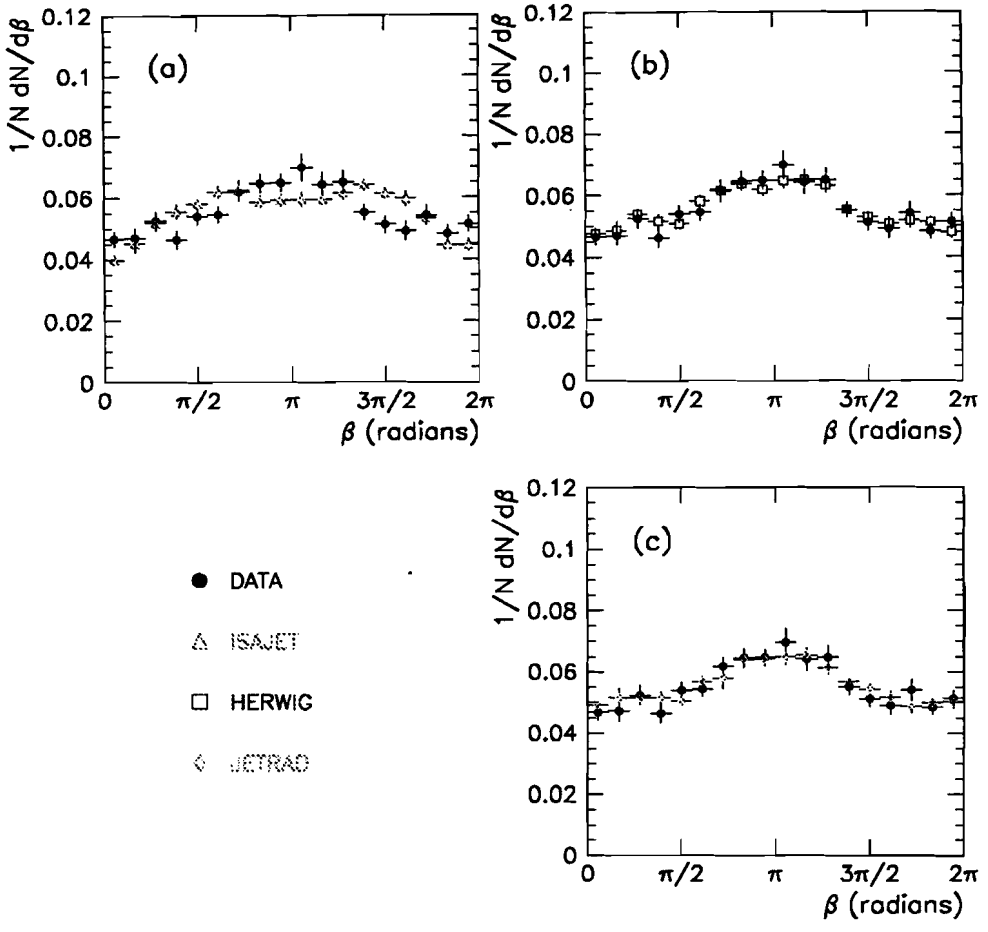

Figure 6.21: β distributions of data (filled circles) and (a) ISAJET, (b) HERWIG and (c) JETRAD for $|\eta_2| < 0.7$. The error bars shown include statistical and uncorrelated systematic uncertainties.

One may also examine the effect of turning off the contributions to color coherence from angular ordering in PYTHIA as well as the effect of the choice of fragmentation by comparing the implementations of these models to the data in the same fash-

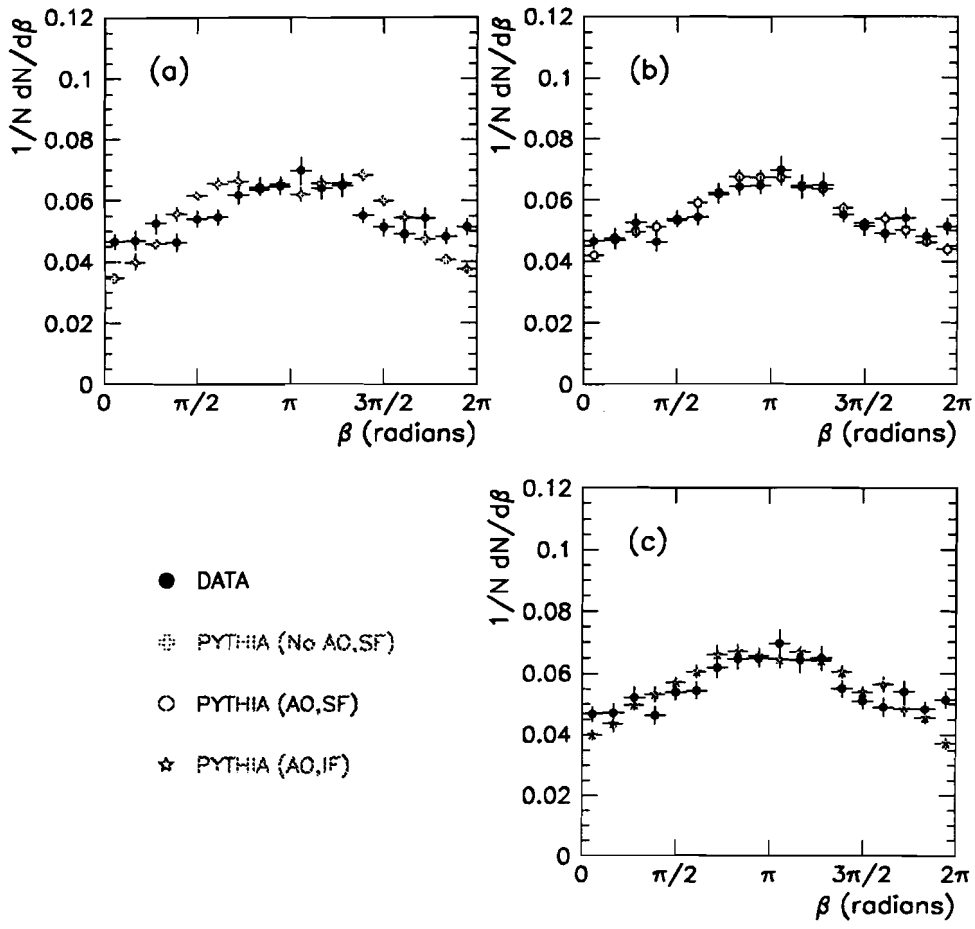

Figure 6.22: β distributions of data (filled circles) and of PYTHIA with (a) AO turned off and String Fragmentation, (b) AO and String Fragmentation and (c) AO and Independent Fragmentation for $|\eta_2| < 0.7$. The error bars shown include statistical and uncorrelated systematic uncertainties.

ion. In Fig. 6.22, the corresponding comparisons of DATA-PYTHIA are presented. With AO turned off (Fig. 6.22a), PYTHIA behaves qualitatively much like ISAJET, exhibiting an excess of radiation in the transverse plane, and a deficit, relative to the data, in the event plane. When AO is turned on with String Fragmentation (Fig. 6.22b), PYTHIA more closely models the data distributions, although, in the near beam region, it produces less radiation than the data. However, the amount of radiation is notably greater than when AO is turned off. The final DATA-PYTHIA comparison is done with AO turned on and Independent Fragmentation. The result is a simulated distribution (Fig. 6.22c) that appears to be a hybrid of the previous PYTHIA patterns. This distribution has a depletion in the far beam region, weak transverse peaking and under-estimates the amount of near-beam radiation, though not as severely as when AO is turned off.

In the forward region, Fig. 6.23 compares ISAJET, HERWIG and JETRAD to the data. ISAJET (Fig. 6.23a) shows a depletion in the far and near beam regions, and a smaller excess near the transverse plane than in the central region, demonstrating once more its kinematical behavior. HERWIG, on the other hand models the data pattern well as does JETRAD (Figs. 6.23a and 6.23b), although the parton-level simulation slightly overstates the radiation in the near beam region.

Figure 6.24 shows the three DATA-PYTHIA comparisons in the forward region. Here, as before, differences are apparent between the various implementations. When AO is turned off PYTHIA shows an excess of radiation in the far-beam region which nearly extends out to the transverse plane (Fig. 6.24a), while at the same time greatly under-estimating the amount of radiation in the near-beam region. With AO turned on and String Fragmentation (Fig. 6.24b), PYTHIA resembles the data in all but the

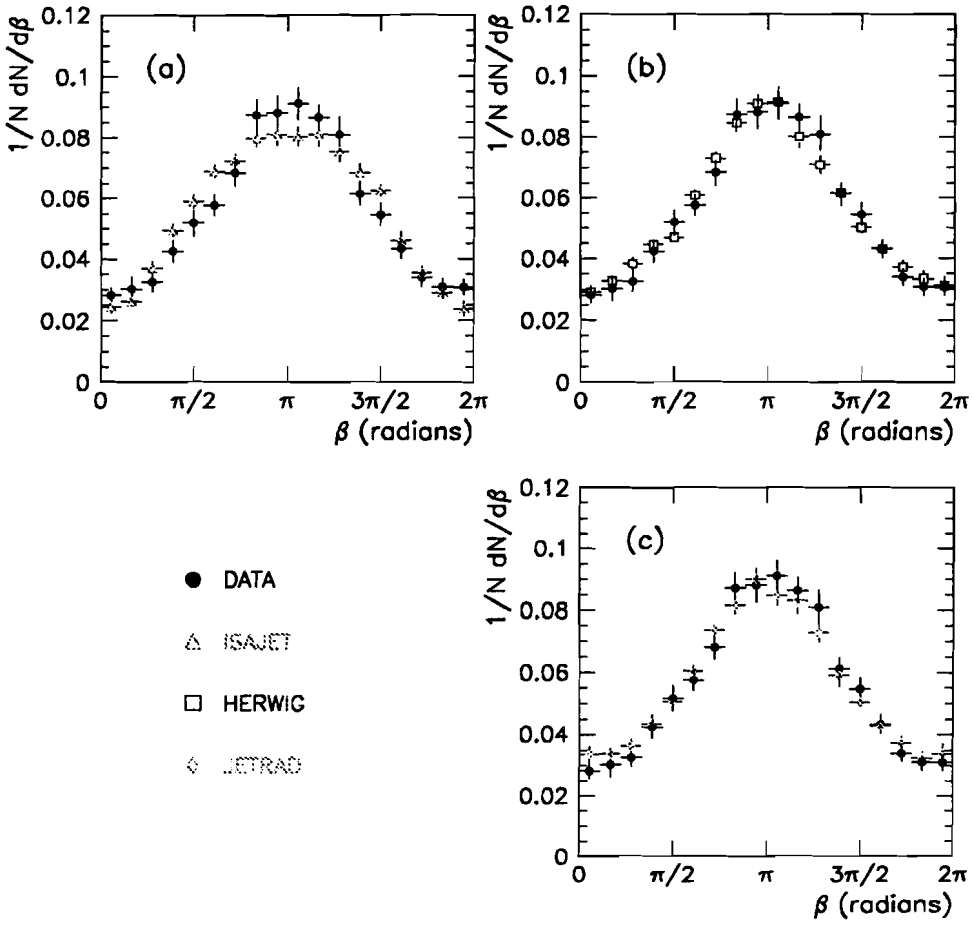

Figure 6.23: β distributions of data (filled circles) and (a) ISAJET, (b) HERWIG and (c) JETRAD for $0.7 < |\eta_2| < 1.5$. The error bars shown include statistical and uncorrelated systematic uncertainties.

with AO turned off, although the excess of radiation in the transverse plane and the deficit in the event plane (particularly in the far beam direction), relative to the data, are considerably smaller.

In the forward region, Figs. 6.26a and 6.26b show the comparison of ISAJET and HERWIG with the data. We notice a similarly shaped interference pattern as that seen in the central region is also visible here in the $\frac{DATA}{ISAJET}$ ratio, indicating that ISAJET does not account well for the radiation pattern observed in the data. HERWIG on the other hand, agrees better with the data as is evidenced by the flatter $\frac{DATA}{HERWIG}$ ratio.

The forward PYTHIA to data comparisons are shown in Figs. 6.26c – e. Here a significant difference between the two implementations of AO is apparent. PYTHIA with AO turned off exhibits a large deficit of radiation in the near beam side, relative to the data, and a much smaller excess on the far beam side. A similar qualitative behavior can be observed when PYTHIA uses Independent Fragmentation, although the disagreement with the data is less severe than in the case when AO is turned off.

When AO effects are turned on and String Fragmentation is used, the near beam deficit is greatly reduced and the far beam excess is nearly eliminated. Nevertheless, some residual differences still remain even with color coherence effects on and this may indicate that PYTHIA could be better tuned for $p\bar{p}$ collisions.

The comparison between data and the parton-level MC JETRAD is presented in Figs. 6.25f and 6.26f for the central and forward regions respectively. It can be seen that JETRAD agrees qualitatively with the data. This is rather remarkable given that JETRAD does not include higher order fragmentation effects and is only a LO calculation to the 3-jet process.

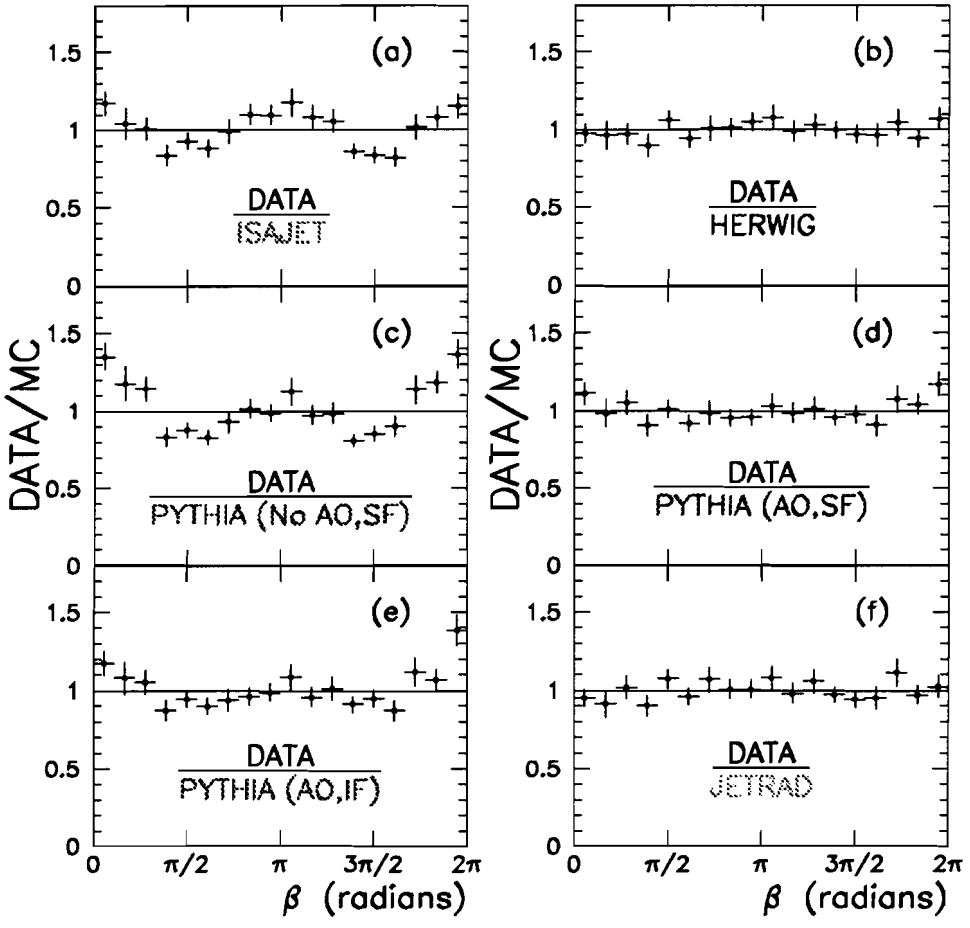

Figure 6.25: β ratios of data and (a) ISAJET, (b) HERWIG, PYTHIA with (c) Angular Ordering off and String Fragmentation, (d) Angular Ordering and String Fragmentation, (e) Angular Ordering and Independent Fragmentation and (f) JETRAD in the central region ($|\eta_2| < 0.7$). The error bars shown include statistical and uncorrelated systematic uncertainties.

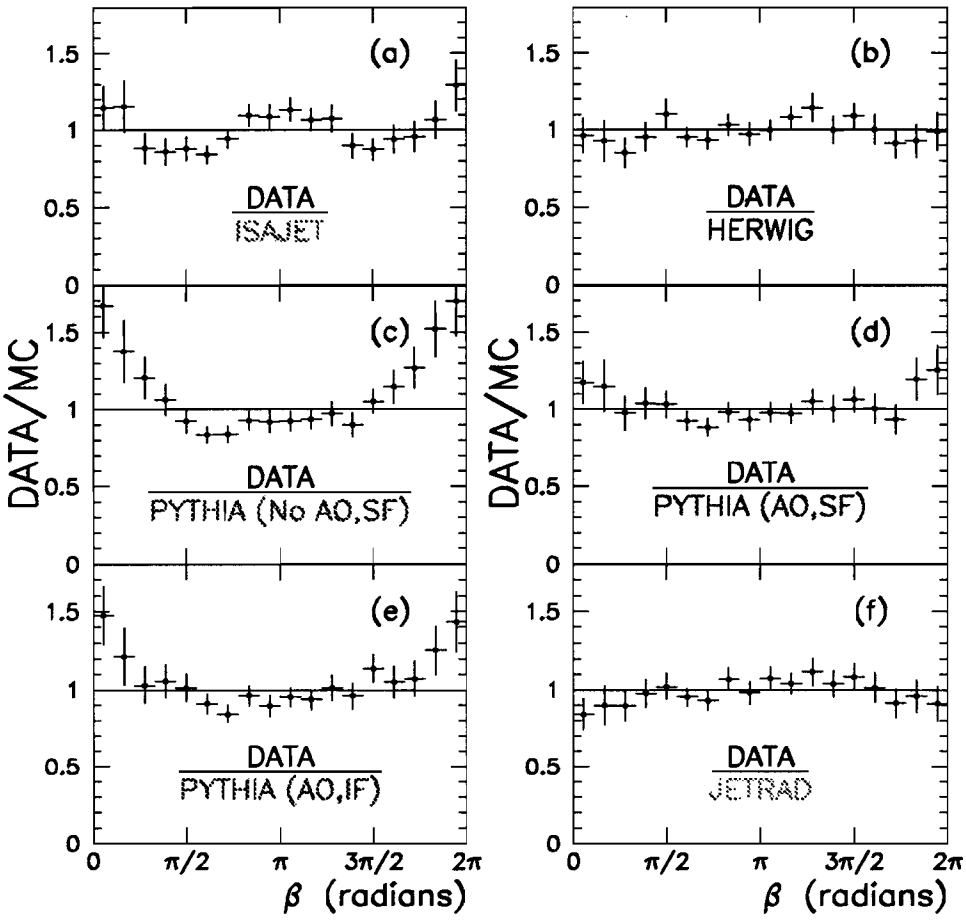

Figure 6.26: β ratios of data and (a) ISAJET, (b) HERWIG, PYTHIA with (c) Angular Ordering off and String Fragmentation, (d) Angular Ordering and String Fragmentation, (e) Angular Ordering and Independent Fragmentation and (f) JETRAD in the forward region ($0.7 < |\eta_2| < 1.5$). The error bars shown include statistical and uncorrelated systematic uncertainties.

By fitting the various $\frac{DATA}{MONTE\ CARLO}$ ratios of the β distributions to a line at 1, taking into account statistical and uncorrelated systematic uncertainties, a quantitative measure of the interference effects is obtained. A summary of these results is presented in Table 6.4, where the reduced χ^2, the total χ^2 value divided by the number of degrees of freedom (ndf), are given.

Monte Carlo Sample	$\lvert\eta_2\rvert < 0.7$	$0.7 < \lvert\eta_2\rvert < 1.5$
HERWIG	0.53	0.68
ISAJET	3.43	1.87
PYTHIA:		
AO, SF	0.91	0.84
No AO, SF	5.78	3.70
AO, IF	2.34	1.82
JETRAD	0.65	0.72

Table 6.4: Reduced χ^2 values (χ^2/ndf) of 18 degrees of freedom of fits to a line at 1 for the various $\frac{DATA}{MONTE\ CARLO}$ ratios of β distributions. Statistical and uncorrelated systematic uncertainties were taken into account.

A clear difference due to fragmentation can be observed, confirming that String Fragmentation is indeed contributing to the color coherence effects in the MC simulation. However, based on the $\frac{DATA}{PYTHIA}$ ratios, we can conclude that the contribution of AO to color coherence effects in the current implementation of PYTHIA is greater than that of the fragmentation scheme used, in both central and forward pseudorapidity regions, as demonstrated numerically in Table 6.4.

Hadronization Effects

An examination of the effect of hadronization on the β ratios was carried out by comparing the data to two otherwise identical HERWIG samples: one generated at

the parton level (before hadronization) and the other at the particle (hadron) level. Figure 6.27 shows the result of this comparison. The overall effect of hadronization can be seen to be quite small, as the ratios of data with the parton level are very similar to those with the particle level in both central and forward regions. Correspondingly, the χ^2 are very similar in both cases.

η Dependence of Color Coherence

It is interesting to examine whether a dependence of coherent radiation on the proximity between partons can be observed. Gluon emission from a dipolar color string is expected to become more intense as the separation between color-connected partons decreases. However, the relative contribution of the various partonic subprocesses that give different color patterns also changes versus η and therefore the net effect expected is not clear.

An examination of this dependence can be carried out by comparing the β patterns of data and ISAJET in the central and forward regions. By dividing the ratios $\frac{DATA}{ISAJET}$ for two distinct η regions with each other, we can examine the relative variation of color coherence radiation as a function of η, devoid of any kinematic effects. This result is presented in Fig. 6.28, together with a linear fit. In order to reduce the statistical uncertainty, the β distributions were folded in half along the ϕ symmetry axis of the annular search disk. Given the current statistical and systematic uncertainties (to be discussed in the next section), no obvious effect is seen, as the pattern is not inconsistent with a line at 1.

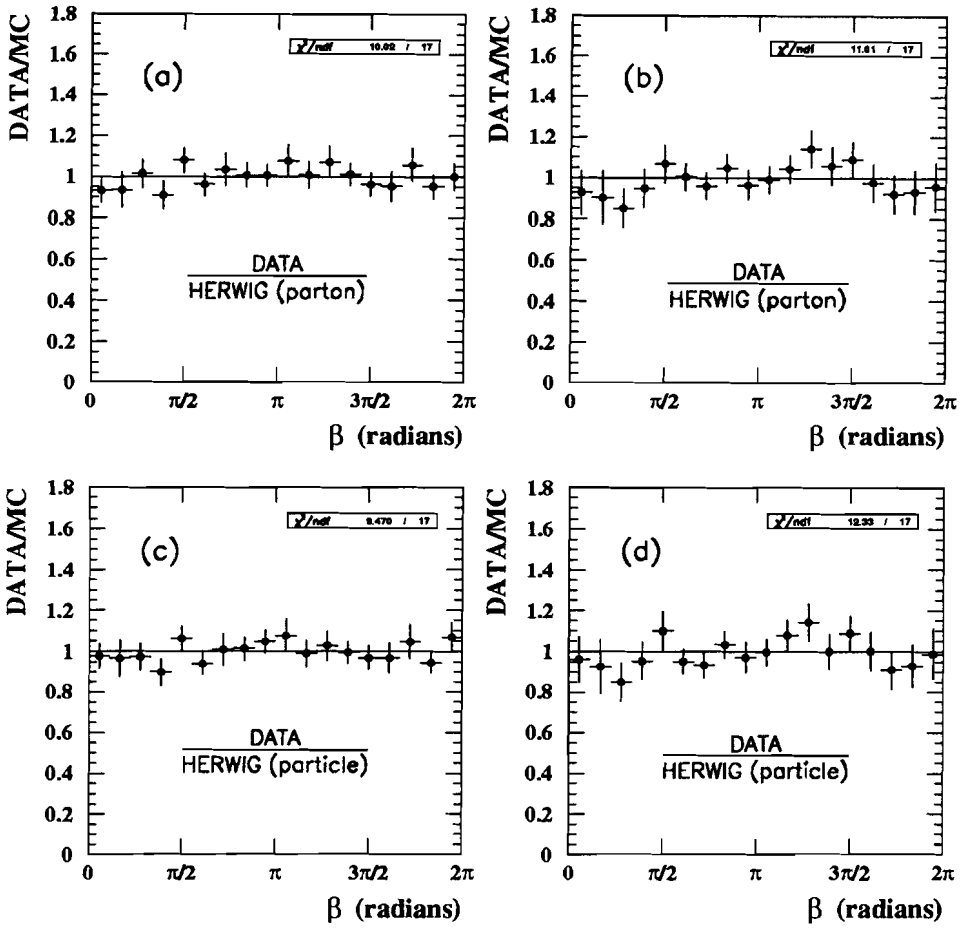

Figure 6.27: Comparison of data and HERWIG with and without hadronization for (a) and (c) central ($|\eta_2| < 0.7$) and (b) and (d) forward ($0.7 < |\eta_2| < 1.5$) regions. The error bars shown include statistical and uncorrelated systematic uncertainties.

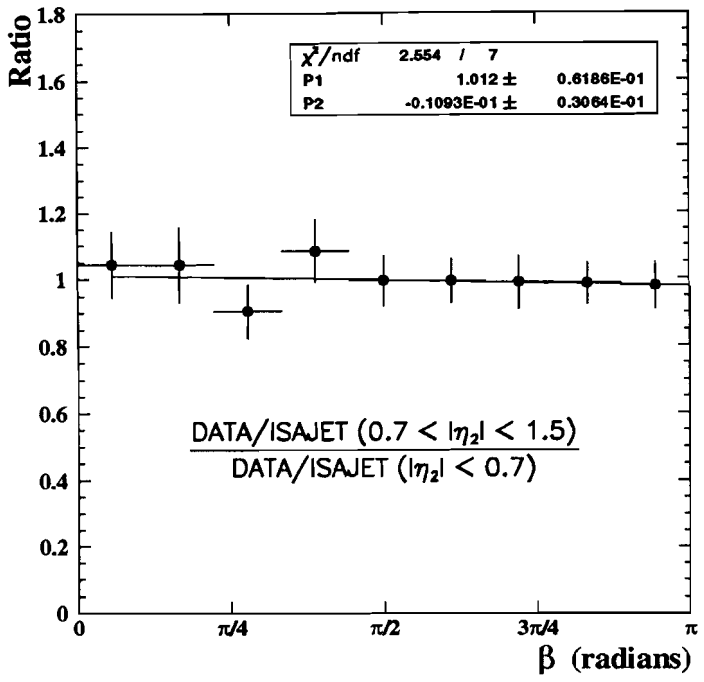

Figure 6.28: Ratio of forward region and central region $\frac{DATA}{ISAJET}$ folded β ratios fit to a line. The error bars shown include statistical and uncorrelated systematic uncertainties.

6.8 Systematic Uncertainties

Results which include statistical and systematic errors have been presented in this chapter. In this section, the sources of systematic uncertainty are investigated and their contribution to the overall error is calculated. Experimental sources of systematic uncertainty examined in this analysis are: the jet energy scale, jet η bias, multiple interactions, jet reconstruction, z vertex dependence and jet quality cuts. Theoretical sources of systematic uncertainty considered are: renormalization/factorization scale and the choice of parton distribution functions. There is an additional source of uncertainty which was evaluated — the calorimeter energy resolution applied to the Monte Carlo simulations at the particle and parton levels. Some of the poten-

tial sources of uncertainty cause no appreciable systematic effects, or their effect is negligible compared to the statistical uncertainty. Therefore, these sources are not included in the cumulative errors.

6.8.1 Summary of Uncertainties and Method Used

Detailed studies of possible sources of systematic uncertainty have been performed. The results are summarized in Table 6.5 for the data and in Table 6.6 for the Monte Carlo simulations, in both η regions for which results were presented. The values tabulated for each error were obtained by taking the RMS (Root-Mean-Square) of the individual bin variations as given in the equation:

$$\text{RMS variation} = \sqrt{\frac{1}{N}\sum_{i=1}^{N}\left(\frac{\mathcal{F}_i'}{\mathcal{F}_i}-1\right)^2}, \tag{6.7}$$

$$\text{where} \quad \mathcal{F}_i = \frac{S_i}{\sum_{i=1}^{N} S_i} \quad \text{and} \quad \mathcal{F}_i' = \frac{S_i'}{\sum_{i=1}^{N} S_i'}.$$

S_i and S_i' represent the number of entries in the i^{th} bin of the reference sample and the sample modified by a given systematic uncertainty, respectively. N, in turn, is the total number of bins into which each sample has been divided. Note that this way of estimating the uncertainties is quite conservative. It utilizes the variation in a given bin without subtracting the statistical contribution to this variation. Also, it does not include the mitigating effect of bin-to-bin correlations, nor of any other correlations among the samples that would decrease the estimated effect.

As shown in Table 6.5, the most significant systematic uncertainty included in the data is the jet energy scale followed closely by the parametrized η dependence [113] of the jet energy scale correction. For the Monte Carlos, the largest systematic effect

Possible Sources of Uncertainty	$\lvert\eta_2\rvert < 0.7$	$0.7 < \lvert\eta_2\rvert < 1.5$
Jet Energy Scale [110]	2.3 (%)	2.9 (%)
η Dependence of Jet E Scale (MPF)	1.8	3.2
Jet Out-of-Cone Showering	1.4	2.2
Jet η Bias [107]	1.3	1.8
(Statistical Uncertainty)	(4.5)	(6.1)
(Statistical $\oplus$ Systematic Uncertainty)	(5.6)	(7.9)
Multiple Interactions	3.4	3.5
Jet Reconstruction [111]	1.4	3.0
Near Beam	[+2.0]	[+4.5]
Far Beam	[-1.0]	[-2.0]
Z vertex	1.0	1.2
Jet quality cuts [112]	1.4	2.4

Table 6.5: Compilation of possible sources of systematic uncertainty in the data β distributions for central and forward η regions. The data uncertainty includes the statistical, jet energy scale, η dependence of jet E scale, jet out-of-cone showering and jet η bias uncertainties. The other uncertainties are listed for comparison.

not seriously limited by the statistics in the samples is the calorimeter resolution, followed by the choice of renormalization/factorization scale and parton distribution functions.

For purposes of comparison, the statistical uncertainties in data and MC are also listed in the appropriate summary tables. The statistical uncertainty in the data dominates all other potential sources of uncertainty. All point-to-point uncorrelated systematic uncertainties in the data (jet energy scale, η dependence of the jet E scale, jet out-of-cone showering and jet η bias) were added in quadrature with the statistical uncertainties and were included in the observed β distributions and in the calculation of the χ^2 values from the $\frac{DATA}{MONTE\ CARLO}$ β ratios. For the Monte Carlos, the statistical uncertainty (approximately half of that in the data) is comparable to the systematic uncertainties. The systematic uncertainty due to jet energy resolution

Possible Sources of Uncertainty	$\|\eta_2\| < 0.7$	$0.7 < \|\eta_2\| < 1.5$
Calorimeter resolution		
JETRAD	3.0 (%)	3.6 (%)
PYTHIA	1.8	3.4
(Statistical Uncertainty)	(2.4)	(3.1)
(Statistical $\oplus$ Systematic Uncertainty)	(4.0)	(5.4)
Renormalization/Factorization scale (JETRAD)	2.5	3.1
Parton Distribution Functions (JETRAD)	2.1	2.9

Table 6.6: Compilation of possible sources of systematic uncertainty in Monte Carlo β distributions for central and forward η regions. The MC uncertainty includes statistical and both calorimeter resolution uncertainties. The other uncertainties are listed for comparison.

of JETRAD and PYTHIA was added in quadrature, point-by-point, to the statistical uncertainties of the Monte Carlo predictions.

In the following sections, the derivation of the individual systematic uncertainties is described and their variation is plotted.

6.8.2 Jet Energy Scale

The RMS variation of the β distribution due to the jet energy scale was obtained from applying the CAFIX v5.0 correction one standard deviation above and below the nominal value. The mean of the absolute variations from each was then used in Equation 6.7. The uncertainty thus obtained — 2.3% and 2.9%, respectively, in the central and forward regions — was included in the overall error. Figure 6.29 illustrates this variation by comparing both the high and the low energy scale corrections to the nominal correction for both the central and the forward regions, by means of a fractional difference from the "nominal" data sample, which is the data

sample used in the analysis. The χ^2 values [3] are not relevant here due to the strong error correlation between the samples used. It may be observed that the points for both η regions are consistent with a line at 0, and therefore, that the shape of the β distribution did not change as a consequence of the jet energy scale.

6.8.3 η Dependence of Jet Energy Scale

To evaluate the effect of the jet energy scale η dependence on the results, we used a parametrization [113] calculated from photon+jet data by means of the MPF (Missing-E_T Projection Fraction) method described in Chapter 5. The parametrization is shown in Fig. 6.30. It was applied as a correction to the E_T of every jet located in the band $|\eta| < 3.0$. For those jets with higher pseudorapidities, the jet energy scale's variation with η was assumed to stabilize and the correction for $|\eta| = 3.0$ was used. The values obtained for this uncertainty, 1.8% (central) and 3.2% (forward), were included in the overall error.

The relative variation on the data β distribution as a result of the correction for the η dependence of the jet energy scale is shown in Fig. 6.31. From that figure, it is clear that the shape of the distribution is unchanged by the correction. The χ^2 values are not relevant here either due to the strong error correlation between the samples used. The results for both η regions are consistent with a line at 0.

6.8.4 Jet Out-of-Cone Showering

In order to examine the contribution of the jet out-of-cone showering correction applied as part of the overall jet energy scale to the data, two samples are compared:

[3] In the this section, the number of degrees of freedom (17) displayed in the plots by the plotting software is incorrect. The correct number of degrees of freedom for these plots is 18.

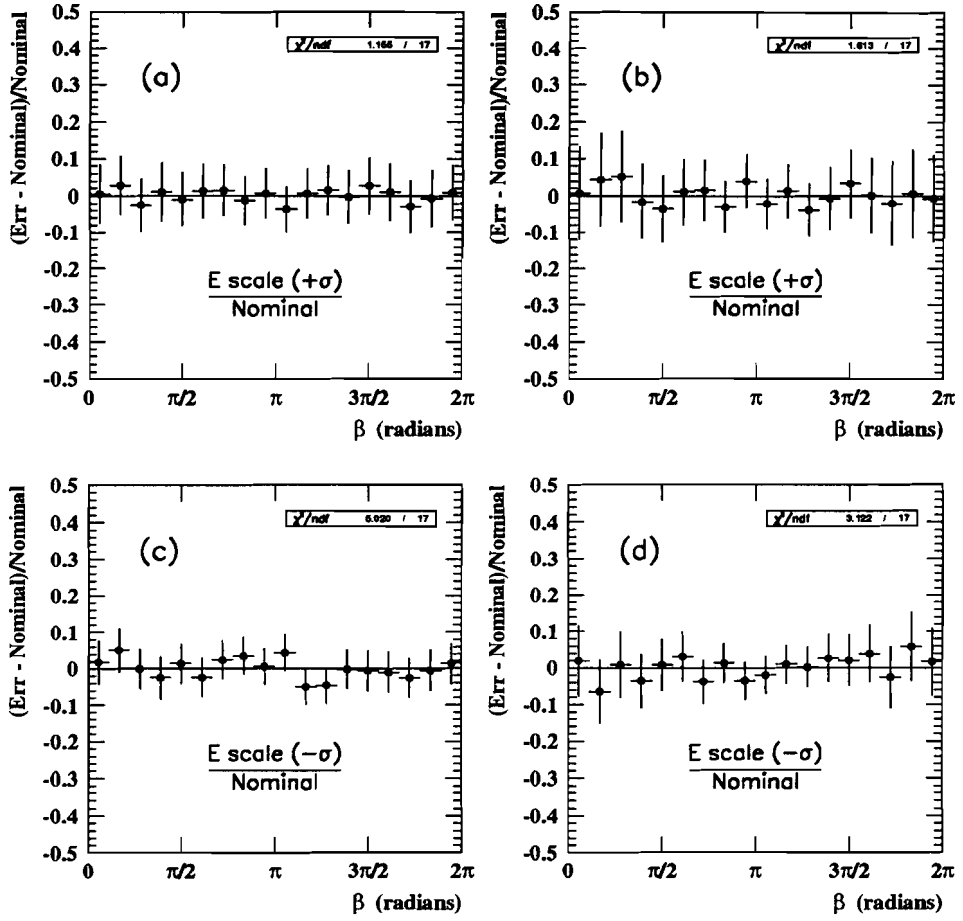

Figure 6.29: Variation in the data β distributions due to the jet energy scale correction for (a) and (c) central ($|\eta_2| < 0.7$) and (b) and (d) forward ($0.7 < |\eta_2| < 1.5$) regions. Corrections of one standard deviation above ($+\sigma$) and below ($-\sigma$) the nominal correction were applied and are indicated in the figure. The error bars shown represent correlated statistical uncertainties.

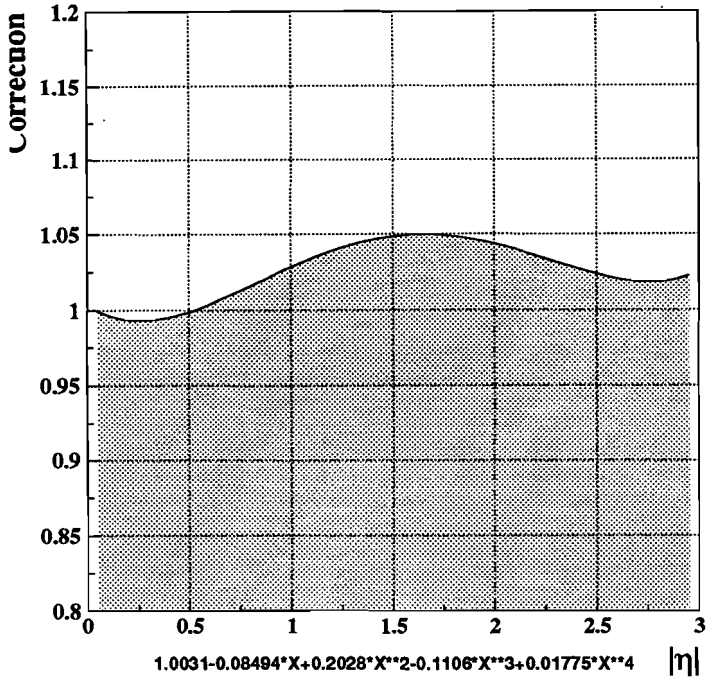

Figure 6.30: Parametrization of the jet energy scale η dependence for $|\eta| < 3.0$ from MPF data. For higher $|\eta|$, the correction for $|\eta| = 3.0$ was used. In the equation above, $X \equiv |\eta|$.

data with the standard CAFIX v5.0 corrections (including out-of-cone showering) and data with the standard corrections minus that for out-of-cone showering. The results of this comparison are shown in Fig. 6.32. Once more, the χ^2 values are not relevant here due to the strong error correlation between the samples used. Both the central and forward region plots can be appropriately represented by a line at 0, as there is no noticeable shape change in the distribution. The calculated uncertainty, 1.4% (central) and 2.2% (forward), was included in the overall error.

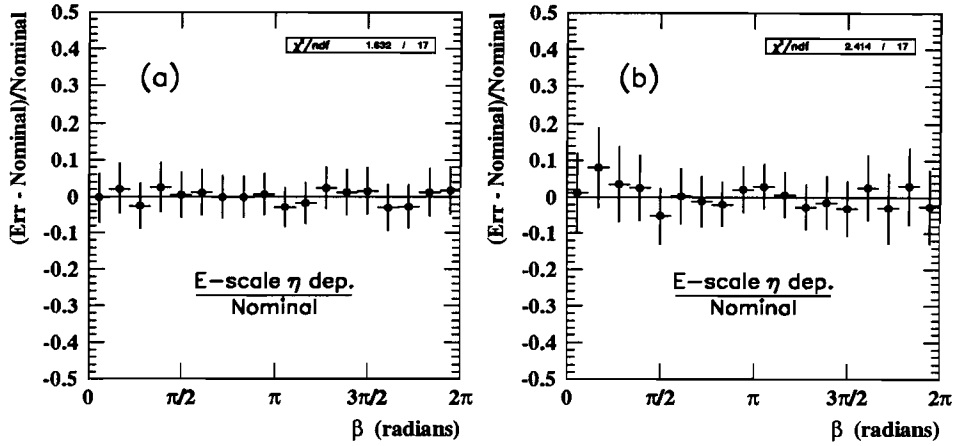

Figure 6.31: Variation in the data β distributions due to the η dependence of the jet energy scale for (a) central ($|\eta_2| < 0.7$) and (b) forward ($0.7 < |\eta_2| < 1.5$) regions. The error bars shown represent correlated statistical uncertainties.

6.8.5 Jet η Bias

A comparison similar to the preceding ones can be performed to study the effect of the systematic jet η bias (described in the previous chapter) on the data β distributions. This bias has been measured [107] and a correction has been developed for jets with a cone size of $\mathcal{R} = 0.7$. The net effect of this bias is systematically to shift a jet's reconstructed η to a more central value, by a small amount (typically, $\Delta\eta < 0.02$). This effect is caused by the η dependence of the calorimeter energy response and to jet algorithm-related effects. For a cone size of $\mathcal{R} = 0.5$, this bias is expected to be less significant than for jets with $\mathcal{R} = 0.7$. In lieu of an η bias correction for the jet cone size ($\mathcal{R} = 0.5$) used in this analysis, the available correction was applied to data to (over)estimate the effect on the β distributions. Figure 6.33 shows the results of this comparison. For the central region, a small systematic shape change can be seen which seems unlikely to have been caused merely by statistical fluctuations.

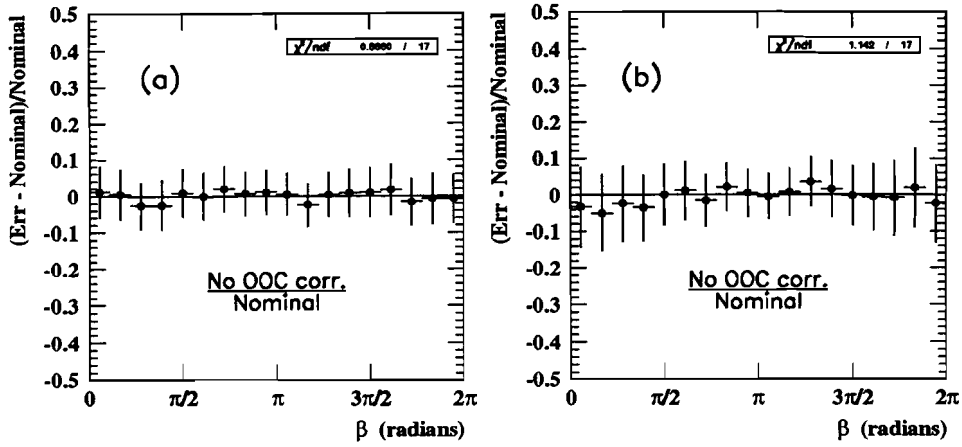

Figure 6.32: Variation in the data β distributions due to the out-of-cone showering component of the jet energy scale correction for (a) central ($|\eta_2| < 0.7$) and (b) forward ($0.7 < |\eta_2| < 1.5$) regions. The error bars shown represent correlated statistical uncertainties.

However, this shape involves a shift of less than 2% which is well below the level of the statistical uncertainties. The jet η bias uncertainty, which is 1.3% in the central region and 1.8% in the forward region, was included in the overall errors.

6.8.6 Multiple Interactions

To examine the effect of multiple interactions on the observed β patterns, we compare the data sample, in which the Multiple Interaction (MI) Flag was allowed to be 0, 1, 2 or 3, with a sample with tight restrictions placed on multiple interactions (MI Flag = 1 or 2) which effectively eliminates many events resulting from multiple $p\bar{p}$ interactions. The results of this comparison are shown in Fig. 6.34 along with binomial statistical errors. From these plots it is clear that there is no systematic change in the shape of the β distributions. The reduced χ^2 values, obtained by fitting the distributions to a line at 0, — 1.08 (central) and 0.59 (forward) — indicate that

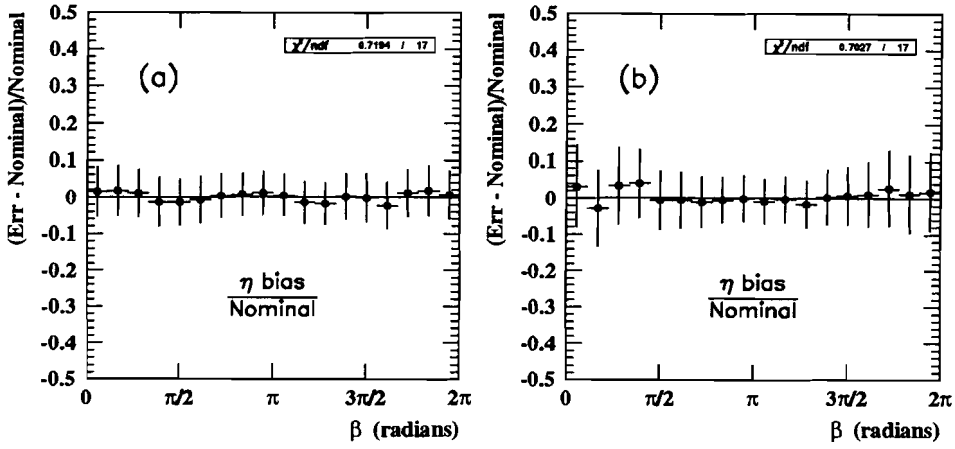

Figure 6.33: Variation in the data β distributions due to the η bias correction for central ($|\eta_2| < 0.7$) and forward ($0.7 < |\eta_2| < 1.5$) regions. The error bars shown represent correlated statistical uncertainties.

the distributions are consistent with the line.

6.8.7 Jet Reconstruction

The next source of systematic uncertainty to be considered is the jet reconstruction efficiency. Preliminary studies [111] done on jet reconstruction by varying the threshold of the jet tower seed have shown that there might be a drop-off in the efficiency for reconstructing jets with $E_T \sim 20$ GeV versus η. A conservative parametrization of the reconstruction efficiency as a function of the E_T and η of Jet 3 was constructed using the results of preliminary observations [114] and is shown in Fig. 6.35.

In addition, as discussed when the $\mathcal{R}$ distributions were examined, there is a systematic decrease of the acceptance of calorimeter jets, relative to particle jets, for jet reconstruction with $\mathcal{R} < 0.8$. In the analysis, the $\mathcal{R}$ distribution is cut below 0.6, so the region most affected by this effect is $0.6 < \mathcal{R} < 0.8$. Using the HERWIG

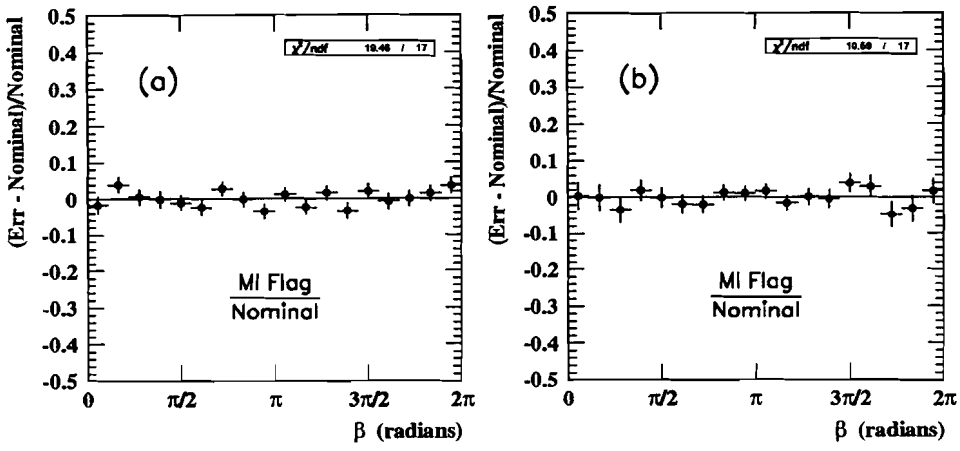

Figure 6.34: Variation in the β distributions due to the cuts applied to the Multiple Interaction (MI) Flag for the (a) central ($|\eta_2| < 0.7$) and (b) forward ($0.7 < |\eta_2| < 1.5$) regions. The error bars shown represent statistical uncertainties.

simulations of both calorimeter and particle jets, the effect of this acceptance in this $\mathcal{R}$ region is determined and the parametrized efficiency found to be:

$$\epsilon = 0.21 + 3.95(\mathcal{R} - 0.6), \text{ for } 0.6 < \mathcal{R} < 0.8. \tag{6.8}$$

Figure 6.36 shows the result of accounting for this effect in the calorimeter-level simulation. The $\mathcal{R}$ spectra above $\mathcal{R} = 0.6$ for particle and calorimeter jets now agree.

By applying these efficiencies to the data we obtain the variation in the β distribution which is shown in Fig. 6.37. Here it is seen that a shape change may occur, particularly in the forward distribution, with up to a 4.5% rise in the near beam direction (corresponding to higher $|\eta|$) and a 2.0% decrease in the far beam region. For the central β distribution, the rise in the near beam region is around 2.0% and the drop in the far beam region is 1.0%. Due to the strong error correlation between the samples used, the χ^2 values are not relevant here.

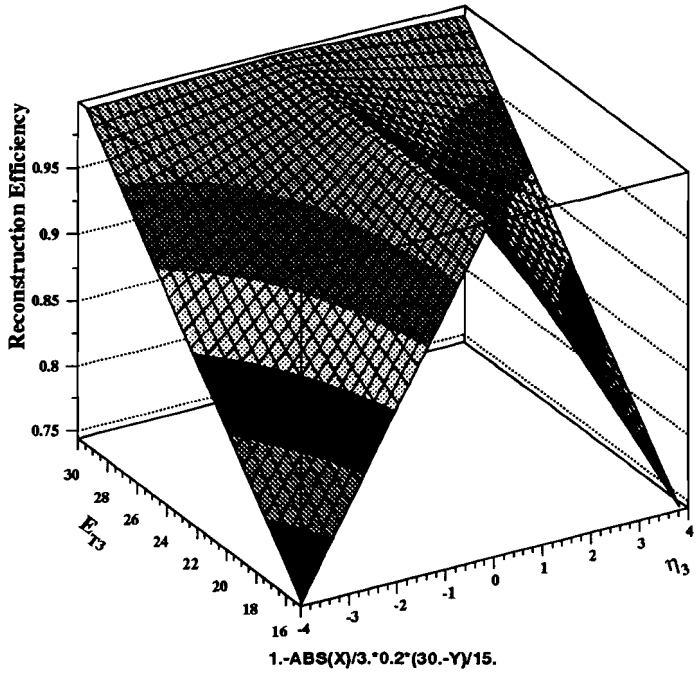

Figure 6.35: Conservatively parametrized reconstruction efficiency as a function of the E_T and η of Jet 3 when $|\eta_3| > 1.0$ or $E_{T3} < 30$ GeV. In the equation above, $X \equiv \eta_3$ and $Y \equiv E_{T3}$.

6.8.8 Z Vertex

The effect of the z vertex cut on the data was examined by comparing a sample that includes all events regardless of their z vertices, with one in which the measured vertex must be in $|z| < 50$cm. Figure 6.38 reflects the variation along with binomial errors. The fluctuations from this effect are small, there is no shape change and the distribution agrees with a line at 0, as is demonstrated by the reduced χ^2 values which are, respectively, 0.78 and 0.60 in the central and forward regions.

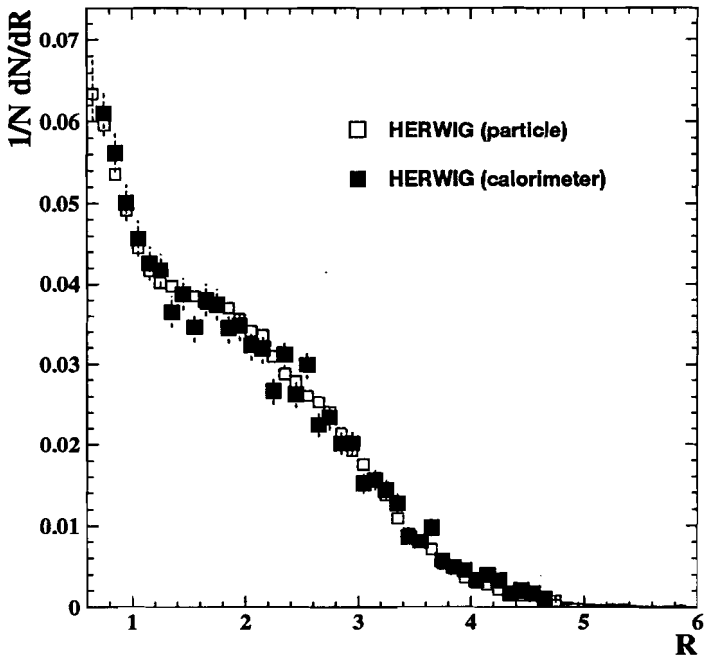

Figure 6.36: $\mathcal{R}$ distributions (cut below $\mathcal{R} = 0.6$), after correcting for calorimeter jet acceptance effects, for HERWIG at the particle level and calorimeter level. The error bars shown represent statistical uncertainties.

6.8.9 Jet Quality Cuts

To calculate the variation in the data due to the jet quality cuts applied we compared events satisfying these cuts (the "Nominal" sample) with those that did not. The rejected events ($\sim$ 10% of the original sample) had β distributions that deviated only slightly from those of accepted events. The jet quality cuts remove all "bad" events with a possible contamination of $\leq$ 2%. Therefore, the ratio $\frac{\text{Nominal}-0.02(\text{"Bad"})}{\text{Nominal}}$ was calculated from the β distributions in order to estimate the uncertainty of these cuts. The results are shown in Fig. 6.39 along with binomial statistical errors. It is clear from the plots that the overall effect of the jet quality cuts is quite small and that there are no systematic shape changes. The distribution is consistent with a line at

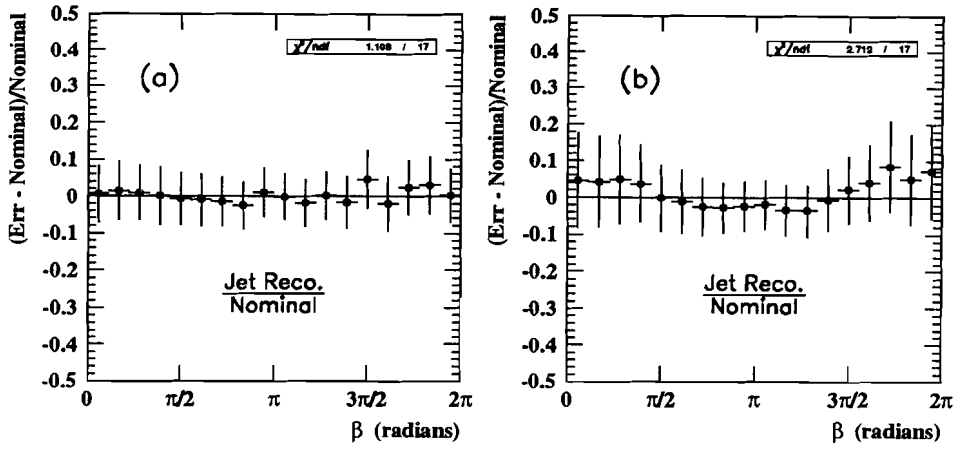

Figure 6.37: Variation in the data β distributions due to the reduced jet reconstruction efficiency for forward and low-E_T jets in the (a) central ($|\eta_2| < 0.7$) and (b) forward ($0.7 < |\eta_2| < 1.5$) regions. The error bars shown represent correlated statistical uncertainties.

0, given the reduced χ^2 values of 0.26 (central) and 0.36 (forward).

6.8.10 Additional Particle-Calorimeter Level Comparisons

Since a number of the conclusions from this analysis are derived from a comparison with MC at both the particle and parton levels, some possible sources of systematic uncertainty in these models must also be examined.

The first of these is the correspondence of the particle level (used in the comparisons with data) to the calorimeter level in the shower Monte Carlos. This would indicate the relative degree of the contributions from showering effects.

A direct comparison of both the particle-level and the calorimeter-level HERWIG samples was made to the data (with only statistical uncertainties included) by fitting the ratio $\frac{DATA}{HERWIG}$ to a line at 1. The results are given in Table 6.7 for the central, forward and combined η regions. From this table it can be concluded that the particle

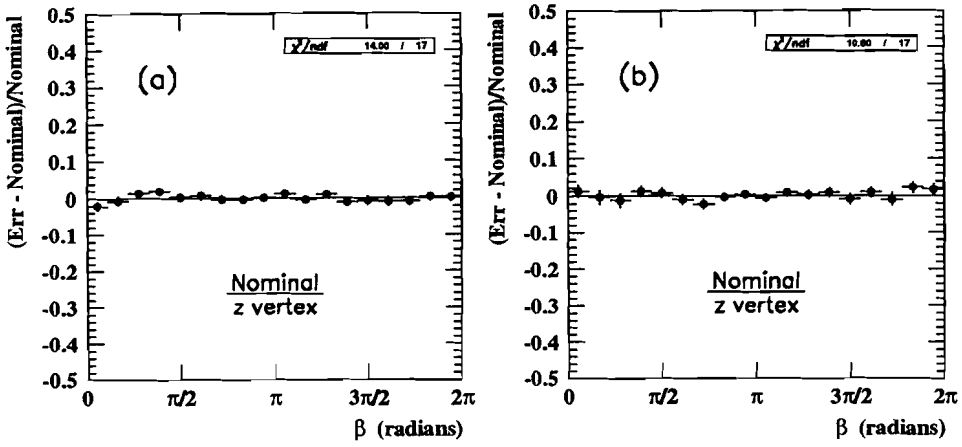

Figure 6.38: Variation in the β distributions due to the z vertex cut applied in both the (a) central ($|\eta_2| < 0.7$) and (b) forward ($0.7 < |\eta_2| < 1.5$) regions. The error bars shown represent statistical uncertainties.

and calorimeter-level β distributions are in comparable agreement with the data.

HERWIG Sample	$\|\eta_2\| < 0.7$	$0.7 < \|\eta_2\| < 1.5$	$\|\eta_2\| < 1.5$
Particle-level	0.94	1.31	1.32
Calorimeter-level	0.69	1.48	1.28

Table 6.7: Reduced χ^2 values of 18 degrees of freedom of fits to a line at 1 for the $\frac{DATA}{HERWIG}$ ratios of β distributions for central, forward and combined η regions. A comparison is thereby made between Monte Carlo simulations at the particle and at the calorimeter levels. The error bars shown represent statistical uncertainties.

The residual effect of the jet energy scale CAFIX v5.0 on the particle and calorimeter level MC β distributions was studied by applying a correction [115] derived from a HERWIG comparison of CAFIX corrected calorimeter jets with their corresponding particle jets. No significant effect was observed.

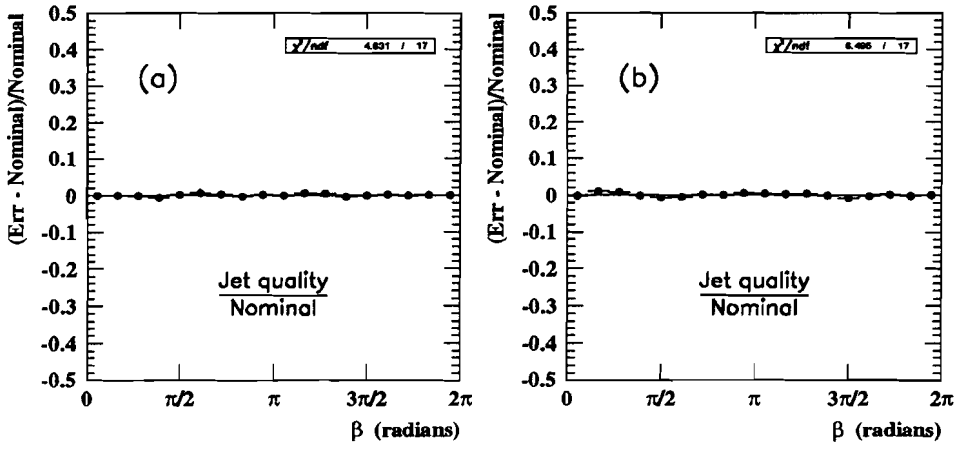

Figure 6.39: Variation in the β distributions due to the jet quality cuts used in the (a) central ($|\eta_2| < 0.7$) and (b) forward ($0.7 < |\eta_2| < 1.5$) regions. The error bars shown represent statistical uncertainties.

6.8.11 Calorimeter Resolution

The sensitivity of our conclusions to the calorimeter energy resolution used on Monte Carlo at the parton and particle levels was evaluated by varying the resolution applied by one standard deviation above and below the nominal value to JETRAD and PYTHIA simulations. The resultant RMS variation from both the high and low resolutions were averaged to obtain the values given in Table 6.6. The results obtained are presented in Figs. 6.40 and 6.41. Although the variation of some individual points is not insignificant, no systematic pattern emerges and the reduced χ^2 of all comparisons is less than 1. The uncertainty due to the calorimeter energy resolution was found to be 3.0% (central) and 3.6% (forward) in JETRAD, and 1.8% and 3.4% in PYTHIA. This uncertainty was included in the overall MC error.

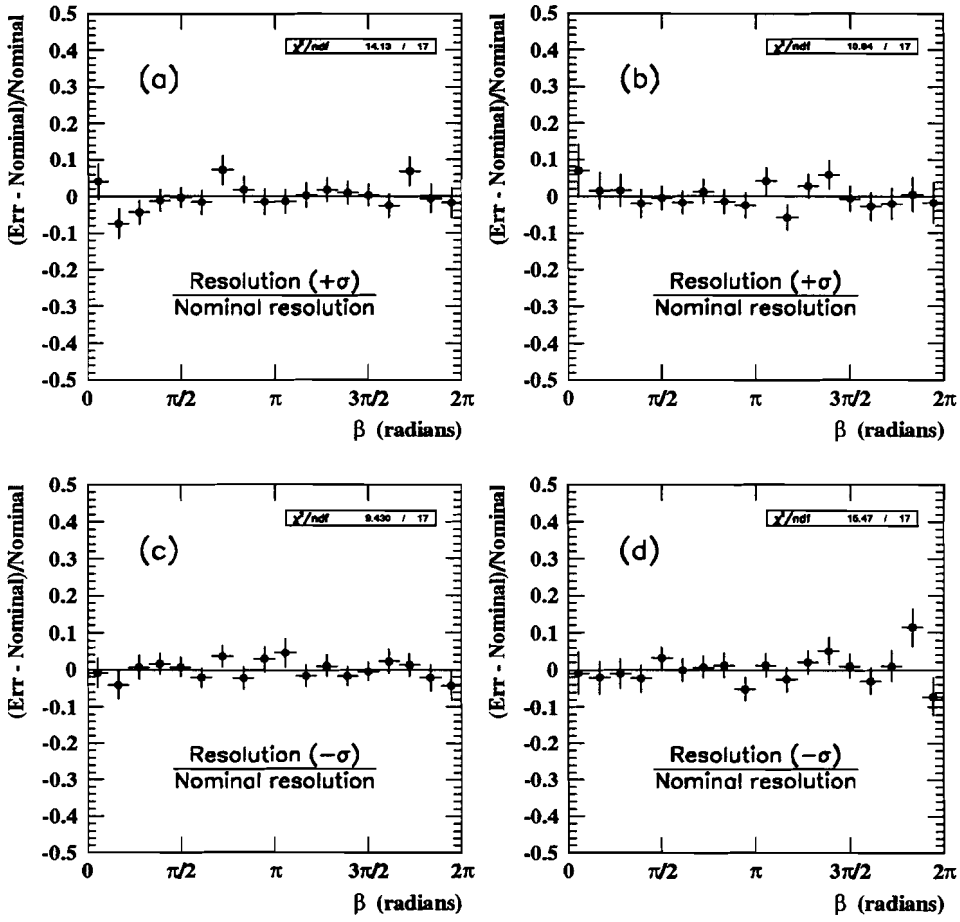

Figure 6.40: Variation in the JETRAD β distributions due to the calorimeter resolution for (a) and (c) central ($|\eta_2| < 0.7$) and (b) and (d) forward ($0.7 < |\eta_2| < 1.5$) regions. Corrections of one standard deviation above ($+\sigma$) and below ($-\sigma$) the nominal resolution were applied. The error bars shown represent statistical uncertainties.

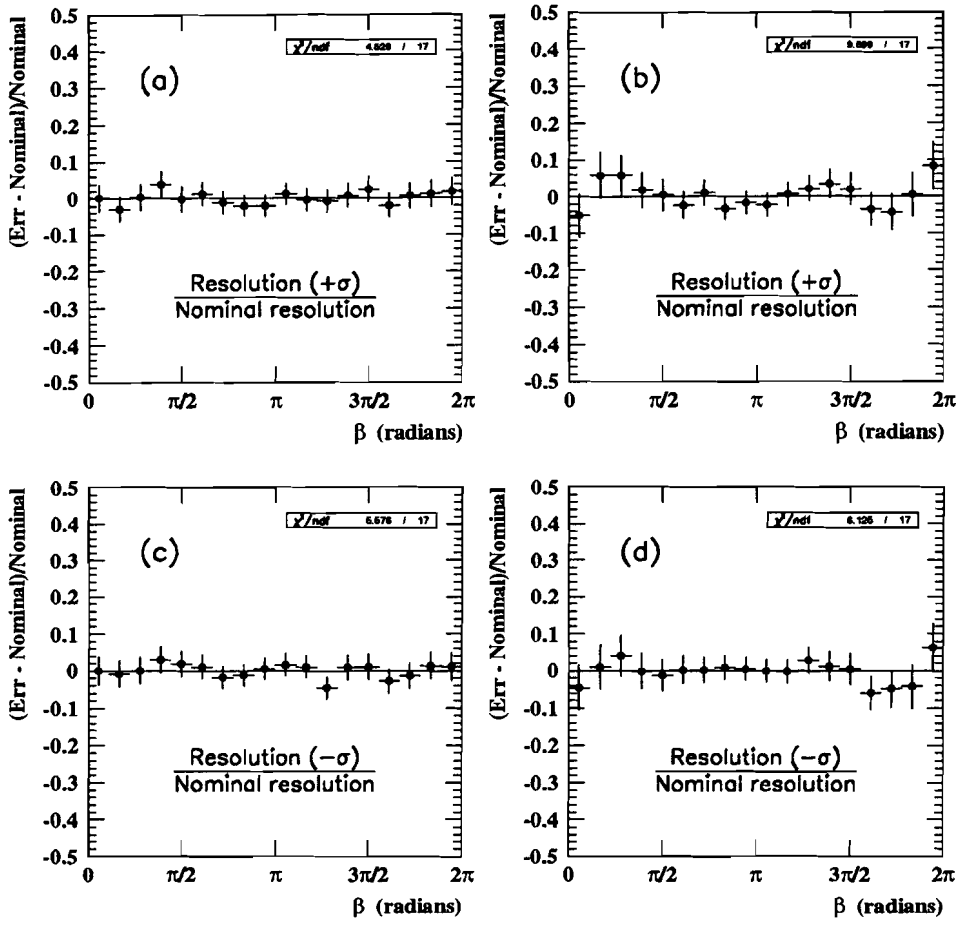

Figure 6.41: Variation in the PYTHIA β distributions due to the calorimeter resolution for (a) and (c) central ($|\eta_2| < 0.7$) and (b) and (d) forward ($0.7 < |\eta_2| < 1.5$) regions. Corrections of one standard deviation above ($+\sigma$) and below ($-\sigma$) the nominal resolution were applied. The error bars shown represent statistical uncertainties.

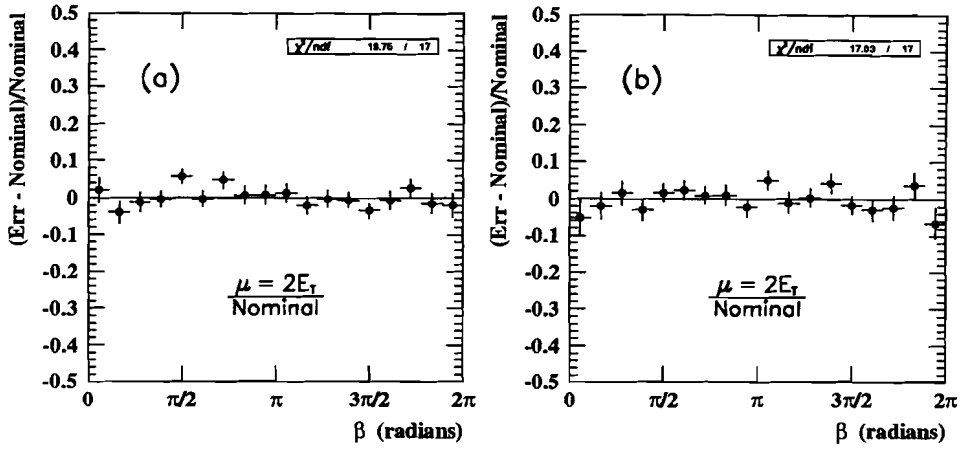

Figure 6.42: Variation in the JETRAD β distributions due to the choice of μ scale for (a) central ($|\eta_2| < 0.7$) and (b) forward ($0.7 < |\eta_2| < 1.5$) regions. The error bars shown represent statistical uncertainties.

6.8.12 Renormalization/Factorization Scale

To investigate the effect of the renormalization/factorization scale used in the MC, two different values were used: $\mu = 2E_T$ was compared to the reference scale used with JETRAD, $\mu = \frac{1}{2}E_T$. The E_T is that of the leading-E_T jet of the event. Figure 6.42 shows the results of this comparison. The statistical errors in this plot are noticeably smaller than in previous plots as the samples contain five and a half times the number of events of the other JETRAD samples used. In both the central and forward regions, the relative fractional differences are small and although there are indications of a possible shape change in the near-beam region, this effect is below the level of uncertainty in the theory.

6.8.13 Parton Distribution Functions

Lastly, the final potential source of systematic uncertainty to be investigated is the dependence of the MC β distributions on the parton distribution functions (pdfs). For this purpose we used JETRAD with two different pdfs which were tested against the reference pdf used in the analysis — CTEQ2MS. The pdfs used for comparison were the two extreme ones which gave the best and worst apparent agreement with the triple-differential cross section measurement [116] with Run 1A data. The mean of the two RMS variations is given in Table 6.6 for each η region. In Fig. 6.43 we can observe that, although CTEQ2ML shows a smaller shift than CTEQ2MF in the forward η region, and a comparable variation in the central region. Both pdfs agree (within statistics) with CTEQ2MS, with no clear change in the shape of the distributions.

6.8.14 Conclusions of Systematics

A number of potential sources of systematic uncertainties were studied in this analysis. While some minor variations in the observed patterns occur, none of the systematics alter the original comparisons of data with the Monte Carlo simulations. Specifically, some point-to-point variations are seen for some of the sources studied, and these uncertainties have been added in quadrature with the statistical variations. Furthermore, these systematic uncertainties are overshadowed by the statistical uncertainties in the study.

In order to relate the significance of the $\frac{DATA}{MONTE\ CARLO}$ comparisons to the magnitude of the overall uncertainty, we may apply the technique used to estimate the latter (the RMS variation) to the former comparisons. A caveat must be inserted

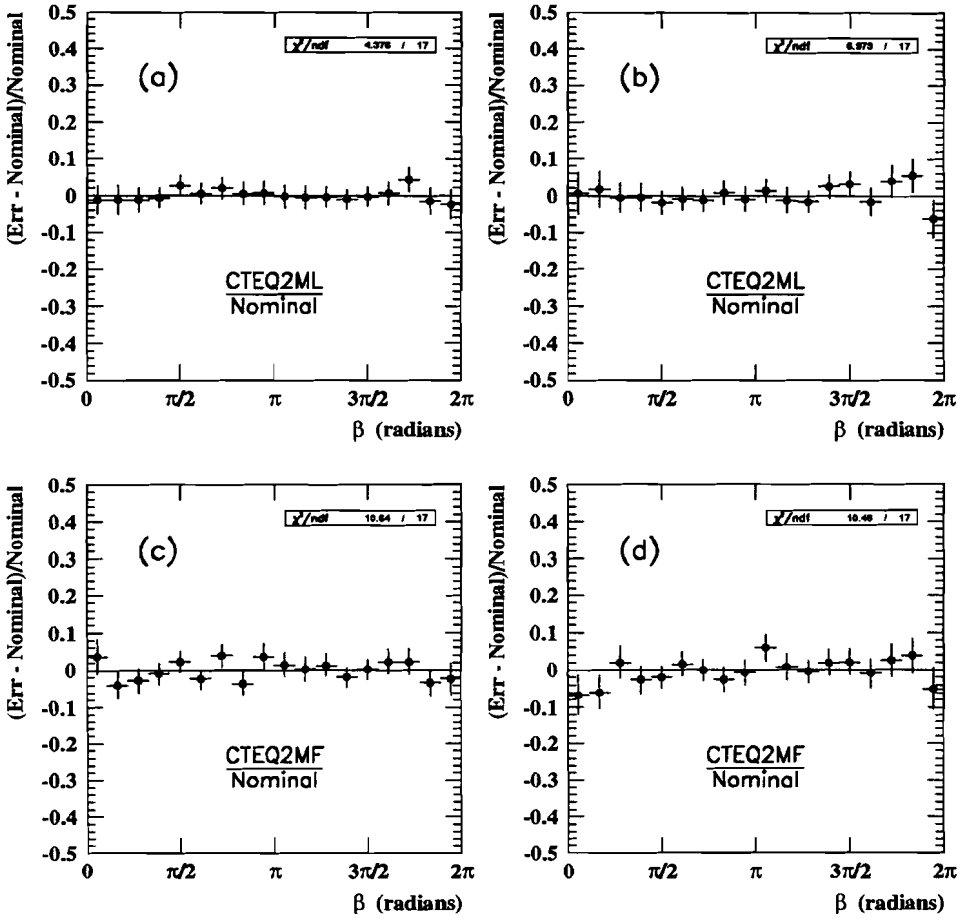

Figure 6.43: Variation in the JETRAD β distributions due to the parton distribution function used for (a) and (c) central ($|\eta_2| < 0.7$) and (b) and (d) forward ($0.7 < |\eta_2| < 1.5$) regions. The error bars shown represent statistical uncertainties.

Monte Carlo Sample	$\|\eta_2\| < 0.7$	$0.7 < \|\eta_2\| < 1.5$
HERWIG	4.9 (%)	7.6 (%)
ISAJET	12.2	12.3
PYTHIA:		
AO, SF	6.5	9.2
No AO, SF	15.5	20.3
AO, IF	10.8	14.2
JETRAD	5.8	8.2
(DATA Uncertainty)	(5.6)	(7.9)

Table 6.8: RMS variation of Monte Carlo β distributions relative to data for central and forward η regions. The overall uncertainty in the data is included for comparison.

before doing so. This method does not take into account any information about the shapes of the distributions [4] to which it is applied; it only considers variations of individual points. The results of this comparison are presented in Table 6.8 for purposes of illustration. The overall uncertainty in the data is also tabulated to facilitate the comparison. The RMS variations of HERWIG, PYTHIA (AO,SF) and JETRAD are comparable to the statistical $\oplus$ systematic uncertainty in the data for both central and forward pseudorapidities. The remaining samples' deviations, however, are significantly greater than the overall uncertainty in the data, as measured by this statistic.

[4] For the results of a shape analysis performed on the $\frac{DATA}{MONTE\ CARLO}$ ratios, please refer to Appendix B.

Chapter 7

Summary and Conclusions

This dissertation is an attempt at studying color coherence effects in multi-jet events in a broad region of pseudorapidity, and the first attempt at studying non-perturbative contributions to soft jet distributions in hadronic collisions. Although this investigation is far from complete, sufficient progress has been made so that it is important to report the current findings in a cohesive fashion.

The distribution of relatively soft jets within the calorimeter was measured in multi-jet events having an energetic primary jet with $E_T > 115$ GeV, as a means of observing the distribution of soft radiation in these events. Multi-jet events were used to investigate which features of color coherence are observed in hard QCD $2 \rightarrow 2$ processes having a variety of color connections among partons. Events with a secondary jets of $E_T > 15$ GeV were chosen in order to measure the soft jet distribution in the vicinity of a primary jet. These distributions were then compared to Monte Carlo simulations with various implementations of color coherence effects. To make the color coherence effects visible in the analysis, an angle β was defined which gives the angular orientation of the soft jet about the second primary jet,

relative to the event and beam plane. The division of the observed and simulated distributions of this angle demonstrates the topological features of the distributions of these soft jets.

The DØ detector has proven an excellent facility for making such a measurement. The segmentation and resolution of the calorimeter have allowed for unambiguous discrimination of relatively low-energy jet patterns. Additionally, the comprehensive trigger framework made possible relatively quick identification of useful events.

The pattern seen in the data was proven not to be the result of simple kinematics or detector effects. It was shown to be stable when subjected to various changes in the jet energy scale and resolution, number of hard interactions in the event, jet reconstruction efficiency, renormalization/factorization scale and the choice of parton distribution functions. The selection criteria used to choose the analysis sample resulted in reduced statistics, but in virtually no background contamination.

The observed β distributions in the central ($|\eta_2| < 0.7$) and forward ($0.7 < |\eta_2| < 1.5$) regions of pseudorapidity were compared to three Monte Carlo event generators: ISAJET, HERWIG and PYTHIA, each with different implementations of color coherence effects. ISAJET employed incoherent parton evolution and independent fragmentation, thus making no use of color connections among partons. HERWIG applied coherent parton evolution by means of angular ordering and azimuthal correlations in conjunction with the cluster model for fragmentation. PYTHIA allowed the turning off or on of the Angular Ordering constraint and the selection of string or independent models for fragmentation, while keeping the other properties of the Monte carlo generator unchanged. Consequently, three PYTHIA samples were compared to the data. One sample employed coherent parton evolution by means of

angular ordering and azimuthal correlations together with the string model for fragmentation. The second utilized incoherent parton evolution, but retained the string model for fragmentation. The third made use of coherent parton evolution and independent fragmentation. For the final sample, the partonic event generator JETRAD was employed to calculate the $\mathcal{O}(\alpha_s^3)$ tree-level $2 \rightarrow 3$ QCD predictions.

It is useful to take another look at the comparisons of data with the six Monte Carlo samples. A good way to highlight the comparisons is to divide the observed β distribution by that from each of the six simulations. Deviations from a flat line thus indicate the the level of disagreement of the simulations with data. A summary of the results of this analysis is now presented by combining the central and forward pseudorapidity regions into one. The $\frac{DATA}{MONTE\ CARLO}$ ratios for the combined region $|\eta_2| < 1.5$ are shown in Fig. 7.1.

By fitting the various $\frac{DATA}{MONTE\ CARLO}$ ratios of the β distributions in the combined η region to a line at 1, taking into account statistical and uncorrelated systematic uncertainties, a quantitative measure of the interference effects is obtained. A summary of these results is presented in Table 7.1, where the reduced χ^2 are given.

Monte Carlo Sample	χ^2/ndf $(\|\eta_2\| < 1.5)$
HERWIG	0.74
ISAJET	4.96
PYTHIA:	
AO, SF	1.28
No AO, SF	7.53
AO, IF	3.03
JETRAD	0.68

Table 7.1: Reduced χ^2 values of 18 degrees of freedom of fits to a line at 1 for the various $\frac{DATA}{MONTE\ CARLO}$ ratios of β distributions in the combined η region. Statistical and uncorrelated systematic uncertainties were taken into account.

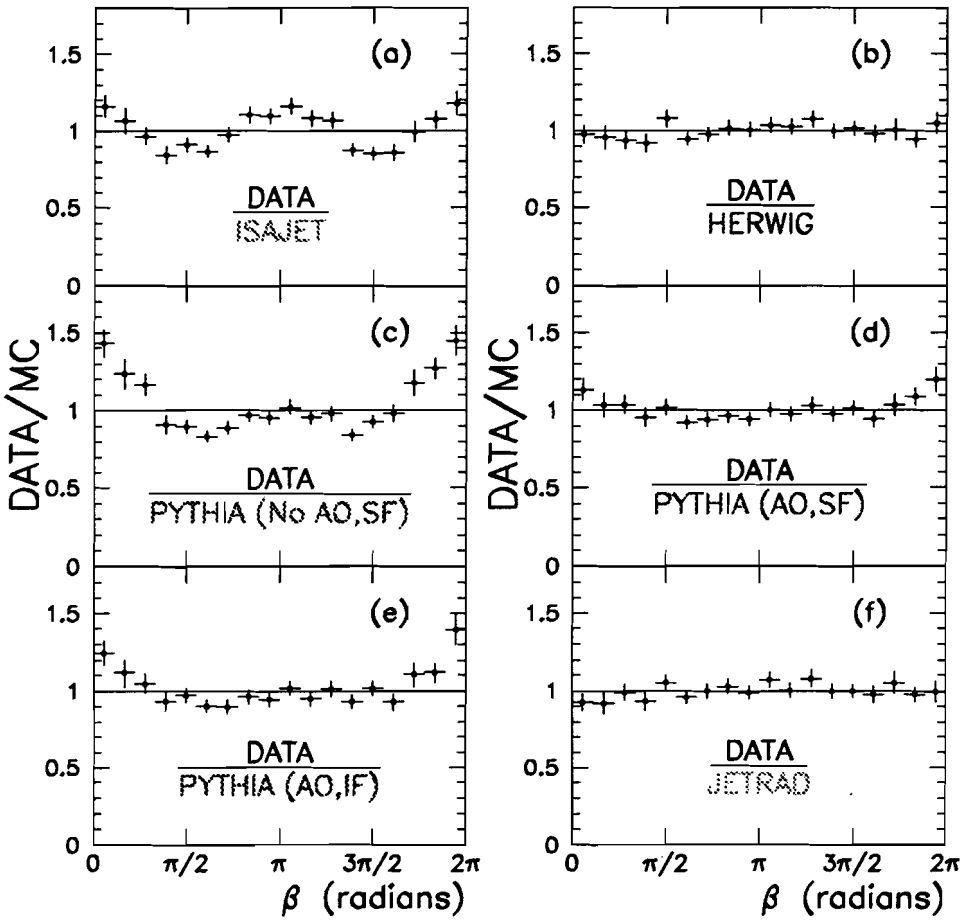

Figure 7.1: β ratios of data and (a) ISAJET, (b) HERWIG, PYTHIA with (c) Angular Ordering off and String Fragmentation, (d) Angular Ordering and String Fragmentation, (e) Angular Ordering and Independent Fragmentation and (f) JETRAD in the combined pseudorapidity region ($|\eta_2| < 1.5$). The error bars shown include statistical and uncorrelated systematic uncertainties.

Comparison of data and Monte Carlo samples in both central and forward regions show that:

- Event generators which incorporate color coherence effects by means of the Angular Ordering Approximation and through fragmentation models that take into account color connections between the partons (HERWIG, and PYTHIA with AO and string fragmentation), are in reasonable agreement with the data, with HERWIG more closely resembling the data.

- Event generators which do not include color coherence effects (ISAJET and PYTHIA with AO turned off) are inconsistent with the data. String fragmentation alone appears incapable of reproducing the the pattern observed in the data. Disregard of the color connections among partons seems to have consequences on the soft jet distributions that string fragmentation alone cannot account for.

- In the hard scattering region studied, an event generator (PYTHIA) demonstrates that Angular Ordering offers a greater contribution than the fragmentation model to color coherence effects, as presently modelled. This implies that perturbative QCD phenomena dominates the non-perturbative realm in this region. Furthermore, it was observed that hadronization, as modelled by HERWIG, had a negligible effect on the manifestation of color interference effects.

- The $\mathcal{O}(\alpha_s^3)$ tree-level QCD calculation (JETRAD) can largely account for the coherence effects seen in the data. This provides a test of perturbative QCD to the Leading Order in perturbation theory and indicates that the color co-

herence inherent in perturbative partonic processes survives non-perturbative hadronization, lending further support to the Local Parton-Hadron Duality hypothesis.

- Results from a comparison of data and ISAJET show no obvious increase in coherent radiation when the spatial separation between initial and final states diminishes.

Two caveats are appropriate with regards to the conclusions just drawn. Better event statistics would improve the comparisons with Monte Carlo and would make feasible expanding the pseudorapidity region examined. Secondly, a fourth PYTHIA sample would round out this investigation into incoherent effects. A sample with incoherent parton evolution and independent fragmentation would provide additional information about the total absence of color coherent contributions.

In summary, this dissertation should be viewed as an early step into the rich topic of color coherence at hadron colliders. There are a number of unexplored avenues remaining with jet events. For instance, it would be interesting to study the energy or particle flow *inside* a jet. Comparing distributions around (or inside) gluon and quark jets would also be illuminating. Lastly, there are other simulations with which the data could be compared. For example, the ARIADNE leading-order event generator uses a dipole approximation for color connections which should be able to model coherence effects.

With the upgrade of the DØ detector and with the great increase in event statistics for jet, W+jets and γ+jets events, it should be possible to expand this and other related analyses into new areas of study not possible with the current sample. To conclude, this dissertation has laid the foundation upon which the author hopes

others will build, through new studies of color coherence in hadronic collisions.

Appendix A

A Sample Three-Jet Event in the DØ Detector

In this appendix, several views of a three-jet event observed with the DØ detector are shown.

A complete view of the detector from above is presented in Fig. A.1. As depicted in the cartoon on the lower left of the picture, two ϕ quadrants (one on either side) of the detector are shown. A large amount of energy was collected in the Central Calorimeter (CC). It extends from the inner electromagnetic layers to the outermost coarse hadronic layer. The filled regions in this picture represent energy depositions greater than one GeV. Tracks of particles emanating from the point of collision are visible in the Central Detector (CD), located at the center of the doughnut-like CC. The planes surrounding the three calorimeter modules represent the muon system, which underwent an increasing number of hits in the small (θ) angle region near the beams from sprays of particles produced by spectator and beam-beam interactions.

Isolating just the calorimeter and the CD, Fig. A.2 is a full-ϕ view from below

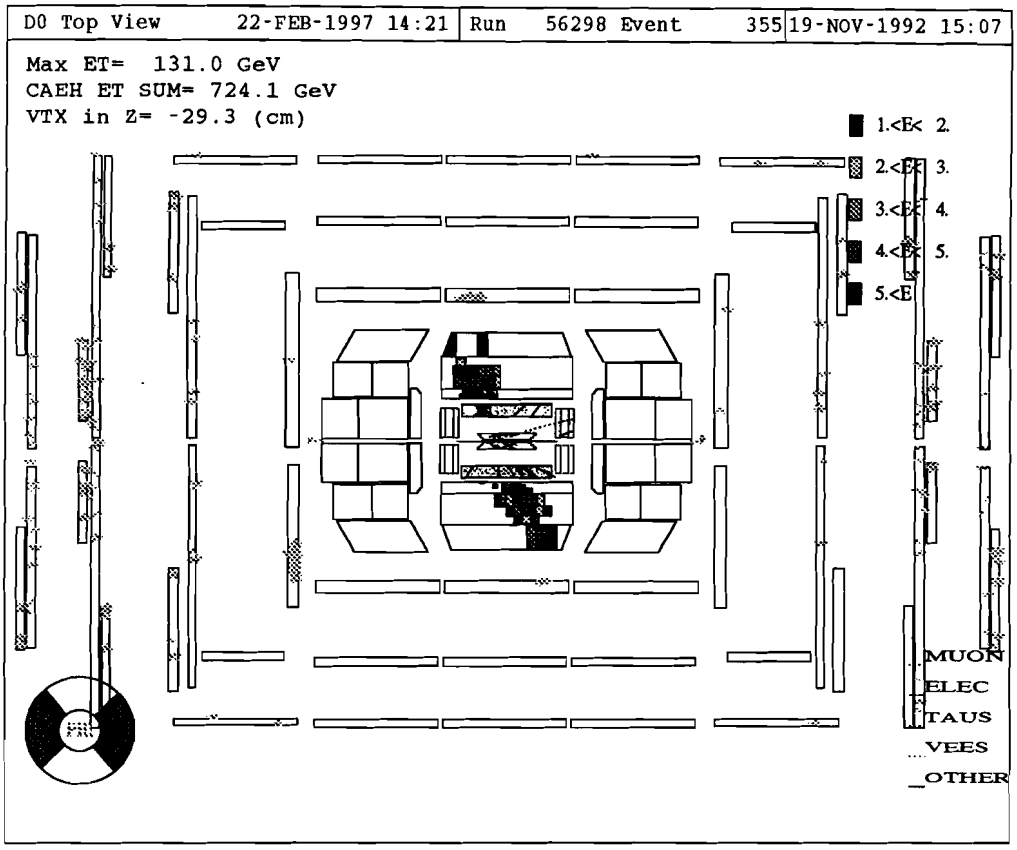

Figure A.1: View from above of a three-jet event in the DØ detector. All major parts of the detector are shown. The arrays of planes represent the muon system, which underwent an increasing number of particle hits near the beams, shown traversing the detector horizontally in the figure. The three calorimeter modules are shown near the middle, with a large amount of energy from the jets deposited in all layers of the Central Calorimeter. The key indicates the energy deposited in each cell. Particle tracks are visible in the Central Detector at the center of the picture.

showing large amounts of energy deposited by the jets in the CC. The particle tracks in the CD were projected to the x-z plane which is shown here. In this view, the two nearby jets (appearing near the bottom of the picture) cannot be clearly distinguished.

A different perspective is useful for observing the individual jets in the event. Figure A.3 is a view along the beam axis illustrating the energy deposition in cylindrical sections of the calorimeter and the tracks of particles in the CD. The radial

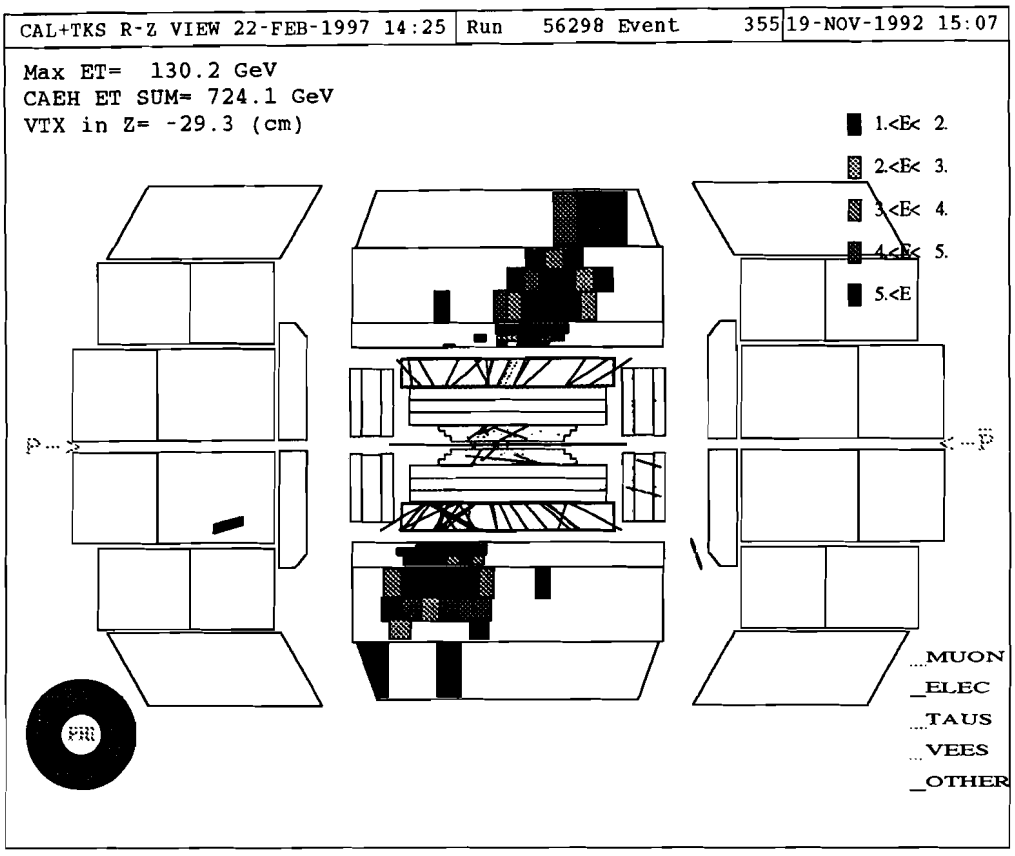

Figure A.2: View from below of a three-jet event in the DØ calorimeter. The key indicates the energy deposited in each cell of the calorimeter. The energy deposition by the jets occurred in all layers of the Central Calorimeter. The Central Detector is shown at the center of the figure.

distance in the calorimeter ϕ-sections illustrates the relative amounts of $\mathrm{E_T}$ measured in each. The jets are represented by localized clusters of electromagnetic and hadronic energy. Two opposing high-E_T jets are present in the event as well as a softer third jet located near one of the primary jets. In this view, it is possible to show the location in ϕ of the $\not\!\!E_{\mathrm{T}}$ vector, which appears as a thin spike, at the top of the figure. Its relatively small magnitude, 10.9 GeV, indicates that the mis-measured energy in this event is quite small.

If the cylindrical calorimeter were unfolded and laid flat, the three-jet event ob-

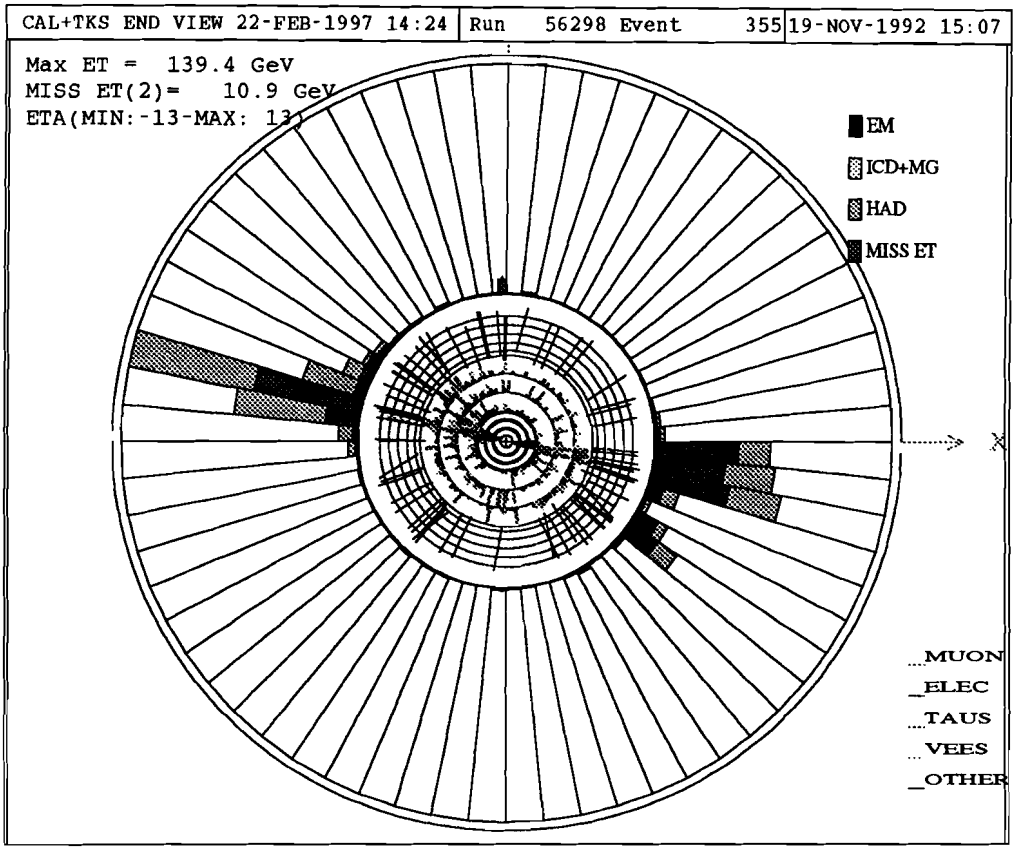

Figure A.3: End view of a three-jet event in the DØ calorimeter (outer) and Central Detector (inner). Two opposing energetic jets are present along with a smaller third jet (below the large jet on the right side of the picture).

served can be projected to the $\eta - \phi$ plane as shown in Fig. A.4, using the calorimeter's coordinates (η, ϕ_{cal}), where $\phi_{cal} \in (1, 64)$ is mapped one-to-one to $\phi \in (0, 2\pi)$. Clusters of energy deposited in the electromagnetic sections of the detector are darkly shaded while those deposited in the hadronic sections of the calorimeter appear in a light shade. The vertical scale corresponds to transverse energy. Note that the highest-E_T jet in the event, located at $(\eta, \phi) = (0.3, \pi)$, is isolated from the other jets and is nearly opposite to the second leading-E_T jet in ϕ. The third leading-E_T jet is found near the second jet. The small unshaded column representing the $\not\!\!E_T$ of the event is also depicted.

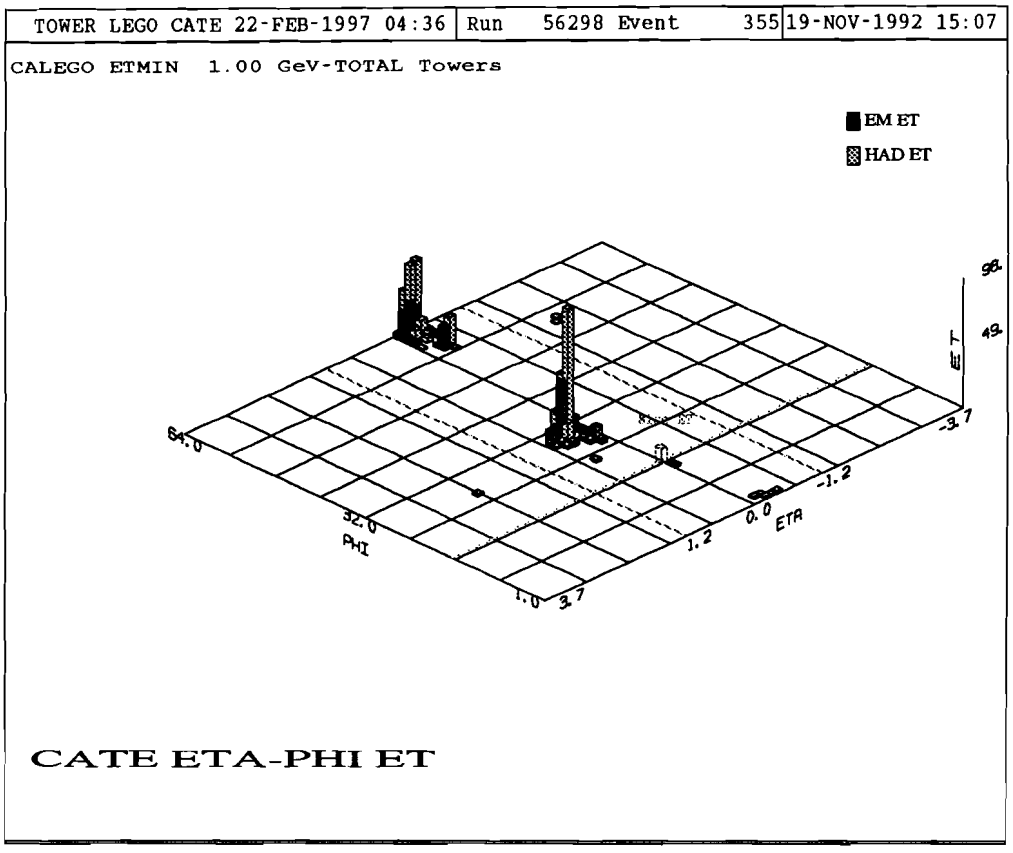

Figure A.4: A sample three-jet event in the unfolded DØ calorimeter. The calorimeter topology was unfolded to show the η–ϕ plane. The coverage of the central detector is indicated, along with the location of the Main Ring beam.

Appendix B

A Shape Analysis of the β Distributions

A study based on the shapes of the observed and simulated β distributions was performed. The Kolmogorov Test probability that two individual distributions arose from the same parent distribution, based solely on the shapes of these distributions, was calculated for each Monte Carlo sample and for the data. These probabilities are listed in Table B.1.

Monte Carlo Sample	$\lvert\eta_2\rvert < 0.7$	$0.7 < \lvert\eta_2\rvert < 1.5$	$\lvert\eta_2\rvert < 1.5$
HERWIG	49.0 (%)	26.4 (%)	11.4 (%)
ISAJET	1.8	0.5	0.1
PYTHIA:			
AO, SF	16.4	17.9	6.9
No AO, SF	0.0	0.0	0.0
AO, IF	0.2	0.6	0.0
JETRAD	23.7	1.4	6.0

Table B.1: Kolmogorov Test probabilities in shape analysis of data and Monte Carlo β distributions for central, forward and combined pseudorapidity regions.

For two histograms sampled randomly from the same parent distribution, the Kolmogorov probability will be evenly distributed from 0 to 100% provided the bin width is smaller than any significant physical effect. For larger binning the Kolmogorov probability is shifted upward. Thus, if one accepts two histograms as compatible when their Kolmogorov probability is greater than 5%, for instance, then truly compatible histograms should fail the test at most 5% of the time.

The results of this test conform with the conclusions of the χ^2 study presented in the main body of this dissertation. HERWIG agrees best with data and PYTHIA with AO and SF also agrees. ISAJET and PYTHIA with either no AO or with IF disagree with data. The agreement of JETRAD and data is fair.

Bibliography

[1] James Trager. *The People's Chronology.* Henry Holt and Company, Inc., 1992.

[2] M. Gell-Mann and Y. Ne'eman. *The Eightfold Way.* Benjamin, 1964.

[3] V. E. Barnes *et al.* "Observation of a Hyperon With Strangeness -3". *Phys. Rev. Lett.*, 12:204–206, 1964.

[4] M. Gell-Mann. "A Schematic Model of Baryons and Mesons". *Phys. Lett.*, 8:214–215, 1964.

[5] G. Zweig. "An SU(3) Model for Strong Interaction Symmetry and its Breaking". *CERN-TH-412*, page 74, February 1964.

[6] J. J. Aubert *et al.* "Experimental Observation of a Heavy Particle J". *Phys. Rev. Lett.*, 33:1404–1406, 1974.

[7] J. Augustin *et al.* "Discovery of a Narrow Resonance in e^+e^- Annihilation". *Phys. Rev. Lett.*, 33:1406–1408, 1974.

[8] S. L. Glashow, J. Iliopoulos and L. Maiani. "Weak Interactions with Lepton-Hadron Symmetry". *Phys. Rev.*, D2:1285–1292, 1970.

[9] M. L. Perl *et al.* "Evidence for Anomalous Lepton Production in e^+e^- Annihilation". *Phys. Rev. Lett.*, 35:1489–1492, 1975.

[10] S. W. Herb *et al.* "Observation of a Dimuon Resonance at 9.5 GeV in 400 GeV Proton-Nucleon Collisions". *Phys. Rev. Lett.*, 39:252–255, 1977.

[11] W. R. Innes *et al.* "Observation of Structure in the Upsilon Region". *Phys. Rev. Lett.*, 39:1240, 1977. *ERRATUM-ibid.39:1640,1977.*

[12] S. Abachi *et al.* (DØ Collaboration). "Obervation of the Top Quark". *Phys. Rev. Lett.*, 74:2632–2637, 1995.

[13] F. Abe *et al.* (CDF Collaboration). "Observation of Top Quark Production in $p\bar{p}$ Collisions". *Phys. Rev. Lett.*, 74:2626–2631, 1995.

[14] G. Arnison *et al.* (UA1 Collaboration). "Experimental Observation of Isolated Large Transverse Energy Electrons With Associated Missing Energy at $\sqrt{s} =$ 540 GeV". *Phys. Lett.*, B122:103–116, 1983.

[15] G. Arnison *et al.* (UA1 Collaboration). "Experimental Observation of Lepton Pairs of Invariant Mass Around 95 GeV/c^2 at the CERN SPS Collider". *Phys. Lett.*, B126:398–410, 1983.

[16] L. Montanet *et al.* "Review of Particle Properties. Particle Data Group". *Phys. Rev.*, D50:1173–1823, 1994.

[17] O. W. Greenberg. "Spin and Unitary Spin Independence in a Paraquark Model of Baryons and Mesons". *Phys. Rev. Lett.*, 13:598–602, 1964.

[18] A. Browman *et al.* "The Decay Width of the Neutral π Meson". *Phys. Rev. Lett.*, 33:1400, 1974.

[19] Francis Halzen and Alan D. Martin. *Quarks and Leptons: An Introductory Course in Modern Particle Physics.* John Wiley & Sons, Inc., 1984.

[20] G. Altarelli. *New Phenomena in Lepton-Hadron Physics*, volume 49 of *NATO Advanced Study Series, Series B.* Plenum Press, New York, 1978.

[21] G. Altarelli. "Partons in QCD". *Phys. Rep.*, 81:1, 1982.

[22] A. C. Benvenuti *et al.* (BCDMS Collaboration). "A High Statistics Measurement of the Proton Structure Functions $F_2(x, Q^2)$ and R from Deep Inelastic Muon Scattering at High Q^2". *Phys. Lett.*, B223:485, 1989.

[23] A. C. Benvenuti *et al.* (BCDMS Collaboration). "A High Statistics Measurement of the Deuteron Structure Functions $F_2(x, Q^2)$ and R from Deep Inelastic Muon Scattering at High Q^2". *Phys. Lett.*, B237:592, 1990.

[24] A. C. Benvenuti *et al.* (BCDMS Collaboration). "A Comparison of the Structure Functions F_2 of the Proton and the Neutron from Deep Inelastic Muon Scattering at High Q^2". *Phys. Lett.*, B237:599, 1990.

[25] M. Arneodo *et al.* (EMC Collaboration). "Measurements of the Nucleon Structure Function in the Range $0.002\ \mathrm{GeV}^2 < x < 0.17\ \mathrm{GeV}^2$ and $0.2\ \mathrm{GeV}^2 < Q^2 < 8\ \mathrm{GeV}^2$ in Deuterium, Carbon and Calcium". *Nucl. Phys.*, B333:1, 1990.

[26] D. Allasia *et al.* (NMC Collaboration). "Measurement of the Neutron and the Proton F(2) Structure Function Ratio". *Phys. Lett.*, B249:366–372, 1990.

[27] P. Amaudruz *et al.* (NMC Collaboration). "The Ratio $F_2(n)/F_2(p)$ in Deep Inelastic Muon Scattering". *Nucl. Phys.*, B371:3–31, 1992.

[28] P. Amaudruz *et al.* (NMC Collaboration). "Proton and Deuteron F_2 Structure Functions in Deep Inelastic Muon Scattering". *Phys. Lett.*, B295:159–168, 1992.

[29] W. T. Giele, E. W. N. Glover and D. A. Kosower. "The Inclusive Two Jet Triply Differential Cross Section". *Phys. Rev.*, D52:1486–1499, 1995. HEP-PH/9412338.

[30] J. Botts *et al.* (CTEQ Collaboration). "CTEQ Parton Distributions and Flavor Dependence of Sea Quarks". *Phys. Lett.*, B304:159–166, 1993. HEP-PH/9303255.

[31] M. Gluck, E. Reya and A. Vogt. "Parton Distributions for High-Energy Collisions". *Z. Phys.*, C53:127–134, 1992.

[32] A. D. Martin, W. J. Stirling and R. G. Roberts. "Parton Distributions Updated". *Phys. Lett.*, B306:145–150, 1993. *ERRATUM-ibid.B309:492,1993.*

[33] A. D. Martin, W. J. Stirling and R. G. Roberts. "Two Jet Hadroproduction as a Measure of the Gluon at Small x". *Phys. Lett.*, B318:184–188, 1993. HEP-PH/9309204.

[34] K. Müller (H1 Collaboration). "Results on the Proton Structure Function F_2 and the Diffractive Contribution to F_2". 1994. Contributed to 29$^{\underline{\text{th}}}$ Rencontres de Moriond: QCD and High Energy Hadronic Interactions, Meribel les Allues, France, 19–26 Mar 1994.

[35] G. Wolf (ZEUS Collaboration). In *Proceedings of International Workshop on Deep Inelastic Scattering*, Eilat, Israel, February 1994.

[36] M. Roco (ZEUS Collaboration). In *Proceedings of* $29^{\underline{\text{th}}}$ *Rencontres de Moriond*, 1994.

[37] Yu. L. Dokshitzer *et al.* *Columbia University Theoretical Physics*, 374, 1987.

[38] S. Abachi *et al.* (DØ Collaboration). "Results on Soft Gluon Resummation and Color Coherence in $p\bar{p}$ Collisions at $\sqrt{s} = 1.8$ TeV". *Fermilab*, Conf-95/182-E, 1995.

[39] W. Bartel *et al.* (JADE Collaboration). "Experimental Study of Jets in Electron - Positron Annihilation". *Phys. Lett.*, 101B:129, 1981.

[40] W. Bartel *et al.* (JADE Collaboration). "Particle Distribution in Three Jet Events Produced by e^+e^- Annihilation". *Z. Phys.*, C21:37, 1983.

[41] W. Bartel *et al.* (JADE Collaboration). "Test of Fragmentation Models by Comparison with Three Jet Events Produced in $e^+e^- \rightarrow$ Hadrons". *Phys. Lett.*, 134B:275, 1984.

[42] H. Aihara *et al.* (TPC/2γ Collaboration). "Tests of Models for Parton Fragmentation Using Three Jet Events in e^+e^- Annihilation at $\sqrt{s} = 29$ GeV". *Phys. Rev. Lett.*, 54:270, 1985.

[43] H. Aihara *et al.* (TPC/2γ Collaboration). "Tests of Models for Quarks and Gluon Fragmentation in e^+e^- Annihilation at $\sqrt{s} = 29$ GeV". *Z. Phys.*, C28:31, 1985.

[44] M. Althoff *et al.* (TASSO Collaboration). "A Study of Three Jet Events in e^+e^- Annihilation Into Hadrons at 34.6 GeV *c.m.* Energy". *Z. Phys.*, C29:29, 1985.

[45] H. Aihara *et al.* (TPC/2γ Collaboration). "Comparison of the Particle Flow in $q\bar{q}g$ and $q\bar{q}\gamma$ Events in e^+e^- Annihilation". *Phys. Rev. Lett.*, 57:945, 1986.

[46] P. D. Sheldon *et al.* (MARK2 Collaboration). "A Comparison of the Particle Flow in Three Jet and Radiative Two Jet Events from e^+e^- Annihilation at $E_{cm} = 29$ GeV". *Phys. Rev. Lett.*, 57:1398, 1986.

[47] M. Z. Akrawy *et al.* (OPAL Collaboration). "A Study of Coherence of Soft Gluons in Hadron Jets". *Phys. Lett.*, B247:617–628, 1990.

[48] M. Z. Akrawy *et al.* (OPAL Collaboration). "A Model Independent Observation of the String Effect Using Quark Tagging at LEP". *Phys. Lett.*, B261:334–346, 1991.

[49] P. D. Acton *et al.* (OPAL Collaboration). "A Study of Two Particle Momentum Correlations in Hadronic Z^0 Decays". *Phys. Lett.*, B287:401–412, 1992.

[50] P. D. Acton *et al.* (OPAL Collaboration). "QCD Coherence Studies Using Two Particle Azimuthal Correlations". *Z. Phys.*, C58:207–218, 1993.

[51] M. Acciarri *et al.* (L3 Collaboration). "Evidence for Gluon Interference in Hadronic Z Decays". *Phys. Lett.*, B353:145–154, 1995.

[52] F. Borcherding (DØ Collaboration). "A Search for Rapidity Gaps in Jet Events and a Study of Color Coherence in Multi-Jet Events at DØ". 1993. Presented at $9^{\underline{\text{th}}}$ Topical Workshop on Proton – Anti-proton Collider Physics, Tsukuba, Japan, 18–22 Oct 1993.

[53] F. Abe *et al.* (CDF Collaboration). "Evidence for Color Coherence in $p\bar{p}$ Collisions at $\sqrt{s} = 1.8$ TeV". *Phys. Rev.*, D50:5562–5579, 1994.

[54] J. Jaques. *Study of Color Coherence Effects in $\bar{p}p$ Collisions at $\sqrt{s} = 1.8$ TeV.* PhD thesis, University of Notre Dame, Notre Dame, Indiana, October 1996.

[55] R. K. Ellis, G. Marchesini and B. R. Webber. "Soft Radiation in Parton-Parton Scattering". *Nucl. Phys.*, B286:643–656, 1987. *ERRATUM-ibid.B294:1180,1987.*

[56] F. Fiorani, G. Marchesini and L. Reina. "Soft Gluon Factorization and Multi-Gluon Amplitude". *Nucl. Phys.*, B309:439, 1988.

[57] G. Marchesini and B. R. Webber. "Monte Carlo Simulation of General Hard Processes with Coherent QCD Radiation". *Nucl. Phys.*, B310:461–526, 1988.

[58] A. Bassetto, M. Ciafaloni and G. Marchesini. "Jet Structure and Infrared Sensitive Quantities in Perturbative QCD". *Phys. Rept.*, 100:201, 1984.

[59] Yu. L. Dokshitzer, V. A. Khoze, A. H. Mueller and S. I. Troyan. *Basics of Perturbative QCD.* Editions Frontières, 1991.

[60] B. Andersson, G. Gustafson and B. Söderberg. "A General Model for Jet Fragmentation". *Z. Phys.*, C20:317, 1983.

[61] A. Krzywicki and B. Petersson. *Phys. Rev.*, D6:924, 1972.

[62] J. Finnkelstein and R. D. Peccei. *Phys. Rev.*, D6:2606, 1972.

[63] B. R. Webber. "A QCD Model for Jet Fragmentation Including Soft Gluon Interference". *Nucl. Phys.*, B238:492–528, 1984.

[64] T. D. Gottschalk. "A Simple Phenomenological Model for Hadron Production from Low Mass Clusters". *Nucl. Phys.*, B239:325, 1984.

[65] T. Sjöstrand. *International Journal of Modern Physics*, A3:751, 1988.

[66] T. Sjöstrand. "Pythia 5.7 and Jetset 7.4 Physics and Manual". *CERN-TH-7112-93*, 1994.

[67] P. Edén. *Lund Theoretical Physics*, 96-20:1, 1996.

[68] A. Ali, J. G. Korner, G. Kramer and J. Willrodt. "Heavy Quarks in e^+e^- Annihilation". *Nucl. Phys.*, B168:409, 1980.

[69] D. Amati and G. Veneziano. "Preconfinement as a Property of Perturbative QCD". *Phys. Lett.*, 83B:87–92, 1979.

[70] H.-U. Bengtsson and T. Sjöstrand. "The Lund Monte Carlo for Hadronic Processes: Pythia Version 4.8". *Comput. Phys. Commun.*, 46:43, 1987.

[71] G. Altarelli and G. Parisi. "Asymptotic Freedom in Parton Language". *Nucl. Phys.*, B126:298, 1977.

[72] T. Sjöstrand. "A Model for Initial State Parton Showers". *Phys. Lett.*, 157B:321, 1985.

[73] M. Bengtsson, T. Sjöstrand and M. van Zijl. "Initial State Radiation Effects on W and Jet Production". *Z. Phys.*, C32:67, 1986.

[74] B. R. Webber. "Monte Carlo Simulation of Hard Hadronic Processes". *Ann. Rev. Nucl. Part. Sci.*, 36:253, 1986.

[75] T. Sjöstrand. Private communication.

[76] G. Marchesini, B. R. Webber, G. Abbiendi, I. G. Knowles, M. H. Seymour and L. Stanco. "HERWIG: A Monte Carlo Event Generator for Simulating Hadron

Emission Reactions With Interfering Gluons. Version 5.1 — April 1991". *Comput. Phys. Commun.*, 67:465–508, 1991.

[77] F. E. Paige and S. D. Protopopescu. "ISAJET 5.20: A Monte Carlo Event Generator for pp and $\bar{p}p$ Interactions". *BNL Report*, 38304, March 1986.

[78] T. Sjöstrand. "A Model for Initial State Parton Showers". *Phys. Lett.*, 157B:321, 1985.

[79] G. C. Fox and S. Wolfram. "A Model for Parton Showers in QCD". *Nucl. Phys.*, B168:285, 1980.

[80] R. Field and R. Feynman. "A Parametrization of the Properties of Quark Jets". *Nucl. Phys.*, B136:1, 1978.

[81] W. T. Giele, E. W. N. Glover and D. A. Kosower. "The Two-Jet Differential Cross Section at $\mathcal{O}(\alpha_s^3)$ in Hadron Collisions". *Phys. Rev. Lett.*, 73:2019–2022, 1994.

[82] Joey Thompson. "Introduction to Colliding Beams at Fermilab". Technical Report FERMILAB-TM-1909, Fermi National Accelerator Laboratory, October 1994.

[83] S. Abachi *et al* (DØ Collaboration). "The DØ Detector". *Nucl. Instrum. Meth.*, A338:185–253, 1994.

[84] Fabrice Feinstein. *Etude d'un Détecteur à Rayonnement de Transition pour l'Expérience DØ au FNAL.* PhD thesis, Université de Paris-Sud, Centre d'Orsay, Paris, France, Juin 1988.

[85] C. W. Fabjan. "Calorimetry in High-Energy Physics". In *Lectures given at the NATO Advanced Studies Institute on Techniques and Concepts in High-Energy Physics, St. Croix, Virgin Islands, USA*, August 2–13 1984.

[86] D. H. Perkins. *Introduction to High Energy Physics.* Addison-Wesley, third edition, 1987.

[87] William Joseph Thompson. *Search for the Top Quark in the Muon + Jets Channel at DØ.* PhD thesis, State University of New York at Stony Brook, Stony Brook, New York, February 1994.

[88] M. Abolins *et al.* (DØ Calorimeter Group). "Hadron and Electron Response of Uranium Liquid Argon Calorimeter Modules for the DØ Detector". *Nucl. Instrum. Meth.*, A280:36, 1989.

[89] S. Abachi *et al.* (DØ Collaboration). "Beam Tests of the DØ Uranium Liquid Argon End Calorimeters". *Nucl. Instrum. Meth.*, A324:53–76, 1993.

[90] M. Banner *et al.* (UA2 Collaboration). "Observation of Very Large Transverse Momentum Jets at the CERN $p\bar{p}$ Collider". *Phys. Lett.*, B118:203, 1982.

[91] G. Arnison *et al.* (UA1 Collaboration). "Observation of Jets in High Transverse Energy Events at the CERN $p\bar{p}$ Collider". *Phys. Lett.*, 123B:115, 1983.

[92] F. Abe *et al.* (CDF Collaboration). "Measurement of the Inclusive Jet Cross Section in $p\bar{p}$ Collisions at $\sqrt{s} = 1.8$ TeV". *Phys. Rev. Lett.*, 62:613, 1989.

[93] G. Arnison *et al.* (UA1 Collaboration). "Hadronic Jet Production at the CERN $p\bar{p}$ Collider". *Phys. Lett.*, 132B:214, 1983.

[94] F. Abe *et al.* (CDF Collaboration). "The Dijet Angular Distribution in $p\bar{p}$ Collisions at $\sqrt{s} = 1.8$ TeV". *Phys. Rev. Lett.*, 69:2896–2900, 1992.

[95] N. J. Hadley. "Cone Algorithm for Jet Finding". DØ Note #904 (unpublished), November 1989.

[96] R. Astur. "Study of Fake Jets in the DØ Detector". DØ Note #1662 (unpublished), March 1993.

[97] V. D. Elvira, G. Blazey and R. Astur. "A Study of Standard Jet Cuts and their Efficiencies Using DØ Collider Data". DØ Note #1763 (unpublished), June 1993.

[98] M. Bhattacharjee, V. D. Elvira and G. Blazey. "Efficiencies of the Standard Jet Cuts for Cone Sizes: 0.3, 0.5, 0.7". DØ Note #2197 (unpublished), July 1994.

[99] A. Milder and R. Astur. DØ Note #1595 (unpublished), December 1992.

[100] R. Kehoe. DØ Note #2052 (unpublished), February 1994.

[101] R. Kehoe. DØ Note #2053 (unpublished), March 1994.

[102] R. Kehoe and R. Astur. "Determination of the Hadronic Energy Scale of DØ Calorimetry (CAFIX version 5.0)". DØ Note #2908 (unpublished), May 1996.

[103] J. Bantly. "Multiple Interaction Tool Study". DØ Note #1849 (unpublished), August 1993.

[104] F. Abe *et al.* (CDF Collaboration). "Measurement of the Isolated Prompt Photon Cross-Sections in $p\bar{p}$ Collisions at $\sqrt{s} = 1.8$ TeV". *Phys. Rev. Lett.*, 68:2734–2738, 1992.

[105] M. Bhattacharjee, S.Y. Choi, V.D. Elvira, S. Grinstein and R. Hirosky. "Jet Energy Resolutions". DØ Note #2887 (unpublished), May 1996.

[106] Victor Daniel Elvira. *Measurement of the Inclusive Jet Cross Sections at* $\sqrt{s} =$ 1.8 *TeV with the DØ Detector.* PhD thesis, Universidad de Buenos Aires, Buenos Aires, Argentina, 1994.

[107] V.D. Elvira. "Jet η Bias and Resolution". DØ Note #2173 (unpublished), June 8 1994.

[108] B. Abbott, M. Bhattacharjee, V. D. Elvira, F. Nang and H. Weerts. "Fixed Cone Jet Definitions in DØ and $\mathcal{R}_{\rm sep}$". DØ Note #2885 (unpublished), March 21 1996.

[109] W. G. D. Dharmaratna and R. Raja. "The DØ Shower Library — Version 2.0". DØ Note #1730 (unpublished), May 12 1993.

[110] T. Joffe-Minor and R. Astur. "A Study of the Effects of the CAFIX Energy Scale Corrections". DØ Note #2211 (unpublished), July 26 1994.

[111] R. Hirosky. "A Data-based Estimate of Jet Reconstruction Efficiencies". DØ Note #2369 (unpublished), November 30 1994.

[112] V. D. Elvira, G. Blazey and R. Astur. "A Study of Standard Jet Cuts and their Efficiencies Using DØ Collider Data". DØ Note #1763 (unpublished), June 1993.

[113] K. Fatyga. Private communication.

[114] R. Hirosky. Private communication.

[115] G. DiLoretto. Private communication.

[116] F. Nang. Private communication.